CHAPTER 5: FREEZE-THAW EFFECT

5.1 Introduction

Recent published data (NIST 2014) indicated that approximately 102 freezing and thawing cycles occur annually in Michigan. The freeze-thaw cycles have their documented detrimental effect on roads and bridges, but little is known about the effect of freeze-thaw cycles on highway bridge beams prestressed with CFRP materials. Earlier research studies showed conflicting results. For instance, on study on FRP material showed that extreme low temperatures can cause micro cracking in the fiber matrix and high residual stress due to discrepancies in coefficients of thermal expansion of the constituent elements (Dutta 1988). However, Karbhari and Pope (1994) showed that FRP strength increases due to hardening at low temperature. On the other hand, Cusson and Xi (2002) reported 10 % reduction in the tensile strength of CFRP bars after exposure to 250 freeze-thaw cycles for 750 hrs.

The performance of CFRP-concrete bond at low temperatures has been the subject of several experimental studies (Green et al. 1997 & 2000; El badry et al. 2000; Subramaniam et al. 2008; Kim et al. 2011). Some researchers reported increased bond strength between CFRP and concrete under certain conditions. Whereas, others highlighted the detrimental effect of freeze thaw cycle on CFRP-concrete bond strength. Part of the dilemma is that concrete itself loses strength with the exposure to extreme temperatures (Shoukry et al. 2011).

Fewer researchers focused on FRP behavior in prestressed members at different temperature conditions. Bryan and Green (1996) studied the short-term behavior of concrete beams prestressed with 8 mm diameter Leadline CFRP tendons at low temperature. Based on the results, the flexural behavior of the beams was unaffected by short-term exposure to low temperature. In addition, the ultimate stresses and strains in CFRP tendons exceeded those reported by the manufacturer. Sayed-Ahmed and Shrive (1998) investigated the thermal variation effect on post-tensioned CFRP prestressing tendons. In their experimental study, thermal and flexural tests were carried out on masonry diaphragm walls prestressed concentrically with CFRP Leadline tendons. It was reported that the level of prestressing force in the Leadline tendons increased with the rise in temperature and decreased with the decrease in temperature. El-Hacha et al. (2004) studied the behavior of precracked concrete beams strengthened with prestressed CFRP sheets at low temperature. It was

concluded that the decrease in temperature did not adversely affect the flexural behavior of beams strengthened with prestressed CFRP sheets. Saiedi et al. (2013) studied the behavior of concrete beams prestressed with CFRP Leadline rods under sustained load and low temperature environments. Results showed that the bond between CFRP rods and concrete was affected negatively by such exposure causing reduction in the strength of prestressed beams.

Many existing design codes and guidelines in USA, Canada and Japan have were developed to account for potential deterioration of CFRP material caused by environmental and long-term effects (Ceroni et al. 2006). This is achieved by multiplying the guaranteed strength of the CFRP material by an environmental reduction factor less than 1.0. However, it should be noted that an unjustified reduction of material strength often leads to multiple design issues and results in congested sections with potential for further construction and service concerns. Therefore, the experimental program outlined in this chapter was conducted to evaluate the effect of freeze-thaw exposure on unbonded prestressed CFRP strands and CFRP prestressed concrete beams.

Two sets of CFRP specimens were prepared and subjected to successive 300 cycles of freezing and thawing induced in a large-scale environmental chamber. The first set included the four decked bulb T beams F1, F2, H1, and H2, that were tested before to the post-cracking stage and presented in the last chapter. The other set included five new CFCC strands stressed to 50.1 kip (223 kN) representing 82.5 % of the guaranteed tensile capacity (60.7 kip or 270 kN). The freeze-thaw test was conducted in accordance with ASTM C666/C 666M-03: “Standard Test Method for Resistance of Concrete to Rapid Freezing and Thawing”. After completing the freeze-thaw test, the CFRP prestressed concrete beams were tested to failure under three-point-load test setup, whereas the post-tensioned CFCC specimens were tested through uniaxial tensile test to determine the impact of successive freeze-thaw cycles on the residual strength of the prestressed CFCC strands. The following sections describe the specimen’s preparation, instrumentation, testing program and main finding and results of freeze-thaw test, flexural test of decked bulb T beams, and uniaxial test of CFCC strands.

5.2 Decked Bulb T Beams

5.2.1 Test setup

A special tempering tank was constructed inside the environmental chamber to accommodate the four decked bulb beams so that the temperature along the beam surfaces is constant at each phase of the test. The tempering tank had a length of 17 ft (5.2 m), a width of 48 in. (1.22 m), and a depth of 35 in. (889 mm) and was placed on a wooden platform deck mounted on steel adjustable chairs spaced at 2 ft (610 mm) on center with a height of 10 in. (254 mm). The tank was designed with two access holes at the sides for installing conduits in order to transfer water from the storage reservoir in the thawing phase of the freeze-thaw test. After constructing the tempering tank, the four decked bulb T beams were instrumented with two thermocouples at the center of the bottom flange and were placed inside the tank. Meanwhile, four concrete cylinders of the same batch of concrete used to cast the beams were prepared, labelled and placed inside the tank to evaluate the effect of freeze-thaw cycles on the concrete compressive strength. Air ducts were arranged inside the chamber and the beams were covered with layers of Styrofoam to ensure constant temperature along the beam length. Figure 5.2-1 through Figure 5.2-7 show the environmental chamber, construction of the tank, and the preparation for the test.

Figure 5.2-1 Environmental Chamber at the CIMR

Figure 5.2-2 Building a steel tank for the freeze-thaw test of bulb T beams

Figure 5.2-3 Decked bulb T beam placed in the tank for freeze-thaw testing

Figure 5.2-4 Concrete cylinders from the same batch as the beams placed with the beams and exposed to freeze-thaw cycles. Other cylinders are stored at Lab. conditions

Figure 5.2-5 Duct work for air freezing and water thawing according to ASTM C666

Figure 5.2-6 Decked bulb T beams during freezing and thawing cycles

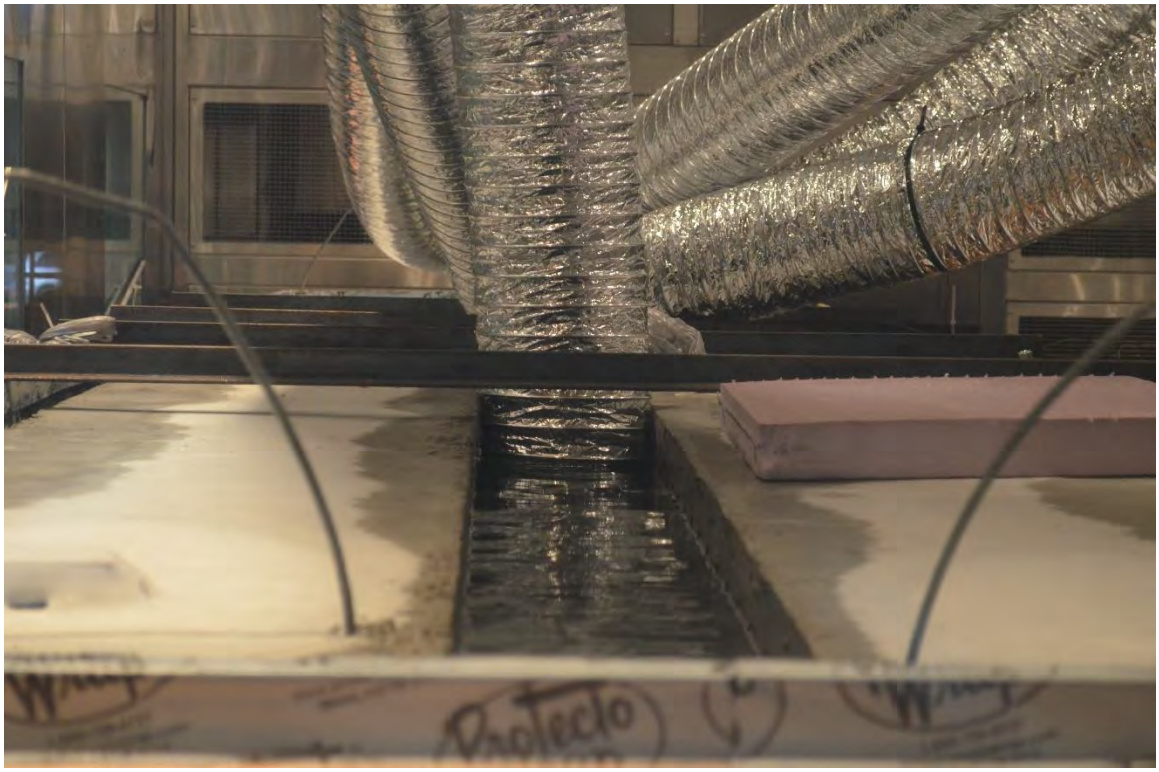

Figure 5.2-7 Water thawing of decked bulb T beams

The temperature profile of the freeze-thaw test for decked bulb T-beams followed the recommendations of ASTM C666-Procedure B, which states that specimens shall be completely surrounded by air during the freezing phase and by water during the thawing phase and that no less than 20 % of the time shall be used for thawing. Also, the temperature of the specimens should be lowered from 40 to 0 °F (4.4 to -18 °C) and then raised from 0 to 40 °F (-18 to 4.5°C) (in a time not less than 2 hrs. and more than 5 hrs. Therefore, the freezing phase of the test was conducted by lowering the air temperature of the environmental chamber to -50 °F (-45.5 °C) until the core temperature of the beams reached 0 °F (-18 °C) in 2 hrs. and 30 min. The thawing phase was executed by flooding the tempering tank with water and raising the air temperature in the chamber to 50 °F (10 °C) until the core temperature of the beams reached 40 °F (4.5 °C) in one hr. and 50 min. The total duration of each freeze-thaw cycle was set to 4 hours and 20 min. Figure 5.2-8 shows the time-temperature variations for freeze-thaw cycles for the prestressed beams. The 300 freeze-thaw cycles were executed in 54 days with a rate of 5.54 cycles per day. A temperature profile was created using VS-1 control system to follow the test program. The air temperature was set to change from -50 °F to 50 °F (-45.5 to 10 °C) in sequences to maintain the assigned core temperature. The control system was set to pump the water into the tempering tank with a proper water level in the thawing phase and continue to re-circulate the water through heat exchanger to maintain set water temperature of 40 °F (4.5 °C). After the beams were thawed, the system diverted the water back to the holding reservoir and maintained the water at 40 °F (4.5 °C) until the next thaw cycle is energized.

After completing 300 freeze-thaw cycles on the beams while monitoring their core temperatures at each cycle, the beams and the concrete cylinders were removed from the tank and were allowed to dry at the room temperature (Figure 5.2-9 and Figure 5.2-10). After proper drying, the four decked bulb T beams and the two control beams, preserved in controlled laboratory conditions, were moved to the testing facility and were loaded under three-point-load test setup to failure. The concrete cylinders were tested under uniaxial compression test to determine the residual concrete compressive strength.

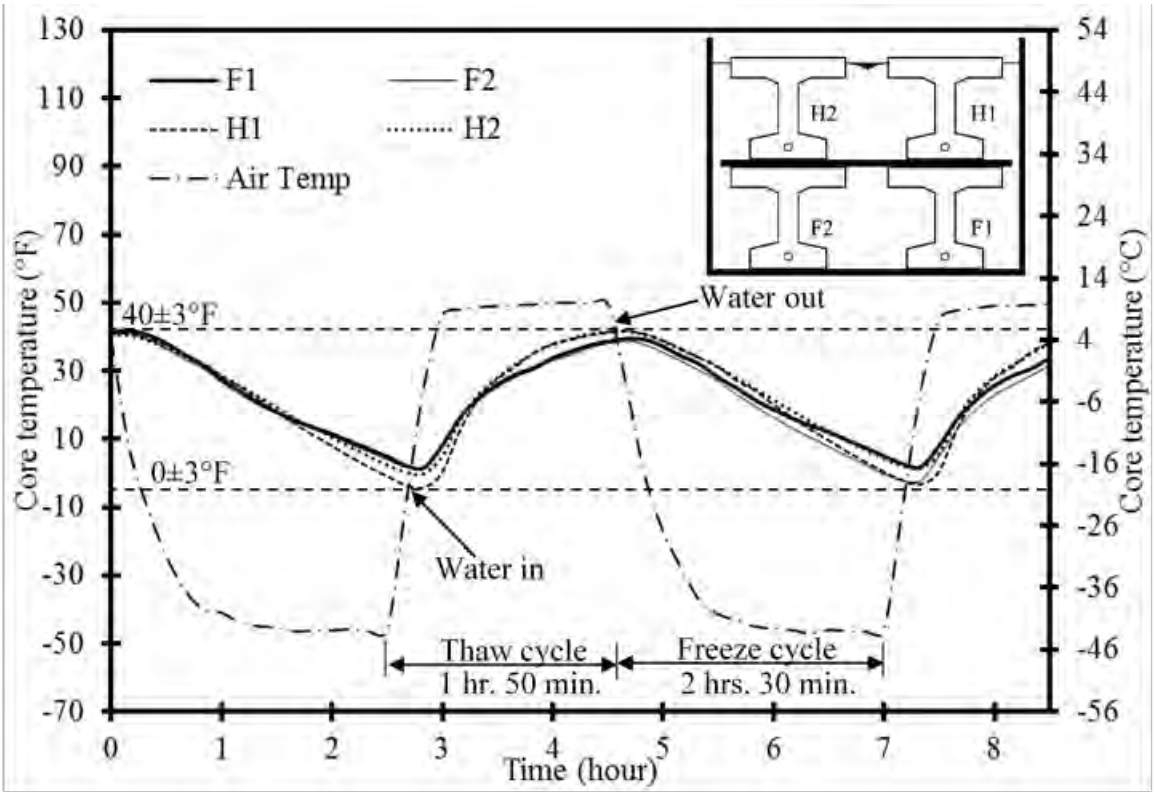

Figure 5.2-8 Air vs beam core temperature during the freezing and thawing cycles

Figure 5.2-9 Deterioration of decked bulb T beams after exposure to 300 freeze-thaw cycles

Figure 5.2-10 Concrete cylinders after exposure to 300 freeze-thaw cycles

The flexural test was conducted after 635 days of concrete casting. Test setup included supporting the beams on two elastomeric bearing pads, positioned on two steel stands spaced 15 ft (4.6 m). Two 2 in. (50 mm) linear strain gages were attached on the top concrete surface near the loading point to capture the concrete strain. Two linear motion transducers (LMTs) string pots were attached to the underside of the beam at mid-span to capture the deflection of the beams. Three linear variable differential transducers (LVDTs) were used to evaluate the strain at different depths at the mid-span section. A 220-kip (980-kN) MTS hydraulic actuator was programmed to apply a vertical concentrated load at the beam mid-span in a force-control mode with rate of 4 kip/min (100 kN/min). All sensors were connected to Mars Lab data acquisition system to collect the necessary data needed to perform a detailed analysis.

5.2.2 Test results

5.2.2.1 Uniaxial compressive test of concrete cylinders

Figure 5.2-11 through Figure 5.2-14 show the testing and failure of the concrete cylinders under a uniaxial test setup. The freeze-thaw cycles on the prestressed beams and concrete cylinders resulted in deterioration of concrete sections. Concrete spalling was observed at the top surface and at the corners of the decked bulb T beams. Similarly, concrete cylinders exhibited vertical cracks and fracture near the ends. This can be attributed to the water absorption and freeze-thaw cycling. During the thawing phase, the pores of concrete were filled with water and the concrete became fully saturated. In the freezing phase, this water in moist concrete froze and produced pressure on the voids that caused expansion, cracking, and scaling of concrete. The distress to critically saturated concrete from freezing and thawing commenced with the first freeze-thaw cycle and continued throughout the rest of the cycles. It resulted in concrete deterioration that was evident through testing the concrete cylinders in uniaxial compressive test setup. The results, presented in Table 5.2-1, showed a severe degradation in the concrete strength due to exposure to 300 freeze-thaw cycles. While average compressive strength of control cylinders was approximately 12,339 psi (85.1 MPa), the compressive strength of concrete cylinders exposed to freeze-thaw cycles averaged at 4,165 psi (28.7 MPa).

Figure 5.2-11 Testing and failure of cylinders after exposure to freeze-thaw cycles

Figure 5.2-12 Testing and failure of concrete cylinders after exposure to freeze-thaw cycles

Figure 5.2-13 Testing and failure of control cylinders

Figure 5.2-14 Typical failure mode of control cylinders not exposed to freeze-thaw cycles

Table 5.2-1 Results of uniaxial compressive test

Date of testing	Concrete compressive strength psi (MPa)	Average concrete compressive strength psi (MPa)
April 4, 2014 28 days after concrete pouring	10,800 (74.5)	11,100 (76.5)
	10,700 (73.8)	
	11,700 (80.7)	
	10,200 (70.3)	
	12,100 (83.4)	
Oct 16, 2015 Control cylinders	13,119 (90.5)	12,339 (85.1)
	11,925 (82.2)	
	11,973 (82.5)	
November 9, 2015 After freeze-thaw test	2,823 (19.5)	4,165 (28.7)
	4,559 (31.4)	
	5,112 (35.2)	

5.2.2.2 Flexural test of decked bulb T beams

The decked bulb T-beams including the control beams were loaded to 60 kip (267 kN) during as discussed in the previous chapter. Therefore, all the beams were cracked before the start of the freeze-thaw test. After freeze-thaw cycles, the beams were loaded under three-point-load test setup in loading-unloading cycles to failure.

The theoretical analysis of the beam cross-section using the force equilibrium and strain compatibility method indicated a tension failure by rupture of prestressing CFCC tendons at theoretical load of 85 kip (378 kN). The first beam, control C1 failed at a load level of 94.8 kip (422kN) with a corresponding deflection of 3.3 in. (84 mm). The failure was characterized by rupture of CFCC strands followed by crushing of concrete at the top flange as shown in. Figure 5.2-15 through Figure 5.2-19. The maximum recorded concrete compressive strain before failure was approximately 2,144 με.

Control Beam C2 failed at a load of 93.3 kip (415 kN) with a corresponding midspan deflection of 2.74 in. (70 mm) and a concrete compression strain of 2,462 με. During the last load cycle, multiple popping sounds were heard while the beam was losing its structural integrity. After failure, the beam was inspected and it was found that there was spalling of concrete at multiple locations and the prestressing CFCC strands ruptured. Figure 5.2-20 through Figure 5.2-23 show the failure of control beam C2 due to rupture of CFCC strands.

Beam F1 was loaded to failure after 300 freeze-thaw cycles. The failure of the beam took place at a load level of 88.5 kip (394 kN) with a corresponding deflection of 2.64 in. (67 mm). The maximum recorded strain before failure was approximately 2,310 με. The failure was characterized by crushing of concrete at the top flange near the mid-span section as shown in Figure 5.2-24 through Figure 5.2-27. The change in the failure mode was attributed to the deterioration of the concrete due to the exposure to freeze-thaw cycles.

Beam F2 was identical in failure mode to Beam F1. Failure initiated by crushing of concrete in the top flange (Figure 5.2-28 through Figure 5.2-31) at a load level of 85.3 kip (380 kN) with a corresponding deflection of 2.47 in. (63 mm) and an extreme compression strain of 2,417 με. No popping sound was heard before failure. Prestressing tendons were checked after failure, and they were found intact.

Beam H1 failed at a load level of 84.3 kip (375kN) with a corresponding deflection of 2.84 in. (72 mm) and a maximum recorded concrete strain in the top flange of approximately 2,248 με. The failure took place by concrete crushing at the top flange near the mid-span section (Figure 5.2-32 through Figure 5.2-35), No rupture of CFCC strands was observed after failure.

Beam H2 experienced a failure mode similar to that of Beam H1. The beam failed at a load level of 89.8 kip (400 kN) with a corresponding deflection of 3.0 in. (76mm) and maximum compression strain at failure of 2,798 με. The failure was characterized by crushing of concrete in the top flange (compression failure) as shown in Figure 5.2-36 through Figure 5.2-39.

Based on the load-deflection curves from all load cycles including the ultimate load cycle, the total energy absorbed by each beam was calculated as the area under the load-deflection curve. For Beams C1 and C2, the total energy absorbed was estimated as 232.7 kip-in. (26.3 kN-mm) and 202.4 kip-in. (22.9 kN-mm), respectively. The freeze-thaw beams had lower energy-absorption capacities at failure compared to the control beams. The total absorbed energy for Beams F1, F2, H1, and H2 were calculated as 159.4 kip-in. (18 kN-m), 147.6 kip-in. (16.7 kN-m), 168.5 kip-in. (19 kN-m), and 185.3 kip-in. (20.9 kN-m) respectively.

The decompression loads for all beams at an age of 635 days, after freeze-thaw cycles were compared with the obtained values at an age of 270 days when the beams were tested at ambient temperature in the seasonal change temperature test. The decompression loads for all beams were

determined by estimating the deviation of the load-deflection curve from linearity as described earlier. For comparison purpose, the deviation from linearity for each test beam for the 60-kip (267-kN) load cycle were overlapped at both ages and the approximate difference in the decompression loads was determined. Using these decompression loads with the assumption that at decompression, there is no stress at the soffit of the beam, effective prestressing at the time of testing was evaluated by back calculation. The effective prestressing force was then used to estimate the prestressing loss from transfer to time of testing as listed in Table 5.2-2.

All beams experienced additional prestress loss at an age of 635 days compared with that at an age of 270 days. The decompression load for control beams, C1 and C2 at an age of 635 days was lower that at an age of 270 days with a difference of approximately 1.5 kip (6.7 kN) and 0.9 kip (4 kN), respectively. This decrease in the decompression load reflects an additional prestress loss, which averaged approximately 3.6 % for the two control beams. This additional prestress loss in the control beams represent the long-term prestress loss in the beams between both ages as the beams were tested at ambient temperature without any exposure to freeze-thaw cycles. On the other hand, Beams F1, F2, H1 and H2 exhibited higher prestress loss compared to that of the control beams. The decompression load for the Beams F1, F2, H1, and H2 at the age of 635 days after 300 freeze-thaw cycles was lower than that at the age of 270 days with an approximate difference of 3.5 kip (15.6 kN), 2.5 kip (11.1 kN), 1.8 kip (8 kN), and 2 kip (8.9 kN) respectively. The estimated prestress loss form decompression loads for all four beams averaged 18.6 % at the age of 635 days and 11.45 % at the age of 270 days with a additional prestress loss of 7.15 %.

Comparing the load-deflection curves of the control beams with those of Beams F1, F2, H1, and H2 revealed that freeze-thaw exposure influenced the flexural test in multiple ways. For instance, the mode of failure shifted from CFCC rupture to concrete crushing. This shift resulted in 7.5 % to 10.3 % decrease in maximum load carrying capacity and corresponding deflection for freeze-thaw beams compared to Beams C1 and C2. Also, a decrease of 24 % in energy absorption capacity of freeze-thaw beams with respect to the control beams was observed.

Beams C1 and C2 failed due to CFRP rupture while the concrete strain in extreme compression fibers is small; 2,144 με and 2,462 με respectively. This matched the design and the anticipated failure mode of the beams. Whereas Beams F1, F2, H1 and H2 experienced compression failure at compression strains of 2,310 με, 2,417 με, 2,248 με, 2,798 με respectively.

Table 5.2-2 Summary of experimental results for decked bulb T-beams

Parameter		Control beams		Freeze-thaw beams			
		C1	C2	F1	F2	H1	H2
Experimental ultimate load, kip (kN)		94.8 (422)	93.3 (415)	88.5 (394)	85.3 (380)	84.3 (375)	89.8 (400)
Midspan deflection at failure, in. (mm)		3.30 (84)	2.74 (70)	2.64 (67)	2.47 (63)	2.84 (72)	3.00 (76)
Mode of failure		Tendon rupture	Tendon rupture	Concrete crushing	Concrete crushing	Concrete crushing	Concrete crushing
Extreme compression strain (με)		2,144	2,462	2,310	2,417	2,248	2,798
Total energy absorbed kip-in. (kN.m)		232.7 (26.3)	202.4 (22.9)	159.4 (18)	147.6 (16.7)	168.5 (19)	185.3 (20.9)
Decompression load, kip (kN)	270 days age	32 (142.4)	31.2 (138.8)	31.5 (140.2)	31 (137.9)	27.8 (123.7)	28 (124.6)
	635 days age	30.5 (136)	30.3 (135)	28 (125)	27.5 (122)	26 (116)	26 (116)
Total prestress loss from transfer to time of testing, %	270 days age	3.5	5.8	5	5.7	15.8	15.2
	635 days age	8	8.5	15.2	16	21	21
Average increase in prestress loss, %		4.5	2.7	10.2	10.3	5.2	5.8

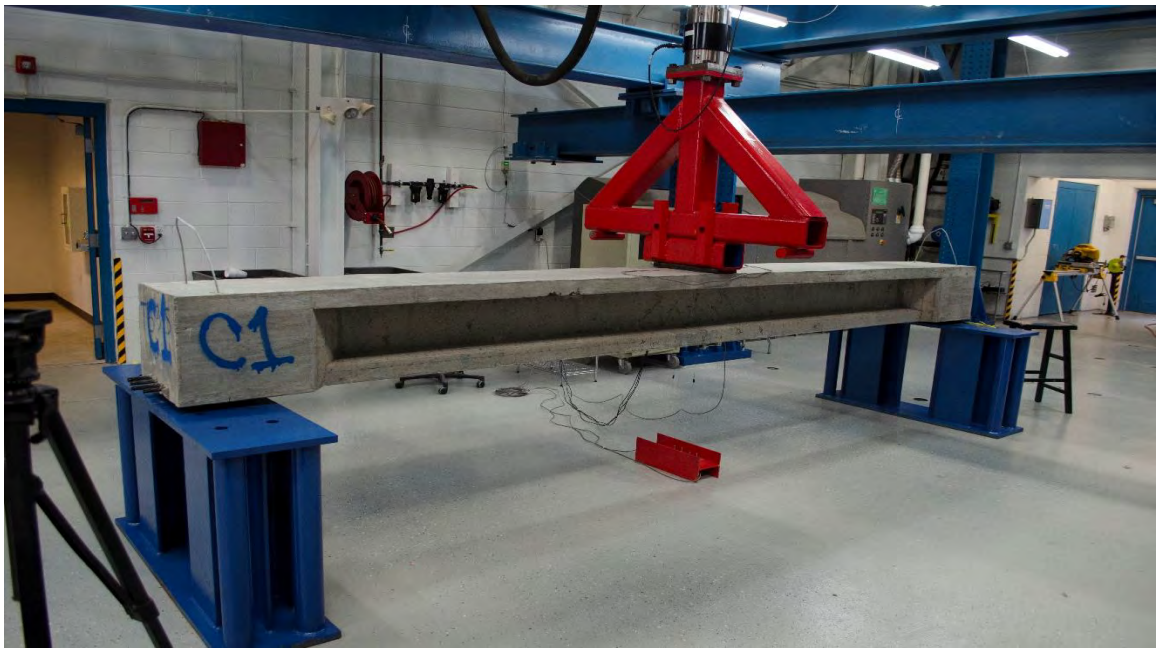

Figure 5.2-15 Flexural test setup for control beam C1

Figure 5.2-16 Instrumentation of Beam C1 for strain and deflection monitoring

Figure 5.2-17 Failure of Beam C1

Figure 5.2-18 Close-up view showing the rupture of CFCC strands in Beam C1

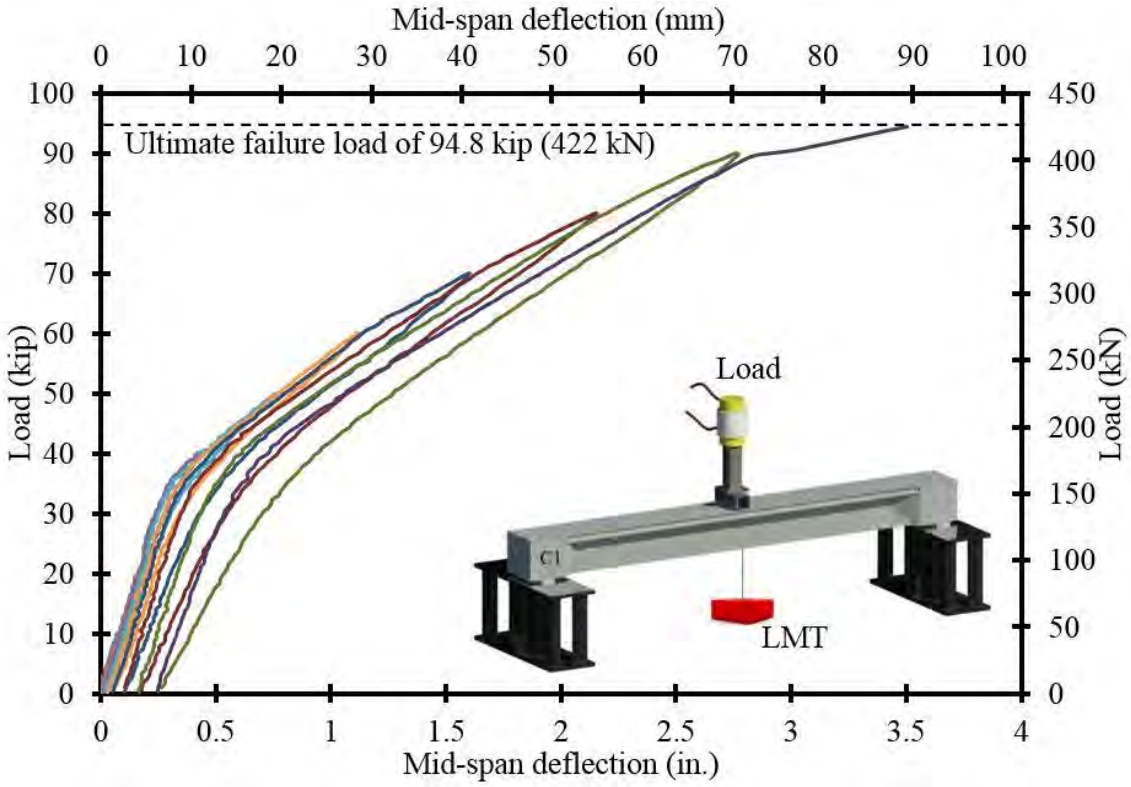

Figure 5.2-19 Load vs. deflection curves for Beam C1

Figure 5.2-20 Test setup of Beam C2

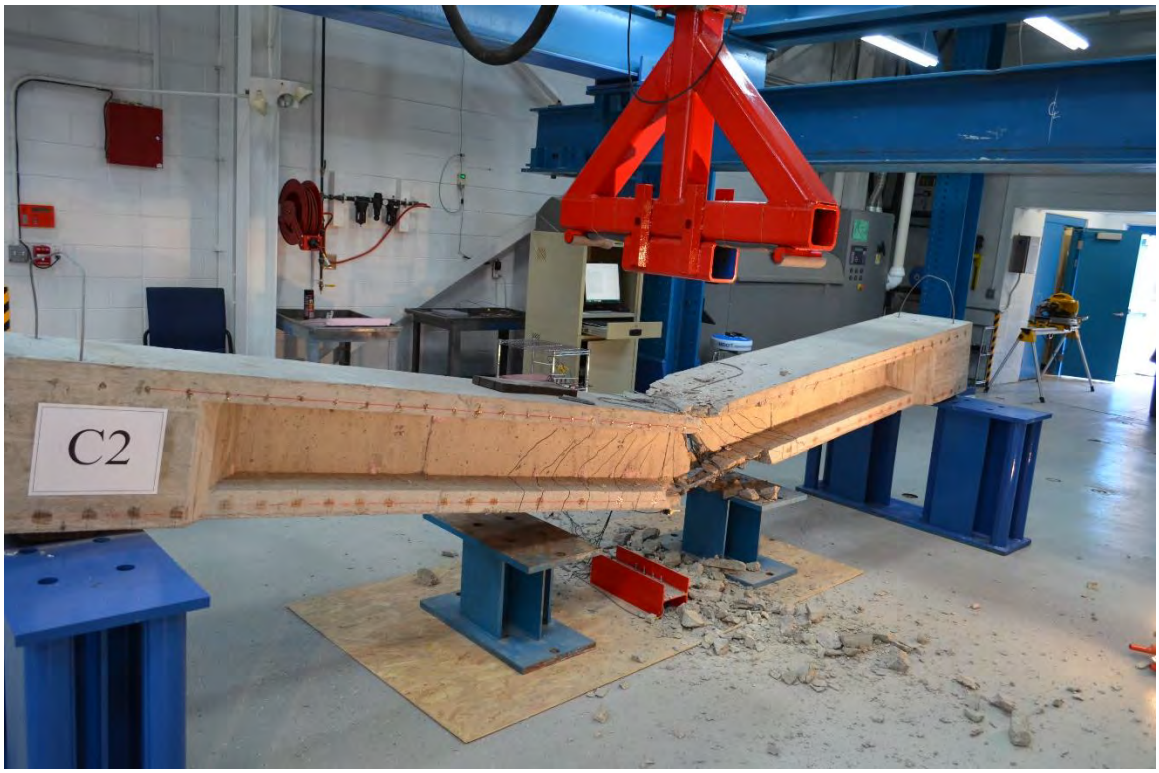

Figure 5.2-21 Failure of Beam C2

Figure 5.2-22 Rupture of strands and concrete spalling of Beam C2

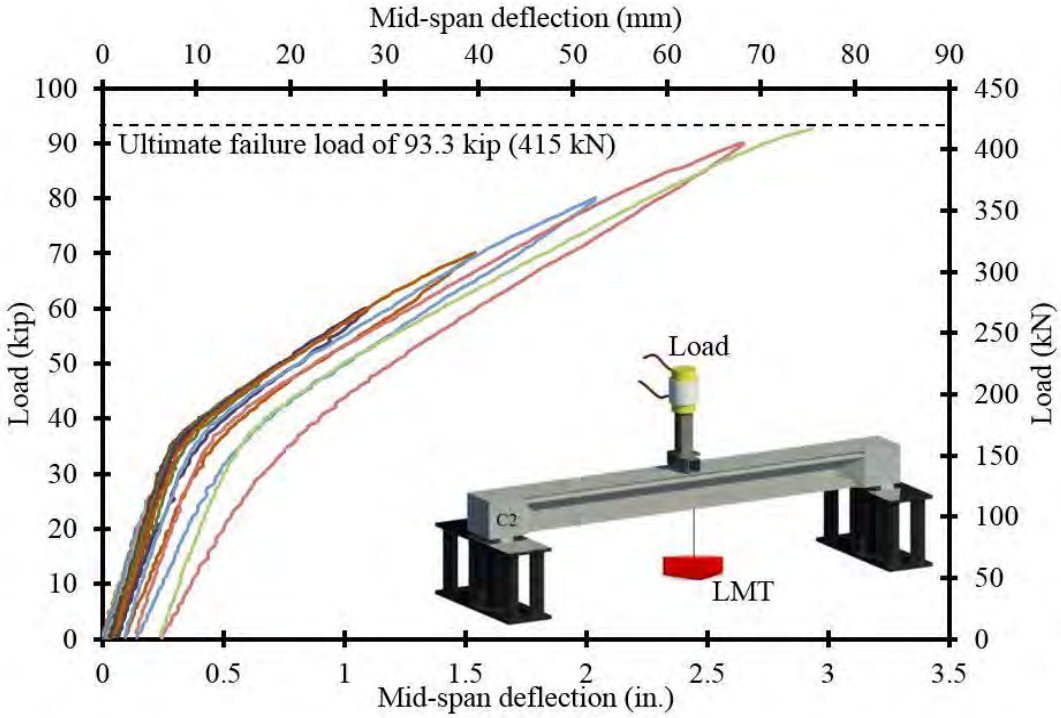

Figure 5.2-23 Load vs. deflection curves for Beam C2

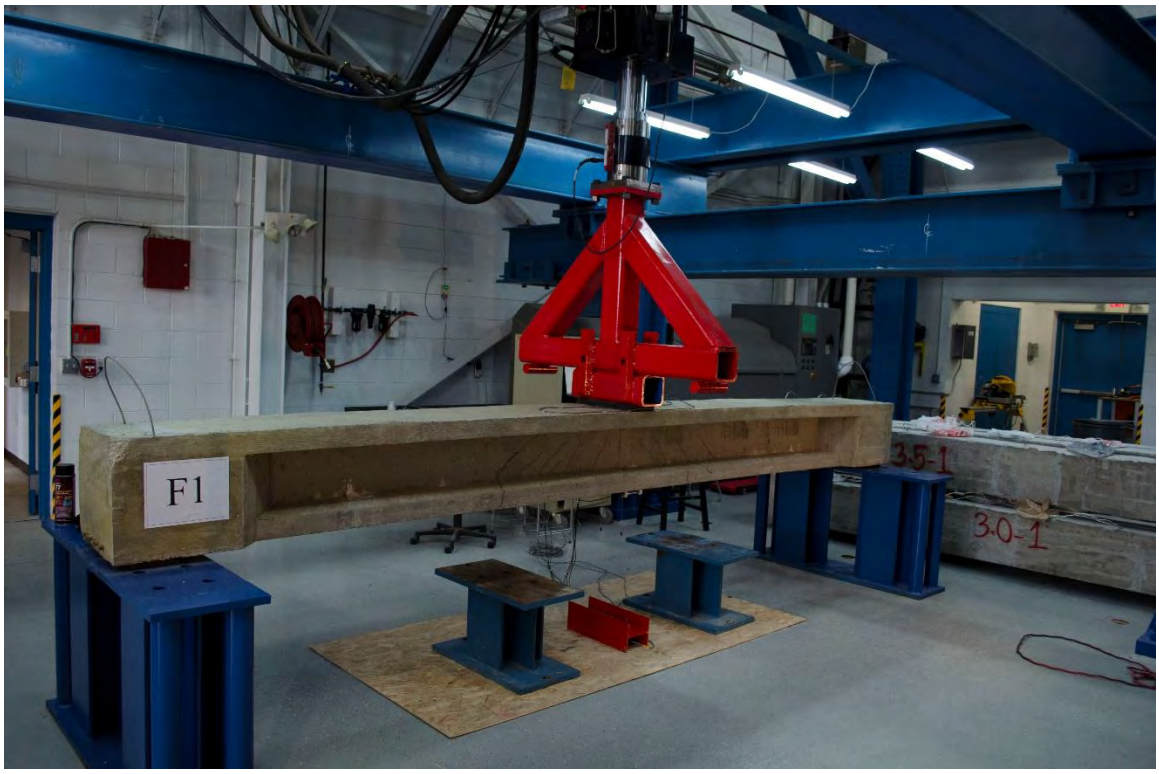

Figure 5.2-24 Test setup of Beam F1 after exposure to freeze-thaw cycles

Figure 5.2-25 Failure of Beam F1

Figure 5.2-26 Close-up picture for CFCC strands in Beam F1 after failure

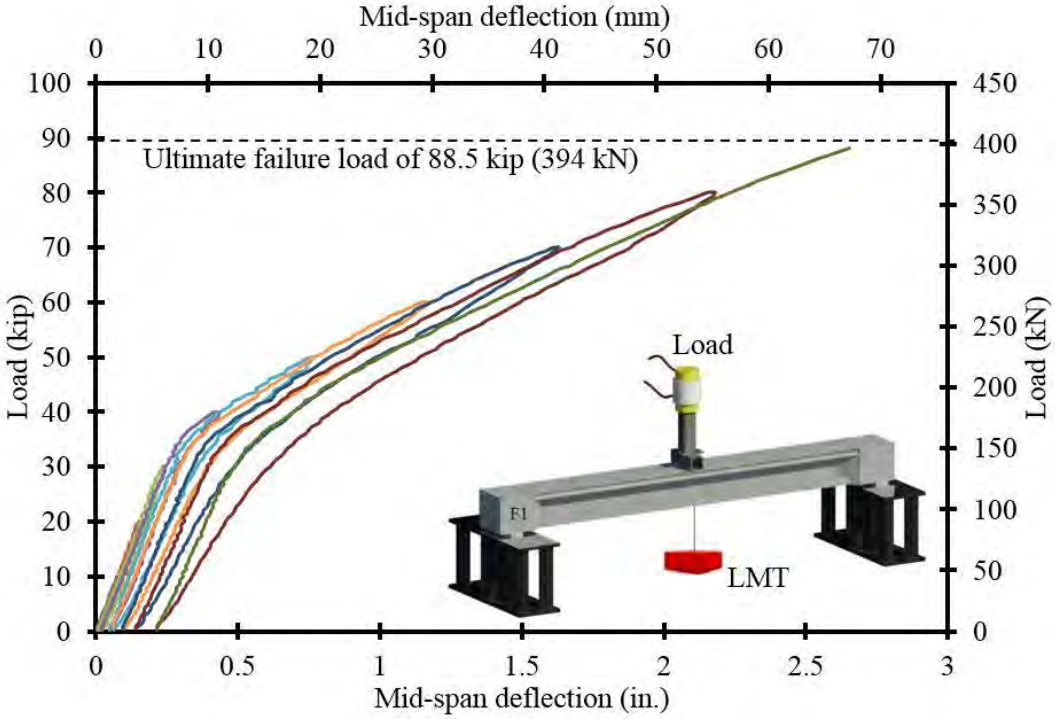

Figure 5.2-27 Load vs. deflection curves for Beam F1

Figure 5.2-28 Test setup for Beam F2 after exposure to freeze-thaw cycles

Figure 5.2-29 Failure of Beam F2

Figure 5.2-30 Close-up picture for CFCC strands in Beam F2 after failure

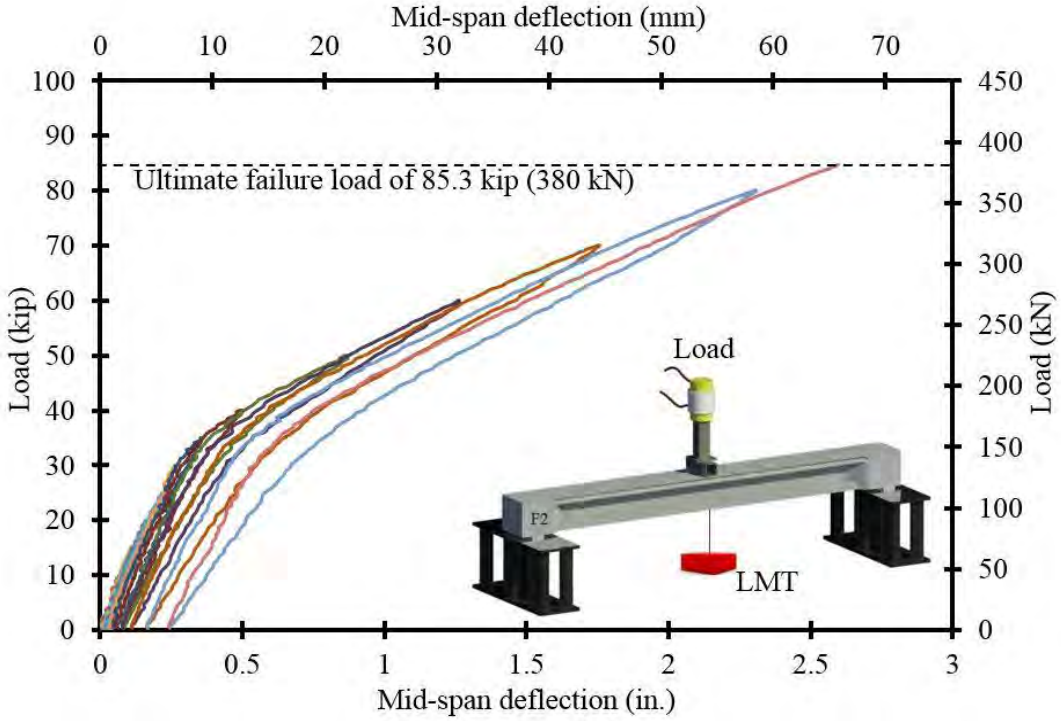

Figure 5.2-31 Load vs. deflection curves for Beam F2

Figure 5.2-32 Test setup for Beam H1 after exposure to freeze-thaw cycles

Figure 5.2-33 Failure of Beam H1

Figure 5.2-34 Close-up picture for CFCC strands in Beam H1 after failure

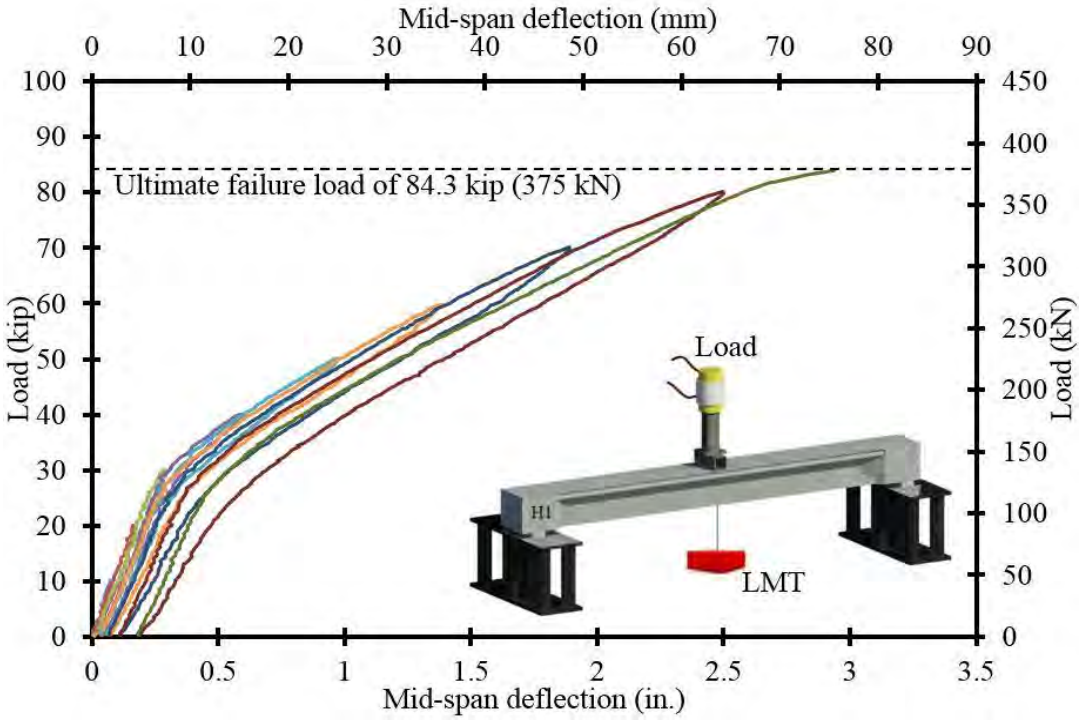

Figure 5.2-35 Load vs. deflection curves for Beam H1

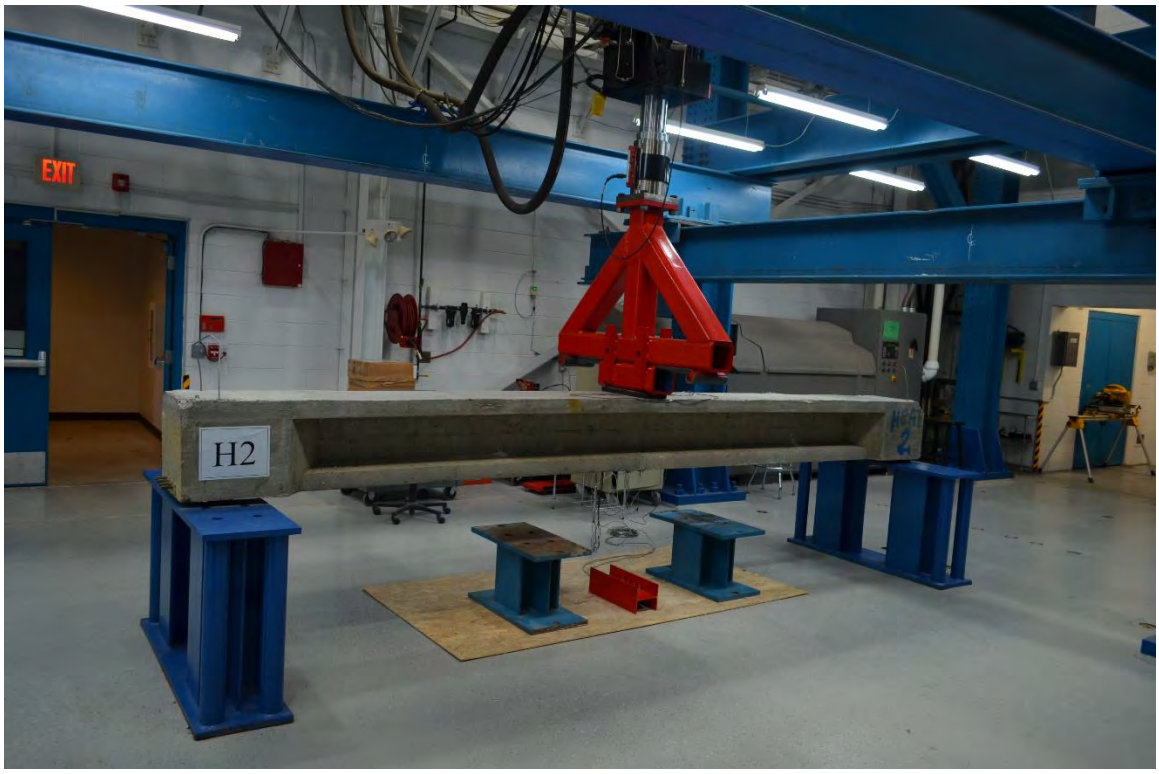

Figure 5.2-36 Test setup for Beam H2 after exposure to freeze-thaw cycles

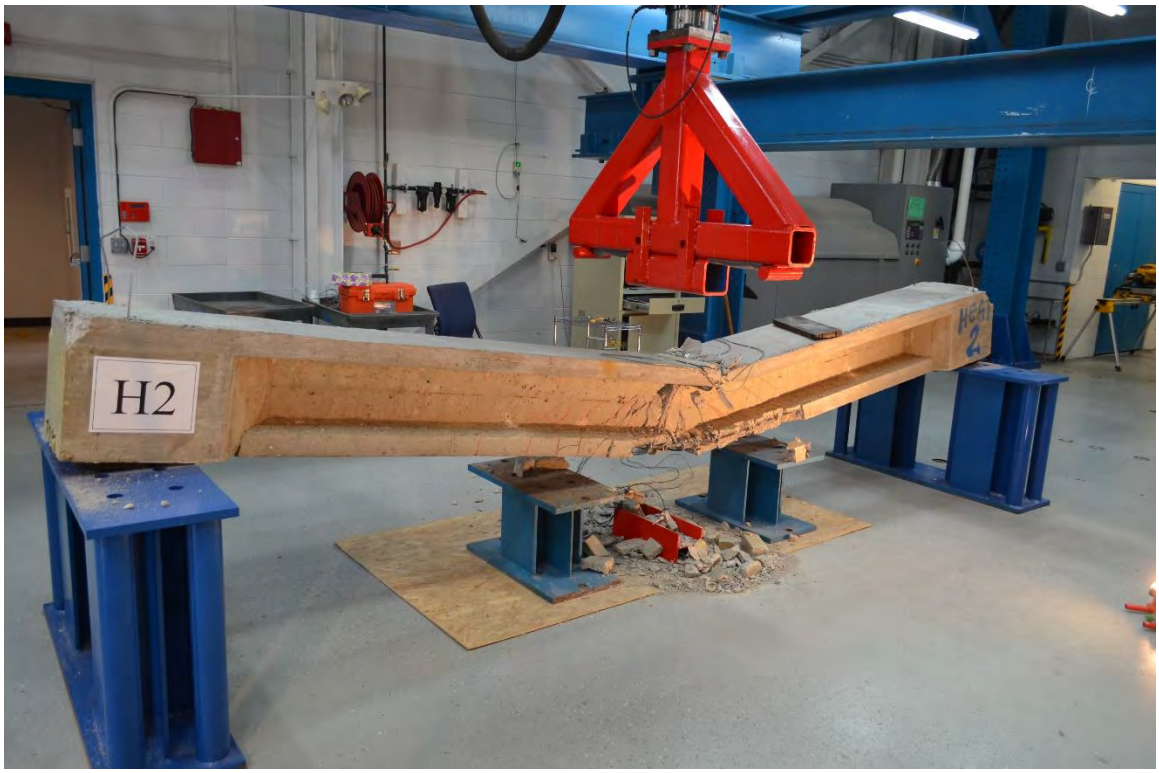

Figure 5.2-37 Failure of Beam H2

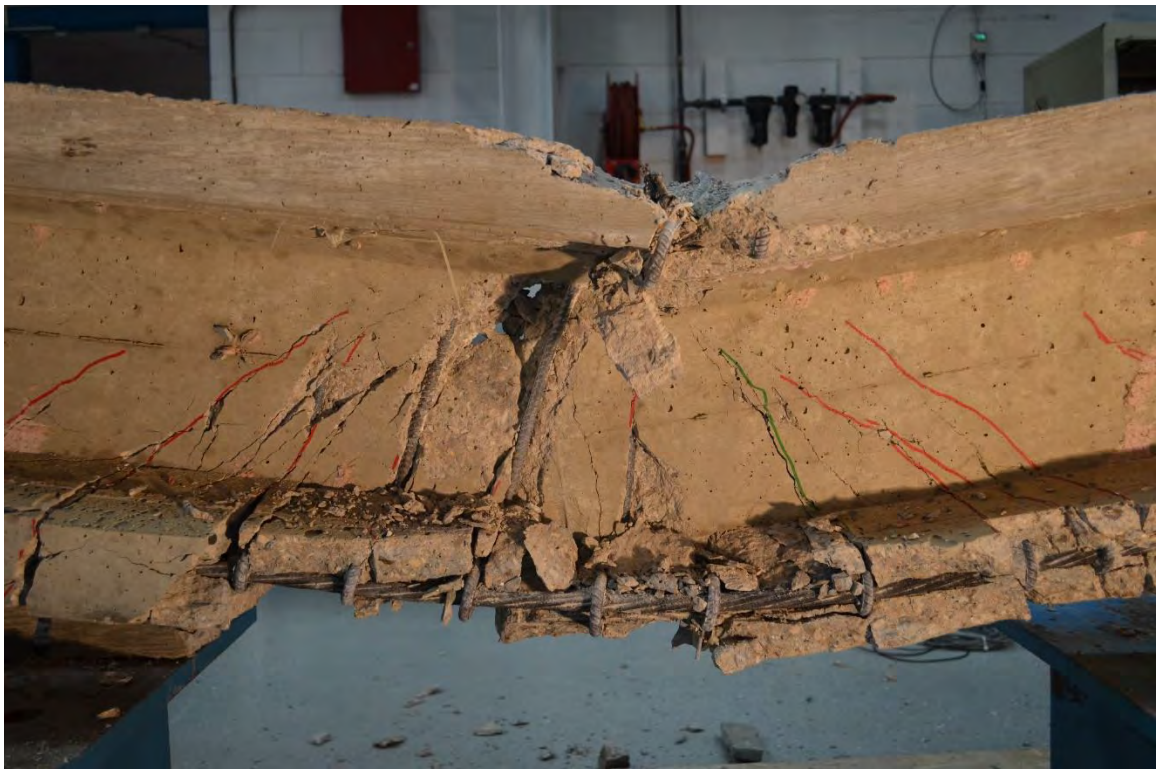

Figure 5.2-38 Close-up picture for CFCC strands in Beam H2 after failure

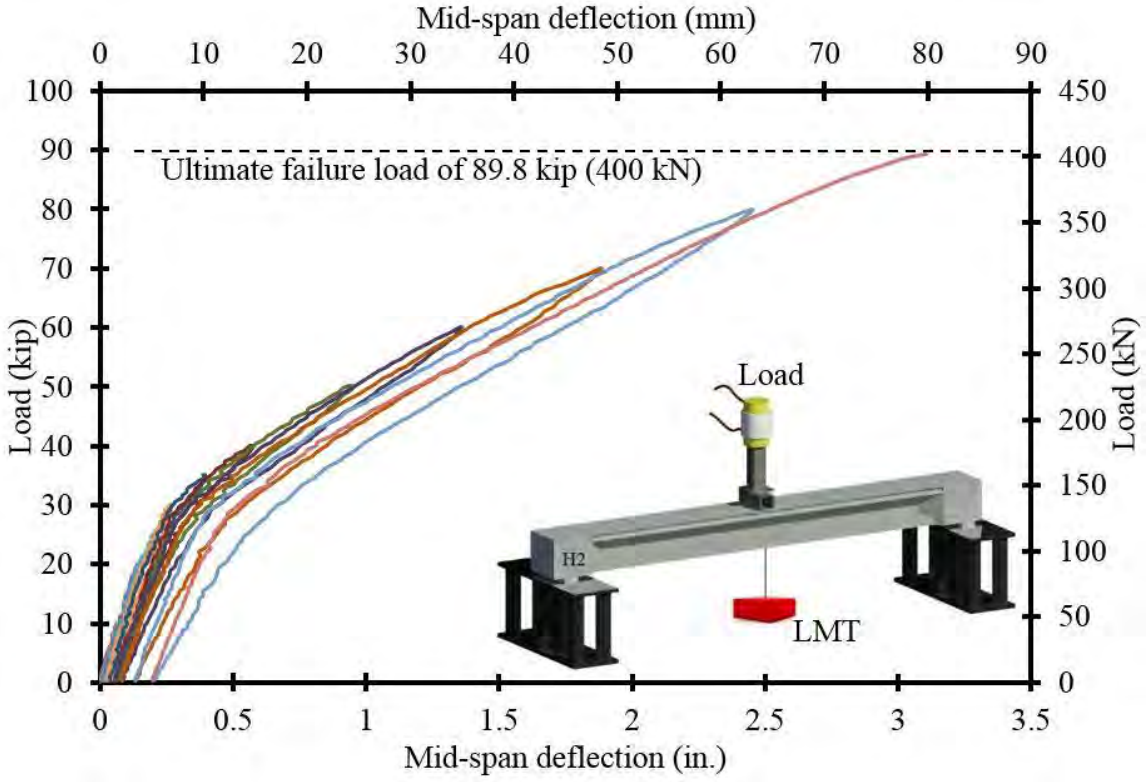

Figure 5.2-39 Load vs. deflection curves for Beam H2

5.3 Freeze-thaw cycles of CFCC specimens

5.3.1 Test setup

Five CFCC 4-ft (1.2-m) long specimens labelled as F/T-S1, F/T-S2, F/T-S3, F/T-S4 and F/T-S5 were constructed with sleeve anchorage at both ends as described earlier in the Report. The test specimens were loaded inside a custom-made high-strength steel frame and were connected to in-line load cells and threaded rods at one end (dead end) and fastened at the other end (live end) with a high-strength steel nut and a washer. The load cells were connected to a data acquisition system to monitor the prestressing force continuously. After installing the specimens inside the steel frame. Prestressing force was applied at the live end through a hydraulic jacking system at a rate of 6 kip/min (27 kN/min) and monitored through the installed load cells. The strands were prestressed in a prearranged sequence to avoid generating any eccentricity in the steel frame. The steel frame was then moved to the environmental chamber, where the specimens, along with the four decked bulb T beams, were subjected to 300 cycles of freezing and thawing. The load cells were covered with insulation layers to minimize the damage during the freeze-thaw cycles of the test. In addition, readings from the load cells were corrected according to the corresponding temperature. Figure 5.3-1 through Figure 5.3-4 document the preparation of the CFCC freeze-thaw test specimens, while Figure 5.3-5 show the change in the prestressing force with the change in temperature during a typical freeze-thaw cycle.

After completion of the freeze-thaw cycles, the test specimens were released from the steel frame as shown in Figure 5.3-6 through Figure 5.3-8 and were transported to the MTS four-post testing facility, where they were loaded in a uniaxial test setup to failure to estimate the residual CFCC strength after exposure to freeze-thaw cycles (Figure 5.3-9 and Figure 5.3-10).

Figure 5.3-1 Steel frame to accommodate 4-ft-long CFCC specimens

Figure 5.3-2 Prestressing CFCC strands and Inline load cell for force monitoring during the test

Figure 5.3-3 CFCC specimens in the Environmental Chamber along with the beams

Figure 5.3-4 CFCC specimens during freeze-thaw testing

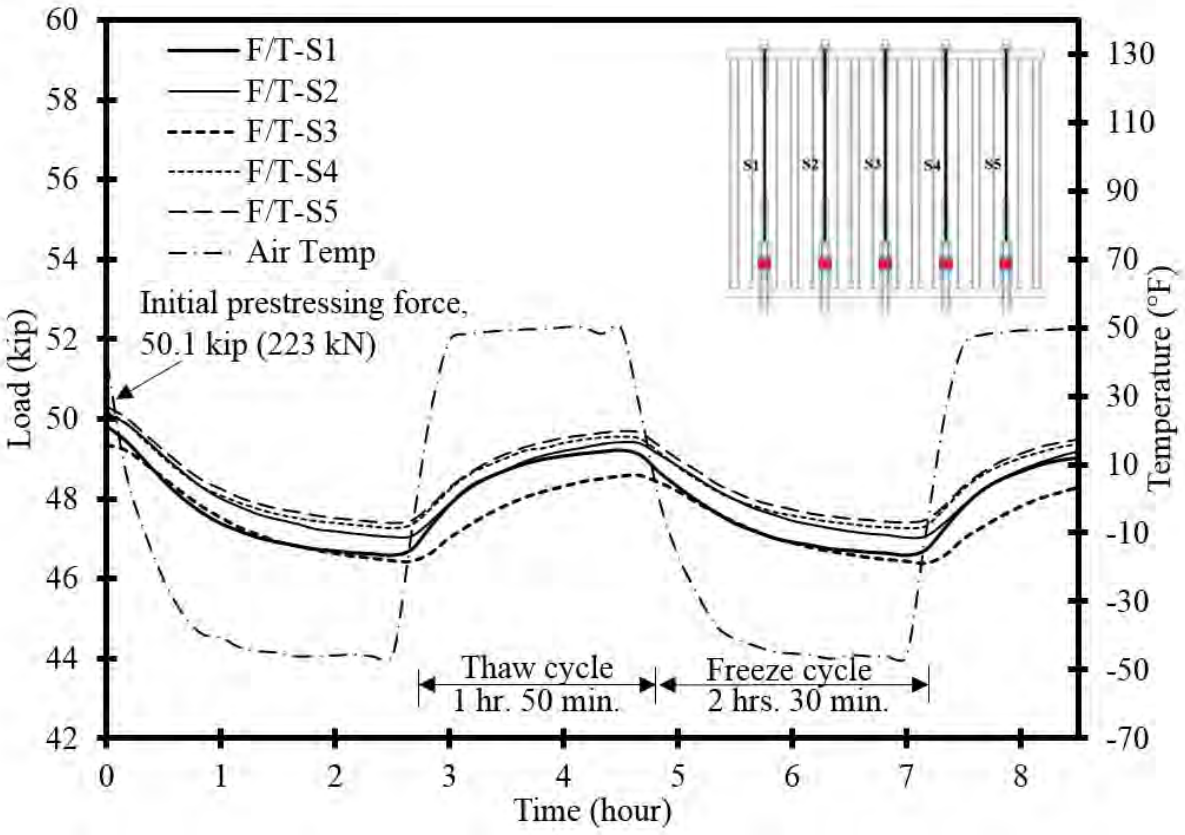

Figure 5.3-5 Change in prestressing force with the change in temperature in CFCC strands

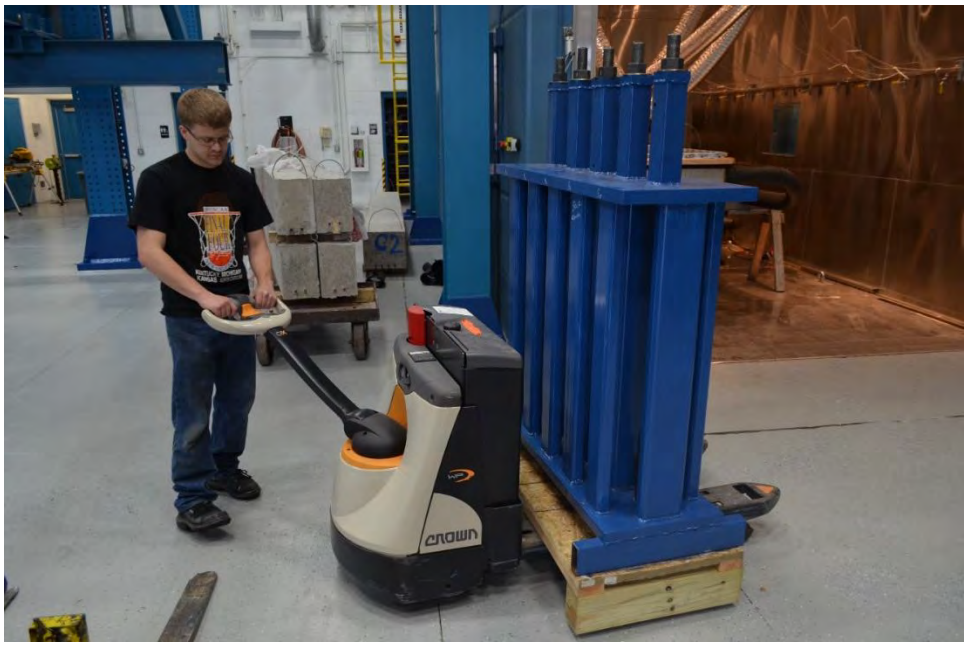

Figure 5.3-6 Removing the CFCC specimens after completion of 300 freeze-thaw cycles

Figure 5.3-7 Releasing CFCC strands after freeze-thaw exposure

Figure 5.3-8 Preparing CFCC strands for uniaxial tensile test to evaluate residual capacity

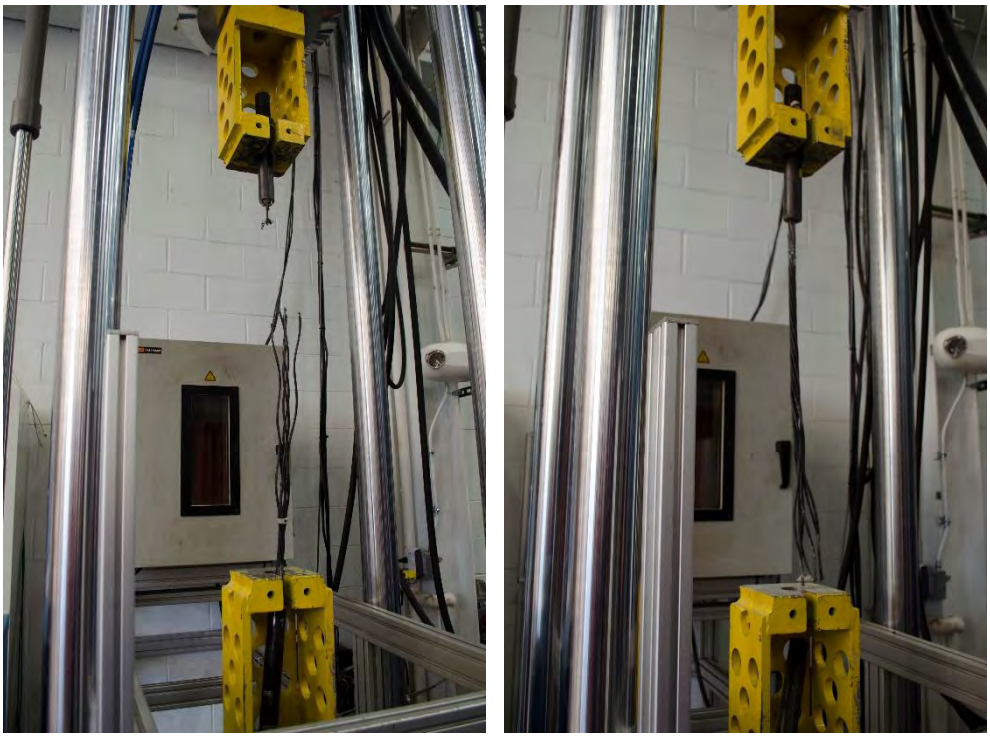

Figure 5.3-9 Loading and failure of CFCC strands

Figure 5.3-10 Failure of CFCC strands under uni-axial load test setup

5.3.2 Test results

Results of freeze-thaw test and uniaxial tensile test for post-tensioned CFCC specimens are provided in Table 5.3-1. Based on the results, the average loss in prestressing force was estimated as 3.6 % over 300 freeze-thaw cycles (54 days). This loss includes the loss due to strand relaxation as well as anchorage relaxation. The failure load of the test specimens averaged at 79.78 kip (355 kN). All specimens ruptured at failure, with no slippage within the anchors. The elastic of the test specimens averaged at 23,844 ksi (164 GPa). The experimental breaking load for all specimens after freeze-thaw exposure was approximately 15% higher than the failure loads from respective batch testing conducted at ambient temperature.

Table 5.3-1 Summary of experimental results for Post-tensioned CFCC strands

Specimen	Freeze-thaw Test			Uniaxial Tensile Test		
	Prestressing Force, kip (kN)		Prestressing Losses, (%)	Breaking Load, kip (kN)		Elastic modulus, ksi (Gpa)
	Before Freeze/thaw Cycles	After Freeze/thaw Cycles		Before Freeze/thaw Cycles	After Freeze/thaw Cycles	
F/T- S1	49.8 (222)	48.1 (214)	3.41	70.35 (313)	72.6 (323)	23,172 (160)
F/T- S2	49.4 (220)	47.7 (212)	3.41	70.35 (313)	82.7 (368)	24,375 (168)
F/T- S3	50.2 (223)	48.2 (215)	3.93	70.35 (313)	82.2 (366)	24,121 (166)
F/T- S4	50.3 (224)	48.4 (215)	3.82	68.61 (305)	78.3 (348)	23,910 (165)
F/T- S5	50.1 (223)	48.5 (216)	3.31	68.61 (305)	83 (370)	23,644 (163)

5.4 Discussion of Test Results

The test results show that freeze-thaw cycles have detrimental effect on concrete but not on CFCC. Concrete lost more than 60 % of its compressive strength, while CFCC gained additional 15 % of strength after exposure to freeze-thaw cycles. This change in strength altered the mode of failure of the test beams from tension-controlled to compression-controlled. The reduction of the nominal moment capacity was approximately 7.5 %, which was not significant because the beams were

designed as tension-controlled sections and therefore, concrete strength was not a significant parameter in establishing the nominal moment capacity. On the other hand, had the beams been designed as compression-controlled sections, the reduction in concrete strength would have led to a significant reduction in the nominal moment capacity since compression-controlled sections are sensitive to concrete strength.

From design perspective, it is strongly recommended to design bridge beam sections as tension-controlled sections. The compression in a bridge beam is resisted by the deck slab, which is the most vulnerable element to environmental conditions. A tension-controlled section will accommodate a reduction in the concrete strength without a significant reduction in the nominal moment capacity, unless the reduction in the concrete strength is severe and alters the mode of failure from tension-controlled to compression-controlled.

CHAPTER 6: FIRE AND HEAT RESISTANCE

6.1 Introduction

Regardless of the material under consideration, loss in strength under high temperature is inevitable (Rafi et al. 2007; Williams et al. 2008; and Grace and Bebawy 2014). For instance, concrete loses 50 % of its compressive strength at approximately 1292 ^{0}F (700 ^{0}C). Note that different concrete constituents exhibit different thermal decomposition trends that result in a wide range in the behavior of concrete at high temperatures (Kodur et al. 2005). Steel is also susceptible to fire and is expected to lose 50 % of its tensile capacity at 932 ^{0}F (500 ^{0}C). Likewise, CFRP is susceptible to fire and extreme high temperature events as the polymer matrix in CFRP softens and deteriorates with the increase in temperature. CFRP loses approximately 50 % of its ambient strength at 392 ^{0}F (200 ^{0}C) according to Robert and Benmokrane (2010).

Precise data regarding the fire endurance of beams prestressed with CFRP strands are not available. However, it is generally accepted that prestressed concrete structures are more susceptible to fire than reinforced concrete structures, since the prestressing strands (whether steel or CFRP) are already stressed to a significant level of their ambient capacity. For instance, Zhang et al. (2017) showed that under hydrocarbon fire, prestressed box beams with higher level of prestressing force have higher ductility and creep and lower fire endurance than those with lower level of prestressing force. In addition, Maluk et al. (2010) studied the fire behavior of CFRP prestressed high strength concrete slabs and observed that when spalling of the concrete was avoided, the fire endurance of the prestressed slabs was influenced by the initial prestressing force as slabs with larger prestressing force achieved shorter fire endurance.

It should be noted that fire endurance of a beam prestressed with CFRP strands may not necessarily be dependent on the heat resistance of CFRP but rather on the ability of the prestressed beam to sustain a specific load at elevated temperatures (Abbasi and Hogg 2006). For instance, Maluk et al. (2010) suggested that the limiting factor for the fire endurance of CFRP reinforced or prestressed concrete is the deterioration in bond strength between CFRP and concrete at elevated temperatures rather than the flammability of the composite material or the deterioration of the epoxy matrix. This opinion is supported by earlier fire test results that showed 80 to 90 % reduction in the bond strength between concrete and CFRP as the temperature increased from 68 to 482 ^{0}F

(20 to 250 ^{0}C) compared to 38 % reduction in bond strength with conventional steel reinforcing bars (Katz et al. 1999; Kodur et al. 2005).

Another aspect of the fire resistance of prestressed concrete structures is the concrete cover and the potential for concrete cover spalling at high temperatures. According to Kodur et al. (2005), the strength of concrete in fire is governed by its moisture content. Test results by Saafi (2002) showed that too much moisture in the concrete generated high pressure in the beam that caused spalling in the concrete cover, which resulted in the premature exposure of the internal reinforcement to high temperature and overall reduction in the strength of the structural element. In addition, the shape of the structural element plays an important role in the fire resistance. For instance, in comparing rectangular-section to I-shape prestressed beams, it was found that the I-shape was more susceptible to spalling than the rectangular sections (Ashton and Malhotra 1953). Furthermore, the increase in concrete cover should provide a fire protection of the internal reinforcement and prestressing strands and extend the fire endurance of structural elements (Kodur et al. 2005; Yu and Kodur 2013). For instance, Terrasi et al. (2010) investigated the performance of CFRP and steel prestressed beams at elevated temperatures. Failure mode was either concrete spalling or deterioration of the bond between the strands and the concrete and consequently loss of prestressing force with evidences of increasing the fire endurance with the increase of concrete cover. It should be noted, however, that concrete cover thicker than 3.0 in. (7.5 mm) are deemed susceptible to spalling (Ashton and Malhotra 1953).

Through this part of the investigation, the performance of unprotected and protected CFCC strands at elevated temperature was evaluated. CFCC specimens with a length of 4 ft (1.2 m) were maintained at elevated temperatures for at least 30 minutes before they were loaded to failure under uni-axial tensile load to evaluate the reduction in the strength with the increase in temperature. In addition, to evaluate the performance of CFCC strands embedded in concrete under a fire event, another research investigation was carried out on a series of 16-ft (4.876-m) long decked bulb T beams prestressed with CFCC strands. The beams were subjected to fire event according to ASTM E119 while sustaining a central load representing the traffic load in real-scale bridge beams. Detailed discussion for both test setups, test results, and main conclusions are provided in the following sections.

6.2 Tensile Strength of CFRP at Elevated Temperatures

6.2.1 Test setup

Twelve test specimens were tested at high temperature to evaluate the effect of temperature increase on the tensile strength of CFCC strands. Each specimen had a length of 4 ft (1.2 m) and was provided with two sleeve anchorages at the ends.

The test setup included passing the test specimen through an INSTRON environmental chamber as shown in Figure 6.2-1 and Figure 6.2-2 and attaching its ends the fixed and moving heads of the MTS four-post testing facility. After the specimen was fixed in place, the environmental chamber was activated to heat the middle portion of the specimen to a predefined temperature. To ensure a uniform temperature throughout the heated length of the specimen, the chamber was maintained at the predefined the temperature for 30 minutes. After that, the MTS actuator was engaged, and the specimen was loaded in a uniaxial tensile test setup to failure with a loading rate of 6.5 kip/min (29 kN/min), while the temperature of the environmental chamber remained at the same predefined level. The specimens were tested at temperatures ranging from 302 °F (150 °C) to 662 °F (350 °C).

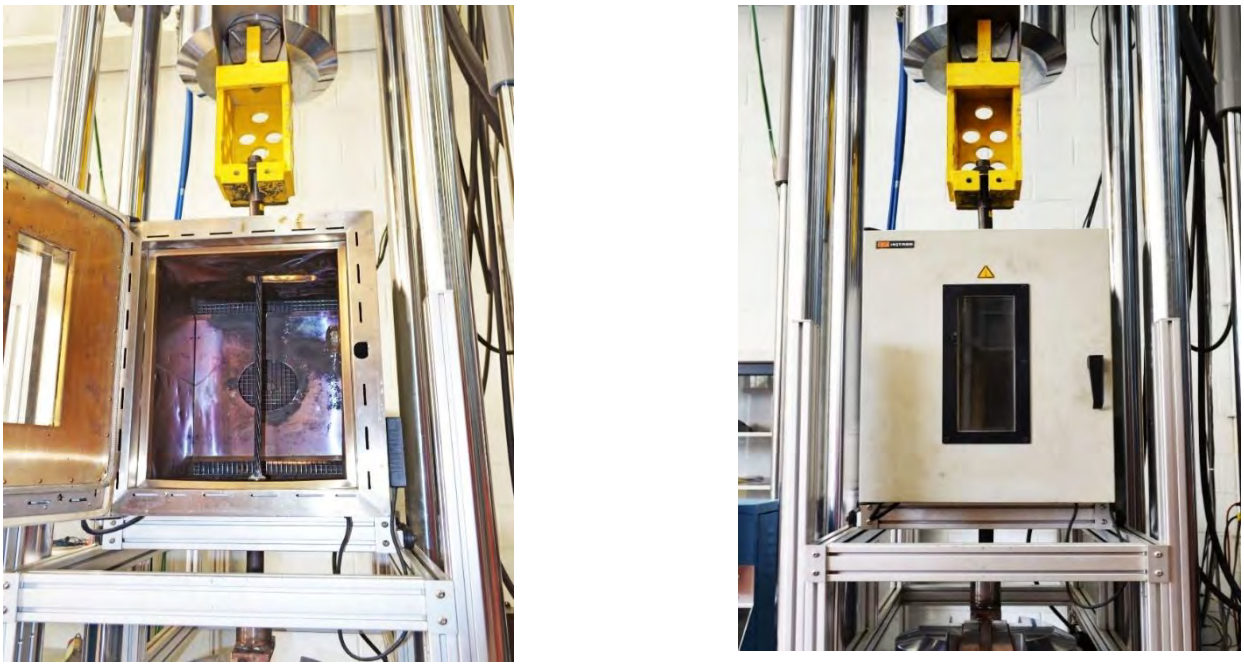

Figure 6.2-1 Test setup to establish tensile strength of CFCC at elevated temperatures

Figure 6.2-2 Anchorage device passing through a central opening in the heat chamber

6.2.2 Test results

Reduction of strength of CFCC strand with increasing the temperature was observed in all test specimens. The common mode of was rupture of stands within the heated length as shown in Figure 6.2-3 through Figure 6.2-11. The tensile strength of CFCC at 302 °F (150 °C) was approximately 54.79 kip (244 kN), while its tensile strength at 662 °F (350 °C) was 34.12 kip (152 kN). Table 6.2-1 shows the test result of all specimens, while Figure 6.2-12 shows a comparison between the test results and those obtained by the manufacturer on CFCC strands with different diameters.

Figure 6.2-3 Typical failure of test specimen at elevated temperature

Figure 6.2-4 Failure of CFCC specimen at 347 °F (175 °C)

Figure 6.2-5 Failure of CFCC specimen at 392 °F (200 °C)

Figure 6.2-6 Failure of CFCC specimen at 437 °F (225 °C)

Figure 6.2-7 Failure of CFCC specimen at 482 °F (250 °C)

Figure 6.2-8 Failure of CFCC specimen at 527 °F (275 °C)

Figure 6.2-9 Failure of CFCC specimen at 572 °F (300 °C)

Figure 6.2-10 Failure of CFCC specimen at 617 °F (325 °C)

Figure 6.2-11 Failure of CFCC specimen at 662 °F (350 °C)

Table 6.2-1 Summary of test results for tensile strength of CFCC at elevated temperature

Specimen ID	Temperature, °F (°C)	Failure Load, kip (kN)	Failure stress, ksi (MPa)	Ratio to guaranteed strength (60.7 kip or 270 kN) (%)
65-01	150 (65)	69 (306)	385 (2654)	1.13
150-01	302 (150)	54.79 (244)	306 (2110)	90
175-01	347 (175)	52.08 (232)	291 (2006)	86
200-01	392 (200)	52.37 (233)	293 (2020)	86
200-02	392 (200)	54.34 (242)	303 (2089)	89
225-01	437 (225)	52.14 (232)	291 (2006)	86
250-01	482 (250)	47.75 (212)	267 (1841)	79
275-01	527 (275)	45.82 (204)	256 (1765)	75
300-01	572 (300)	41.74 (186)	233 (1606)	69
325-01	617 (325)	36.16 (161)	202 (1393)	60
325-02	617 (325)	36.74 (163)	205 (1413)	60
350-01	662 (350)	34.12 (152)	191 (1317)	56
350-02	662 (350)	34.88 (155)	195 (1344)	57

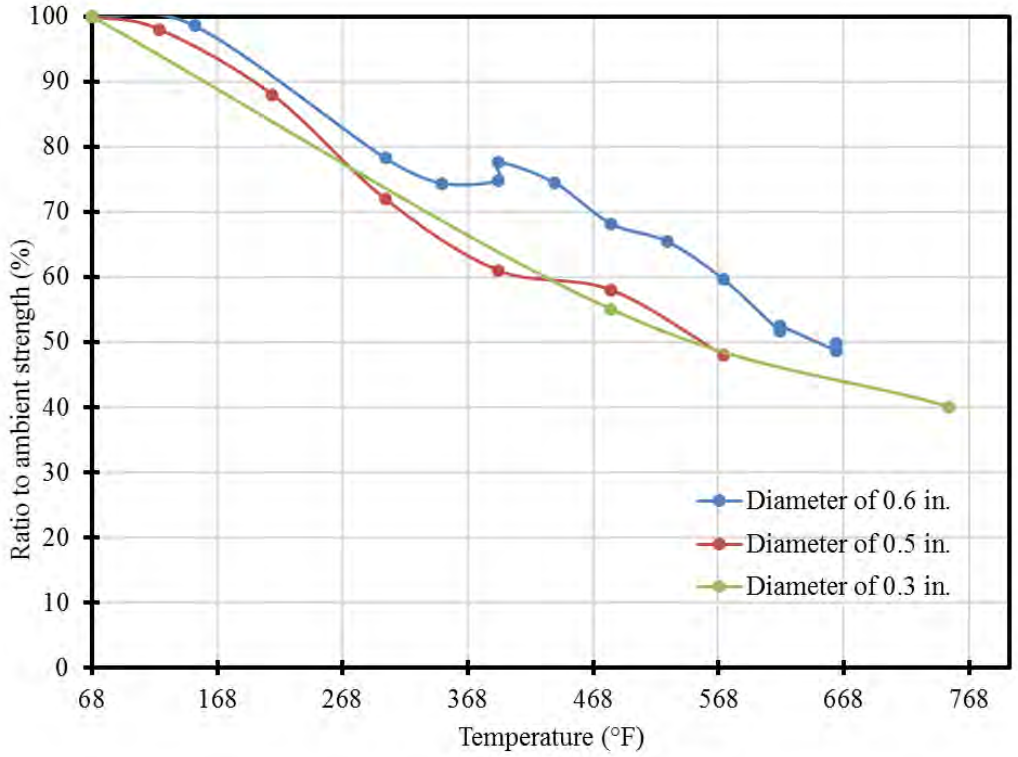

Figure 6.2-12 Decrease in tensile strength with increase in Temperature for CFCC strands

Table 6.2-2 Comparison with Manufacturer's test results

Temperature °F (°C)	Ratio to CFCC strength @ ambient (%)		
	0.6 in. (15.2 mm)*	0.5 in. (12.5 mm)**	0.3 in. (7.5 mm)**
68 (20)	100	100	100
122 (50)	-	98	
212 (100)	-	88	-
302 (150)	79	72	-
392 (200)	76	61	-
482 (250)	69	58	55
572 (300)	61	48	-
662 (350)	49	-	-
752 (400)	-	-	40

* Based on ultimate strength of 70 kip (311 kN) for 0.6 in. (15.2 mm) CFCC strands
** Tokyo Rope Mfg. Co., Ltd. based on tensile strengths of : 38.2 kip (145 kN) for 0.5 in. (12.5 mm) CFCC, and 15 kip (67 kN) for 0.3 in. (10 mm) CFCC strands.

6.3 CFCC Prestressed Decked Bulb T Beams Under Fire/Loading Event

Seven CFCC prestressed and one steel prestressed decked bulb T beams with varying prestressing force levels were tested under fire/loading events to evaluate the fire endurance of CFCC prestressed highway bridge beams in the case of fire. The beams had a total length of 16 ft (4.87 m) and cross section dimensions as shown in Figure 6.3-1.

Fire is an unlikely/unpredictable event that might happen anytime during the lifespan of the structure (Highway Bridge) or even during construction. However, the most critical time is when the bridge is in service and there is a traffic on the bridge when it engulfs in fire. The research investigation aimed at addressing this scenario by taking multiple key steps in specimen preparation and test setup.

First, to simulate the case of an aged structure that has been in service for many years and may have some level of deterioration, the beam specimens were not a freshly constructed specimen but were salvaged from an earlier shear research study that aimed at establishing the shear resistance of prestressed beams by applying loads near their ends (details and finding of the study is described later in the Report). The research team was therefore, able to salvage the middle portion of those test beams and recondition them for fire testing. At the time of fire testing, the beams were approximately three years old and they kept outdoors where they were exposed to different weather condition for at least two years. Originally, the beams had a length of 31 ft (9.5 m) but approximately a segment of 6 ft (1.82 m) from each end was damaged beyond repair. Nevertheless, the middle segment of each beam was in good conditions and was deemed a perfect fit for fire testing.

6.3.1 Test setup

The eight test beams, seven prestressed with CFCC strands. One with steel strand, were provided with CFCC stirrups through half of the span and steel stirrups through the other half. The steel stirrups were made of No.3 Grade 60 reinforcing bars, whereas the CFCC stirrups had a nominal diameter of 0.44 in. (10.5 mm) and effective cross-sectional area of 0.09 in.^{2} (57.8 mm^2). The stirrups were provided at a spacing of 4, 6 & 8 in. (101, 152, 203 mm). Both prestressing CFCC and steel strands had a nominal diameter of 0.6 in. (15.2 mm). The initial prestressing force per beam was 72 kip (320 kN) in one beam, 100 kip (445 kN) in five beams, and 132 kip (587 kN) in

two beams including steel prestressed beam. The average concrete strength was 6.4 ksi (44.1 MPa) and 9 ksi (62 MPa) at the time of prestress transfer and after 28 days, respectively. A clear cover to the outer edge of the stirrups of 0.75 in. (19 mm) was provided at the soffit and top of the beam, while a clear cover of 0.5 in. (13 mm) was provided at the sides.

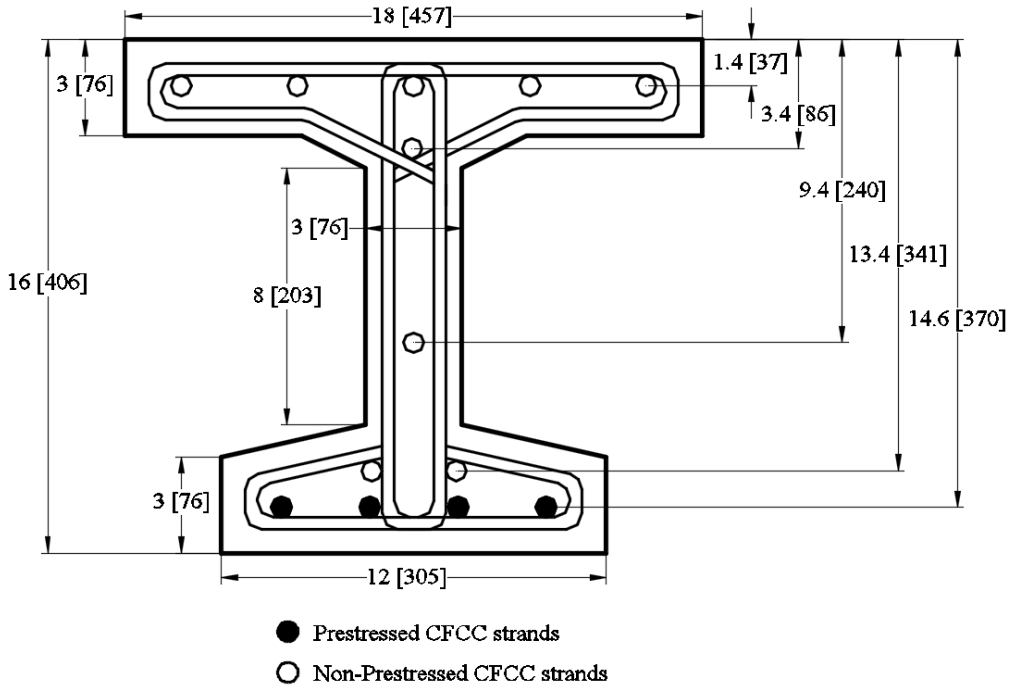

Figure 6.3-1 Cross-section of prestressed decked bulb T-beam, all dimensions are in in. [mm]

Each test beam was instrumented with 22 thermocouples Type-K. Eighteen thermocouples were placed at the mid-span and both quarter-span sections and four were placed at the end of the beam (Figure 6.3-2 through Figure 6.3-7). For the mid-span and quarter span sections, two thermocouples were placed at the top flange to measure concrete temperature, two in web and two in bottom flange at the level of prestressed strands to measure CFCC/steel temperature. The thermocouples were placed at their specified locations by drilling holes in the concrete section. The holes were sealed after placing the thermocouple using a thermal insulator. Six thermocouples were placed outside the beam to measure the air temperature of the fire chamber within 12 in. (305 mm) from the beam.

To simulate the traffic load in case of a fire event, all beams were simply supported and were loaded by a 110-kip (489-kN) MTS hydraulic actuator while conducting the fire test as shown in

Figure 6.3-7. The beams were loaded at their mid-span in a force control mode with a loading rate of 2 kip/minute (8.89 kN/minute) to a predetermined load. This predetermined load was maintained for the entire test until the failure of the beam. As this predetermined load represented typical service loads on the beams, it was taken slightly less than the anticipated cracking load of the beam, which was a function of the prestressing force. Predetermined load values of 14, 20, and 25 kip (62, 89, 111 kN) were applied on beams initially prestressed with prestressing forces of 72, 100, and 132 kip (320, 445, and 587 kN), respectively.

The testing scenario included loading the beam first before heating. After the load reached the assigned predetermined load level, the MTS actuator maintained the load level during the entire test in force-control mode.

After loading the beam, the door of the fire chamber was closed and the fire test started by heating the chamber following the time-temperature curve of ASTM E-119. The test continued until the beam was not able to support the applied load. After failure was confirmed, the fire testing ended and the fire chamber was allowed to cool down before the door was opened and the test specimen was inspected. The fire endurance for each beam was recorded as the time from the start of ASTM E119 temperature curve (start of the fire) to the failure of the beam. The nomenclature of each beam indicating the initial prestressing force, prestressing reinforcement, sustained load during testing and serial number of the beam is shown in Figure 6.3-8.

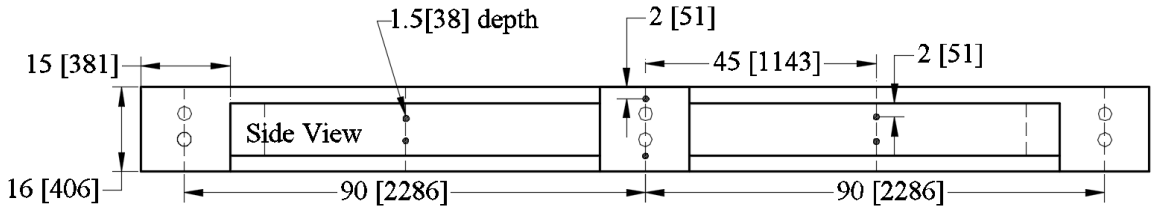

Figure 6.3-2 Side view of beam with thermocouple locations, all dimensions are in in. [mm]

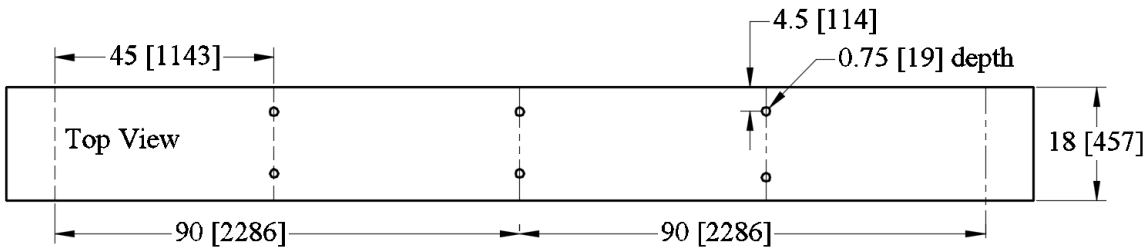

Figure 6.3-3 Thermocouple location in the beam, top view, all dimensions are in in. [mm]

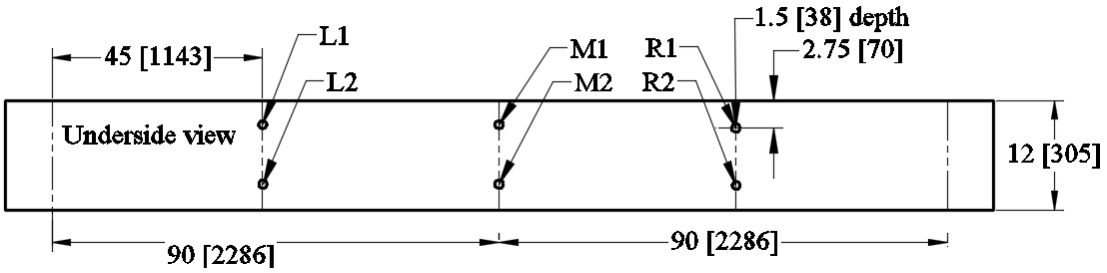

Figure 6.3-4 Thermocouple location in the beam, underside view, all dimensions are in in. [mm]

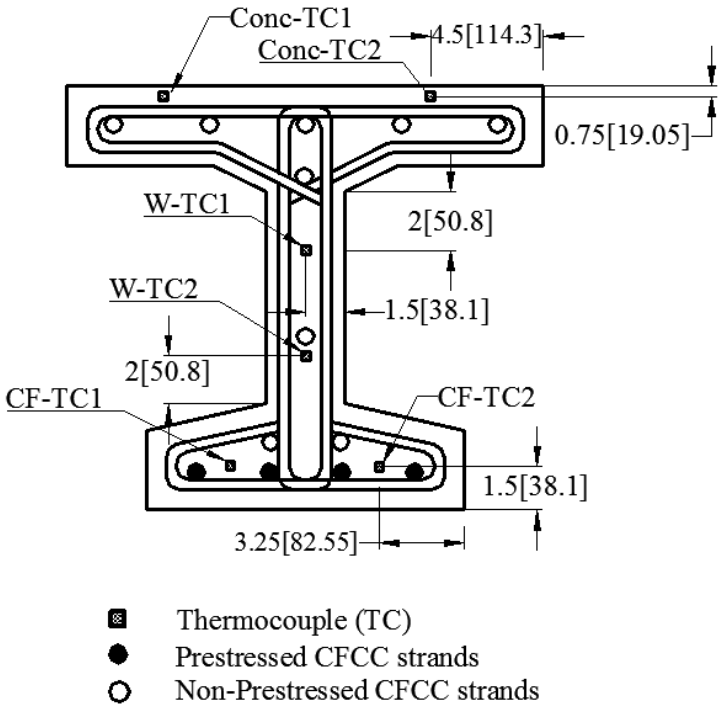

Figure 6.3-5 Thermocouple location in the quarter sections, all dimensions are in in. [mm]

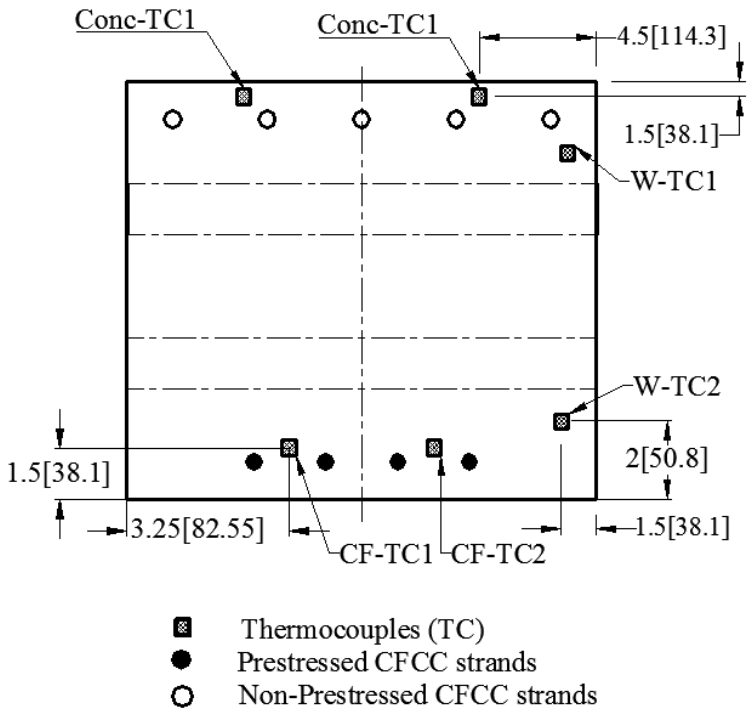

Figure 6.3-6 Thermocouple location in the mid-section, typical, all dimensions are in in. [mm]

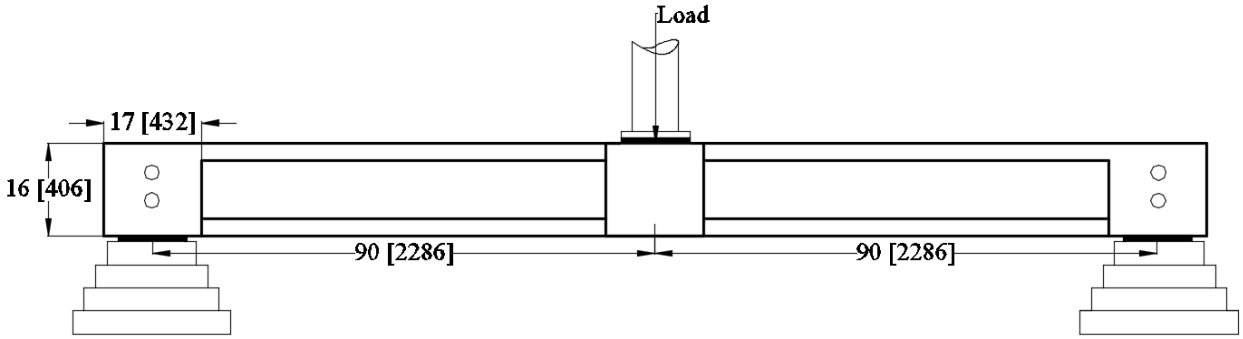

Figure 6.3-7 Sketch of test set-up, all dimensions are in in. [mm]

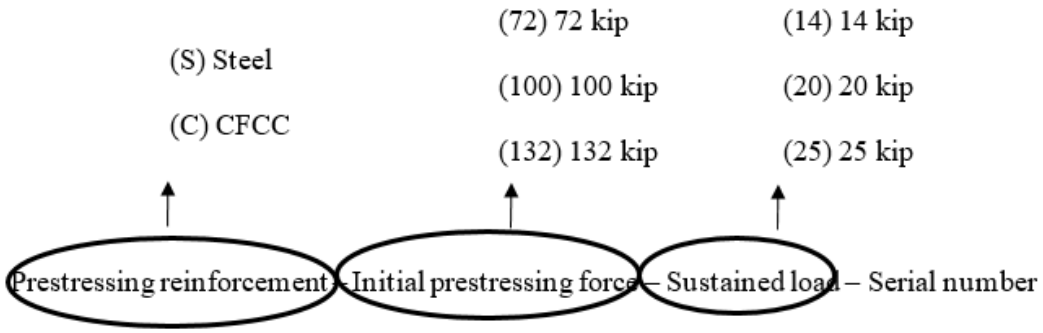

Figure 6.3-8 Beam notation

6.3.2 Test Results

6.3.2.1 Control beam S132-25-1

The first control beam (S132-25-1) was prestressed with steel strands. The initial prestressing force was 132 kip (587 kN) per beam and it was tested according to ASTM E119 with a central point load of 25 kip (111 kN). Linear transducer of hydraulic load actuator was connected to the data acquisition unit of the MTS to monitor the deflection of the beam. The beam was loaded to 25 kip (111 kN) with a rate of 2 kip/minute (8.9 kN/minute) in a force control mode. Since the applied load was less than the cracking load of the beam, no cracks were noticed under this load. The beam was exposed to fire (ASTM E119) to failure. The thermocouples were connected to the data acquisition unit to record the temperature.

First spalling of concrete was observed on the top flange of CFCC stirrup side of the beam. The beam started to lose stiffness and deflect after 50 minutes and failed completely after 98 minutes. The failure was detected by a sudden loss in the load carrying capacity. The mid-span deflection just before failure was 5.3 in. (136 mm). The side with CFCC stirrup was more effected by fire than the side with steel stirrup. At failure, the maximum recorded temperature of the prestressed steel strands was approximately 1082 °F (583 °C) and the maximum air temperature was 1827 °F (977 °C). At onset of deflection, these temperatures were 558 °F (292 °C) and 1655 °F (902 °C), respectively.

Figure 6.3-9 to Figure 6.3-10 show the test specimen before, during and after the fire test. In addition, and as shown in the time-deflection curve presented in Figure 6.3-13, the beam did not lose any stiffness during the first 50 minutes of the test, as there was no increase in deflection. Figure 6.3-14 shows the time-temperature curves for the six thermocouples placed at the mid-span section. The time-temperature curves for the six thermocouples placed at the level of prestressed steel strands are shown in Figure 6.3-15.

Figure 6.3-9 Beam S132-25-1 before fire

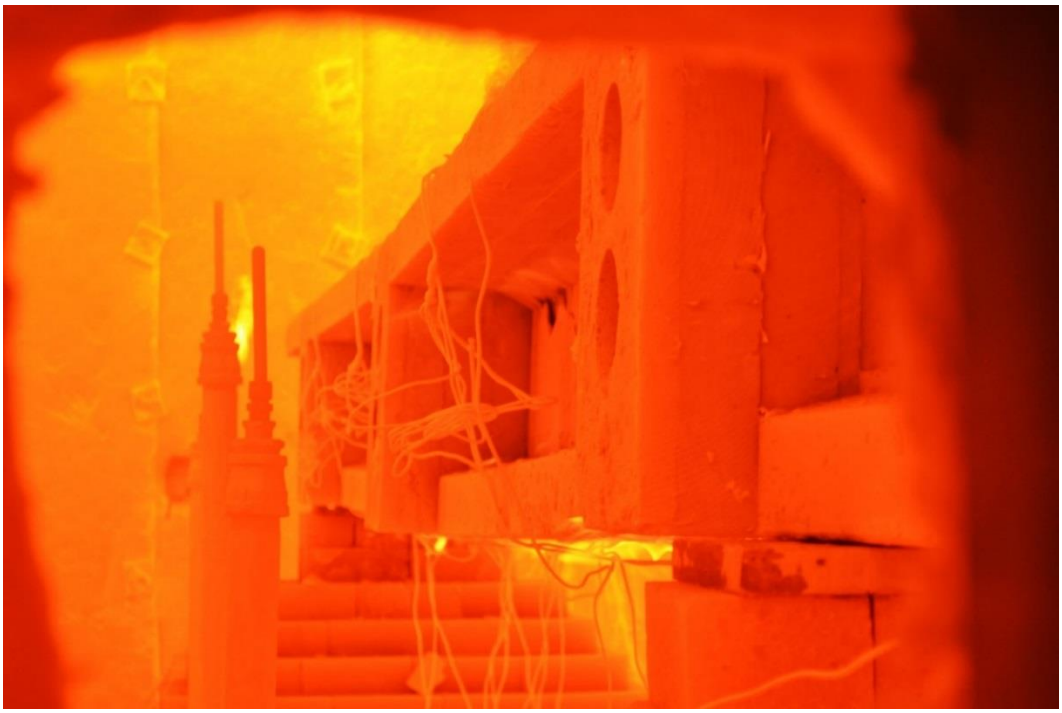

Figure 6.3-10 Beam S132-25-1 during fire

Figure 6.3-11 Beam S132-25-1 after fire

Figure 6.3-12 Rear view of Beam S132-25-1 after fire

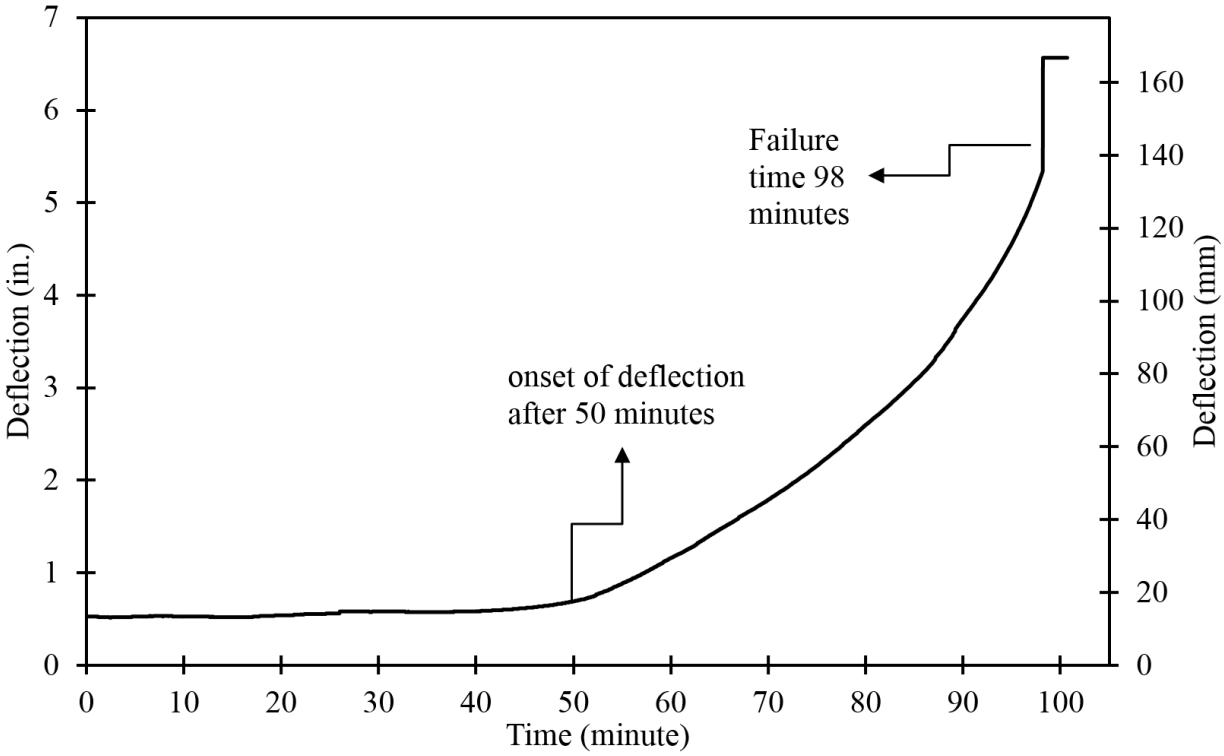

Figure 6.3-13 Time-deflection curve for Beam S132-25-1

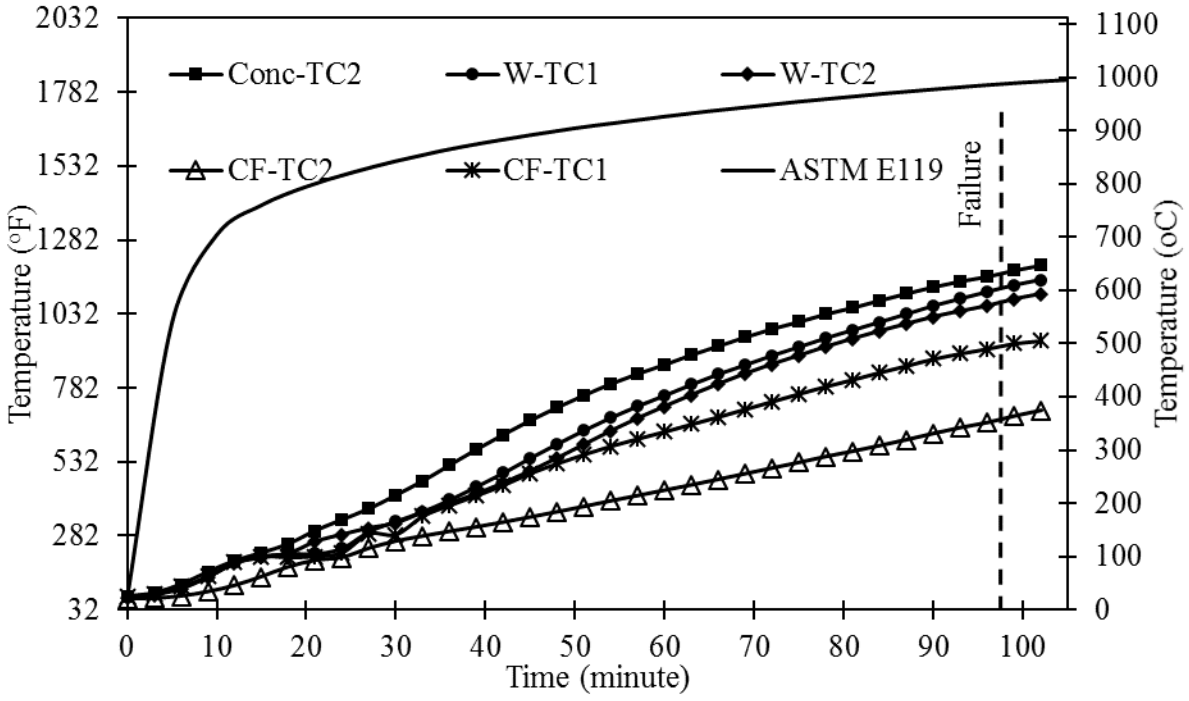

Figure 6.3-14 Time-temperature curves for Beam S132-25-1 at the mid-span

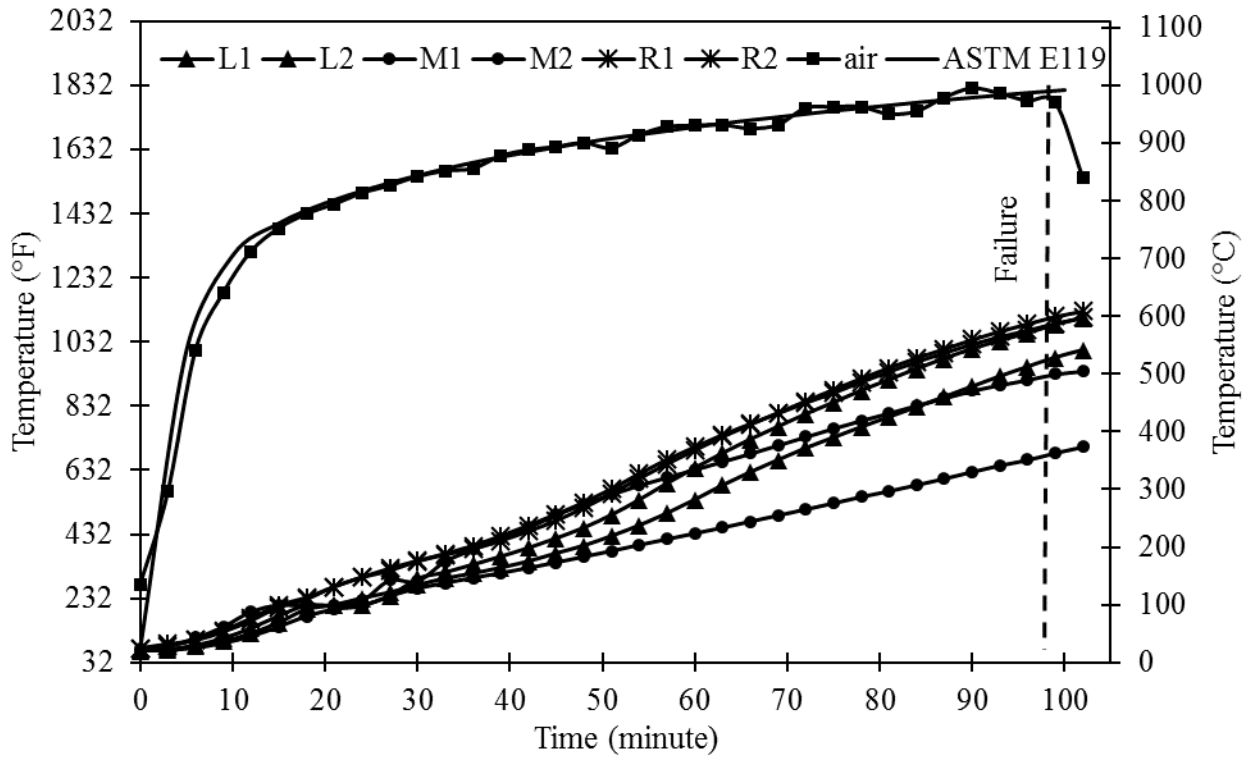

Figure 6.3-15 Time-temperature curves for Beam S132-25-1 at level of prestressed steel strands

6.3.2.2 Beam C72-14-1

Beam C72-14-1 was prestressed with CFCC strands. The initial prestressing force in the beam was 72 kip (320 kN) and it was tested according to ASTM E119 with a central point load of 14 kip (62 kN). Linear transducer of hydraulic load actuator was connected to the data acquisition unit of the MTS to monitor the deflection of the beam. Beam was loaded to 14 kip (62 kN) with a rate of 2 kip/minute (8. 9 kN/minute) under force control. The thermocouples were connected to the data acquisition unit to record the temperature.

Figure 6.3-16 to Figure 6.3-20 show the test specimen before, during, and after the fire test. No deflection was noticed during the first 33 minutes after the start of the fire test. After 33 minutes, there was a gradual increase in deflection from 0.3 in. (8 mm) to 1.9 in. (48 mm). The failure took place after 69 minutes with a corresponding deflection of 6.3 in. (160 mm) (Figure 6.3-21). Figure 6.3-22 shows the temperature-time curve for the six thermocouples placed at the mid-span section. The temperature-time curve for the six thermocouples placed at the level of prestressed CFCC strands are shown in Figure 6.3-23.

No concrete crushing was observed near the mid span although slight spalling of concrete was observed on the top flange. At failure, the maximum temperature of the prestressed CFCC strand was 955 °F (513 °C) and the maximum air temperature was 1710 °F (932 °C). At onset of deflection, CFCC and air temperatures were 517 °F (269 °C) and 1560 °F (849 °C), respectively.

Figure 6.3-16 Beam C72-14-1 before fire

Figure 6.3-17 Beam C72-14-1 during fire

Figure 6.3-18 Burning of CFCC stirrups in Beam C72-14-1 during fire

Figure 6.3-19 Beam C72-14-1 after fire

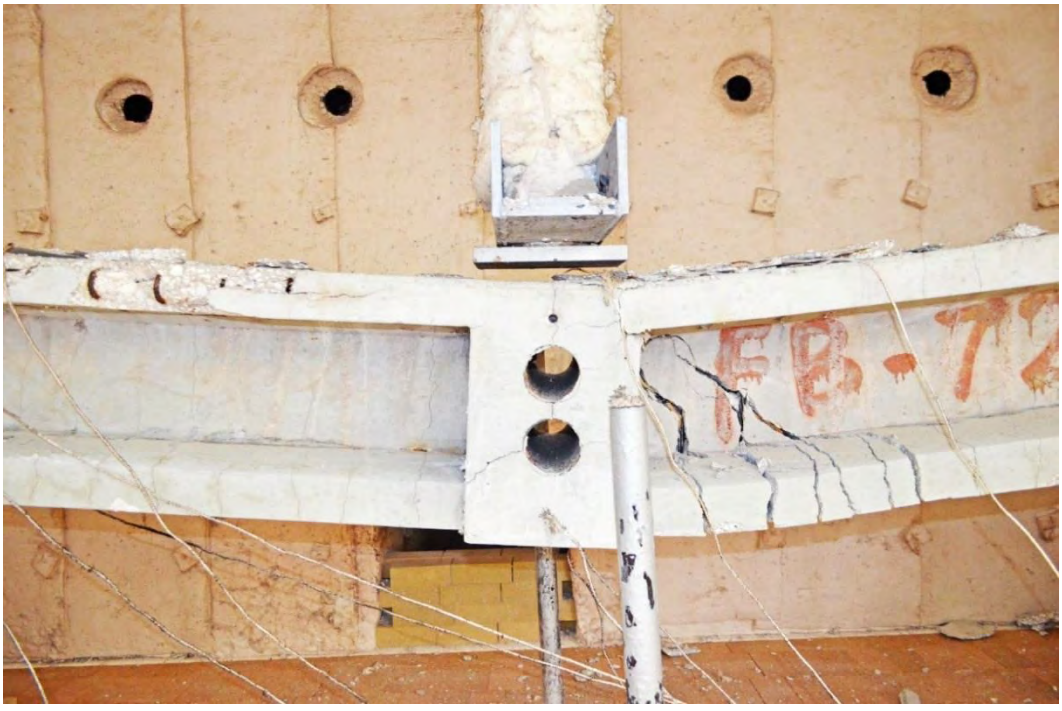

Figure 6.3-20 Close-up view of Beam C72-14-1 after failure

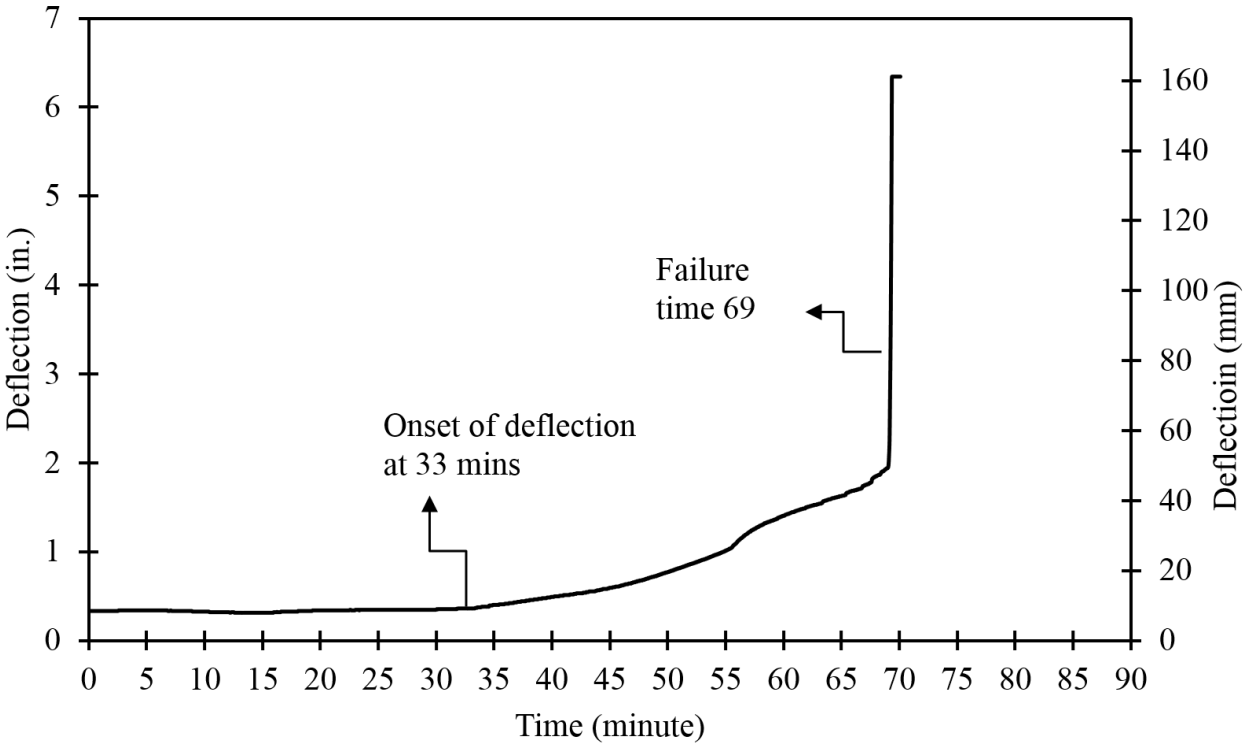

Figure 6.3-21 Time-deflection curve for Beam C72-14-1

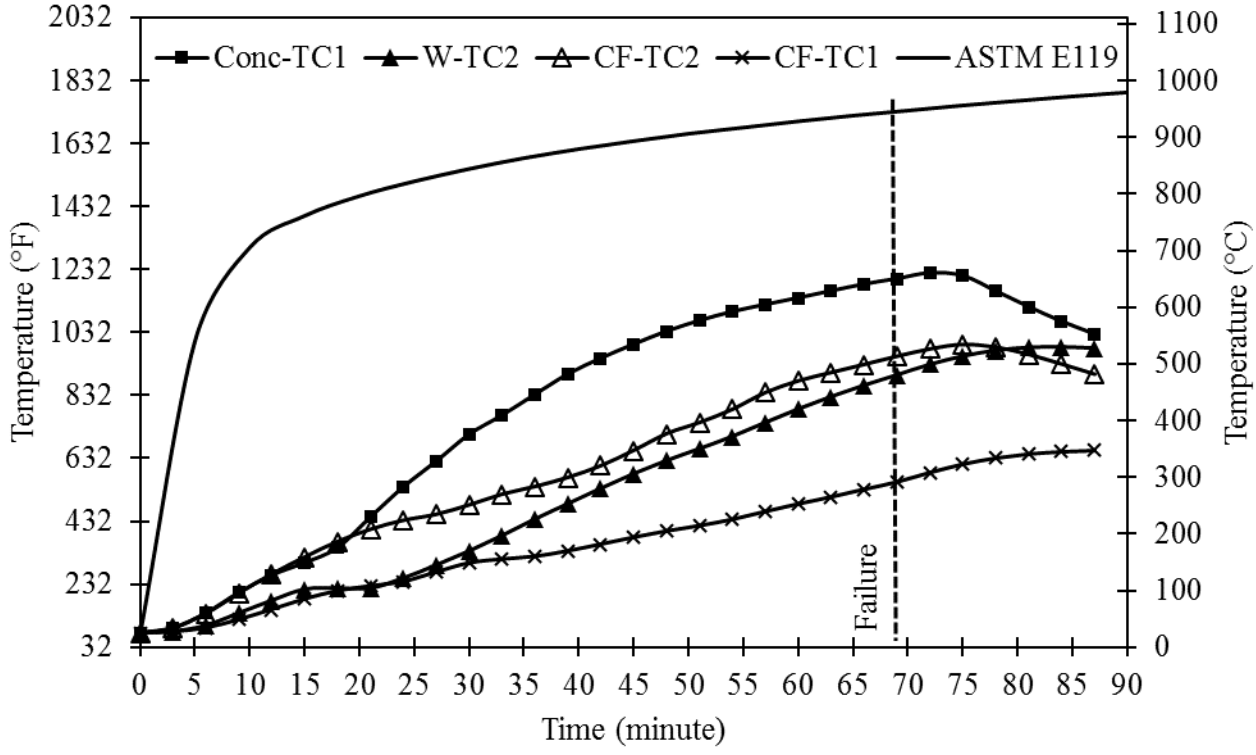

Figure 6.3-22 Time-temperature curves for Beam C72-14-1 at mid-span

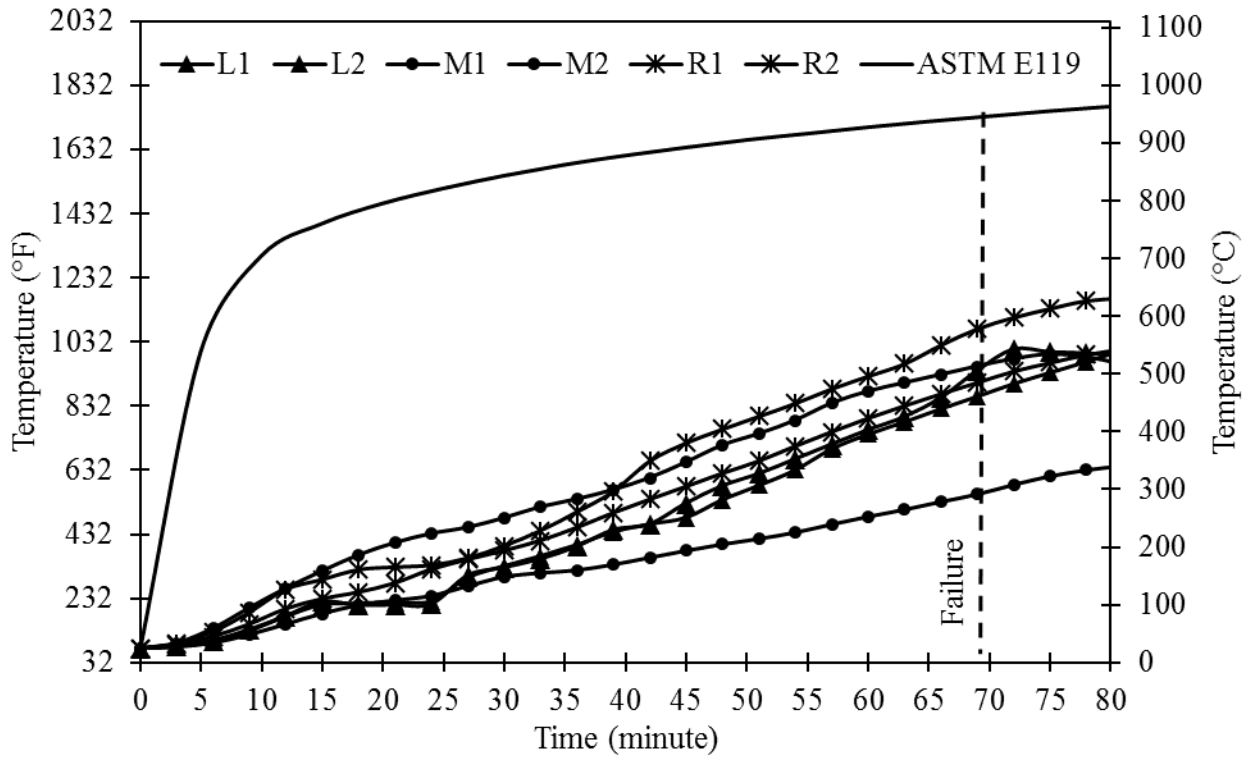

Figure 6.3-23 Time-temperature curves for Beam C72-14-1 at level of prestressed CFCC strands

6.3.2.3 Beam C100-20-1

Beam C100-20-1 was prestressed with CFCC strands. The initial prestressing force in the beam was 100 kip (445 kN) and it was tested according to ASTM E119 with a central point load of 20 kip (89 kN). Linear transducer of hydraulic load actuator was connected to the data acquisition unit of MTS to monitor the deflection of the beam. The beam was loaded to 20 kip (89 kN) with a rate of 2 kip/minute (8.9 kN/minute) under force control. The thermocouples were connected to the data acquisition unit to record the temperature.

Figure 6.3-24 to Figure 6.3-26 show the test specimen before and after the fire test. As shown in Figure 6.3-27, no deflection was noticed during the first 20 minutes at the start of the fire test. After 20 minutes, there was a gradual increase in the deflection from 0.6 in. (15 mm) to 1.7 in. (43 mm). The failure took place after 48 minutes with a corresponding deflection of 4.6 in. (117 mm). Heavy spalling of concrete was observed on the top flange. At failure, the maximum temperature of the prestressed CFCC strand was 956 °F (513 °C) and the maximum air temperature was 1650 °F (899 °C). At onset of deflection, CFCC and air temperatures were 595 °F (312 °C) and 1460 °F (793 °C), respectively. Figure 6.3-28 shows the temperature-time curve for the six thermocouples

placed at the mid-span section. The Time-temperature curves for the six thermocouples placed at the level of prestressed CFCC strands are shown in Figure 6.3-29.

Figure 6.3-24 Beam C100-20-1 before fire

Figure 6.3-25 Beam C100-20-1 after fire

Figure 6.3-26 Concrete spalling on CFCC stirrups side of Beam C100-20-1 after fire

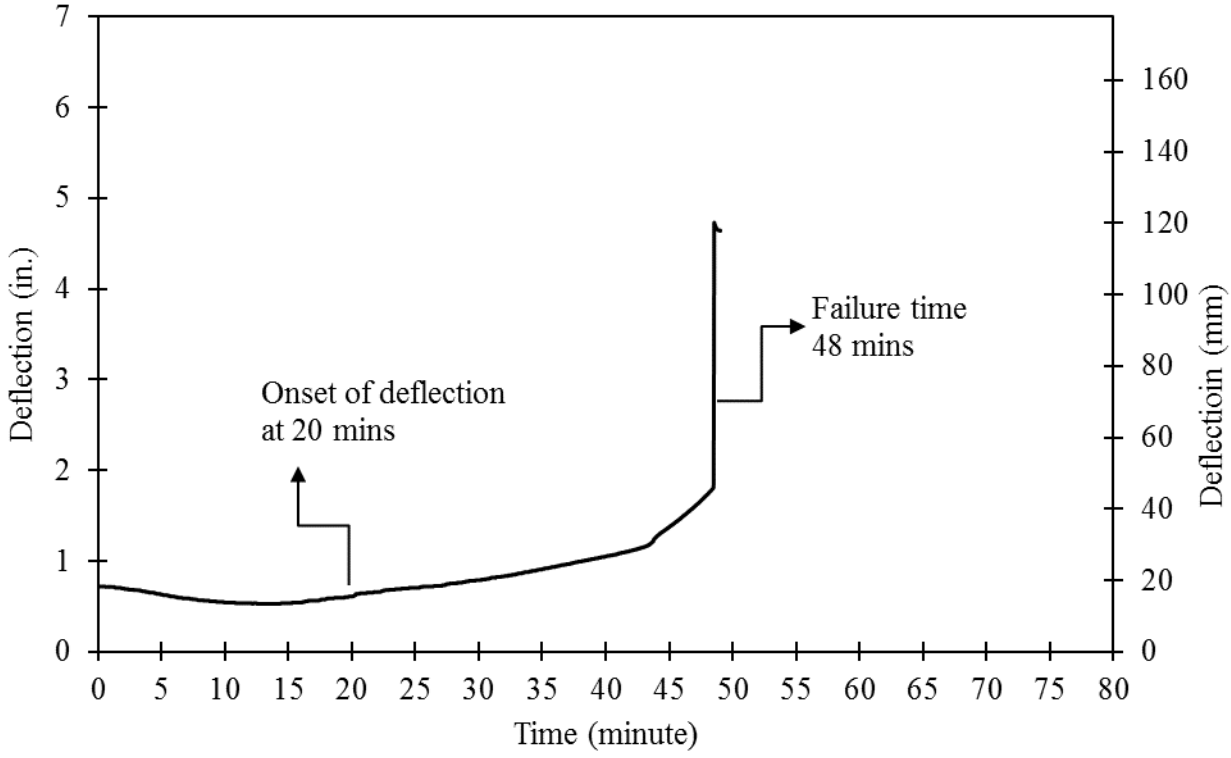

Figure 6.3-27 Time-deflection curve for Beam C100-20-1

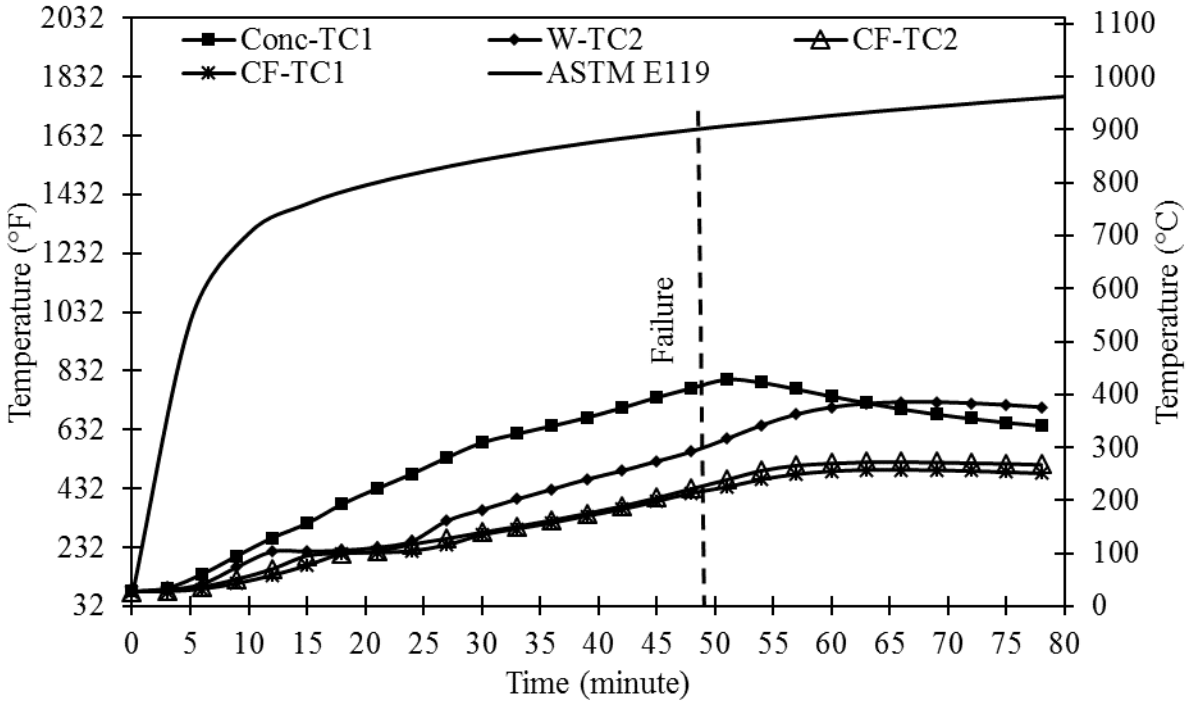

Figure 6.3-28 Time-temperature curves for Beam C100-20-1 at mid-span

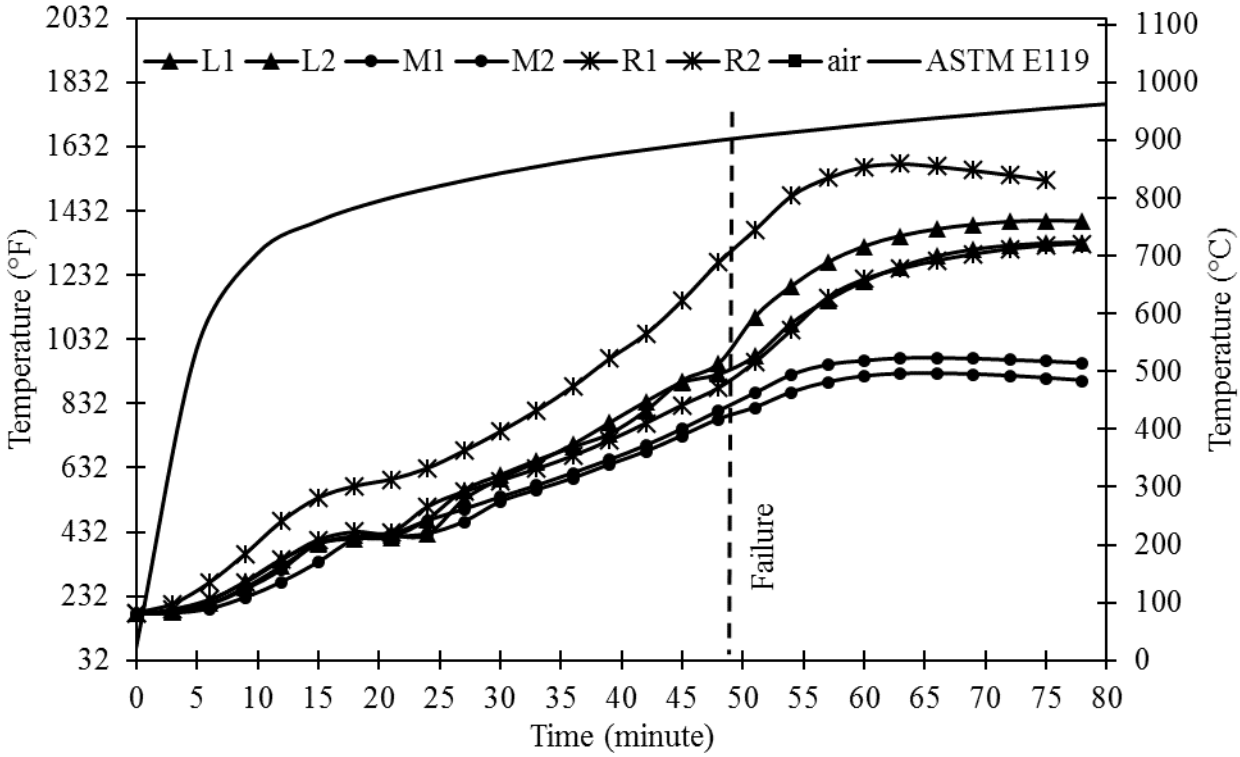

Figure 6.3-29 Time-temperature curves for Beam C100-20-1 at prestressed CFCC strands

6.3.2.4 Beam C100-20-2

Beam C100-20-2 was prestressed with CFCC strands. The initial prestressing force in the beam was 100 kip (449 kN) and it was tested according to ASTM E119 with a central point load of 20 kip (89 kN). Linear transducer of hydraulic load actuator was connected to the data acquisition unit of MTS to monitor the deflection of the beam. The beam was loaded to 20 kip (89 kN) with a rate of 2 kip/minute (8.9 kN/minute) under force control. The thermocouples were connected to the data acquisition unit to record the temperature.

Figure 6.3-30 to Figure 6.3-32 show the test specimen before and after the fire test. Figure 6.3-33 shows time-deflection curve for the beam during the test. No deflection was noticed during the first 30 minutes at the start of the fire test. After 30 minutes, there was a gradual increase in the deflection from 0.6 in. (15 mm) to 2.4 in. (61 mm). The failure took place after 52 minutes with a corresponding deflection of 6.4 in. (153 mm). At failure, the maximum temperature of the prestressed CFCC strand was 686 °F (363 °C) and the maximum air temperature was 1671 °F (910 °C). At onset of deflection, CFCC and air temperatures were 396 °F (202°C) and 1552 °F (844 °C), respectively. Figure 6.3-34 shows the time-temperature curve for the six thermocouples placed at the mid-span section. The time-temperature curves for the six thermocouples placed at the level of prestressed CFCC strands are shown in Figure 6.3-35

Figure 6.3-30 Beam C100-20-2 before fire

Figure 6.3-31 Beam C100-20-2 after fire

Figure 6.3-32 Concrete spalling of bottom flange of Beam C100-20-2 after fire, bottom side view

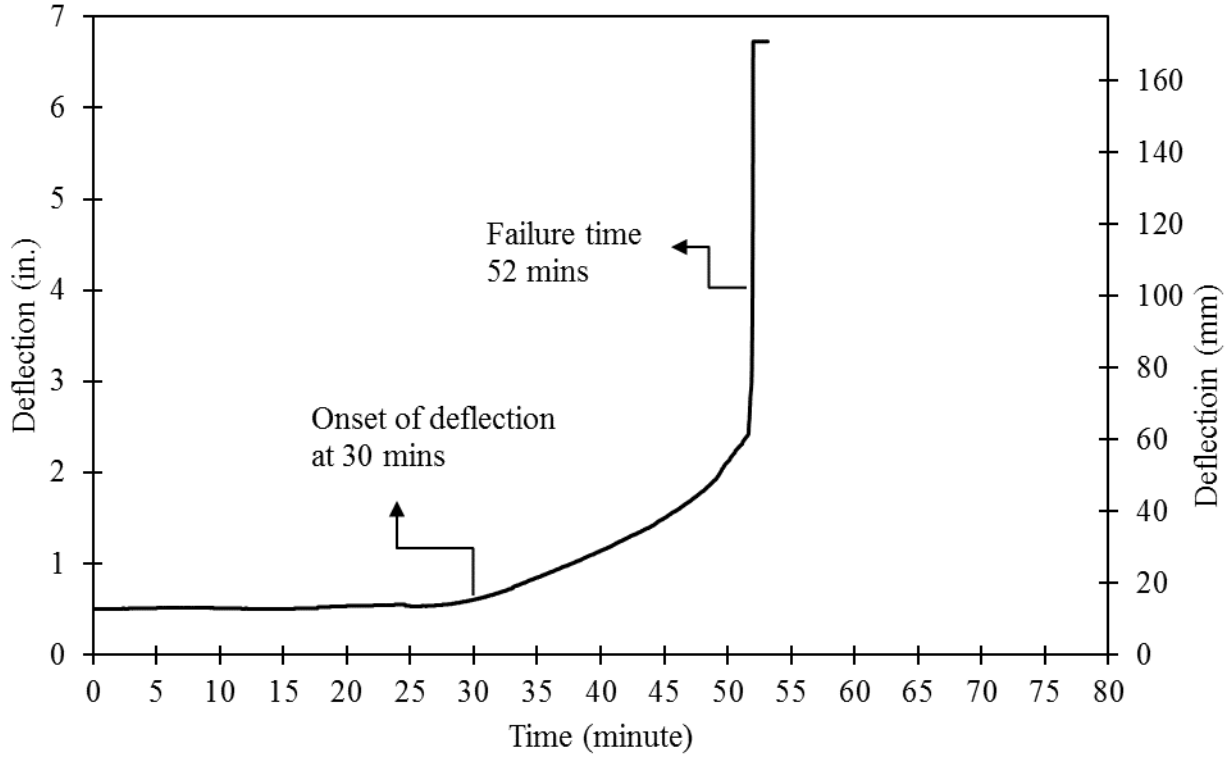

Figure 6.3-33 Time-deflection curve for Beam C100-20-2

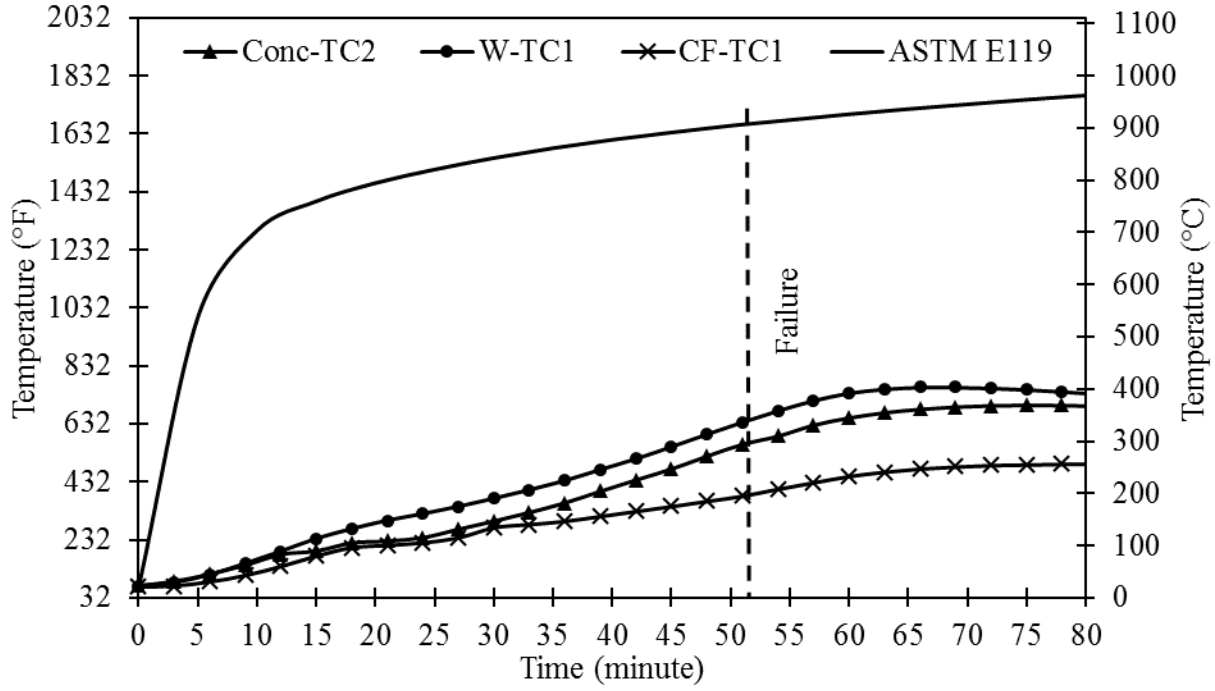

Figure 6.3-34 Time-temperature curves for Beam C100-20-2 at mid-span

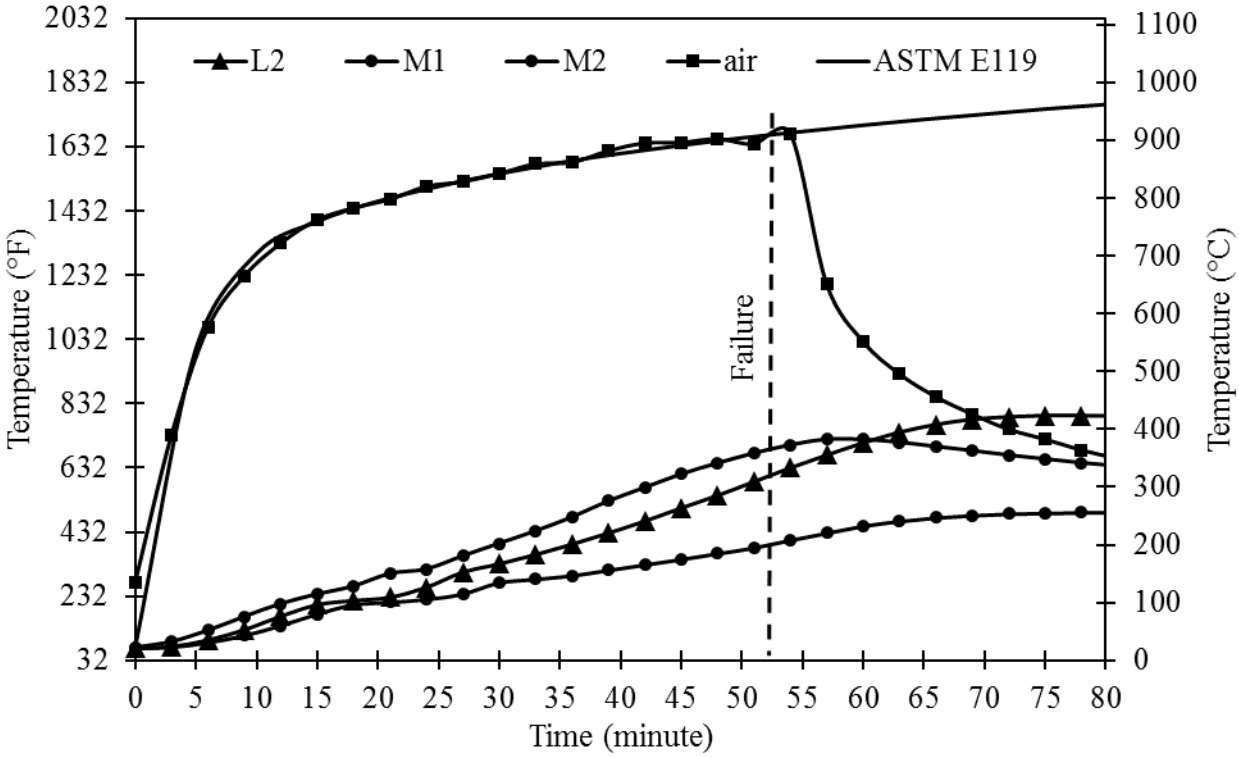

Figure 6.3-35 Time-temperature curves for Beam C100-20-2 at prestressed CFCC strands

6.3.2.5 Beam C100-20-3

Beam C100-20-3 was prestressed with CFCC strands. The initial prestressing force in the beam was 100 kip (445 kN) and it was tested according to ASTM E119 with a central point load of 20 kip (89 kN). Linear transducer of hydraulic load actuator was connected to the data acquisition unit of MTS to monitor the deflection of the beam. The beam was loaded to 20 kip (89 kN) with a rate of 2 kip/minute (8.9 kN/minute) under force control. The thermocouples were connected to the data acquisition unit to record the temperature.

Figure 6.3-36 to Figure 6.3-38 show the test specimen before and after the fire test. Figure 6.3-39 shows time-deflection curve for the beam during the test. No deflection was noticed during the first 23 minutes at the start of the fire test. After 23 minutes, there was a gradual increase in the deflection from 0.5 in. (13 mm) to 1.8 in. (46 mm). The failure took place after 53 minutes with a corresponding deflection of 6.7 in. (171 mm). At failure, the maximum temperature of the prestressed CFCC strand was 678 °F (359 °C) and the maximum air temperature was 1680 °F (915 °C). At onset of deflection, CFCC and air temperatures were 277 °F (136 °C) and 1493 °F (812 °C), respectively.

Figure 6.3-40 shows the time-temperature curve for the six thermocouples placed at the mid-span section. The time-temperature curves for the six thermocouples placed at the level of prestressed CFCC strands are shown in Figure 6.3-41.

Figure 6.3-36 Beam C100-20-3 before fire

Figure 6.3-37 Beam C100-20-3 after fire

Figure 6.3-38 Carbon fiber filaments after burning of epoxy adhesive in Beam C100-20-3

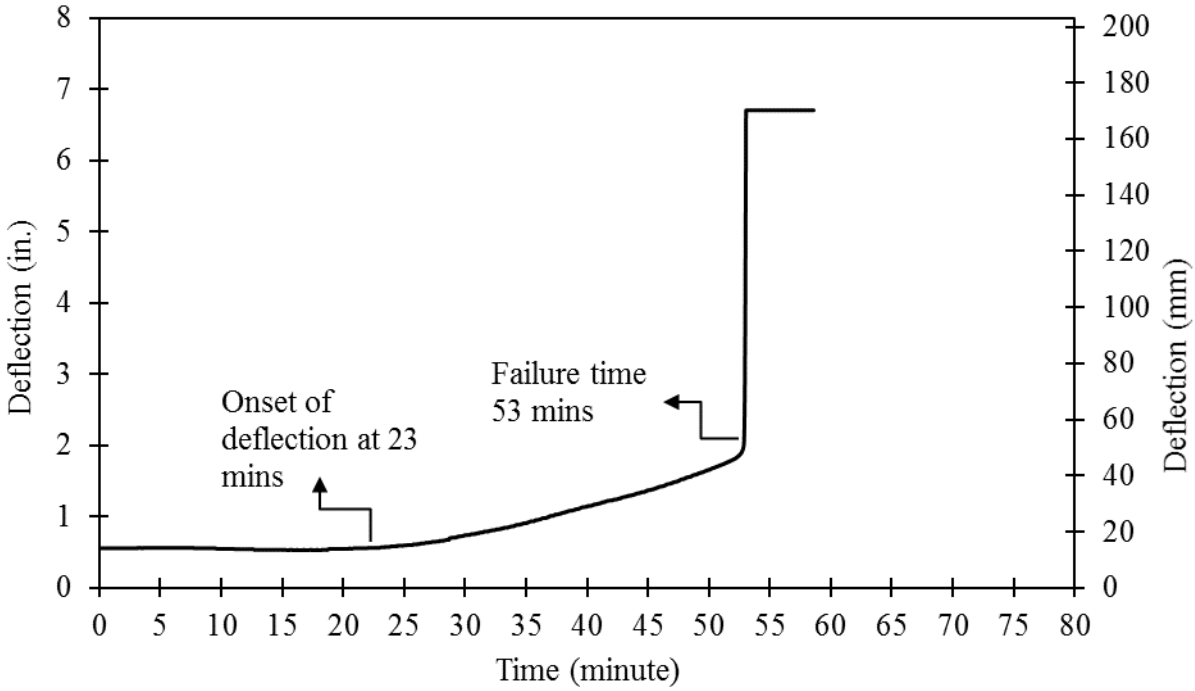

Figure 6.3-39 Time-deflection curve for Beam C100-20-3

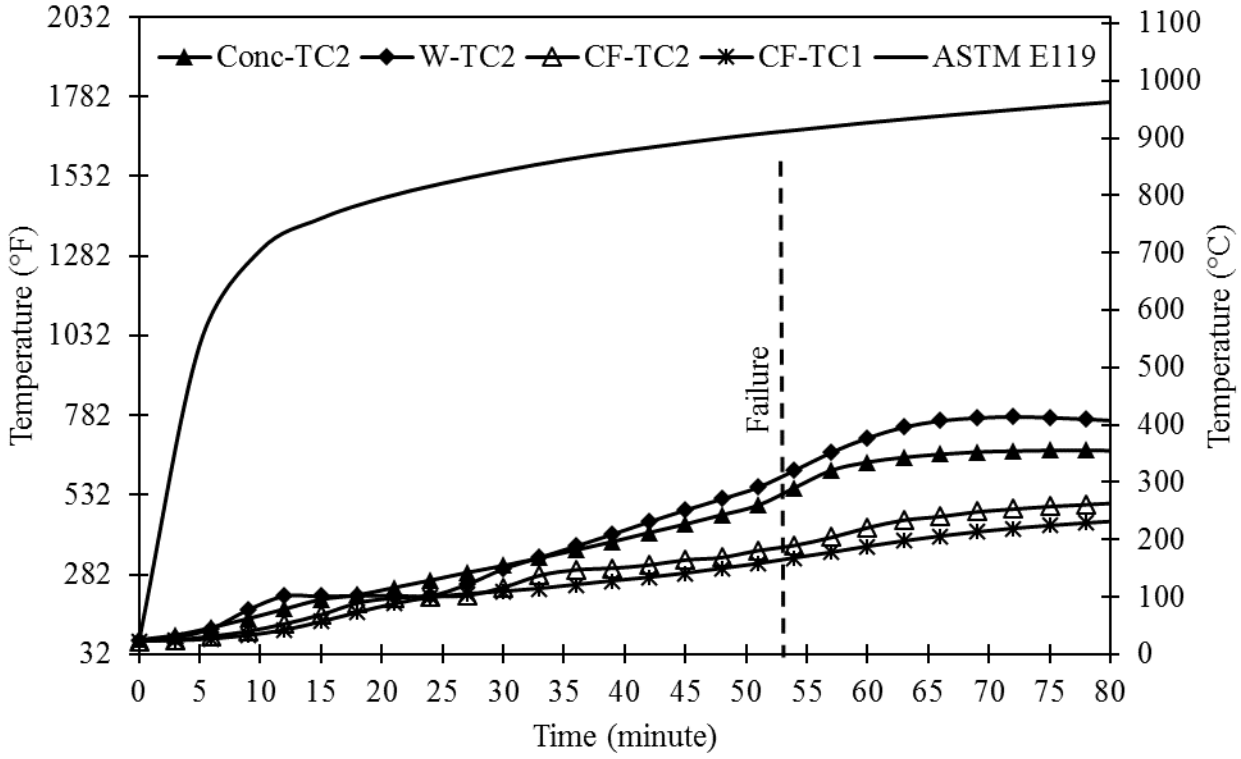

Figure 6.3-40 Time-temperature curve for Beam C100-20-3 at mid-span

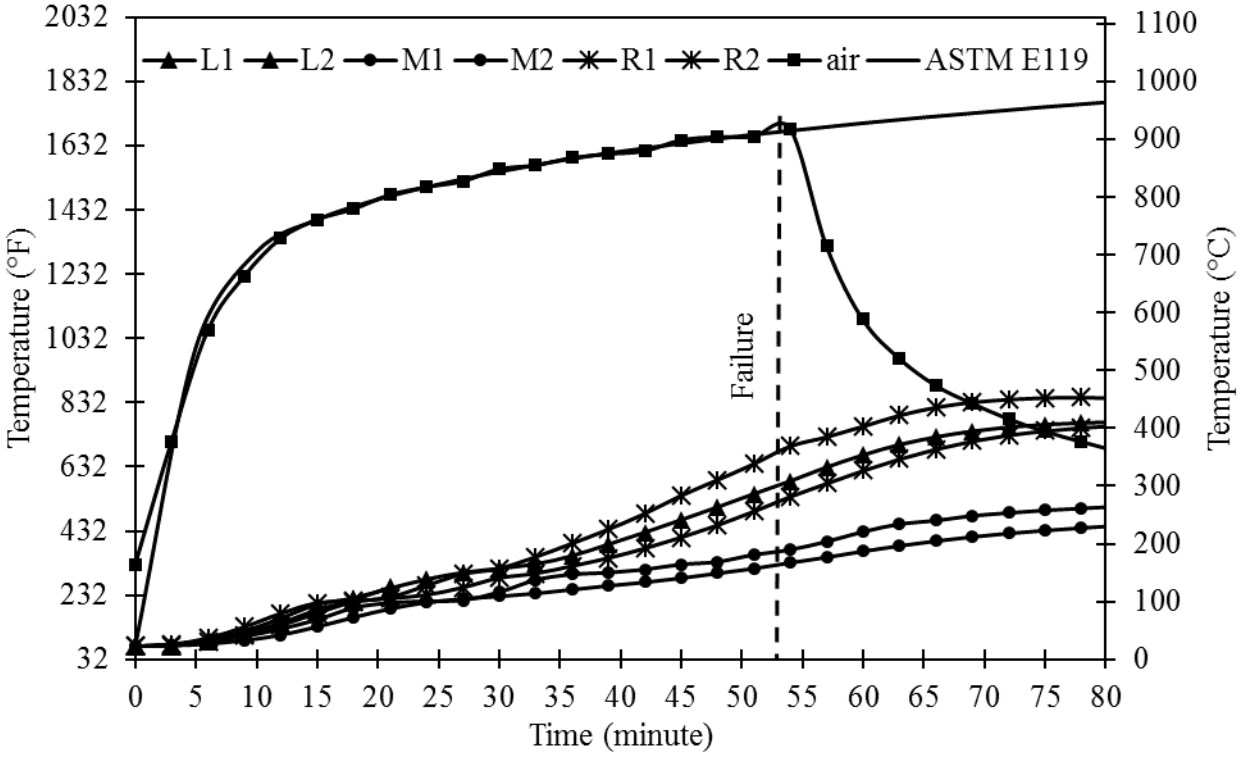

Figure 6.3-41 Time-temperature curves for Beam C100-20-3 at prestressed CFCC strands

6.3.2.6 Beam C100-20-4

Beam C100-20-4 was prestressed with CFCC strands. The initial prestressing force in the beam was 100 kip (445 kN) and it was tested according to ASTM E119 with a central point load of 20 kip (89 kN). Linear transducer of hydraulic load actuator was connected to the data acquisition unit of MTS to monitor the deflection of the beam. The beam was loaded to 20 kip (89 kN) with a rate of 2 kip/minute (8.9 kN/minute) under force control. The thermocouples were connected to the data acquisition unit to record the temperature.

Figure 6.3-42 to Figure 6.3-44 show the test specimen before and after the fire test. Figure 6.3-45 shows deflection-time curve for the beam during the test. No deflection was noticed during the first 21 minutes at the start of the fire test. After 21 minutes, there was a gradual increase in the deflection from 0.5 in. (13 mm) to 1.9 in. (48 mm). The failure took place after 58 minutes with a corresponding deflection of 6.2 in. (157 mm). At failure, the maximum temperature of the prestressed CFCC strand was 771 °F (322 °C) and the maximum air temperature was 1706 °F (930 °C). At onset of deflection these temperatures were 293 °F (145 °C) and 1470 °F (799 °C), respectively.

Figure 6.3-46 shows the time-temperature curves for the six thermocouples placed at the mid-span section. The time-temperature curves for the six thermocouples placed at the level of prestressed CFCC strands are shown in Figure 6.3-47.

Figure 6.3-42 Beam C100-20-4 before fire

Figure 6.3-43 Beam C100-20-4 after fire

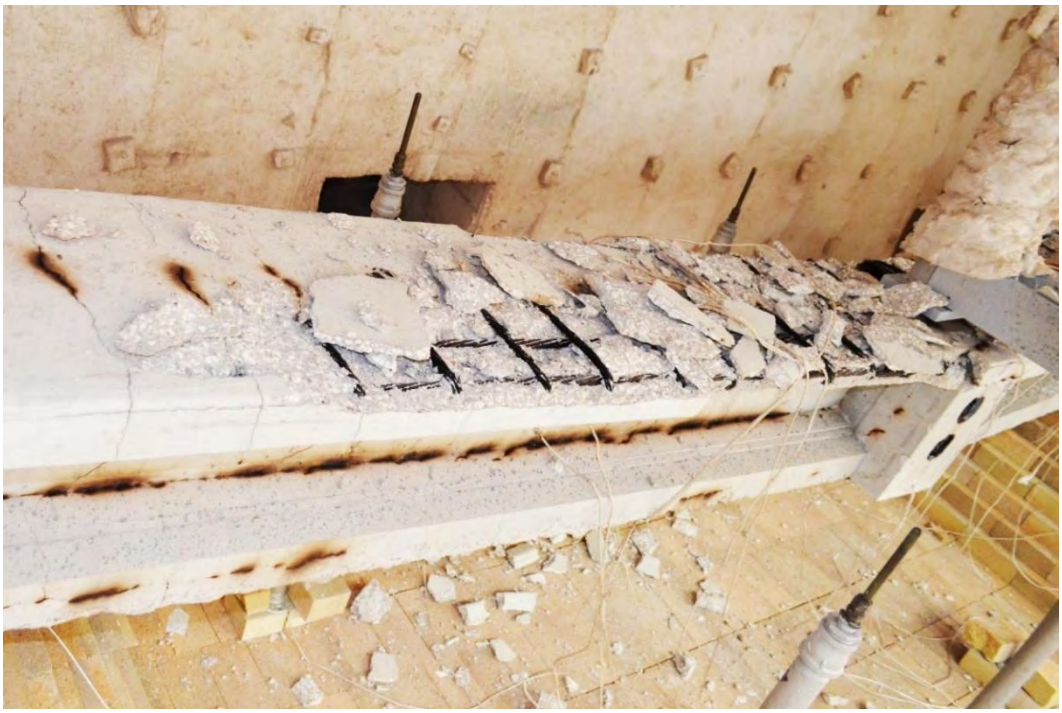

Figure 6.3-44 Concrete spalling of Beam C100-20-4 after fire

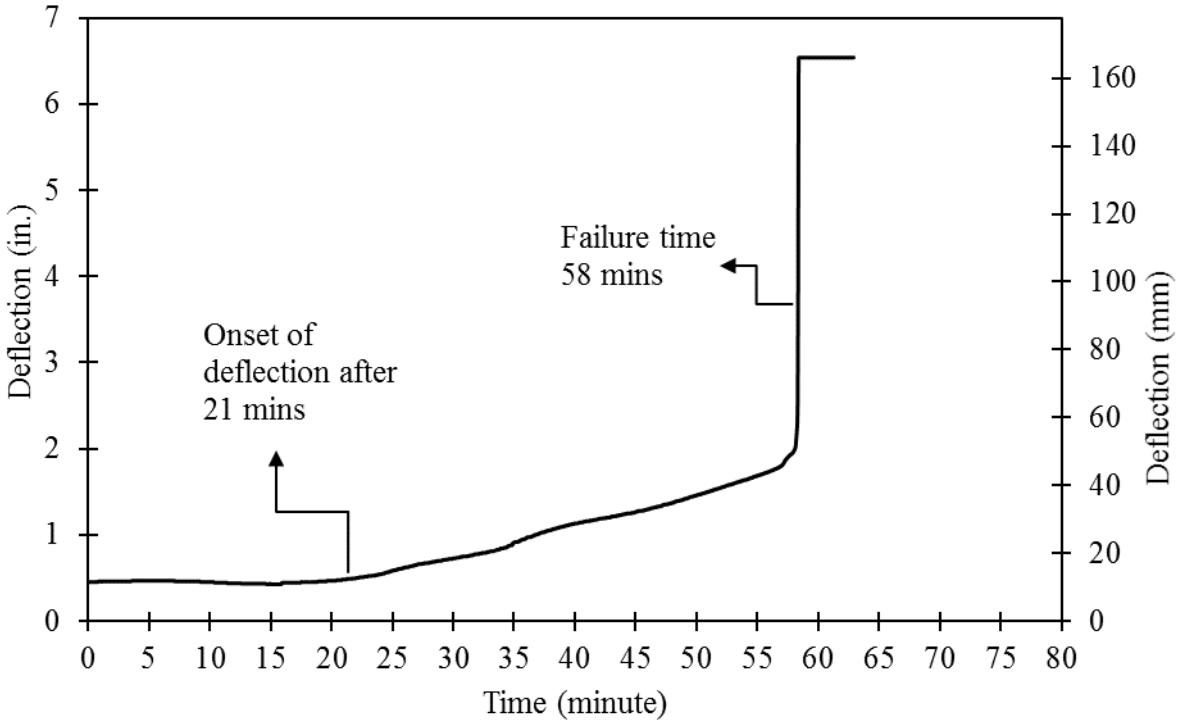

Figure 6.3-45 Time-deflection curve for Beam C100-20-4

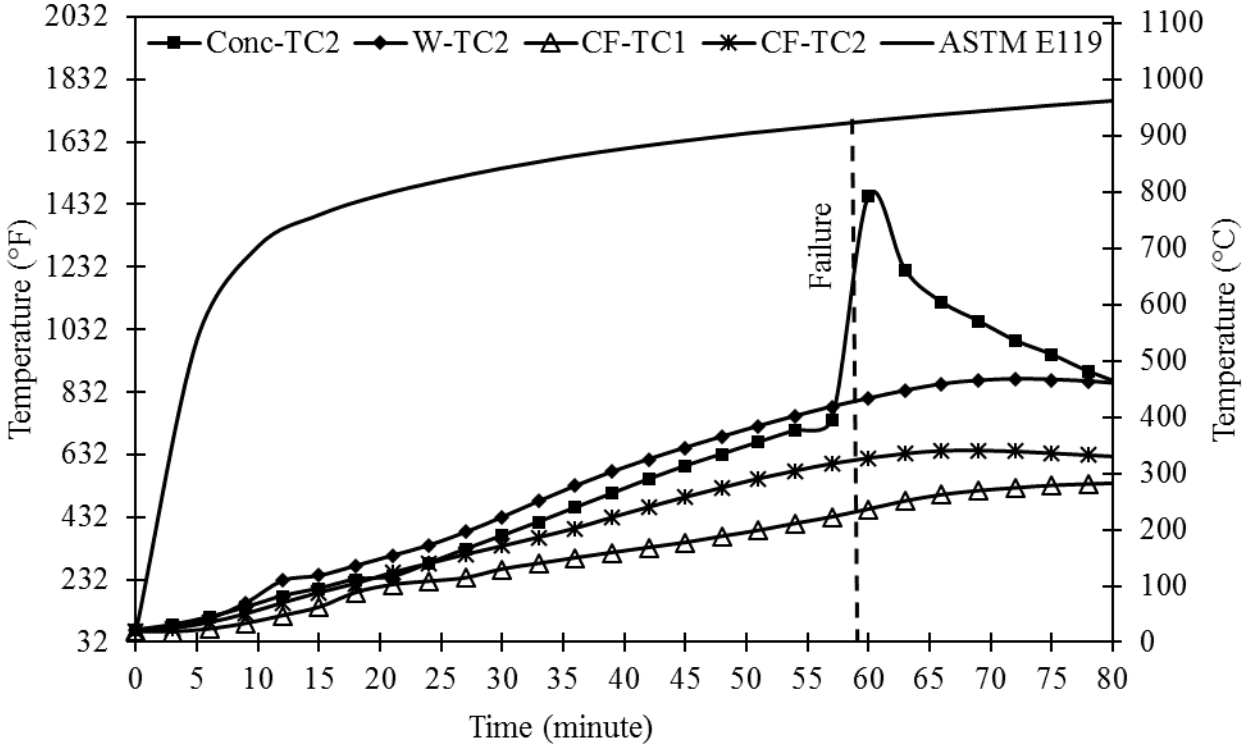

Figure 6.3-46 Time-temperature curves for Beam C100-20-4 in the mid-span

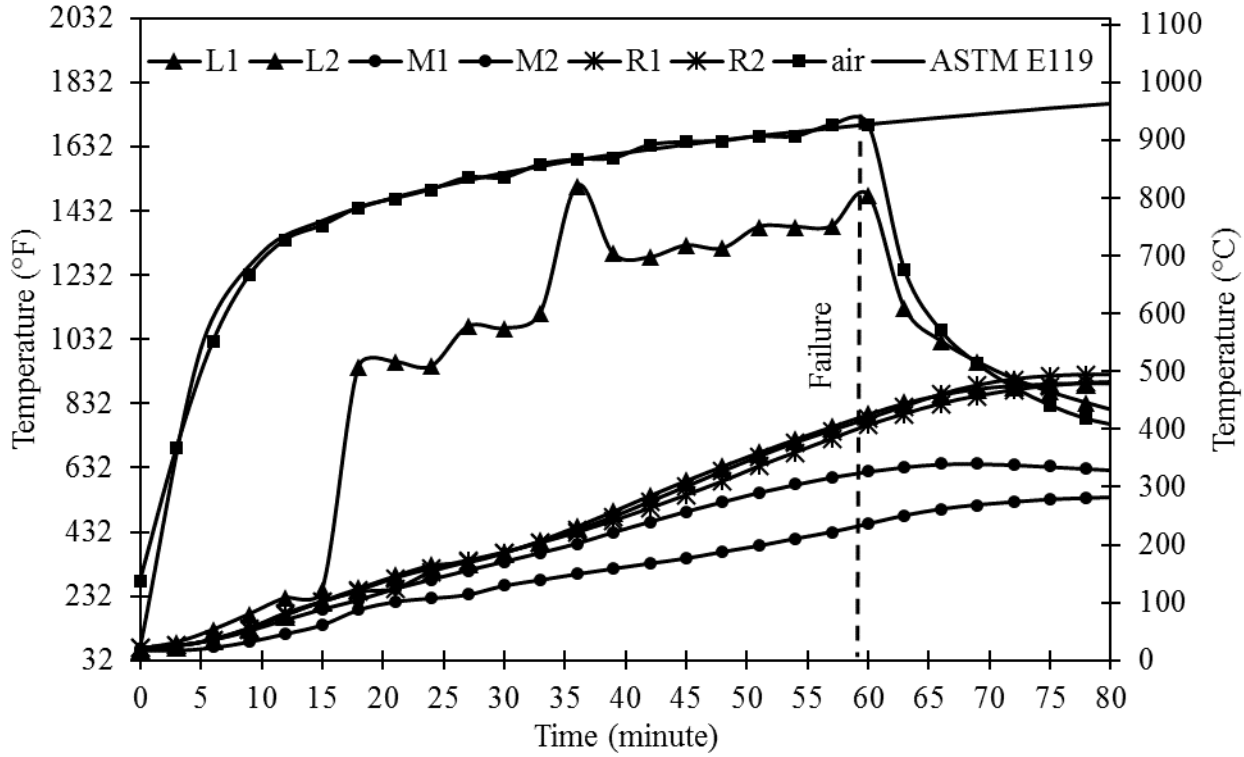

Figure 6.3-47 Time-temperature curves for Beam C100-20-4 at prestressed CFCC strands

6.3.2.7 Beam C100-20-5

Beam C100-20-5 was prestressed with CFCC strands. The initial prestressing force in the beam was 100 kip (445 kN) and it was tested according to ASTM E119 with a central point load of 20 kip (89 kN). Linear transducer of hydraulic load actuator was connected to the data acquisition unit of MTS to monitor the deflection of the beam. The beam was loaded to 20 kip (89 kN) with a rate of 2 kip/minute (8.9 kN/minute) under force control. The thermocouples were connected to the data acquisition unit to record the temperature.

Figure 6.3-48 to Figure 6.3-49 show the test specimen before and after the fire test. Figure 6.3-51 shows deflection-time curve for the beam during the test. No deflection was noticed during the first 20 minutes at the start of the fire test. After 20 minutes, there was a gradual increase in the deflection from 0.4 in. (10 mm) to 1.6 in. (41 mm). The failure took place after 52 minutes with a corresponding deflection of 6.7 in. (170 mm). At failure, the maximum temperature of the prestressed CFCC strand was 623 °F (328 °C) and the maximum air temperature was 1665 °F (907 °C). At onset of deflection these temperatures were 254 °F (123 °C) and 1463 °F (795 °C), respectively.

Figure 6.3-52 shows the time-temperature curves for the six thermocouples placed at the mid-span section. The time-temperature curves for the six thermocouples placed at the level of prestressed CFCC strands are shown in Figure 6.3-53.

Figure 6.3-48 Beam C100-20-5 before fire

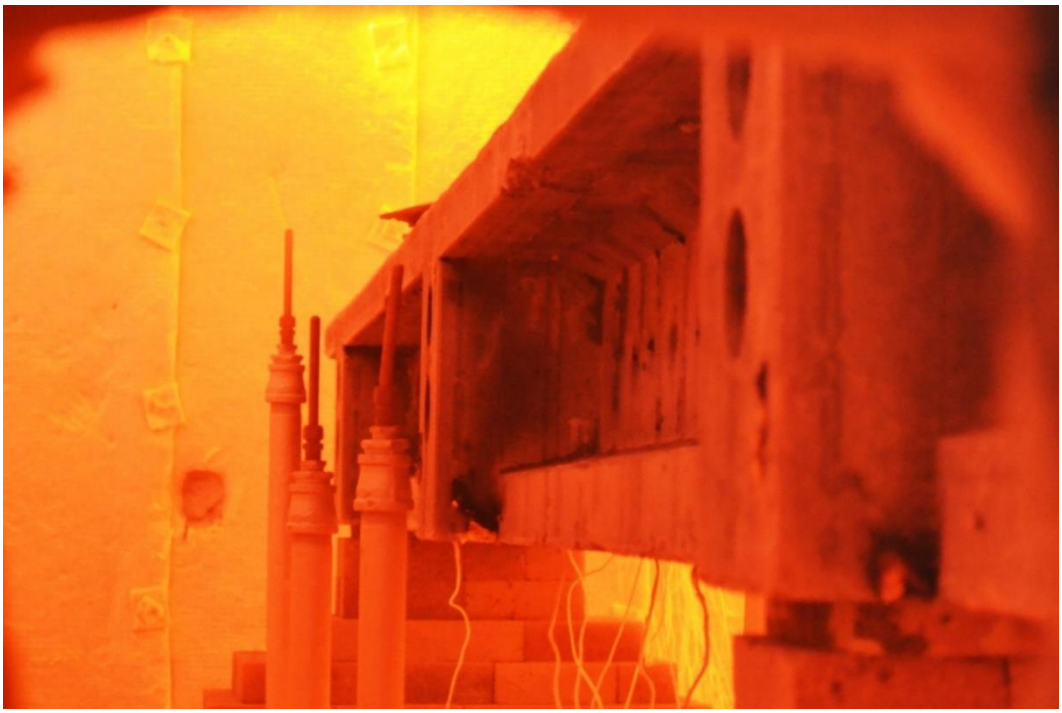

Figure 6.3-49 Beam C100-20-5 during fire

Figure 6.3-50 Beam C100-20-5 after fire

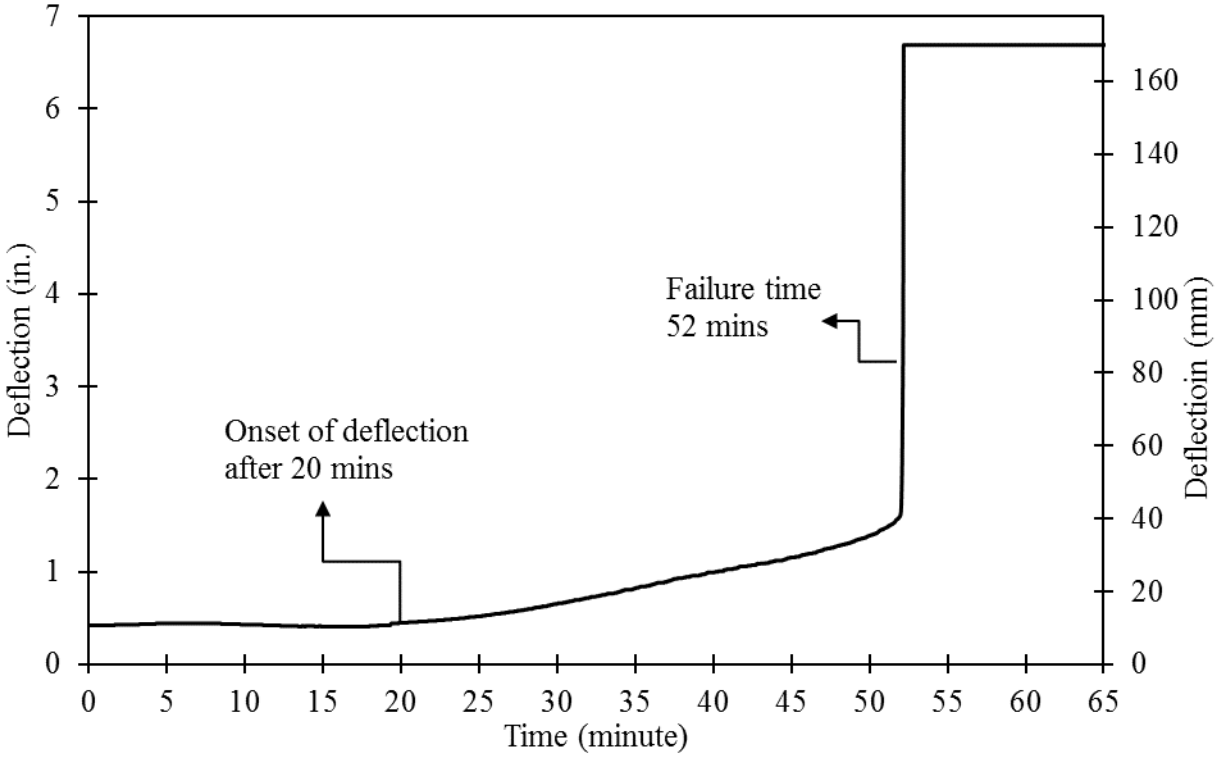

Figure 6.3-51 Time-deflection curve for Beam C100-20-5

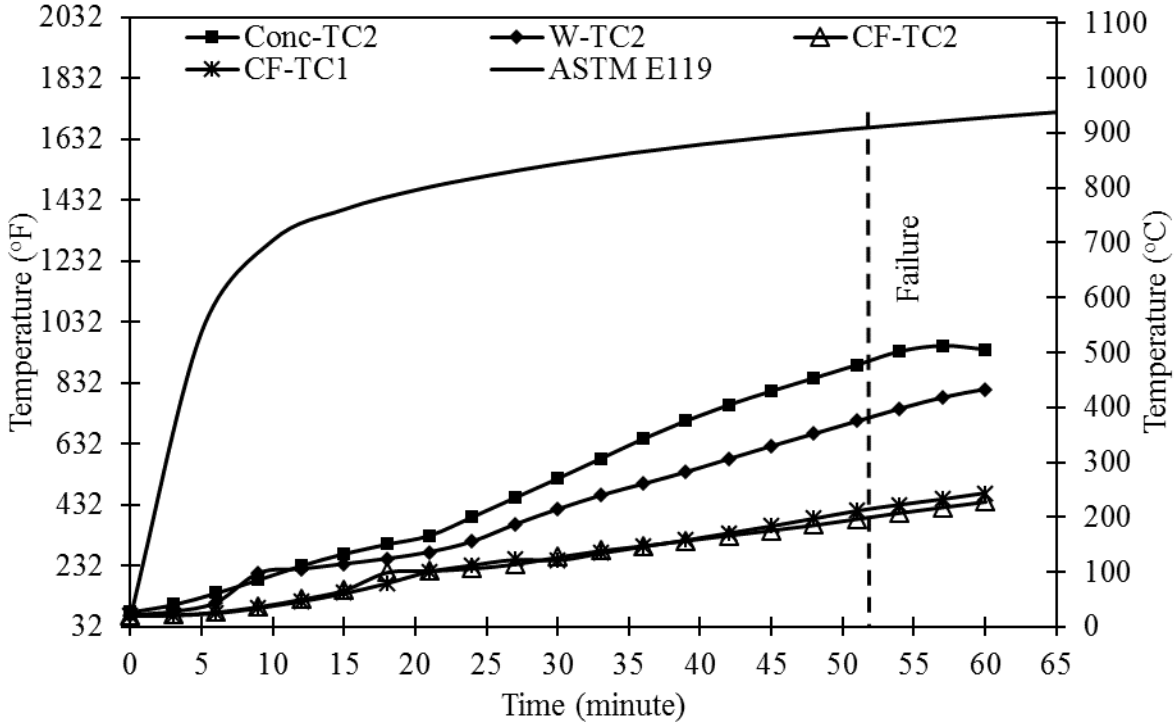

Figure 6.3-52 Time-temperature curves for Beam C100-20-5 at mid-span

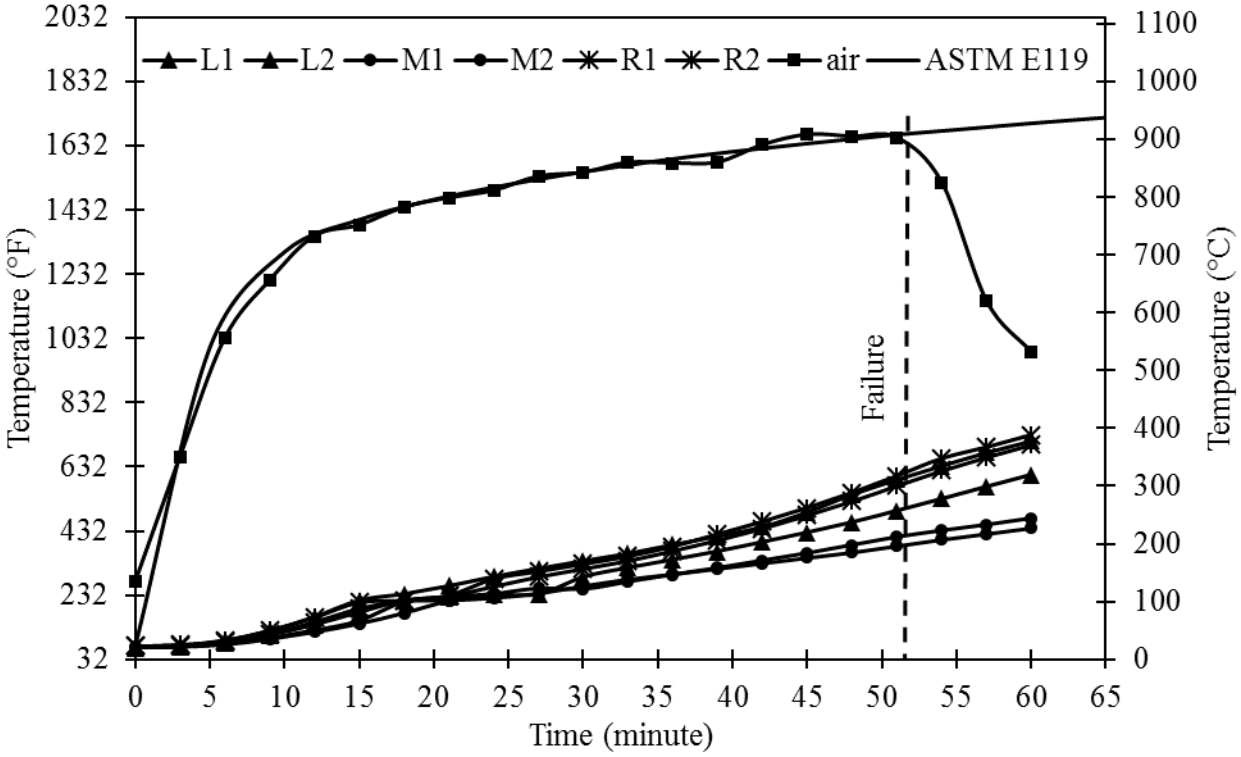

Figure 6.3-53 Time-temperature curves for Beam C100-20-5 at prestressed CFCC strands

6.3.2.8 Beam C132-25-1

Beam C132-25-1 was prestressed with CFCC strands. The initial prestressing force in the beam was 132 kip (587 kN) and it was tested according to ASTM E119 with a central point load of 25 kip (111 kN). Linear transducer of hydraulic load actuator was connected to the data acquisition unit of MTS to monitor the deflection of the beam. The beam was loaded to 25 kip (111 kN) with a rate of 2 kip/minute (8.9 kN/minute) under force control. The thermocouples were connected to the data acquisition unit to record the temperature.

Figure 6.3-54 to Figure 6.3-56 show the test specimen before and after the fire test. Figure 6.3-57 shows time-deflection curve for the beam during the test. No deflection was noticed during the first 13 minutes at the start of the fire test. After 13 minutes, there was a gradual increase in the deflection from 0.7 in. (18 mm) to 2.7 in. (68 mm). The failure took place after 47 minutes with a corresponding deflection of 6.7 in. (170 mm). At failure, the maximum temperature of the prestressed CFCC strand was 803 °F (428 °C) and the maximum air temperature was 1664 °F (907 °C). At onset of deflection, these temperatures were 269 °F (132 °C) and 1357 °F (736 °C), respectively.

Figure 6.3-58 shows the time-temperature curves for the six thermocouples placed at the mid-span section. The time-temperature curves for the six thermocouples placed at the level of prestressed CFCC strands are shown in Figure 6.3-59.

Figure 6.3-54 Beam C132-25-1 before fire

Figure 6.3-55 Beam C132-25-1 after fire

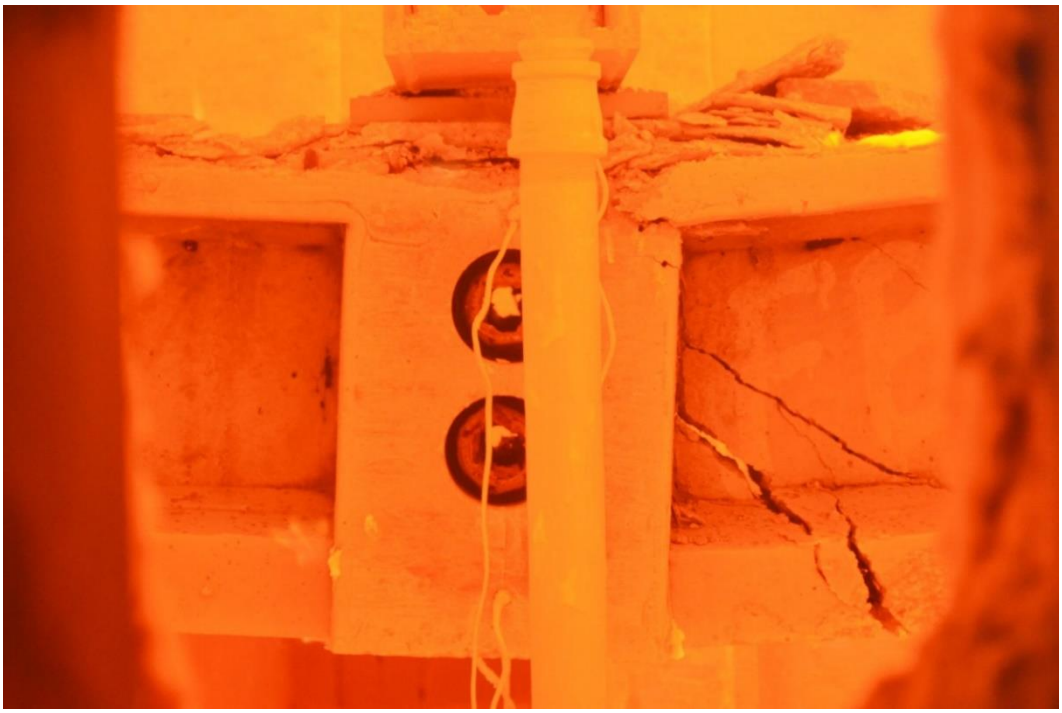

Figure 6.3-56 Close up view of mid-section of Beam C132-25-1 just after failure

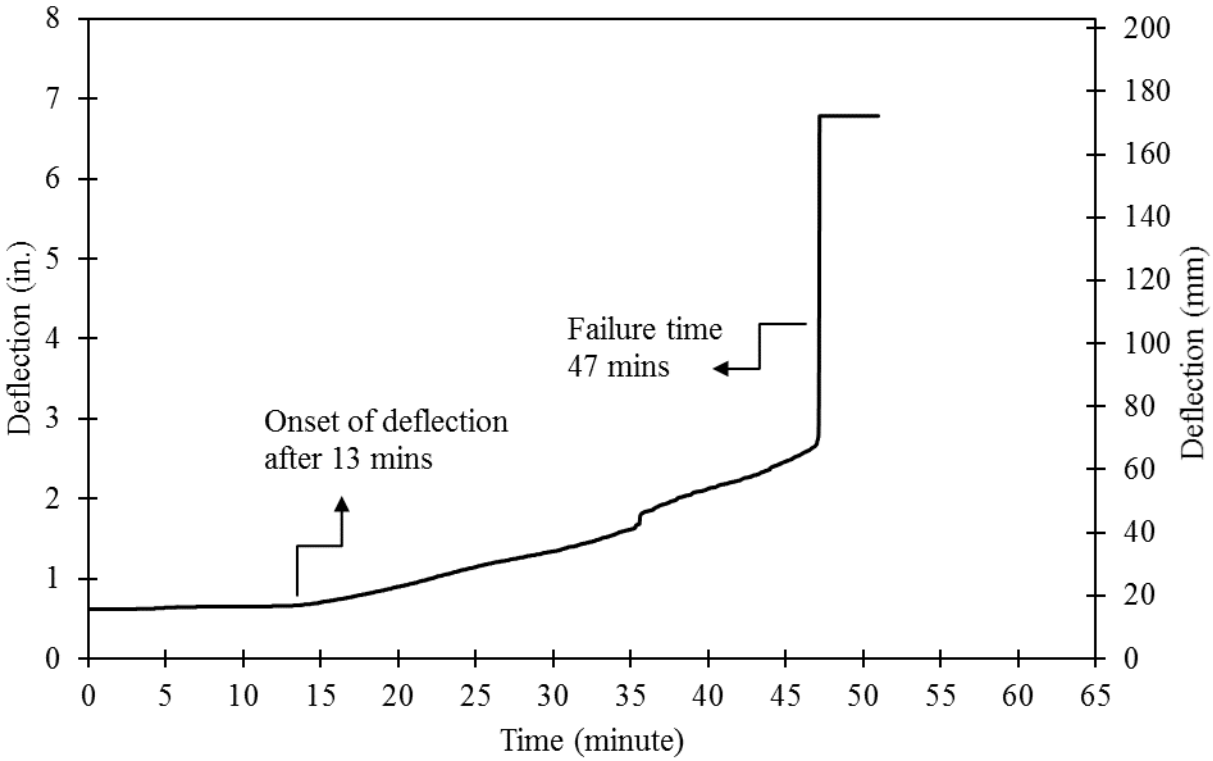

Figure 6.3-57 Time-deflection curve for Beam C132-25-1

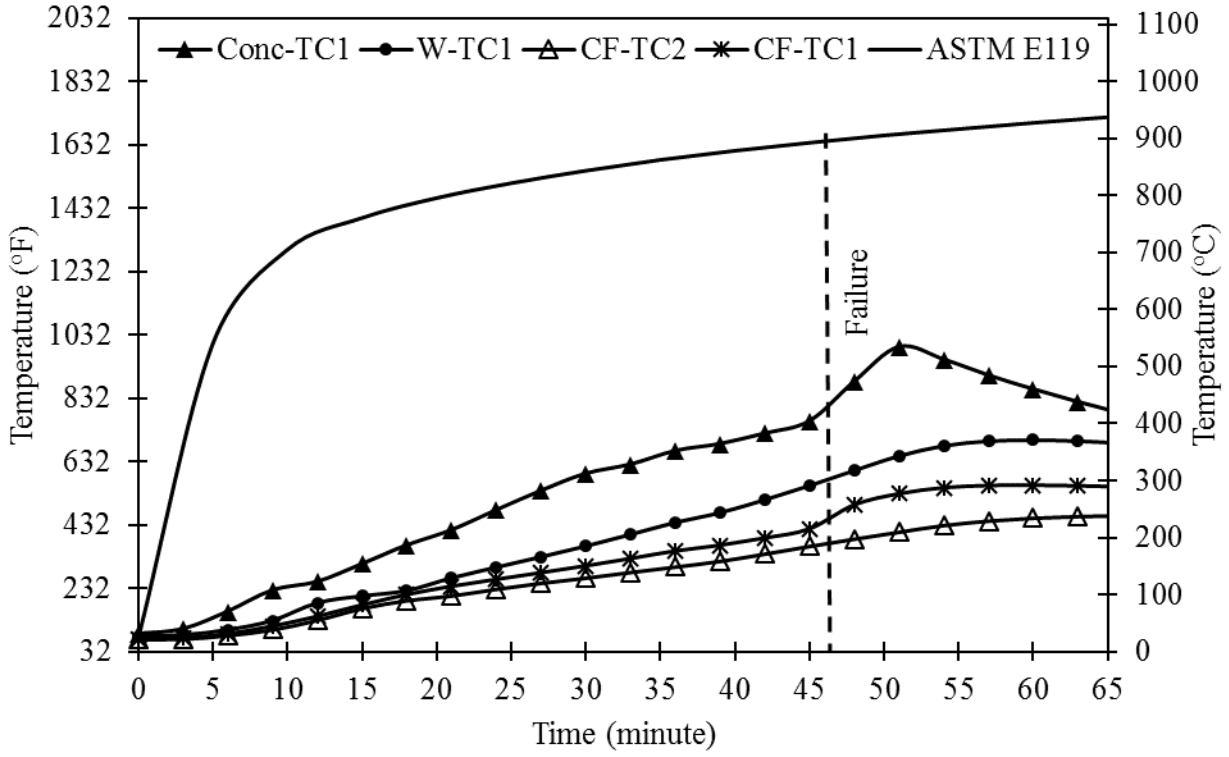

Figure 6.3-58 Time-temperature curves for Beam C132-25-1 at mid-span

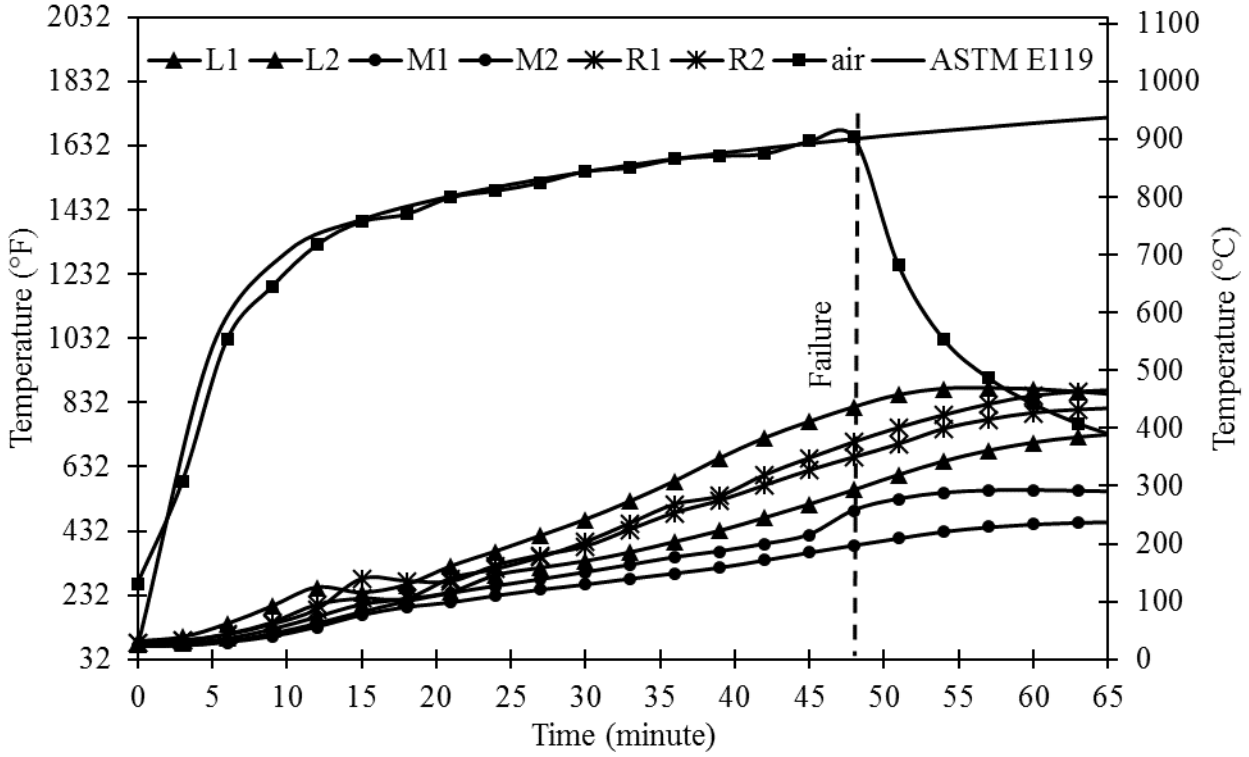

Figure 6.3-59 Time-temperature curves for Beam C132-25-1 at prestressed CFCC strands

6.4 Discussion of Test Results

The fire endurance of all test beams is shown in Table 6.4-1. As anticipated, the overall fire endurance of beams prestressed with CFCC strands is less than that of beam prestressed with steel strands. Comparing Beam C132-25-1 with S132-25-1 shows that CFCC prestressed beams can achieve approximately 50 % of fire endurance of steel prestressed beams. In addition, higher level of prestressing resulted in slightly lower fire endurance time. Similar result was observed for onset of deflection.

Stirrup spacing do not seem to have an influence on the fire endurance of the beams although it should be mentioned that in all beams, the side with CFCC stirrups experienced significantly more cracks and concrete spalling than the side with steel stirrups.

Temperature readings of the prestressing strands at failure spread over a wide range in all the beam. This can be attributed to the difference in cracks pattern and concrete spalling between the beams. When cracks develop near the location of the thermocouple, it can lead to higher temperature readings. But overall, it appears that Beam C72-14-1 achieved the highest CFCC temperature range among all beams with CFCC strands, mainly because of its extended fire endurance. Between Beams C100-20-1 through C100-20-5 and Beam C132-25-1, there is no significant difference in the fire endurance or the CFCC temperature at the time of failure. But there is a notable difference between Beam C132-25-1 and Beam S132-25-1 in both the fire endurance and the temperature of the prestressing strands at the time of failure.

Table 6.4-1 Fire resistance time of CFCC prestressed decked bulb T beam

Beam	Stress ratio of prestressing strand to guaranteed strength	Fire endurance	Time to onset of deflection	Stirrup Spacing,	Temp. range of strands @ failure (°F)
	(%)	minutes	minutes	in. (mm)	°F (°C)
C72-14-1	25	69	33	4 (102)	556-1073 (291-578)
C100-20-1	35	48	20	6 (152)	416-689 (213-365)
C100-20-2	35	52	30	4 (102)	390-686 (199-363)
C100-20-3	35	53	23	6 (152)	334-696 (168-369)
C100-20-4	35	58	21	6 (152)	440-759 (227-404)
C100-20-5	35	52	20	6 (152)	392-623 (200-328)
C132-25-1	44	47	13	4 (102)	381-803 (194-428)
S132-25-1	50	98	50	4 (102)	678-1103 (359-595)

CHAPTER 7: SPLICING & BOND FATIGUE

7.1 Introduction

Bond between CFRP strands and surrounding concrete is the key in establishing the integrity of the section and achieving the design flexural and shear capacities especially in prestressing applications (Grace et al. 2000a). The bond can be achieved through chemical adhesion, shear resistance, and interlock mechanisms between the FRP bars and the concrete (Kanakubo et al. 1993).

Test standards that evaluate the bond strength between CFRP and concrete were developed and included in different design guides such as ACI. Pullout testing is considered the simplest and is commonly accepted. However, stress conditions during pullout experiments are rarely found in practice and bond strength values established under this test setup may vary considerably from those in practical circumstances (Achillides and Pilakoutas 2004). Other test standards are also available and different research teams developed multiple bond and bond-slip analytical models to estimate the bond strength between concrete and internal reinforcement. For instance, a bond slip model was developed by Alsiwat and Saatcioglu (1992), using the distribution and transfer of forces between steel rebars and concrete. Harajli (2009) studied on the impact of reinforced concrete and examined the bond slip relationship for different concrete cover and confinement conditions. Tastani and Pantazopoula (2010) also conducted detailed experiments that showed that the force distribution along the embedment length is not uniform along the rebar.

While the bond between steel reinforcement and concrete have been the focus of decades of research studies (Akbas et al, 2016), bond between CFRP and concrete lacks the experimental work and the corresponding analytical models. Nevertheless, it is widely accepted that, similar to steel, bond-slip relationship between CFRP and concrete depends on factors such as degree of confinement, bar size, bar composition, surface conditions, casting position, concrete cover, embedment length, and surface deformation (Achillides and Pilakoutas 2004; Malvar 1994). Current guidelines such as ACI 440 (2018) provides formula and equations to estimate the bond strength between CFRP and concrete but recent research work suggests that these formulae are too conservative (Harajli and Abouniaj 2010; Hao et al 2008).

Fatigue is described as the progressive deformation that occurs in a material that is subjected to cyclic stress and strains at elevated stress locations may result in cracks or complete fracture after enough fluctuations. While many studies focused on the fatigue of the composite material itself (Talreja 1987; Natarajan et al. 2005; and Akbas et al. 2016), the bond fatigue between CFRP and concrete has not drawn enough attention with few exceptions. For instance, Katz (2000) and Den-Ujil (1995) recorded a reduction in bond strength after cyclic loading. Curtis (1989) reported around 5 to 8 % reduction in the bond strength between concrete and CFRP due to cyclic loading per decade of logarithmic life. On the other hand, Wang and Belarbi (2010) reported an increase in bond stiffness and bond capacity after cyclic loading. They explained that this increase in bond stiffness and strength was due to the closing of micro voids between the concrete after cylcic loading. Ezeldin and Balaguru (1989) showed that the addition of fibers to concrete will change the bond performance due to the fact the concrete properties were altered.

This chapter presents a detailed experimental investigation that was executed with the main objective of establishing the characteristics of the bond strength between CFRP and concrete. The experimental investigation is composed of three test programs. The first test program included evaluating the bond strength between CFCC strands and uncracked concrete in a pull-out test setup. The second test program evaluated the bond strength in rectangular beams provided with different configurations of bottom lap-spliced CFCC reinforcement and loaded in a four-point-load setup to failure. The third test program evaluated different configurations of lap-spliced CFCC stirrups in precast prestressed box beams. Details of each test program and the main findings and conclusions are provided in the following sections.

7.2 Pull-out Test

7.2.1 Test setup

A total of 29 CFCC specimens were constructed according to ACI 440.3R-12-B.3: “Test Method for Bond Strength of FRP Bars by Pullout Testing”. Each specimen consisted of a single 0.6 in. (15.2 mm) CFCC strand with a sleeve anchorage on one side and embedded vertically at the center of a concrete cube with a side length of 8 in. (203 mm). The bonded length of CFCC strand was limited to five times the diameter or 3 in. (76 mm) according to the test method. The remaining embedded length was shielded against concrete bonding using a bond breaker Polyvinyl Chloride (PVC) pipe. Specimen configuration is shown in Figure 7.2-1. As shown on the figure, the strand

extended 0.5 in. (12.7 mm) beyond the concrete cube to facilitate monitoring the slippage of the CFCC strand when the specimen was loaded.

Figure 7.2-2 through Figure 7.2-4 show the construction of the test specimen. A wooden formwork was prepared with a side length of 8 in. (203 mm) and the CFCC specimen was passed through the formwork and protruded 0.5 in. (12.7 mm) from the bottom side. PVC pipe was provided for debonding,

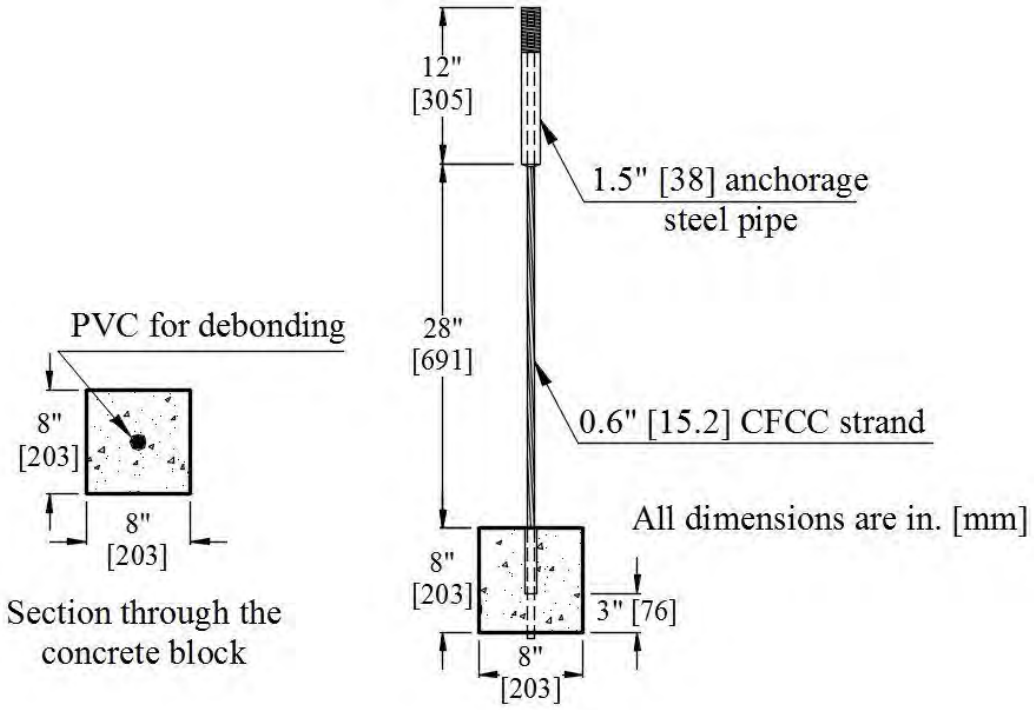

Figure 7.2-1 Specimen configuration of pull-out test

Figure 7.2-2 Formwork for pull-out test specimens

Figure 7.2-3 CFCC specimens in the formwork before pouring the concrete

Figure 7.2-4 Pouring concrete and completed pull-out specimen after removal of formwork

The concrete cube specimens were cast using a concrete mix with a design strength of 7000 psi (48 MPa). After casting the concrete, the specimens were covered with wet burlap and plastic sheets and were allowed to cure for 72 hours. The specimens were removed from formwork and testing was commenced 28 days after casting.

Pull-out test was conducted on two phases. Phase I included establishing the average static pull-out strength of the test specimens. This was achieved by testing to failure five test specimens in a test setup as shown in Figure 7.2-5. Phase II was similar to Phase I in the test setup, but the monotonic load was replaced by a cyclic load.

Figure 7.2-5 Test setup for bond specimens

As shown in the figure, the specimens were mounted in a two-post MTS uniaxial testing machine. The sleeve anchorage of the CFCC strand was threaded into the moving head of testing machine. A special high-strength steel head was prepared to accommodate and hold the concrete block. In addition, an LVDT was attached at the free end of the strand under the concrete block to capture the slippage of the strand. During Phase I, the specimens were loaded monotonically at a load rate of 4 kip/min (18 kN/min) to failure.

In Phase II, test standard ACI 440.3R-12-B.7: "Test Method for Tensile Fatigue of FRP Bars" was implemented to establish the cyclic load rate and amplitude. Based on the test standard, a total of 24 test specimens were loaded to load levels ranging from 60 % to 75 % of the average pull-out strength that was established in Phase I. The frequency of the cyclic load was 4 Hz with a ratio between the cycle lowest to the highest amplitudes of 10 %. Each specimen was tested under its assigned cyclic load to failure or 2 million cycles, which ever came first as recommended by ACI 440.3R-12.

7.2.2 Test results

In Phase I, the average pull-out strength was 12 kip (54 kN) and the minimum and maximum pull-out strengths were 10.4 kip (46 kN) and 14.4 kip (64 kN), respectively (Table 7.2-1). The pullout of the CFCC strand from the concrete cube was detected by a sudden drop in the load and a sudden increase in the reading from the LVDT attached to the free end of the specimen as shown in Table 7.4-2. Since the bonded length of CFCC strand was 76 mm (3 in.), the static average bond strength was approximately 4 kip/in. (0.7 kN/mm). In all cases, the failure was due to pure slippage of CFCC strand. No concrete splitting was observed.

Table 7.2-1 Pull-out test results

Specimen #	Failure Load kip (kN)
1	10.4 (46.4)
2	11.5 (51)
3	11.3 (50.2)
4	14.4 (64)
5	12.6 (56.1)
Average pullout load	12 (53.5)

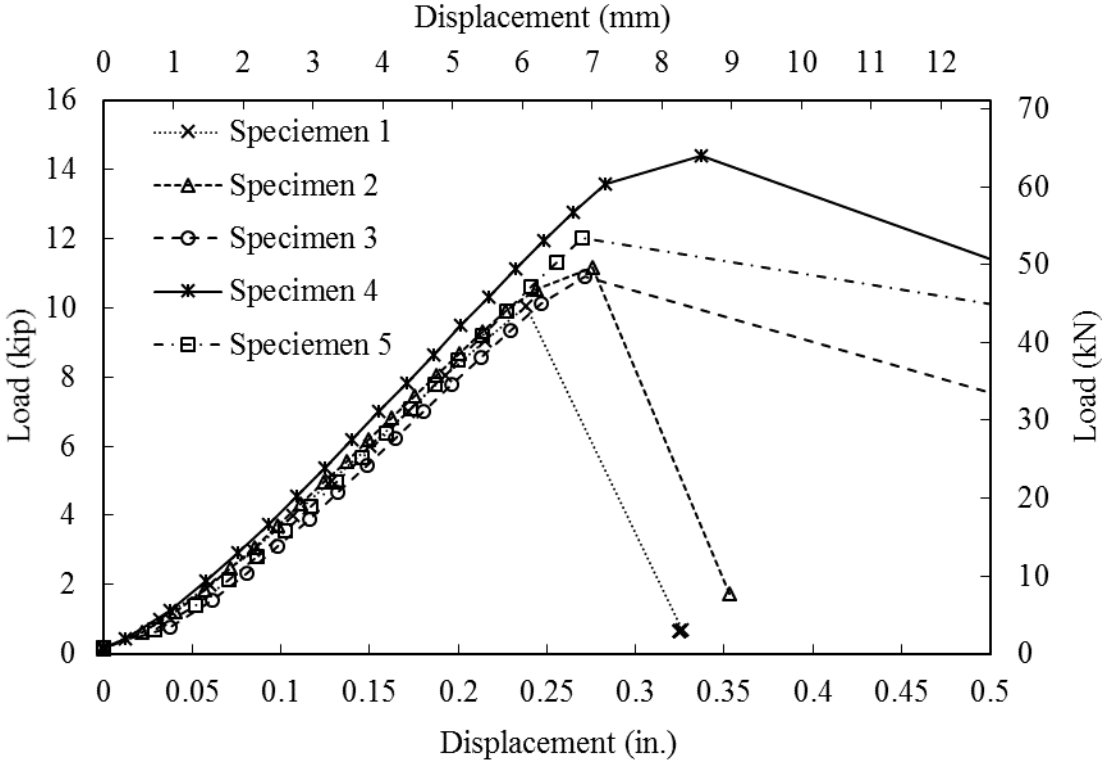

Figure 7.2-6 Load-displacement curve for static pullout test

Test results of Phase II are presented in Table 7.2-2. As shown in the table six load levels were selected for the testing. The selection of the load level aimed at achieving number of load-cycles-to-failure between 1000 and two million cycles, according to test standard. The minimum load ratio was limited to 60 % after one specimen survived two million cycles at this load ratio.

The S-N curve was plotted as shown in in Figure 7.2-7 to determine the pullout strength at 2 million cycles according to ACI 440.3R-12-B7. The stress ratio was represented on a linear scale on the vertical axis, and the number of cycles to failure was represented on a logarithmic scale on the horizontal axis. The S-N line was plotted as the trend line from the test results by the least-square method. The 2 million cycle pull-out strength was calculated by interpolation from the S-N curve and was found to be between 64 % of the static average pullout strength. In other words, to avoid pull-out failure due to cyclic loading, the bond strength shall not exceed 64 % of the average static pull-out strength. For instance, since pull-out strength of CFCC strands averaged at 4.0 kip/in. (0.7 kN/mm), the maximum bond strength to avoid pullout failure under static load is

approximately 2.56 kip/in. (0.45 kN/mm). This limit can be established by simply extending the development length of the CFCC strand by 56 %.

Table 7.2-2 Bond fatigue test results

Load/stress ratio to pull-out (%)	Specimen Identification	Cycles to Failure	Maximum stress ratio (%)	Minimum stress ratio (%)
60	A	2000000 »	69	50
65	A	142000	75	54
	B	2000000 »	75	54
	C	854700	75	54
	D	37200	75	54
	E	796900	75	54
67.5	A	2000000 »	78	56
	B	302800	78	56
	C	152620	78	56
	D	126867	78	56
	E	2000000 »	78	56
70	A	20000	81	59
	B	490000	81	59
	C	6475	81	59
	D	830	81	59
	E	246900	81	59
	F	1541	81	59
72.5	A	1290	84	61
	B	228400	84	61
	C	1914	84	61
	D	29261	84	61
	E	229650	84	61
75	A	85	86	63
	B	627	86	63
» No failure occurred by the end of 2000000 cycles				

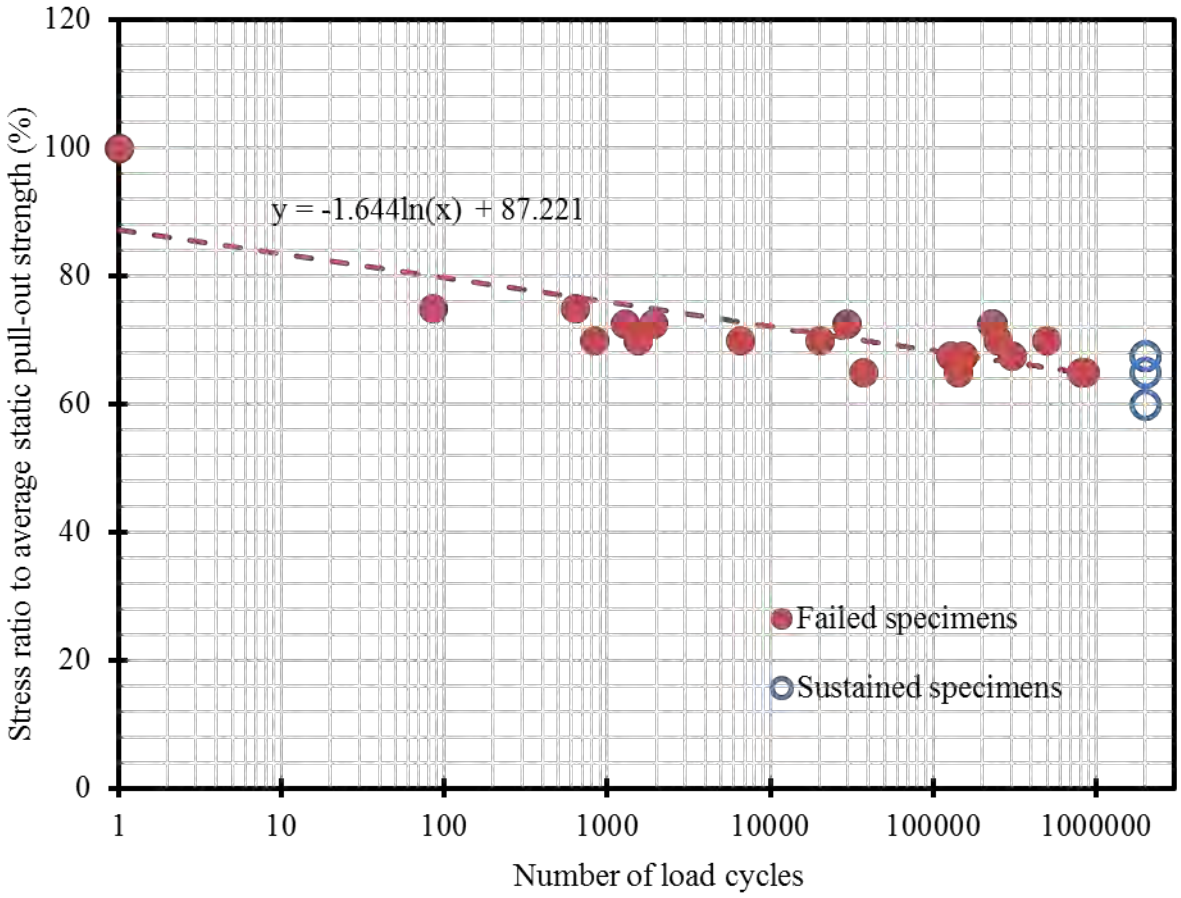

Figure 7.2-7 Stress ratio vs No. of load cycles to failure in CFCC specimens tested for bond fatigue strength

7.3 Flexural Bond Strength

The bond strength established by pullout test method is only valid if the concrete is uncracked and/or in compression. In case of cracked concrete or concrete in tension, the bond strength between the reinforcement and concrete typically depends on the amount of confinement provided by the concrete and the confinement provided by the lateral reinforcement.

This test program of the experimental investigation focused on establishing the bond strength between CFRP and cracked concrete or concrete subjected to tensile/flexural stresses. The test program included the design, construction, and testing of ten CFCC reinforced concrete beams under four-point-load test setup to failure. Continuous CFCC strands served as the bottom reinforcement for two control beams, while the remaining eight beams were reinforced with CFCC

strands that were lap-spliced within the constant moment region between the two points of load. Different splice lengths and different diameters of CFCC strands were investigated.

7.3.1 Test setup

All ten beam specimens had a width of 10 in. (254 mm), a depth of 14 in. (356 mm), and an effective span of 11 ft (3.35 m). All the beams were provided with 2 No. 4 (12 mm) top steel reinforcement and No. 3 (10 mm) steel stirrups every 4 in. (102 mm) except through the constant moment region as shown in Figure 7.3-1 and Figure 7.3-2 . Five beams were reinforced with two bottom CFCC strands with a diameter of 0.6 in. (15.2 mm). The other five beams were reinforced with two bottom CFCC strands with a diameter of 0.5 in. (12.5 mm). Out of the five beams in each group, one beam was provided with continuous CFCC strands, while the CFCC strands in the remaining four beams were spliced though the constant moment region with splice length of 1, 2, 3, and 4 ft (305, 610, 914, 1219 mm).

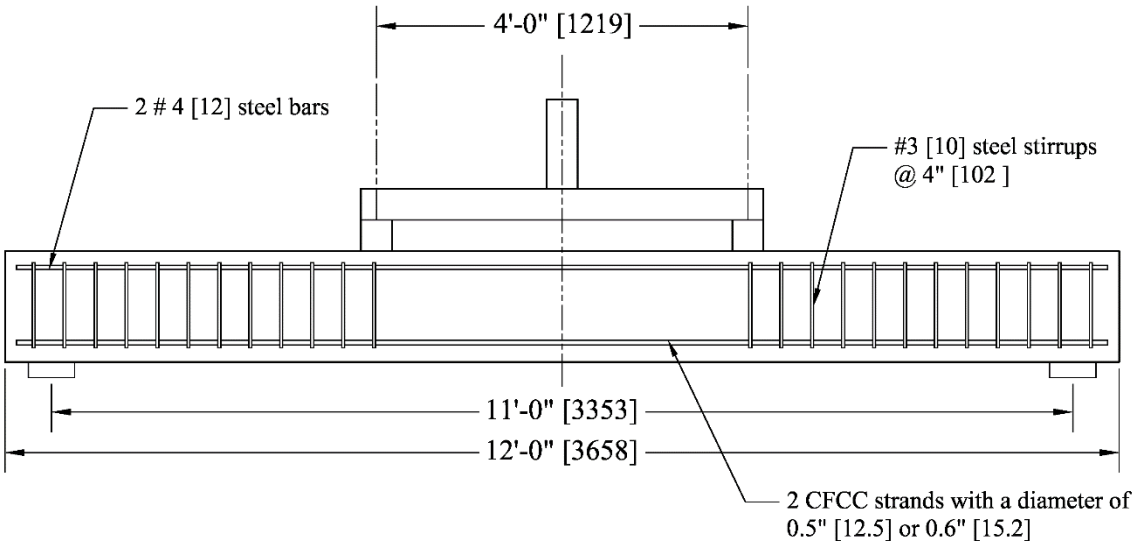

Figure 7.3-1 Test setup of evaluation of flexural bond splice length

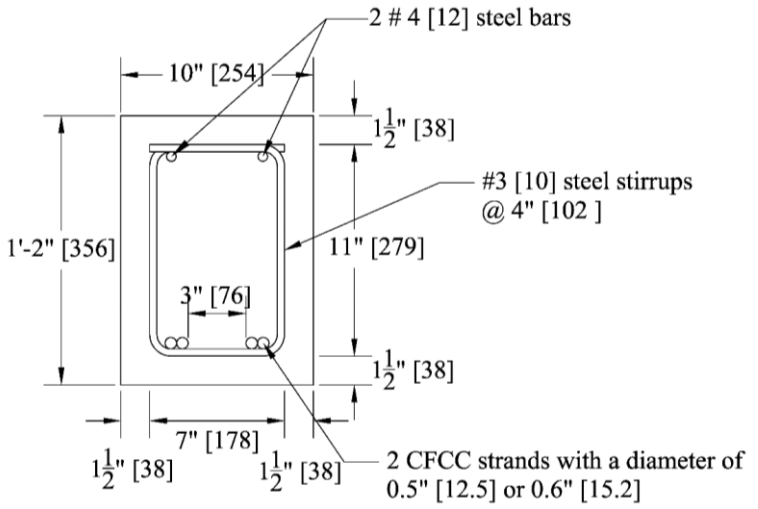

Figure 7.3-2 Cross section and dimensions of test beams

The nomenclature of the specimens is given as: "B- length of splice in ft-diameter of CFCC". For instance, B4-0.5 is a beam reinforced with two bottom CFCC strands with a diameter of 0.5 in. (12.5 mm) spliced with a lap splice length of 4 ft (1219 mm) through the constant moment region. The control beams with continuous CFCC reinforcement were denoted BC-0.5 and BC-0.6 for CFCC diameter of 0.5 in (12.5 mm) and 0.6 in. (15.2 mm), respectively. The size and properties of all the different reinforcement are shown in Table 7.3-1 Properties of reinforcement, while Figure 7.3-3 through Figure 7.3-6 show the construction process of the test specimens. A ready-mix concrete was used to cast the beams. The concrete mix was designed to achieve a 28-day compressive strength of 7000 psi, and a desired slump of 8 in. (203 mm) to achieve the required workability. A slump of 8.25 in. (210 mm) was verified prior to pouring concrete in accordance with ASTM C143/C143M-15a specifications. Several test cylinders were prepared from the same concrete batch and were tested to determine concrete compressive strength at different ages (Figure 7.3-7). After concrete casting, the beams were cured by covering them with wet burlap sheets and spraying with water for 7 days.

Table 7.3-1 Properties of reinforcement

	Flexural Reinforcement			Shear Reinforcement
Material Properties	CFCC		Steel No.4	Steel No.3
Diameter, in. (mm)	0.5 (12.5)	0.6 (15.2)	0.5 (12)	0.38 (10)
Effective cross-sectional area, in.^{2} (mm^2)	0.12 (77.5)	0.179 (115.6)	0.2 (129)	0.11 (71)
Breaking load, kip (kN)	46.09 (205)	64.3 (286)	18 (80)	9.9 (44)
Ultimate tensile strength, psi (MPa)	379,000 (2,613)	358,240 (2,470)	90,000 (621)	90,000 (621)
Modulus of elasticity, psi (MPa)	21.7×10^6 (149,900)	20.9×10^6 (144,000)	29×10^6 (200,000)	29×10^6 (200,000)
Yield strength, psi (MPa)	---------	---------	60,000 (414)	60,000 (414)
Elongation (%)	1.70	1.70	5.00	5.00

Figure 7.3-3 Assembling the reinforcement cages of the test beams

Figure 7.3-4 Completed reinforcement cage showing the location of the splice and stirrups

Figure 7.3-5 Placing the reinforcement cages in the formwork

Figure 7.3-6 Casting the concrete in the test specimens

Figure 7.3-7 Completed beams and preparing concrete cylinders for uniaxial testing

The uniaxial compressive strength of the concrete was determined according to ASTM C39/C39M-12 specifications, at 7, 14, 21, and 28 days after beams casting. Three concrete cylinders were tested each time and the average test results were taken to determine the average

concrete compressive strength. An average 28-day compressive strength of 10 ksi was achieved as shown in Figure 7.3-8.

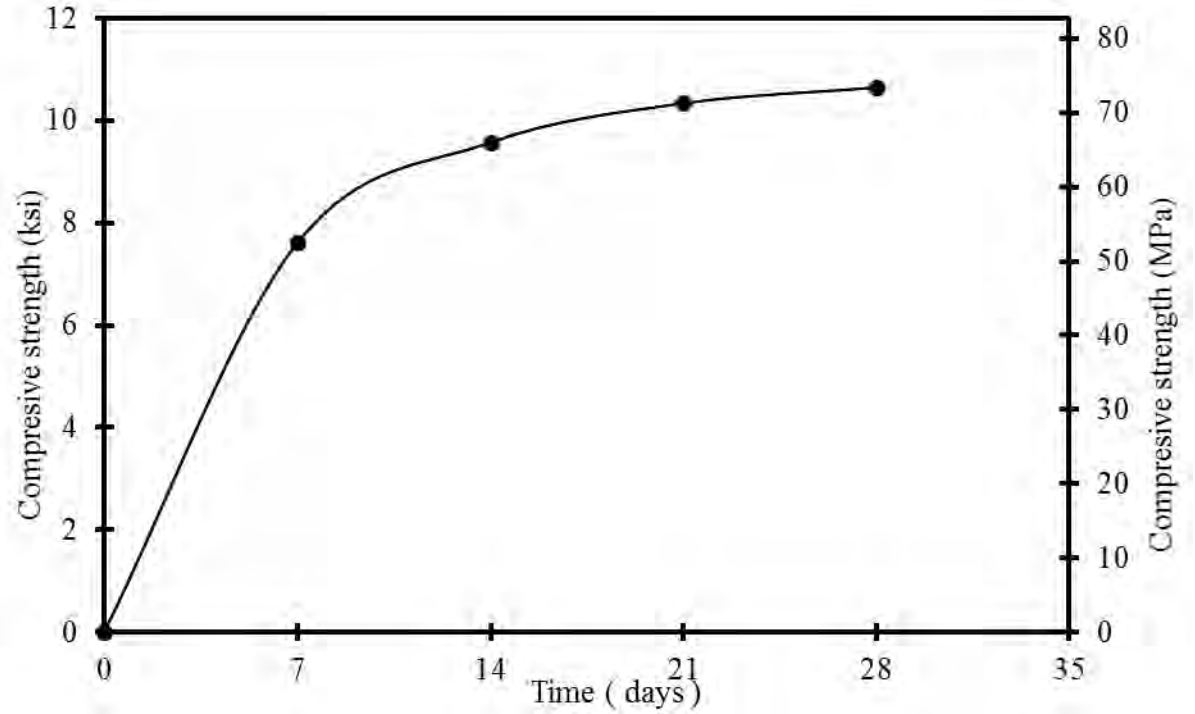

Figure 7.3-8 Average compressive strength of concrete over time

The beam specimens were instrumented with concrete strain gages, linear variable differential transducers (LVDTs), load cells, and linear motion transducers (LMTs). At mid-span section, two electric resistance strain gages were installed externally on the top concrete surface to monitor the concrete compression strain. In addition, Three LVDTs were attached to the side of the specimens to capture the strain through the depth of the beam. A load cell attached to the hydraulic actuator with a maximum capacity of 220 kips (1000 kN) was used to monitor the applied vertical load on the beam during testing. LMTs were attached to the underside of the beams to monitor the deflection. All sensors were connected to a computer with a data acquisition interface system to monitor and record test data.

The beam specimens were loaded in four-point-load flexural test in a displacement control mode with a loading rate of 0.1 in/min (2.54 mm/min). The distance between the two points of load (the constant moment region) was 4 ft (1.22 m). Beams were simply supported over a steel-reinforced elastomeric bearing pads with a thickness of 1.0 in. (25.4 mm).

7.3.2 Test results

Table 7.3-2 provides a summary for the test results of all beam specimens. In addition, Figure 7.3-9 through Figure 7.3-37 show the test setup, loading, and failure mode of failure for all test specimens. The cracking load for all beam was around 10 kip (44 kN). Control beam BC-0.5 failed by rupture of CFCC strands, while control beam BC-0.6 failed by crushing of the concrete. Other beam specimens failed by pullout of the lap splice that was accompanied by spalling and cracking (splitting) of the concrete at the splice location. In addition, in all beam specimens with a lap splice, a wide flexural crack developed at the end of the lap splice at the time of the failure as shown in the figures.

Figure 7.3-38 and Figure 7.3-39 show the load deflection curves for the test specimens. It should be noted that due to the size of the reinforcement relative to the size of the beam and due to the increased concrete cover in the test beams, the load deflection curves exhibited slight drops in the load with the development of the flexural cracks. The load level was quickly regained after the internal flexural reinforcement was engaged and carried the tensile force across the crack.

Table 7.3-2 Summary for test results of beam specimens in flexural bond test

Beam	Splice length	Failure load	Conc. strain	Mode of failure	Deflection @ failure	CFCC strain @ failure
	in. (mm)	lb (kN)	με		in. (mm)	με
B1-0.5	12 (305)	17,980 (80)	-890	Pullout/split	1.10 (28)	6,360
B2-0.5	24 (610)	35,360 (157)	-1570	Pullout/split	2.16 (55)	12,550
B3-0.5	36 (914)	35,211 (157)	-1557	Pullout/split	1.93 (49)	12,470
B4-0.5	48 (1219)	36,787 (164)	-1870	Pullout/split	2.58 (66)	12,950
BC-0.5	Cont.	46,838 (208)	-2601	Tension	3.42 (87)	16,600
B1-0.6	12 (305)	26,026 (116)	-1376	Pullout/split	1.09 (28)	6,490
B2-0.6	24 (610)	29,874 (133)	-1398	Pullout/split	1.51 (38)	7,400
B3-0.6	36 (914)	35,892 (160)	-1742	Pullout/split	1.68 (43)	8,910
B4-0.6	48 (1219)	47,312 (210)	-2738	Pullout/split	2.00 (51)	11,730
BC-0.6	Cont.	58,973 (262)	-2252	Compression	2.98 (76)	14,670

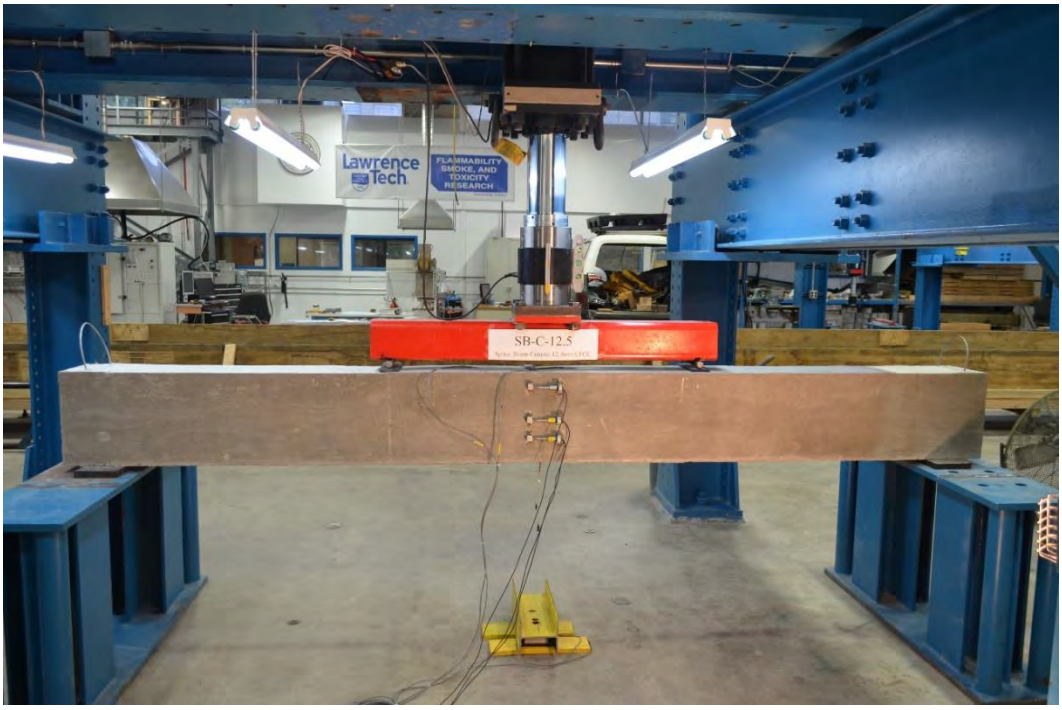

Figure 7.3-9 Setup and Testing of BC-0.5

Figure 7.3-10 Failure of BC-0.5

Figure 7.3-11 Close-up view of BC-0.5 showing the rupture of steel strands

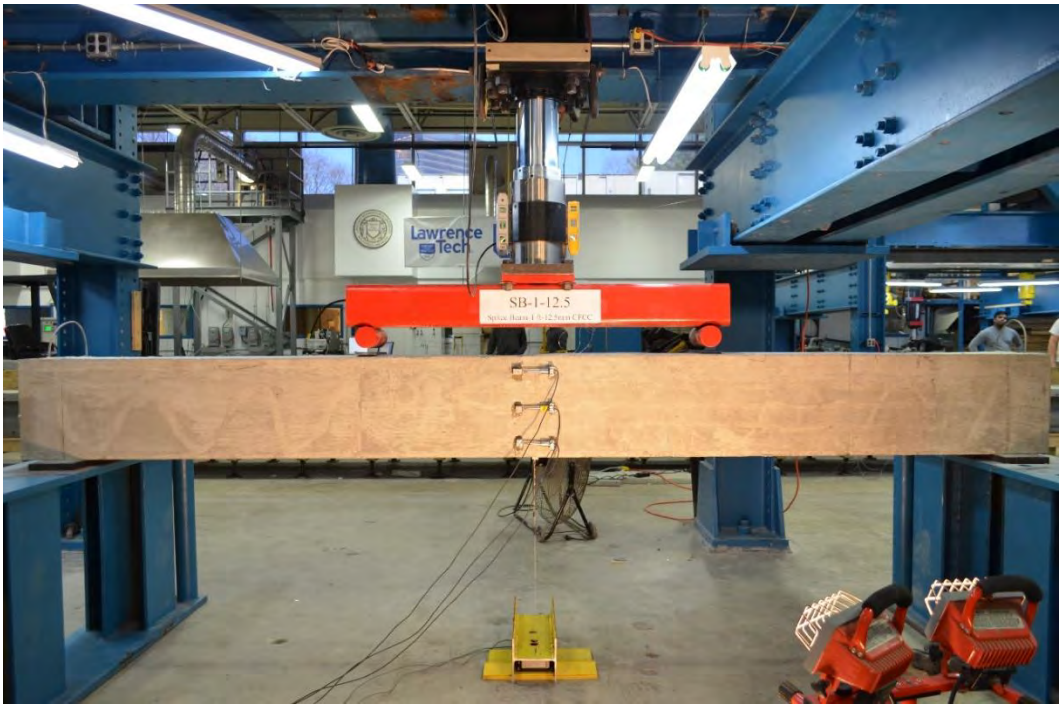

Figure 7.3-12 Setup and testing of B1-0.5

Figure 7.3-13 Failure of B1-0.5

Figure 7.3-14 Close-up view of B1-0.5 showing a large crack at the end of splice

Figure 7.3-15 Setup and testing of B2-0.5

Figure 7.3-16 Failure of B2-0.5

Figure 7.3-17 Close-up view of B2-0.5 showing CFCC slippage at the end of splice

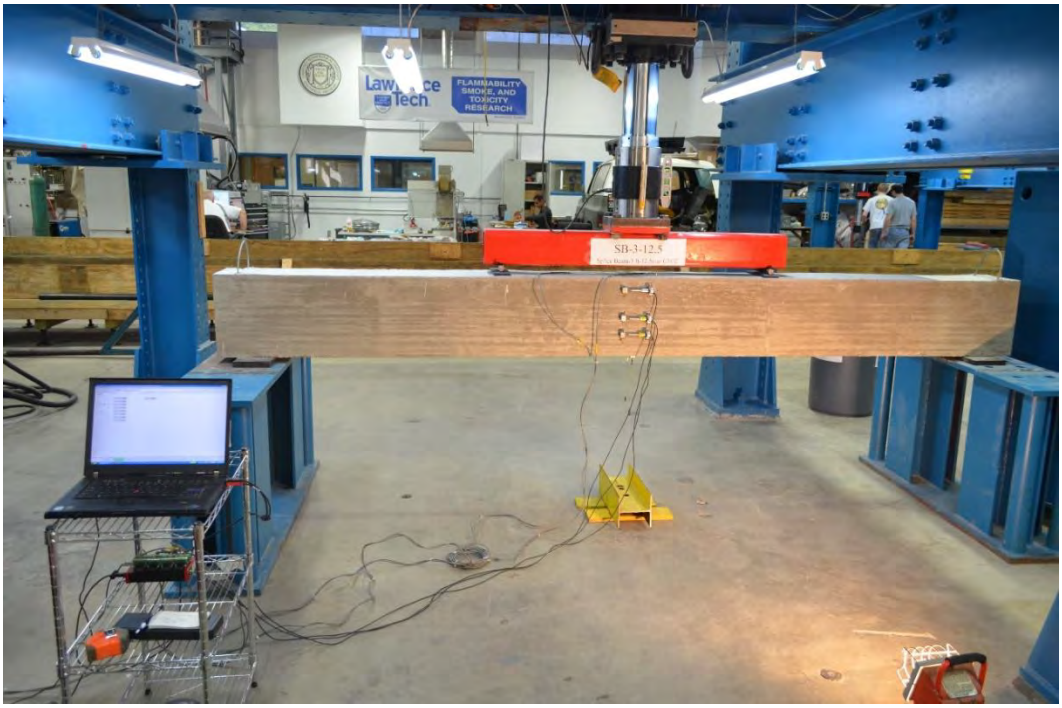

Figure 7.3-18 Setup and testing of B3-0.5

Figure 7.3-19 Failure of B3-0.5

Figure 7.3-20 Close-up view of B3-0.5 showing CFCC slippage at the end of splice

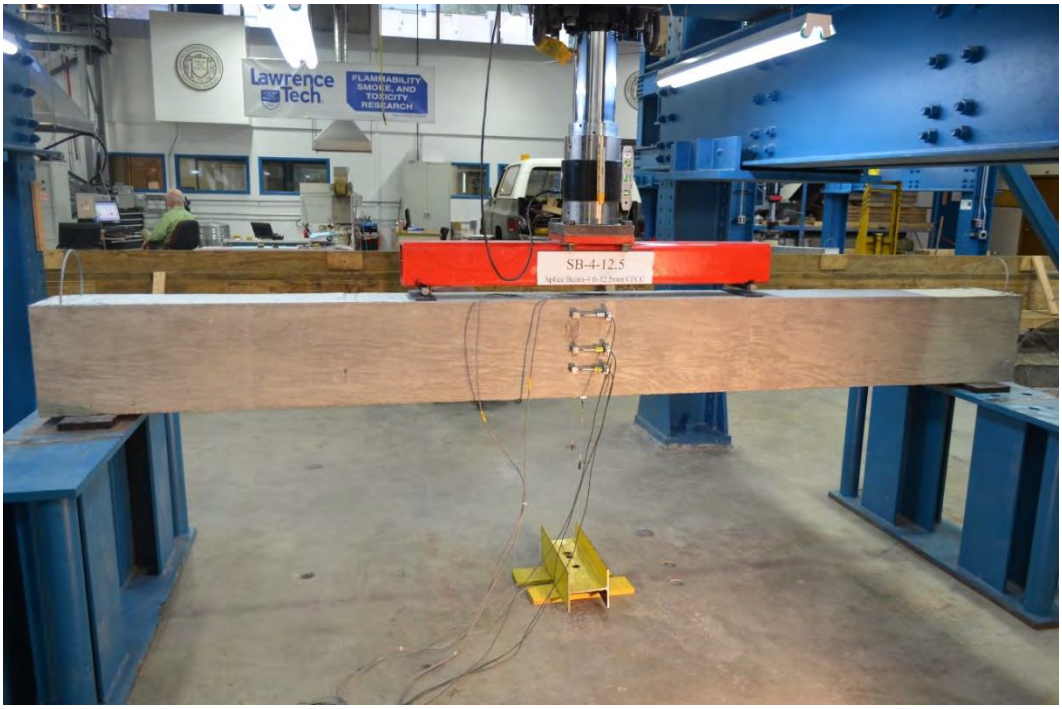

Figure 7.3-21 Setup and testing of B4-0.5

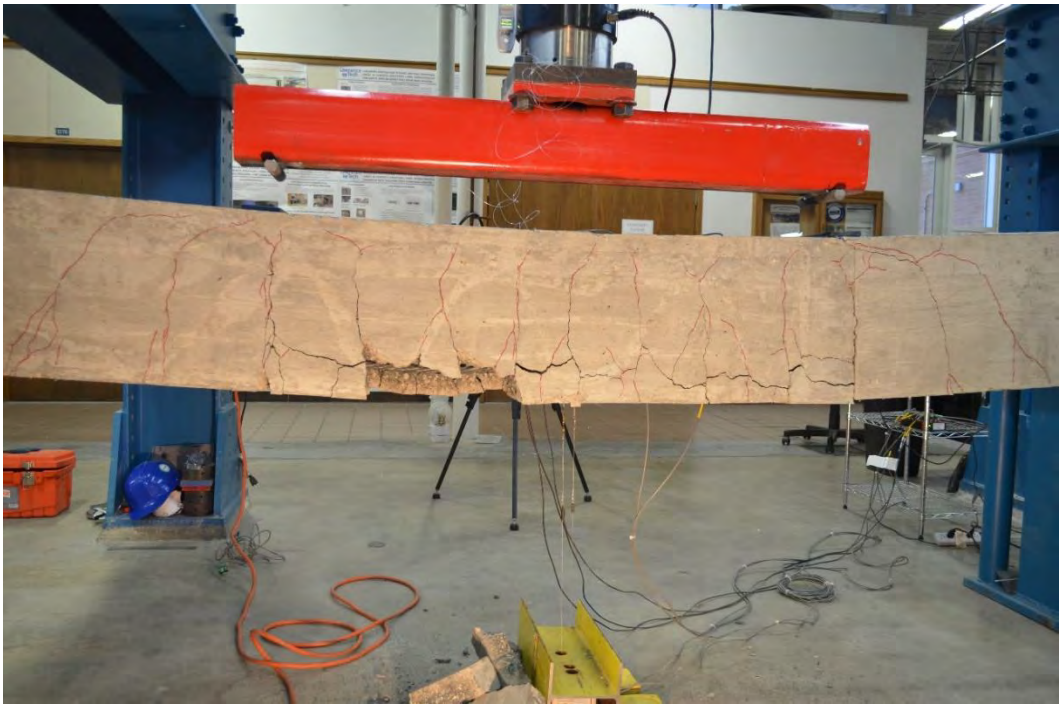

Figure 7.3-22 Failure of B4-0.5

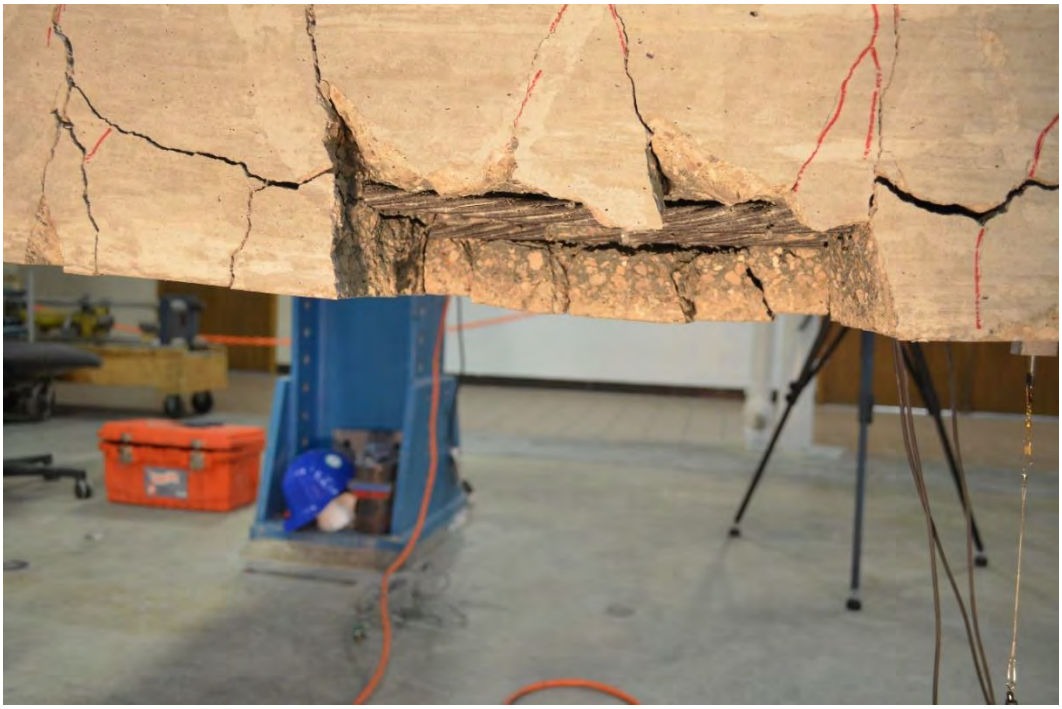

Figure 7.3-23 Close-up view of B4-0.5 showing CFCC slippage at the end of the splice

Figure 7.3-24 Failure of BC-0.6

Figure 7.3-25 Crushing of concrete followed by rupture of CFCC strands in BC-0.6

Figure 7.3-26 Setup and testing of B1-0.6

Figure 7.3-27 Failure of B1-0.6

Figure 7.3-28 Close-up view of B1-0.6 showing the CFCC slippage at the end of the splice

Figure 7.3-29 Setup and testing of B2-0.6

Figure 7.3-30 Failure of B2-0.6

Figure 7.3-31 Close-up view of B2-0.6 showing CFCC slippage at the end of the splice

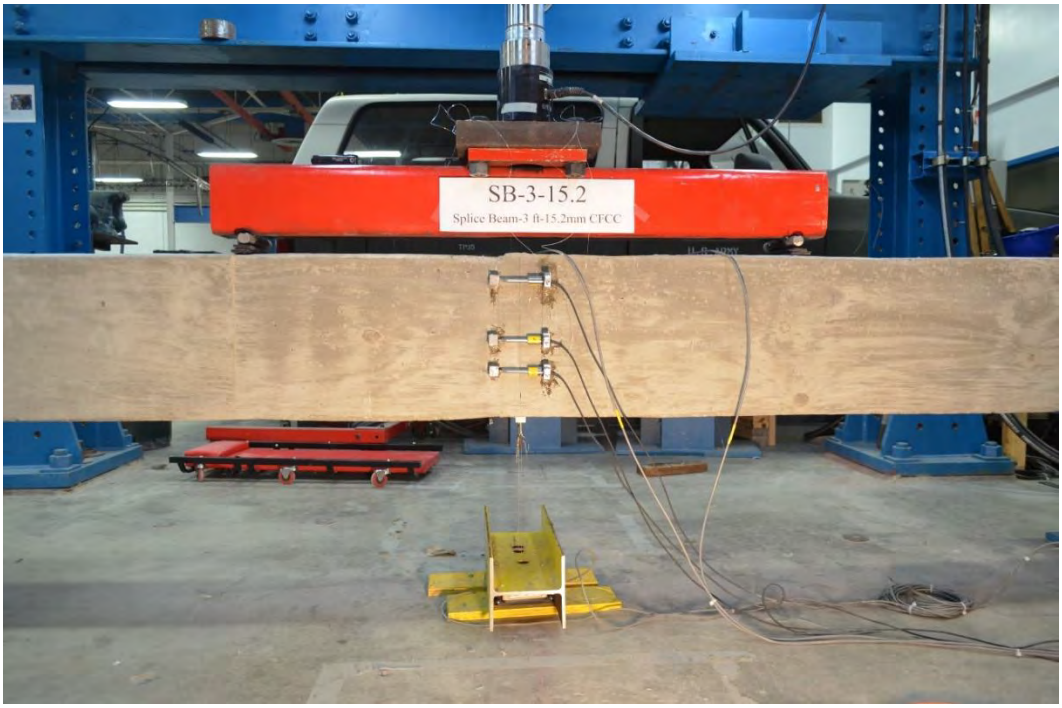

Figure 7.3-32 Setup and testing of B3-0.6

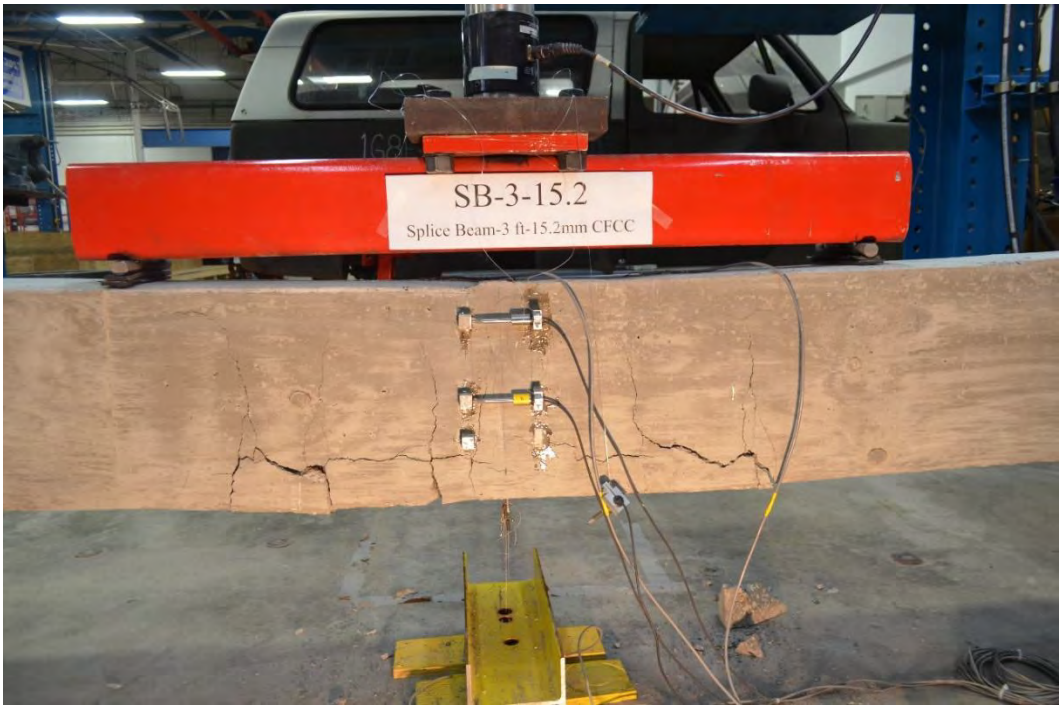

Figure 7.3-33 Failure of B3-0.6

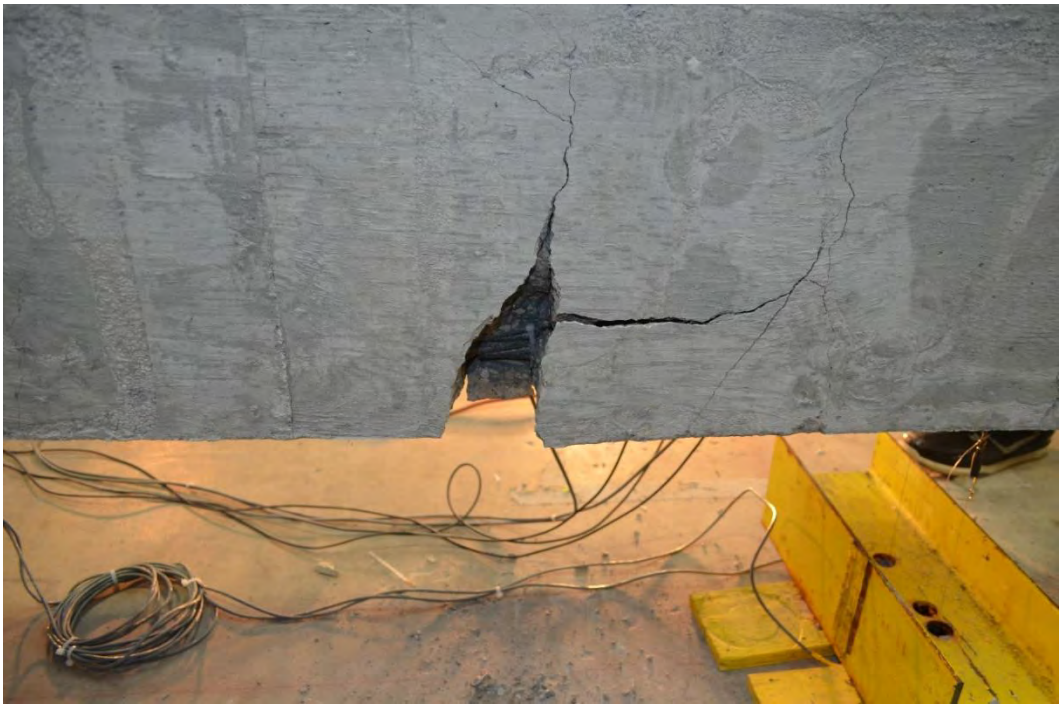

Figure 7.3-34 Cracking and failure of B3-0.6 at the end of the splice

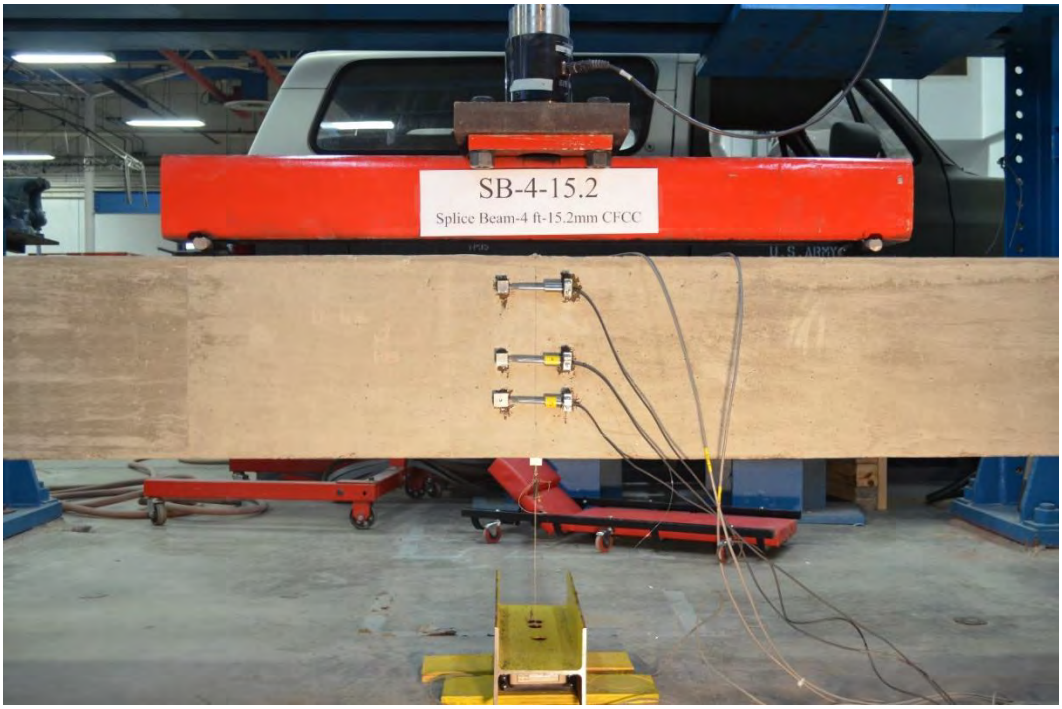

Figure 7.3-35 Setup and testing of B4-0.6

Figure 7.3-36 Failure of B4-0.6

Figure 7.3-37 Close-up view of B4-0.6 showing CFCC slippage at splice end

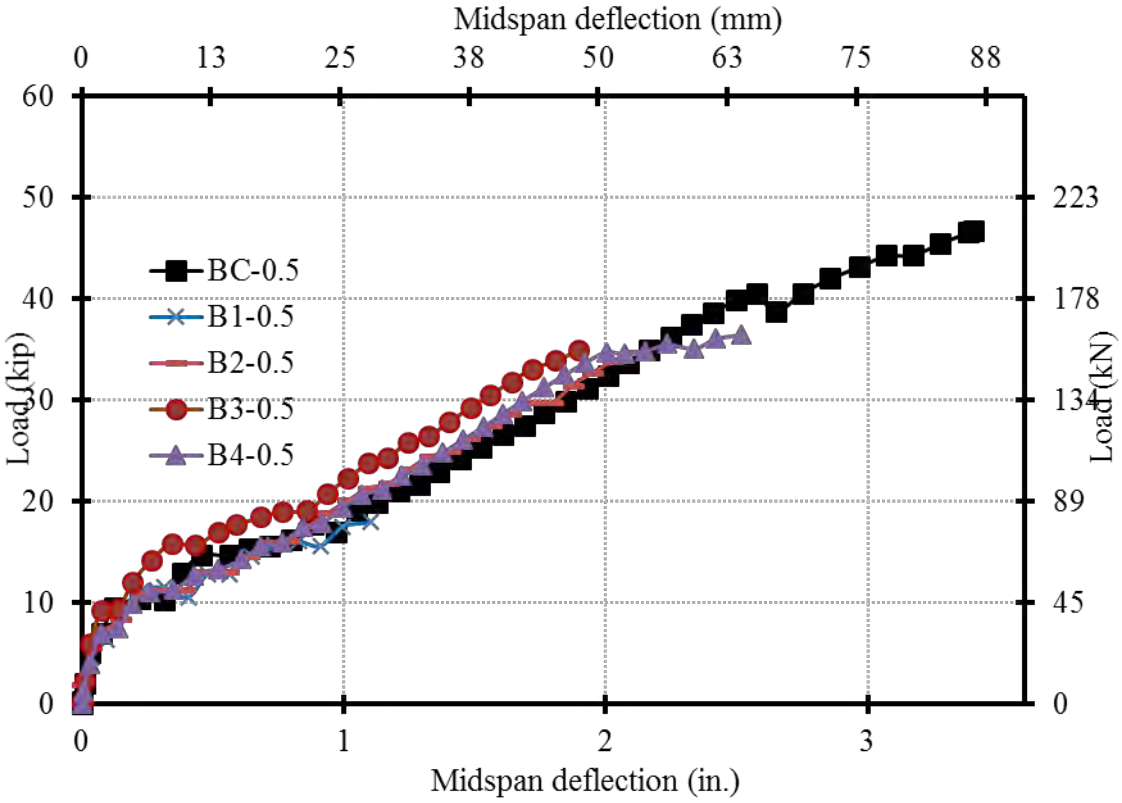

Figure 7.3-38 Load vs. mid-span deflection of beams with 0.5-in. (12.5-mm) CFCC strands

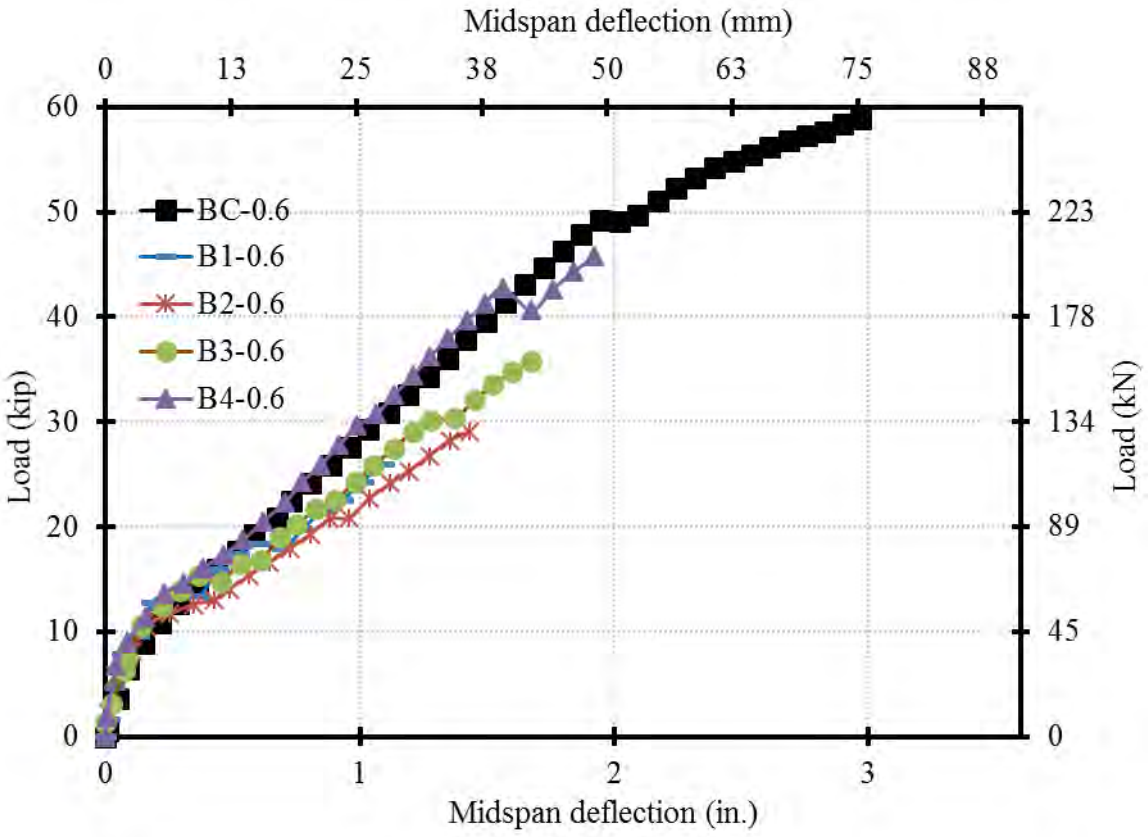

Figure 7.3-39 Load vs. mid-span deflection of beams with 0.6-in. (15.2-mm) CFCC strands

7.3.3 Discussion of test results

Failure by concrete splitting or reinforcement pullout are two widely recognized forms of bond and lap splice failure in case of steel reinforced concrete when the concrete is in tension. Concrete splitting dominates when there is not sufficient concrete cover or when there is not enough lateral reinforcement to provide confinement and control the longitudinal cracks. If enough concrete cover is provided along with enough lateral reinforcement, the pullout failure dominates. In this case, the failure can be delayed by increasing the bonded length until yield of reinforcement is achieved before the pullout failure.

The dimensions of the cross section and the concrete cover at the bottom and on the sides of the beams were selected to avoid typical splitting failure according the ACI-318 (2014). In addition, ACI 440.1R-06 reported that to avoid and concrete splitting a limit of at least 3.5 for the normalized cover c/d_b should be maintained, where c is the concrete cover and d_b is the diameter

of the strands. All beam specimens satisfied the minimum concrete cover requirements. Therefore, typical concrete splitting of the test specimens was unlikely.

Control Beam BC-0.5 exhibited a tension-controlled failure, while control beam BC-0.6 exhibited a compression-controlled failure. Difference in failure modes in control beams is attributed to the increased reinforcement ratio that was attained by increasing the diameter of CFCC stands from 0.5 in. (12.5 mm) to 0.6 in. (15.2 mm).

Beams with lap-spliced 0.6 in. (15.2 mm) CFCC strands showed a near-linear increase in the maximum load with the increase in the splice length as shown in Figure 7.3-40. On the other hand, beams with lap-spliced 0.5 in. (12.5 mm) CFCC strands, exhibited an increase in the maximum load when the lap splice length increased from 12 in. (305 mm) to 24 in. (610 mm) as the load nearly doubled. Further increase in the splice length did not yield any significant increase in the maximum load of the specimens.

Test results can be explained by examining the CFCC strain at the time of beam failure as shown in Figure 7.3-41. With a splice length of 12 in. (305 mm), the strain in CFCC strands exceeded 6000 με in both BC-0.5 and BC-0.6. This strain level was nearly three times the typical yield strain of steel reinforcing bars (2000 με). On the other hand and as mentioned earlier, the design criteria and equations that govern the design of lap splices in common steel design codes and guidelines such as ACI 318 are based on the yield strength of the steel reinforcement. In other words, those equations were developed to guard against failure of lap splice until the reinforcement achieves its yield strength. Since the minimum strain of the test specimens was much higher than the yield strain of the steel reinforcement, the failure mode of the test specimens was neither concrete splitting nor reinforcement pullout as defined by general steel design codes. Rather, the failure mode can be assumed as severe concrete cracking followed by bond loss and pullout of CFCC strands.

Beams B2-0.5, B3-0.5, B4-0.5 achieved the same failure load regardless of the splice length due to the significant concrete tensile strain (cracking) at the time of failure. The strain of the CFCC strands at the time of failure ranged from 12,500 to 13,000 με in those beams. At this strain level, the bond strength of the concrete surrounding the reinforcement had nearly diminished and that allowed the CFCC strands to pullout of the concrete that fell into pieces when the pullout took place.

The failure loads of B2-0.6, B3-0.6, and B4-0.6 test continued to increase with increasing the splice length, which indicated that degradation in the bond strength of the concrete due to increased strain was countered and surpassed by the increase in the splice bond length. However, it is not expected that the failure load would continue to increase with increasing the splice length. Every increase in the splice length leads to an increase in the maximum load and increase in the CFCC and surrounding concrete strain, which further degrades the bond strength and limits the increase in the maximum load. Therefore, the full strength of CFCC strand at the splice may not be achieved because the concrete, surrounding the strand, becomes severely cracked and can no longer develop adequate bond strength to the CFCC reinforcement.

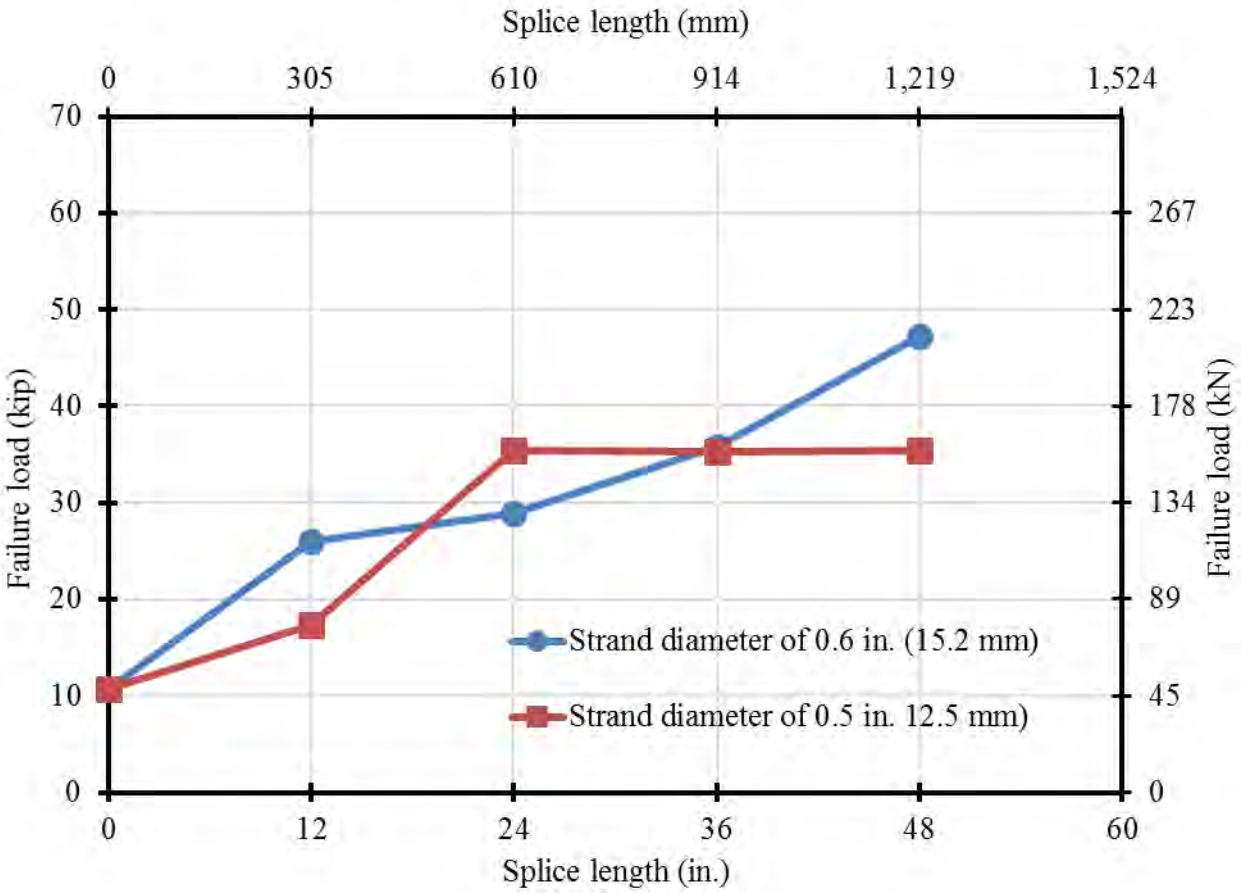

Figure 7.3-40 Splice length vs. Maximum load in all test beams

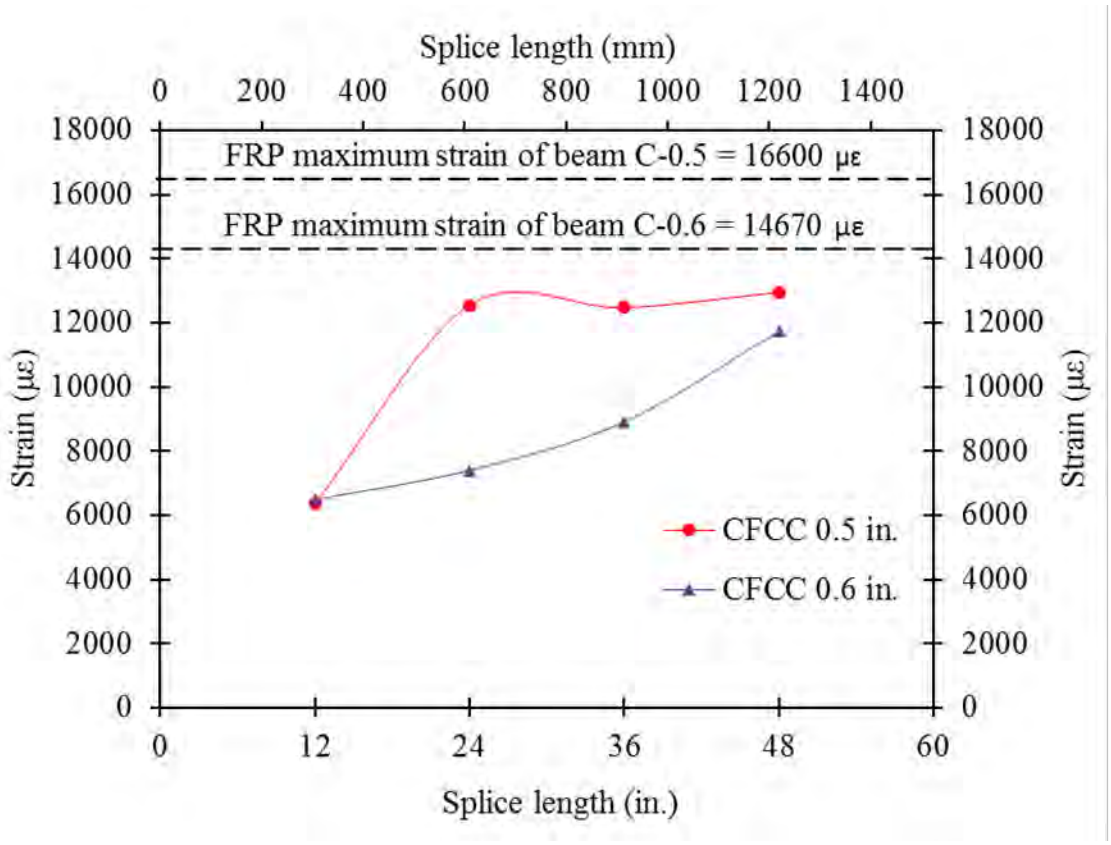

Figure 7.3-41 Strain versus splice length of the spliced CFCC strands

7.4 Lap-spliced CFRP Stirrups

The use of spliced U-shape stirrups in highway bridge box beams is a common construction practice that facilities pouring the concrete and eliminates any potential for honeycombing in the bottoms flange. The stirrup splice (overlap) extends through the full depth of the beam when stirrups are made of steel and this has been proven adequate through testing and construction. Nevertheless, enough data or test results are currently unavailable to support the same for spliced U-shape CFRP stirrups. Therefore, this test program focused on verifying the splice length in CFRP stirrups. . Four CFCC prestressed concrete box beams with spliced U-shaped stirrups were design, constructed, and tested to verify the use of spliced CFRP stirrups in bridge beam construction.

7.4.1 Test setup

As shown in Figure 7.4-1 and Figure 7.4-2, the box beams had a width of 17 in. (432 mm), a depth of 19 in. (483 mm), and a length of 24 ft (7.32 m), while the cavity inside the beams had a depth

of 10 in. (254 mm) and a width of 11 in. (279 mm). The beams were also provided with 12-in. (305-mm) thick end blocks and 10 in. (254 mm) thick interior diaphragms at the load location at a distance of 5ft (1524 mm) from each end.

All beams were reinforced in tension with four 0.6 in. (15.2 mm) prestressed CFCC strands and five 0.6 in. (15.2 mm), non-prestressed CFCC strands. In the transverse direction, the stirrups were provided at a center-to-center spacing of 8 in. (203 mm).

The beams were loaded in a three-point-load shear test setup and the shear load was placed at a distance of 4.91 ft (1.5 m) from the center of the end support as shown in Figure 7.4-3. The beam was loaded over a span of 18.083 ft (5.51 m) since one support was placed under an end block and the other support was placed under the interior diaphragm on the other side of the beam. The distance from the load to the nearest support presented the critical shear span of the beam. Each beam was loaded twice to evaluate the shear capacity of both ends.

Closed steel stirrups No.5 (16 mm) were provided between the interior diaphragms. In addition, CFCC stirrups with a diameter of 0.6 in. (15.2 mm) were provided on one end of each beam within the critical shear span, while the other end of each beam was provided with No.5 (16 mm) steel stirrups. The steel and CFCC stirrups that were provided within the shear span had four configurations in the four beams; one beam was provided with closed CFCC and steel stirrups at the ends. The other three beams were provided with U-shape spliced CFCC and steel stirrups with splice lengths of 4, 7, and 10.5 in. (102, 178, and 267 mm). It should be noted that the splice length of 10.5 in. (267 mm) represents the full-depth splice as shown in Figure 7.4-4. The nomenclature of the test beams is written as: “material of stirrups -splice length in inches”. Material do the stirrups is denoted C for CFCC and S for steel. In case of closed stirrups, the splice length was replaced with a letter C. For instance, C7 is a beam specimen with U-shape spliced CFCC stirrups on a splice length of 7 in. (178 mm). SC is a beam specimen with closed steel stirrups. Material properties of stirrups are shown in Table 7.4-1. All stirrups had a center to center spacing of 8 in. (203 mm). Figure 7.4-5 shows the general configuration and dimensions of the stirrups.

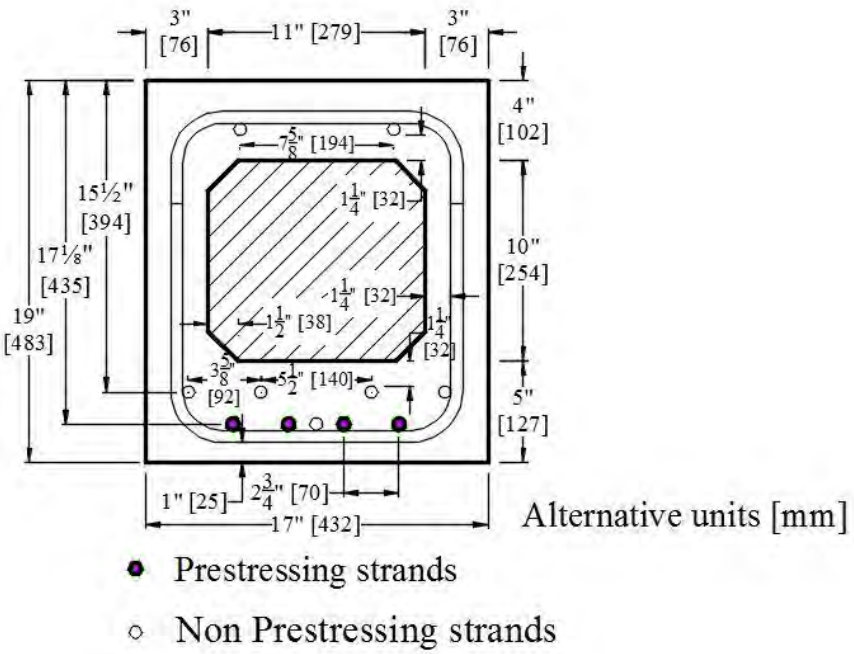

Figure 7.4-1 Cross-sections of prestressed box-beam

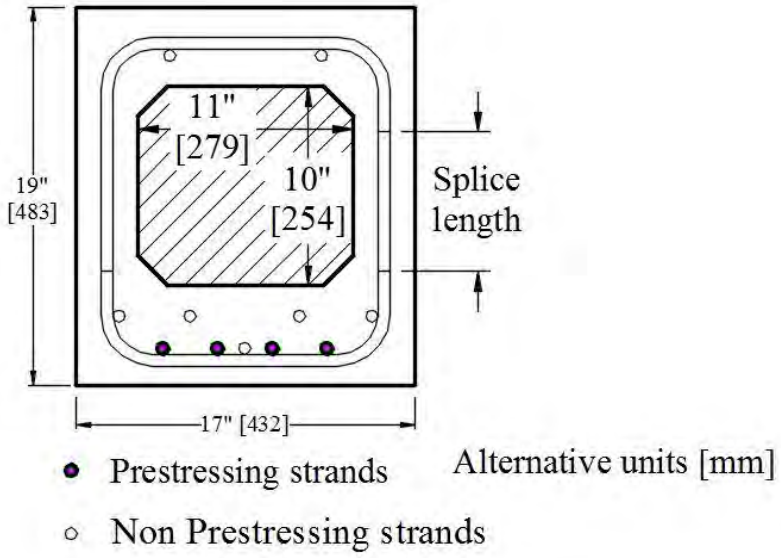

Figure 7.4-2 Cross-sections of prestressed box-beam reinforced with spliced stirrups in shear

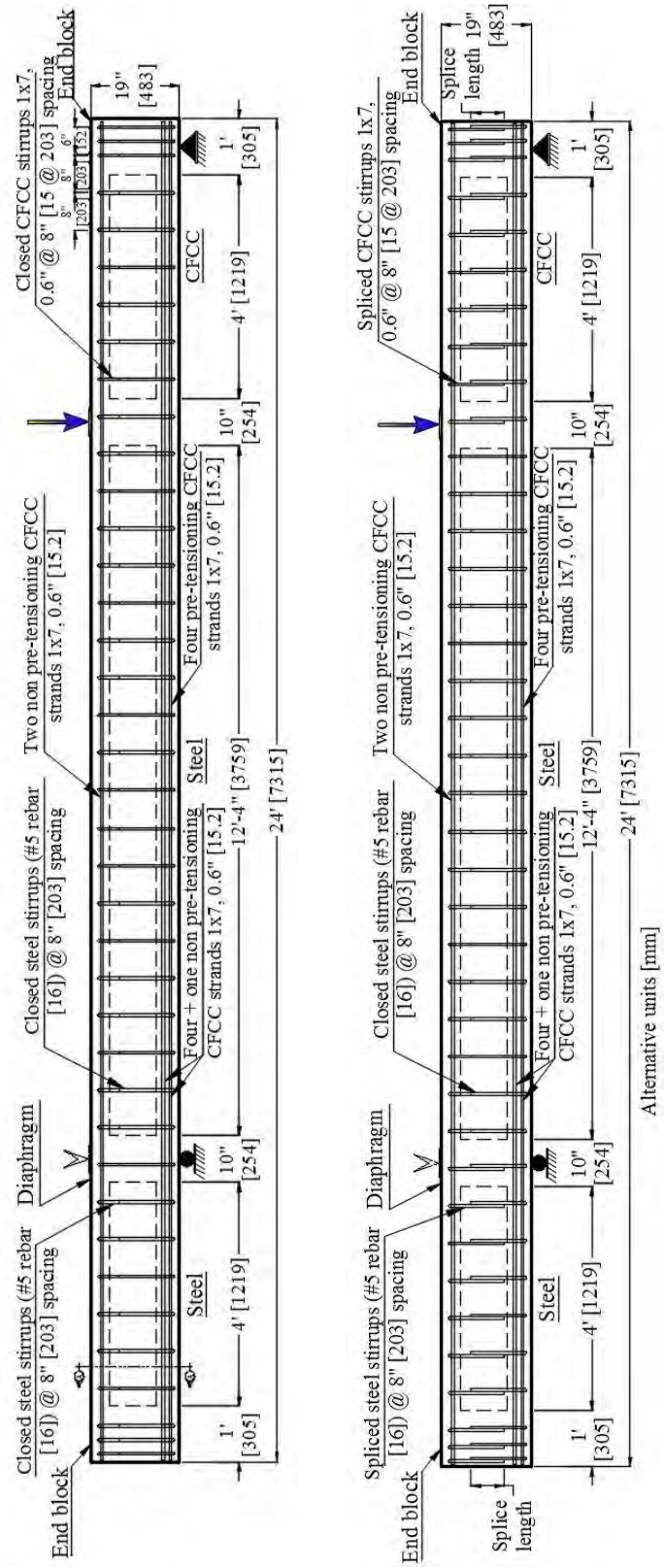

Figure 7.4-3 Longitudinal sections of prestressed concrete box-beams

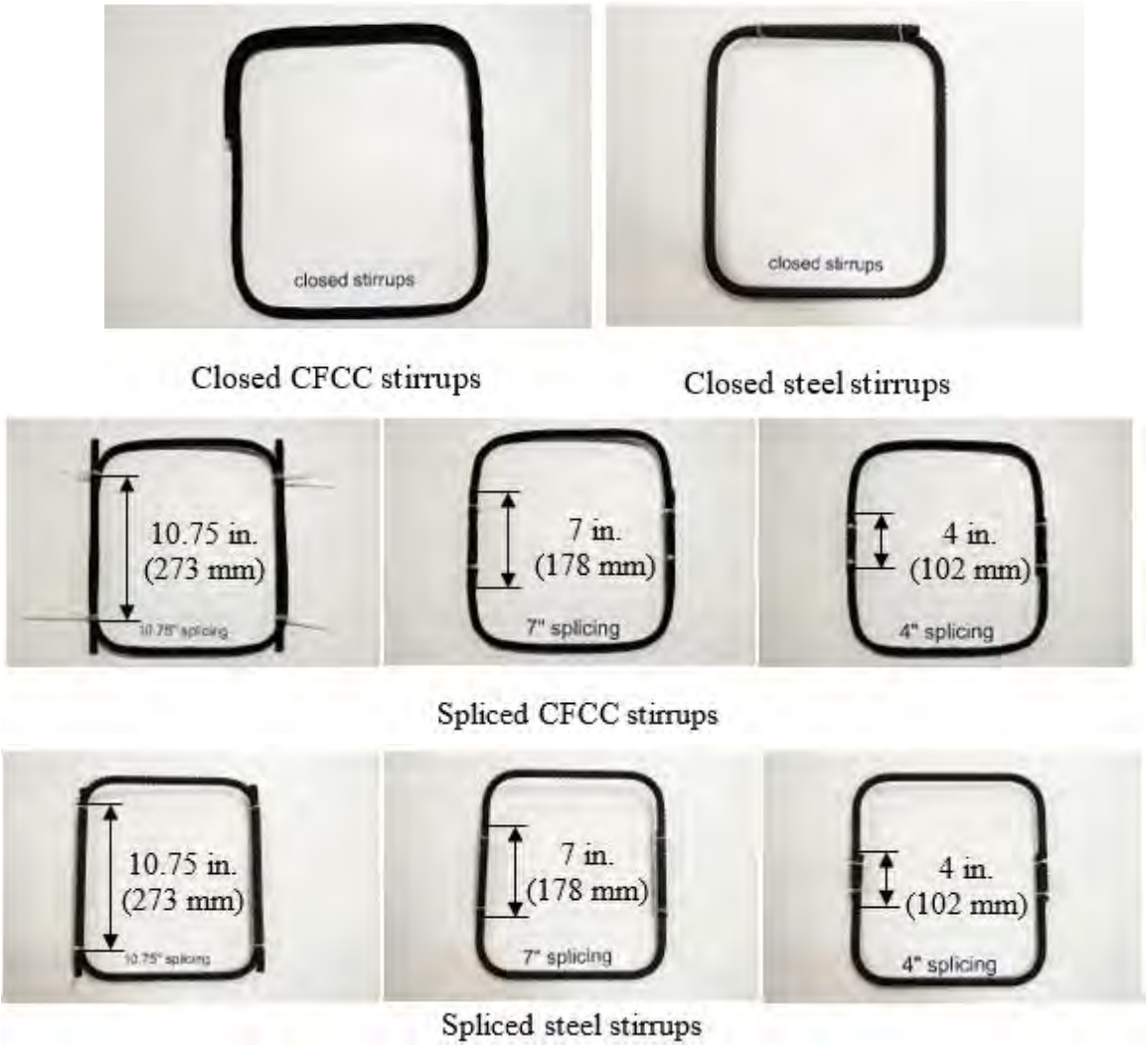

Figure 7.4-4 Configuration of stirrups in the beam specimens

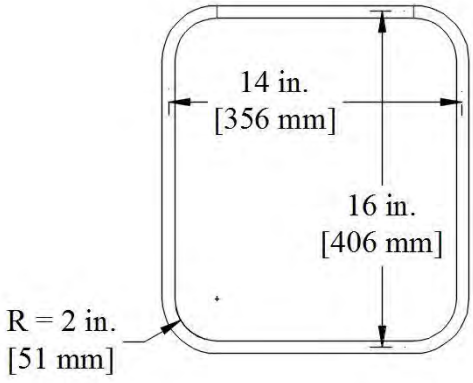

Figure 7.4-5 Stirrup dimensions

Table 7.4-1 Material properties of shear reinforcement

Material properties of stirrups	CFCC	No.5 steel
Diameter, in. (mm)	0.6 (15.28)	0.625 (16)
Effective cross-sectional area, in.² (mm²)	0.179 (115.6)	0.31 (200)
Average breaking load, kip (kN)	69.9 (311)	27.9 (124)
Ultimate tensile strength, ksi (MPa)	390 (2,690)	90 (621)
Modulus of elasticity, ksi (GPa)	21,320 (147)	29,000 (200)
Yield strength, ksi (MPa)	---------	60 (414)
Elongation (%)	1.8	≈ 5.00

The construction of the box-beams consisted of building the formwork, assembling the reinforcement cages, prestressing the CFCC strands, casting the box beams, and cutting the prestressed CFCC strands. All four box beams were cast at the same time from the same concrete batch with a design 28-day concrete strength of 7000 psi (48 MPa).

The formwork consisted of wooden platform, center walls, and side walls as shown in Figure 7.4-6 and Figure 7.4-7. The hollow portion inside the box beams was formed from 11-in. (279-mm) wide by 10-in. (254-mm) high Styrofoam blocks as shown in the figures. The stirrups in the critical shear spans at the ends of each beam were instrumented with strain gages attached to their vertical legs. Bottom prestrsssing strands were also instrumented with strain gages.

Each box beam was prestressed with four prestressing CFCC strands with a total average initial prestressing force of 120 kip (534 kN) per beam. The prestressing of the strands was carried out in a 50-ft (15.2 m) long reinforced concrete prestressing bed with two abutment-type bulk heads that were anchored to the bed. Figure 7.4-8 through Figure 7.4-11 show the process of prestressing the box beams. At the live end, CFCC strands were coupled with steel strands using a special mechanical anchorage system. The steel strands were anchored to the bulk head using conventional steel anchorage devices. At the dead end, the CFCC strands were coupled with high-strength steel threaded rods that were anchored to the bulkhead using high-strength steel nuts and washers. The dead-end couplers were provided with in-line load cells to monitor the prestressing force. Prestressing was executed using a hydraulic jack from the live end.

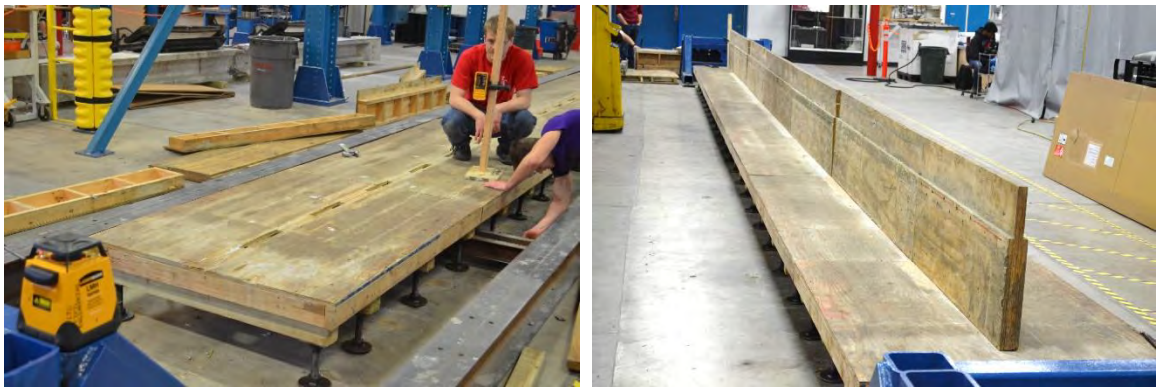

Figure 7.4-6 Construction of the formwork for the box beams

Figure 7.4-7 Preparing and instrumenting the reinforcement cages

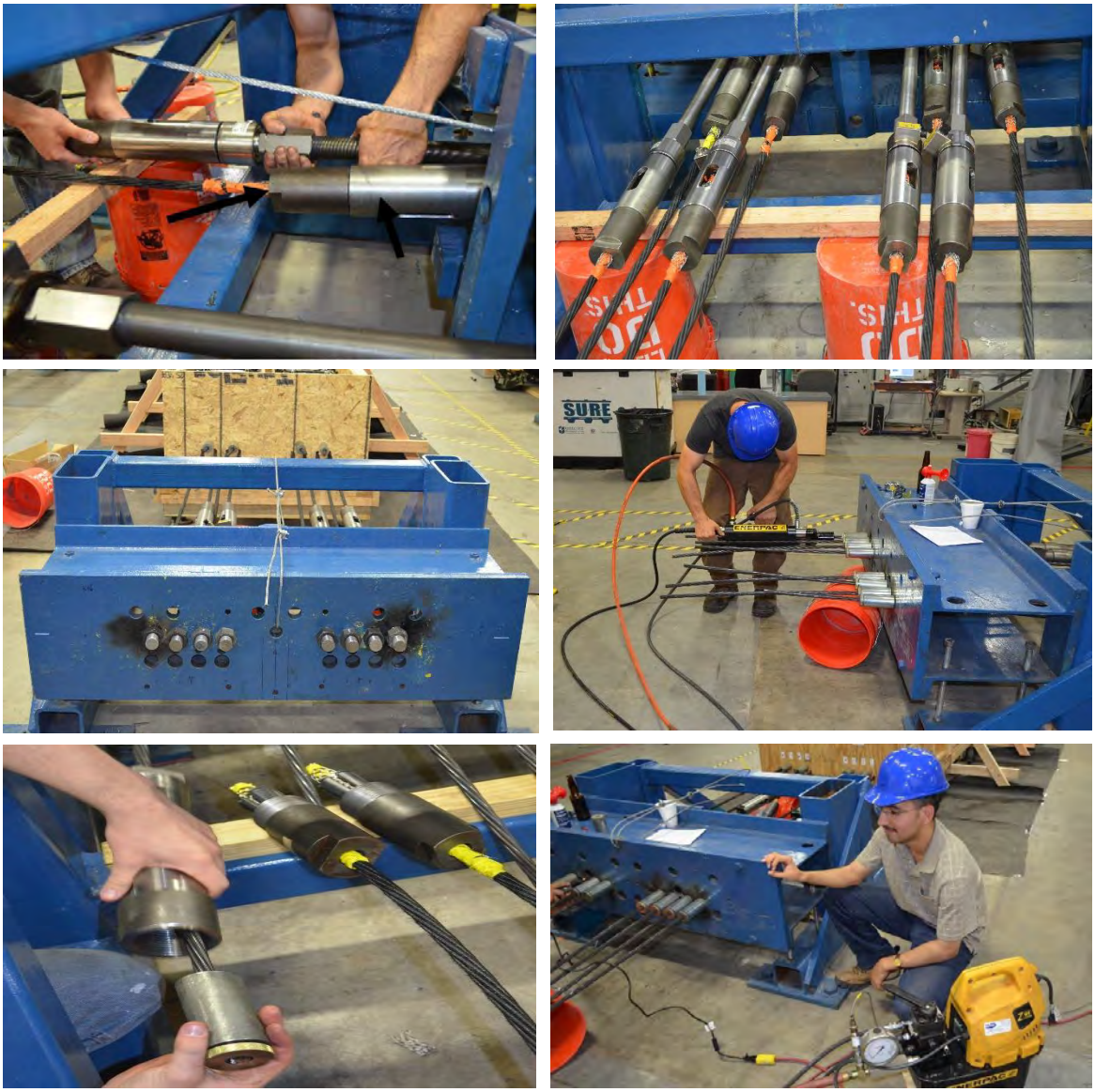

Figure 7.4-8 Prestressing CFCC strands from the live end with load cell on the dead end

To eliminate a possible rotation of the bulkhead during prestressing the CFCC prestressing strands were pulled in a specific order as illustrated in Figure 7.4-10. Couplers were staggered at both ends of the prestressing strands with 2 ft (0.61 m) spacing to avoid contacting while prestressing as shown in Figure 7.4-11.

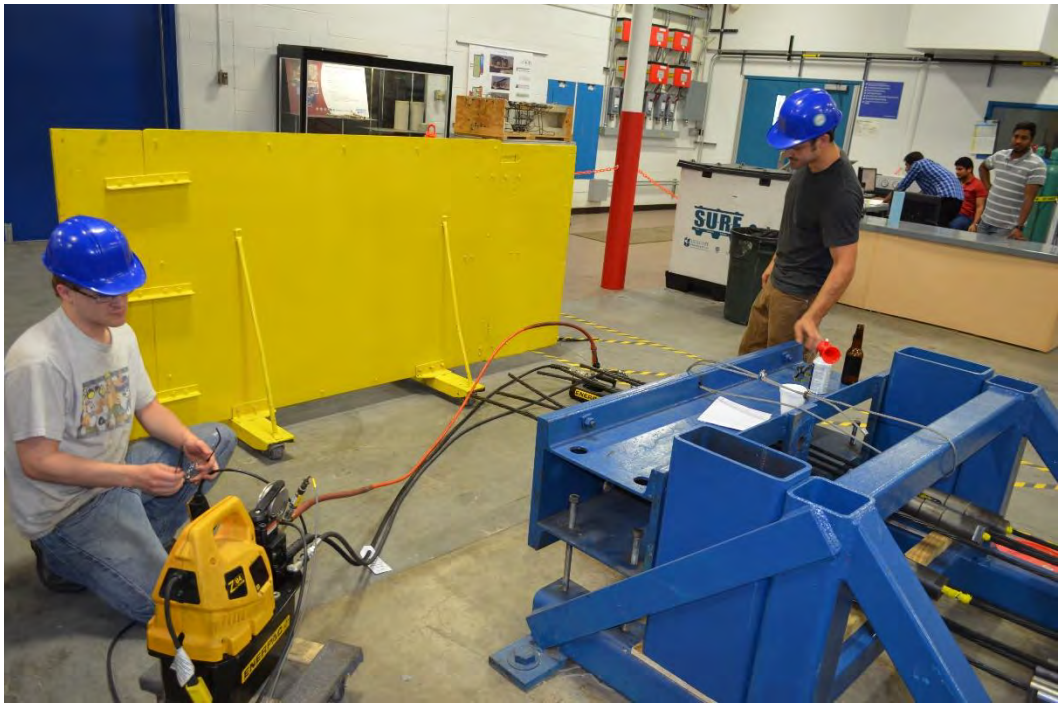

Figure 7.4-9 Prestressing CFCC strands from the live end

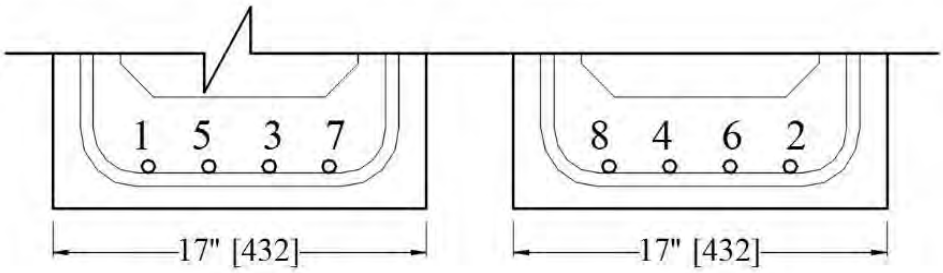

Figure 7.4-10 Prestressing order of CFCC strands

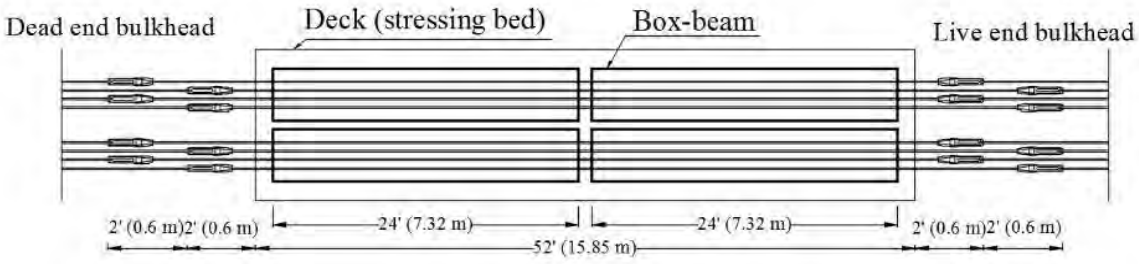

Figure 7.4-11 Couplers spacing

The box-beams were cast using a ready-mix concrete with a slump of 8 in. (203 mm) which was verified prior to pouring. In addition, twenty test cylinders were constructed from the same concrete batch to determine concrete compressive strength at different ages. After concrete casting, the beams were cured by covering them with wet burlap sheets and spraying water for 7 days (Figure 7.4-12.

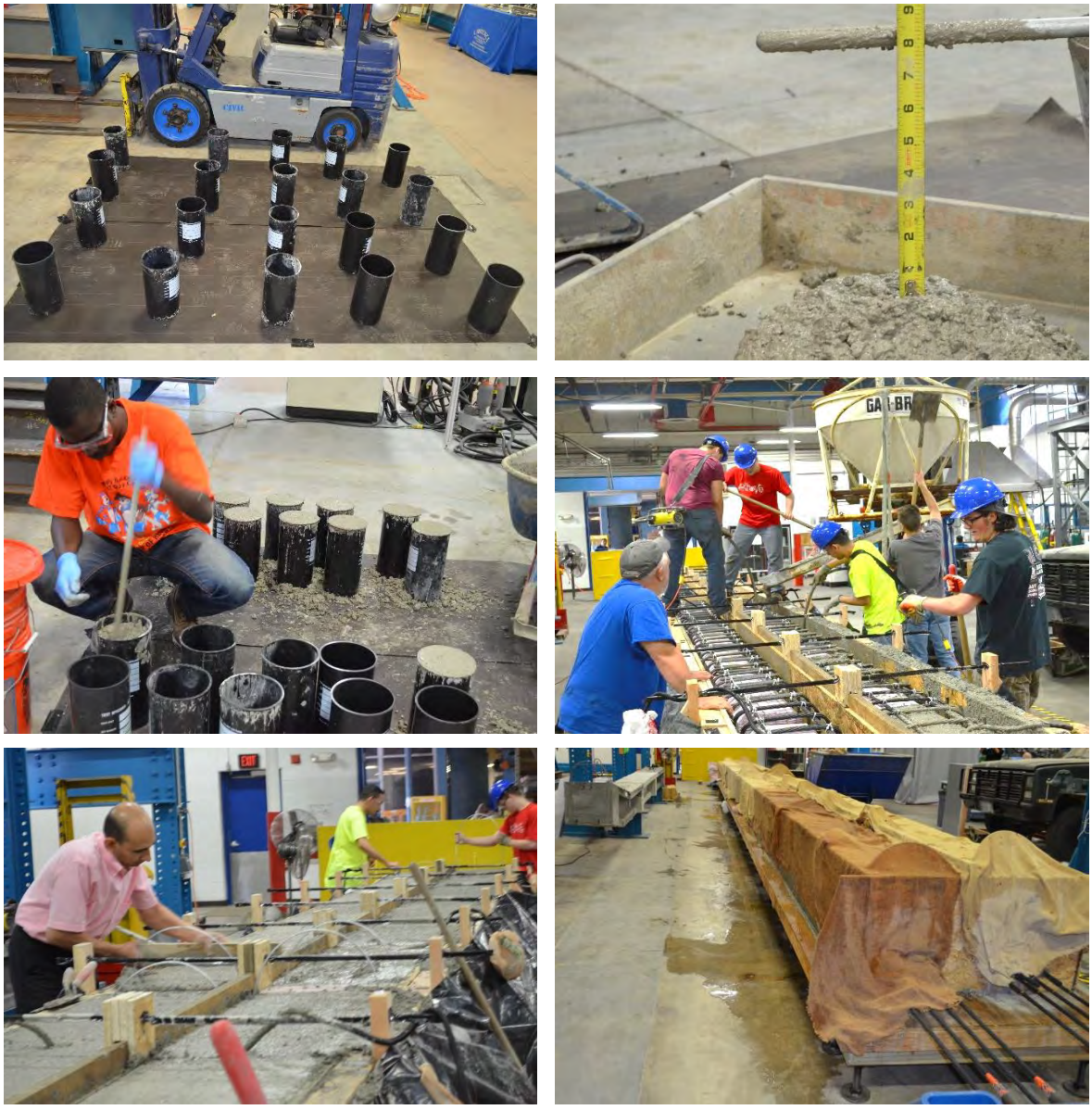

Figure 7.4-12 Casting the concrete of the box beams

The next day after casting the box-beams the side walls were removed from the formwork. After 13 days as the concrete gained the initial compressive strength, the prestressing force was transferred to the concrete by heating and cutting the steel strands coupled to the CFCC strands using oxy-acetylene torch as shown in Figure 7.4-13. As with prestressing, prestress release was executed in a proper sequence to avoid any possible rotation to the bulkheads. The beams were removed from the formwork and transferred to storage. The prestressing forces were recorded through the in-line load cells from the time of stressing until the release of strands as shown in Figure 7.4-14. In addition, the uniaxial compressive strength of the concrete was determined with an average concrete compressive strength of 11,305 psi after 28 days as shown in Figure 7.4-15.

After prestress release, the beams were moved to the testing facility and were externally instrumented for testing. Multiple sensors were installed externally including concrete strain gages, linear variable differential transducers (LVDTs), load cells, and linear motion transducers (LMTs). A computer with a data acquisition interface system was used to monitor and record test data.

Figure 7.4-13 Releasing of prestressed strands

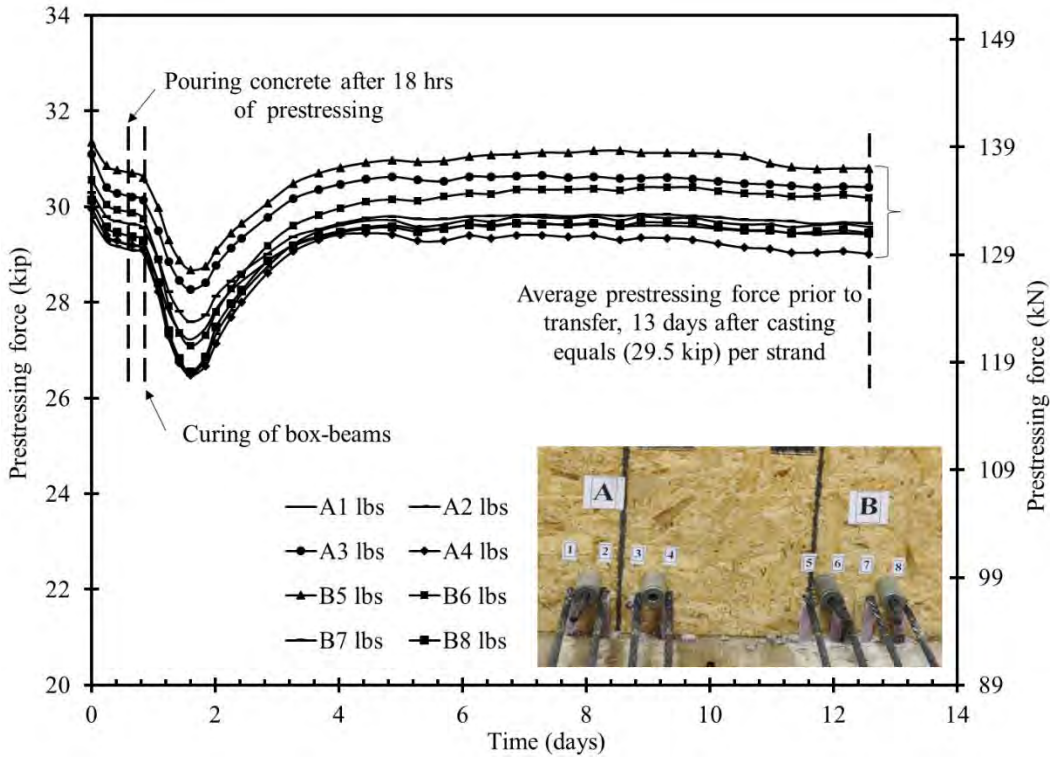

Figure 7.4-14 Prestressing force prior to transfer

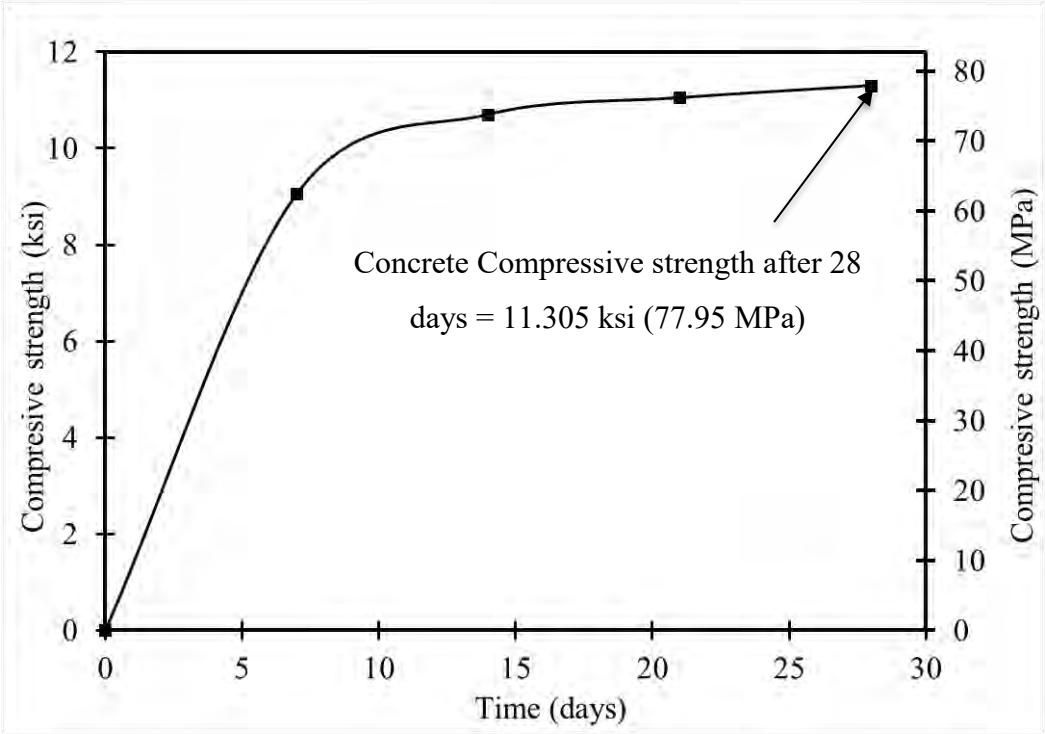

Figure 7.4-15 Concrete compressive strength

7.4.2 Test Setup

Box beams were simply supported over steel reinforced elastomeric bearing pads with a thickness of 1.0 in. (25.4 mm). Shear test in each beam started with testing beam end with CFCC stirrups then the end with steel stirrups. The beams were subjected to several loading/unloading cycles with a load increment of 5 kip (22.2 kN) to a load level of 40 kip (177.9 kN) then an increment of 10 kip (44.5 kN) to failure. The load was applied through a controlled actuator displacement rate of 0.1 in/min (2.54 mm/min). Crack development was inspected and marked by the end of each load cycle. Beam test setup and instrumentation are shown in Figure 7.4-16 and Figure 7.4-17.

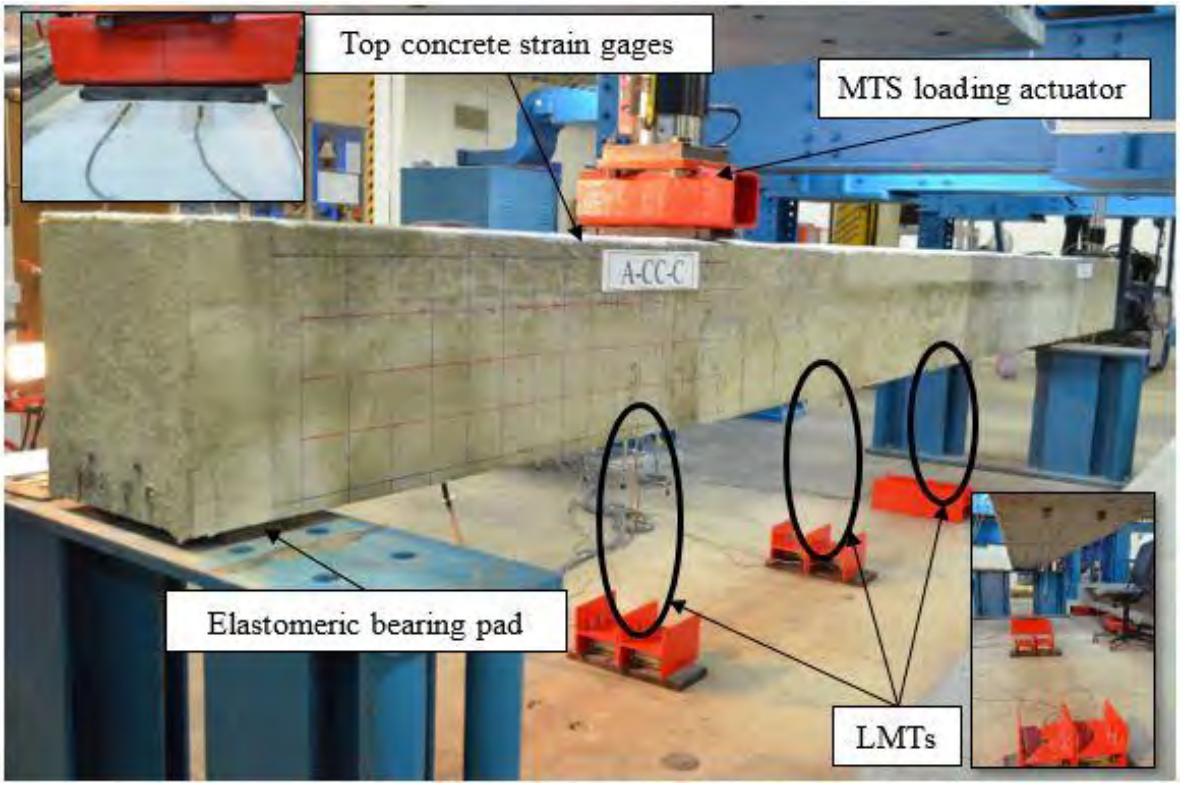

Figure 7.4-16 Instrumentation and test setup of the box beams

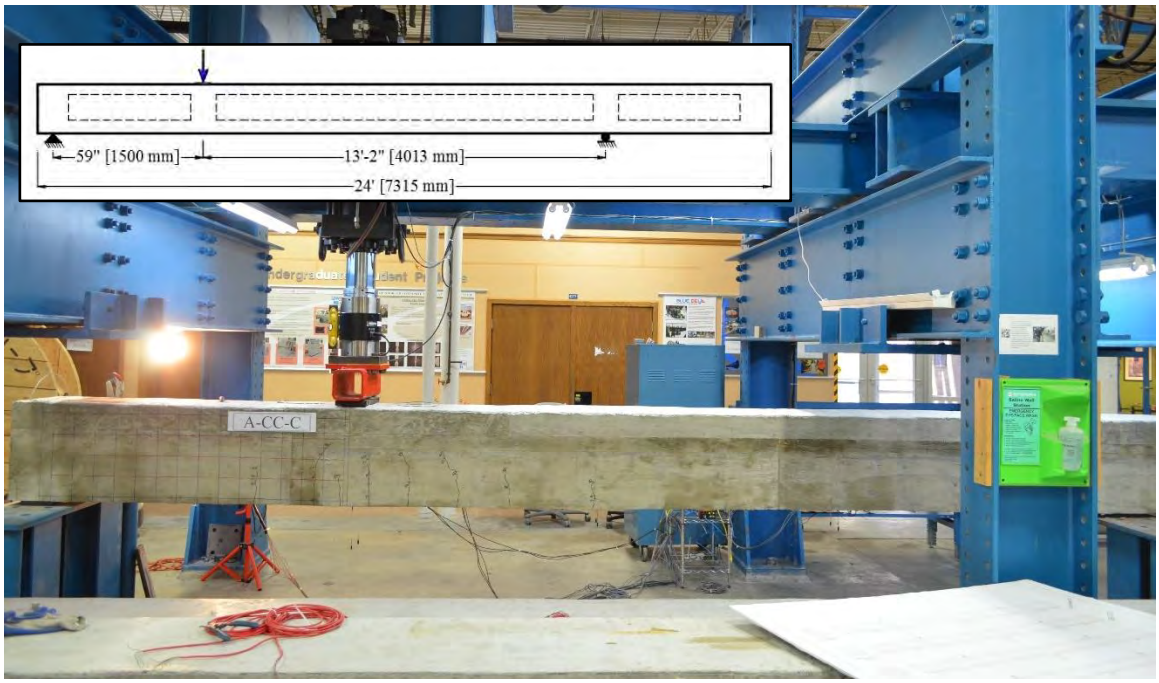

Figure 7.4-17 Shear test setup of box beams

7.4.3 Test results

7.4.3.1 Control Box-Beam (C-C)

Beam C-C was a beam end provided with closed CFCC stirrups. The first observed flexural crack under the load developed at a shear force of 32.7 kip (145 kN). A decompression shear force of 19.5 kip (87 kN) was also observed in post-cracking load cycles. By increasing the load, the flexure cracks extended diagonally through the web. At a shear force of 43.7 kip (194 kN), the first web shear crack initiated on the side of the beam, while the existing flexure cracks propagated towards the point of loading, as shown in Figure 7.4-18. A sudden failure took place when the shear force approached 96 kip (427 kN). The failure took place through top concrete crushing in the compression zone under the load as shown in Figure 7.4-19. The shear force-deflection response for all load cycles is presented in Figure 7.4-20, while the shear force-deflection curve for the last load cycle is presented in Figure 7.4-21. The deflection under the loading point at failure was around 1.92 in. (49 mm). No rupture of the CFCC stirrups was observed at failure. No rupture or debonding of the longitudinal CFCC prestressing strands was observed either.

Figure 7.4-18 Crack pattern in beam C-C

a) Front side

b) Back side

Figure 7.4-19 Failure of beam C-C

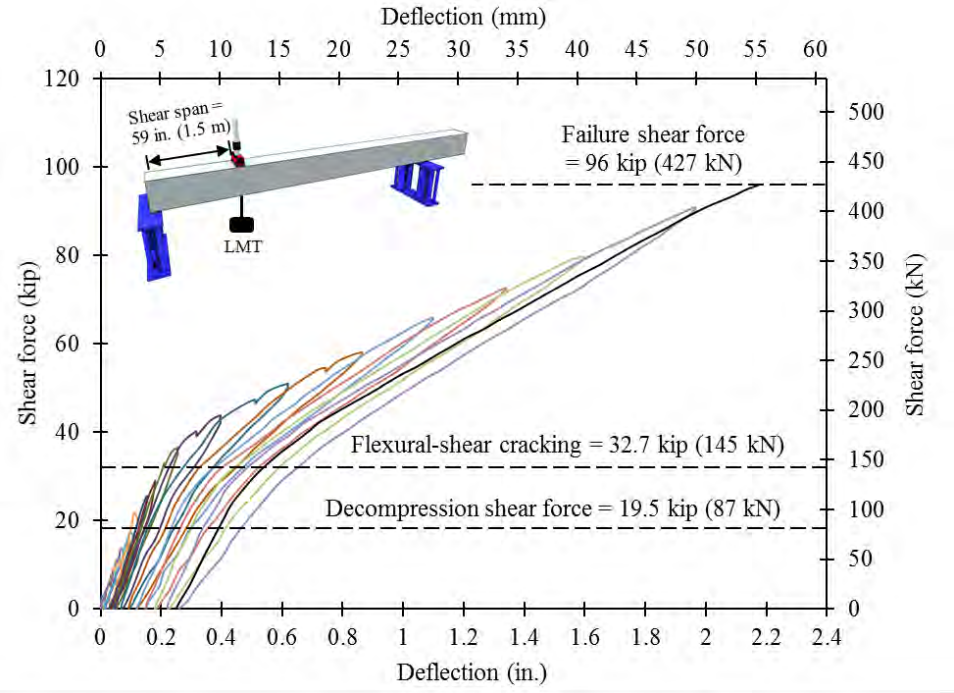

Figure 7.4-20 Shear force vs under-load-deflection in Beam C-C for all load cycles

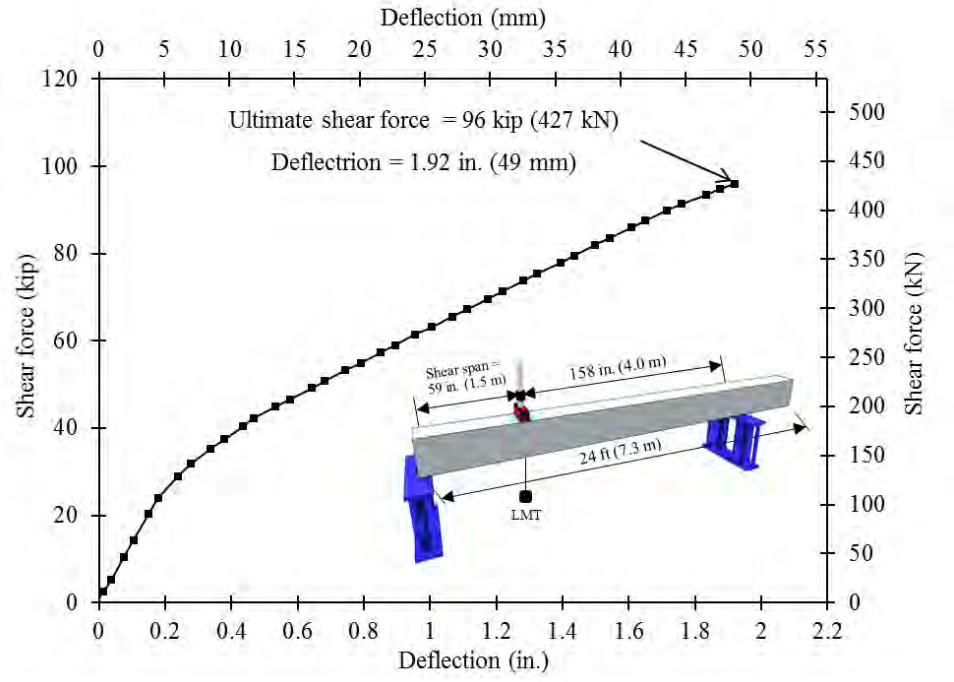

Figure 7.4-21 Shear force vs under-load-deflection in Beam C-C for last load cycle

7.4.3.2 Beam (C-10.75)

Beam C-10.75 was a beam end provided with lap spliced CFCC stirrups with a splice length of 10.75 in. (273 mm).The first observed flexure-shear crack developed at a shear force of 32.3 kip (144 kN) in Bema C-10.75. In addition, a decompression shear force of 19.7 kip (88 kN) was observed in post-cracking load cycles. The flexural cracks extended diagonally through the web with increasing the load. At a shear force level of 58.2 kip (259 kN), the first web shear crack developd, while the existing flexure cracks propagated towards the point of loading, as shown in Figure 7.4-22. A sudden failure took place when the shear force approached 93.5 kip (416 kN). Failure took place through crushing and shearing of the concrete in the compression flange as shown in Figure 7.4-23. The shear force-deflection response for all load cycles is shown in Figure 7.4-24, while the shear force-deflection for last load cycle is shown in Figure 7.4-25. The deflection under the loading point at failure was around 1.84 in. (47 mm). No rupture or pullout of the CFCC stirrups was observed at failure. There was also no rupture or debonding of the longitudinal CFCC prestressing strands.

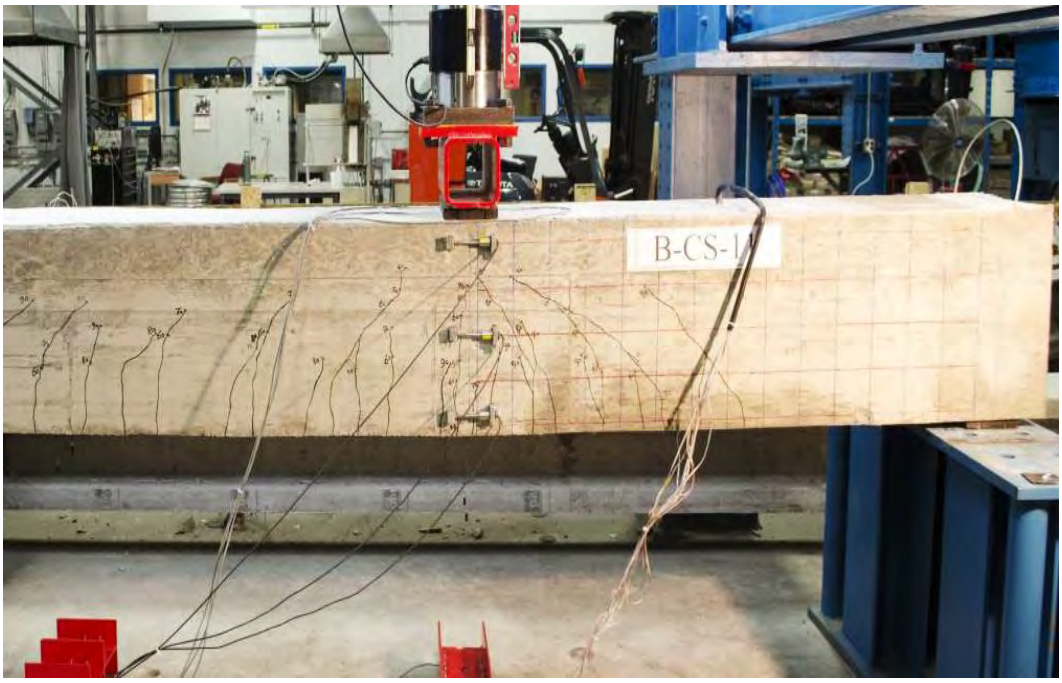

Figure 7.4-22 Crack pattern of beam C-10.75

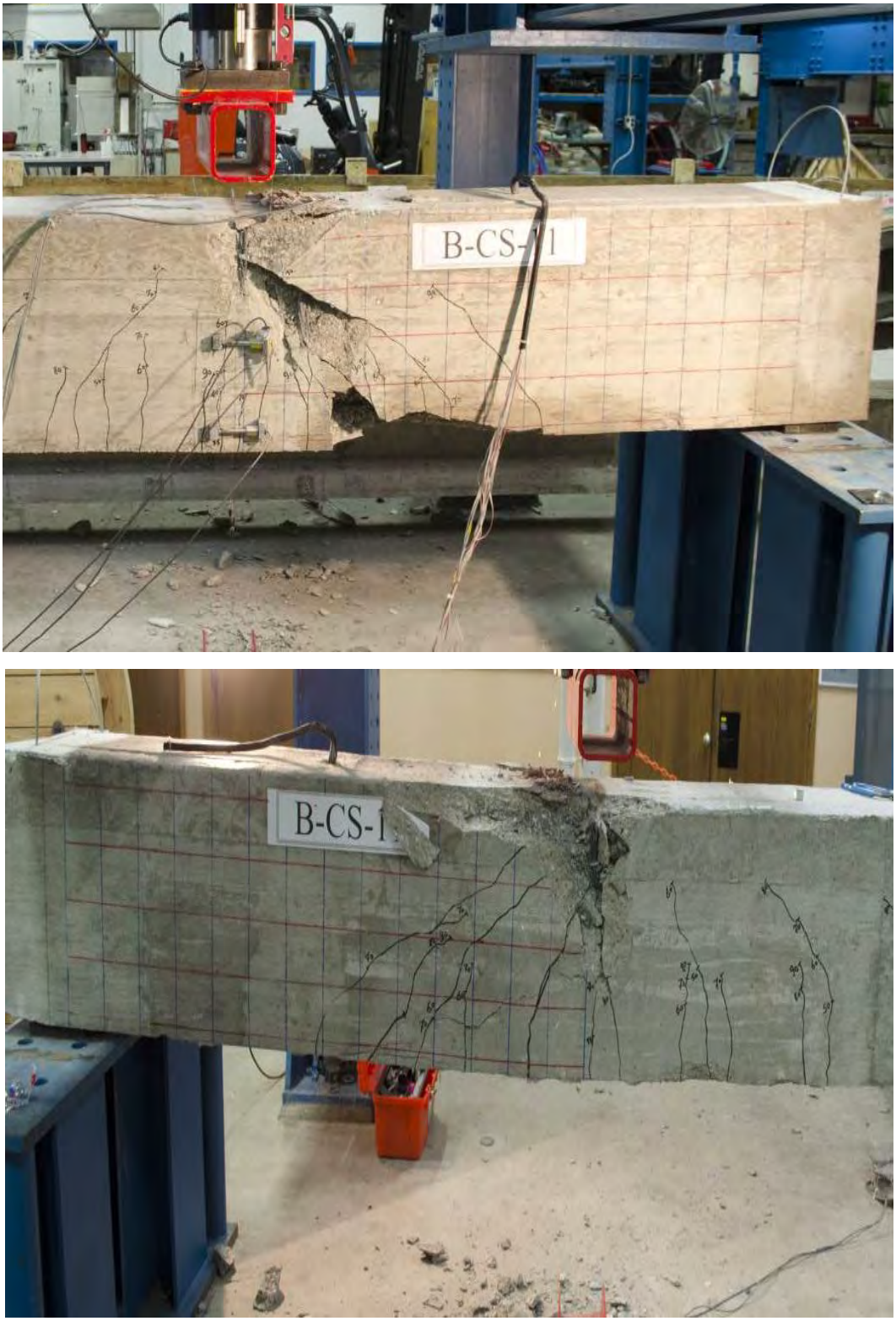

Figure 7.4-23 Failure of beam C-10.75

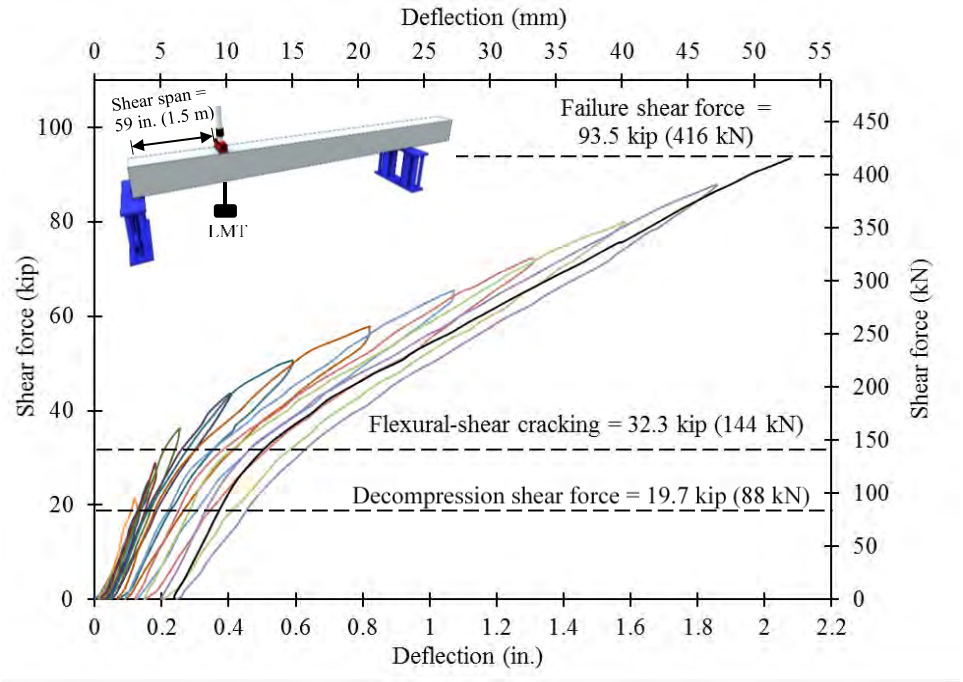

Figure 7.4-24 Shear force vs under-load-deflection in Beam C-10.75 for all load cycles

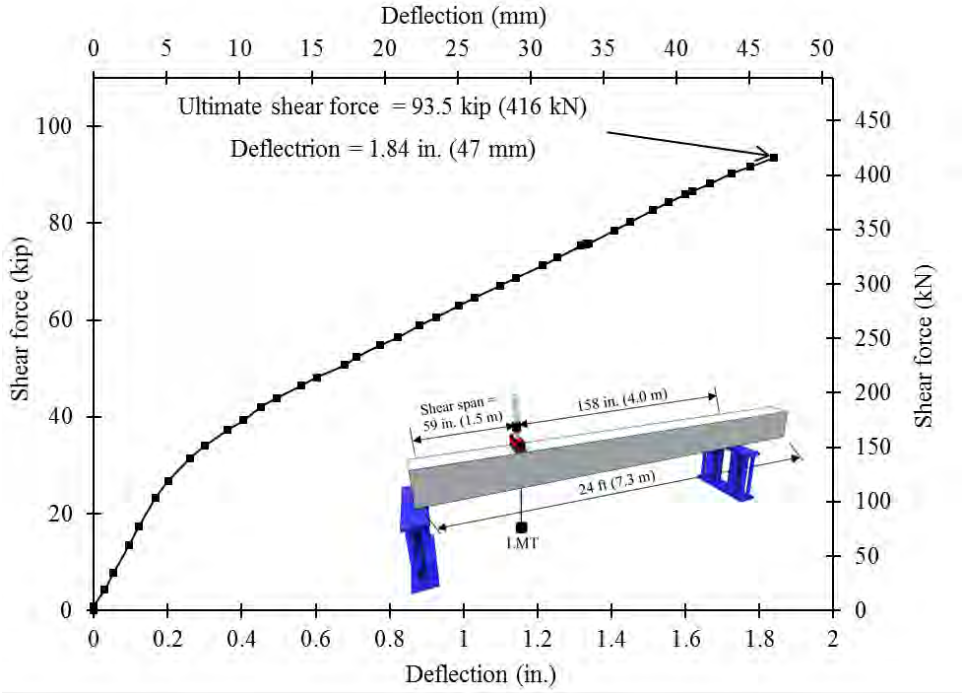

Figure 7.4-25 Shear force vs under-load-deflection in Beam C-10.75 for last load cycle

7.4.3.3 Beam (C-7)

Beam C-7 was a beam end provided with lap spliced CFCC stirrups with a splice length of 7 in. (178 mm). The first observed flexure-shear crack in Beam C-7 developed at a shear force of 30.5 kip (136 kN). In addition, a decompression shear force of 18.6 kip (83 kN) was observed in post-cracking load cycles. At an average shear force of 51 kip (227 kN) three web shear cracks initiated simultaneously and crossed the spliced stirrups in the shear zone, while the existing flexure cracks propagated towards the point of loading, as shown in Figure 7.4-26. A sudden failure took place when the shear force approached 69.2 kip (308 kN). Failure was characterized by pullout of the CFCC stirrups followed by shear failure of the concrete at the major crack as shown in Figure 7.4-27. The shear force-deflection response for all load cycles is shown in Figure 7.4-28, while that for the last load cycle is shown in Figure 7.4-29. The deflection under the loading point at failure was around 1.14 in. (29 mm). No rupture of the CFCC stirrups was observed at failure. However, all the spliced stirrups pulled out of the concrete in the region where the inclined web crack crossed the lapped splice. There was also no rupture or debonding of the longitudinal CFCC prestressing strands.

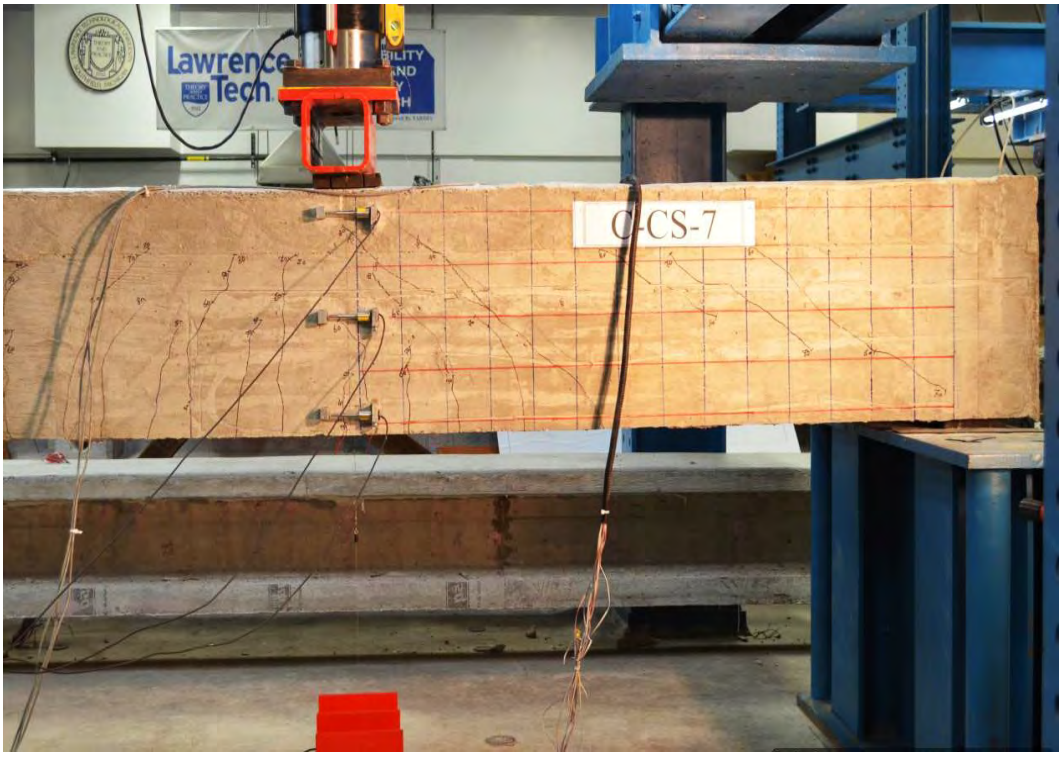

Figure 7.4-26 Crack pattern of beam C-7

a) Front side

b) Back side

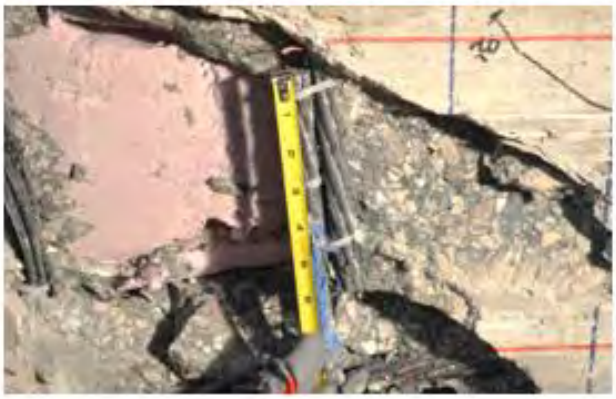

c) Slippage of the 7 in. (178 mm) spliced stirrups

Figure 7.4-27 Failure of beam C-7

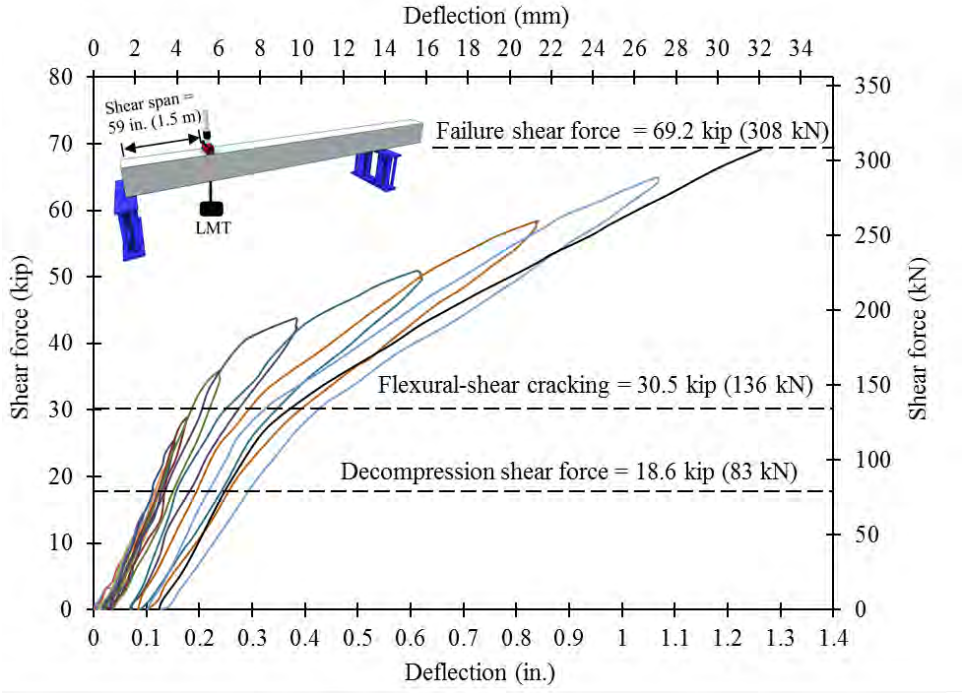

Figure 7.4-28 Shear force vs under-load-deflection in Beam C-7 for all load cycles

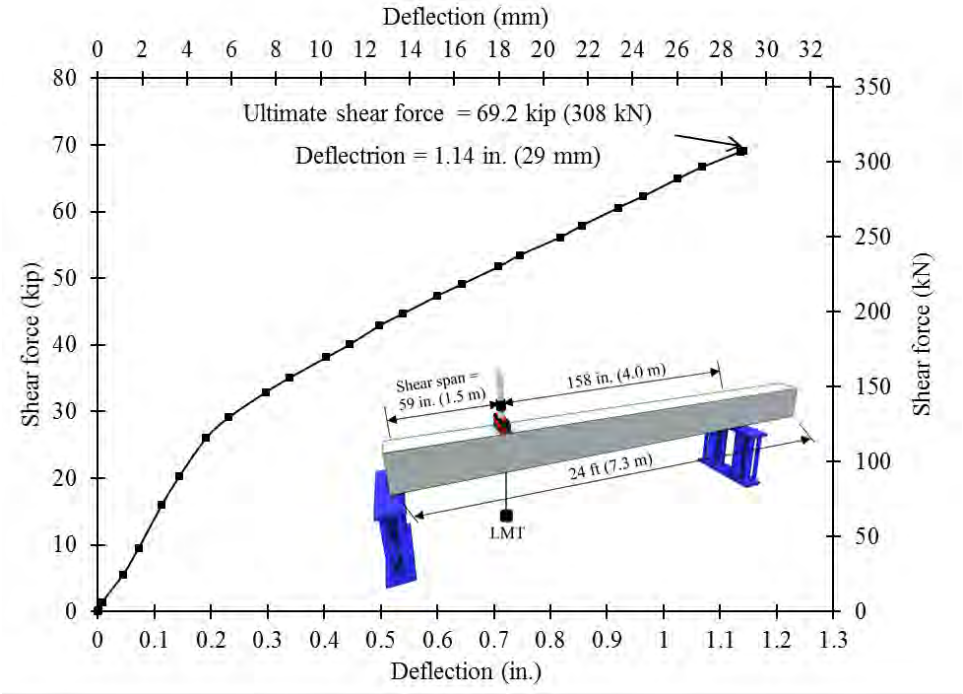

Figure 7.4-29 Shear force vs under-load-deflection in Beam C-7 for last load cycle

7.4.3.4 Beam (C-4)

Beam C-4 was a beam end provided with lap spliced CFCC stirrups with a splice length of 4 in. (102 mm). The first observed flexure-shear crack developed at a shear force of 32.8 kip (146 kN). In addition, a decompression shear force of 20.8 kip (93 kN) was observed in post-cracking load cycles. At a shear force level of 51 kip (227 kN), the first web shear crack initiated, while the existing flexural cracks propagated towards the point of loading, as shown in Figure 7.4-30. A sudden failure took place when the shear force approached 63.6 kip (283 kN). Failure took place through a pullout of the CFCC stirrups followed by a shear failure of the concrete at the major crack as shown in Figure 7.4-31. The shear force-deflection response for all load cycles is shown in Figure 7.4-32, while the shear force-deflection curve for last load cycle in shown in Figure 7.4-33. The deflection under the loading point at failure was around 0.96 in. (24 mm). No rupture of the CFCC stirrups was observed at failure. However, all the spliced stirrups pulled out of the concrete in the region where the inclined web crack crossed the lapped splice. There was also no rupture or debonding of the longitudinal CFCC prestressing strands.

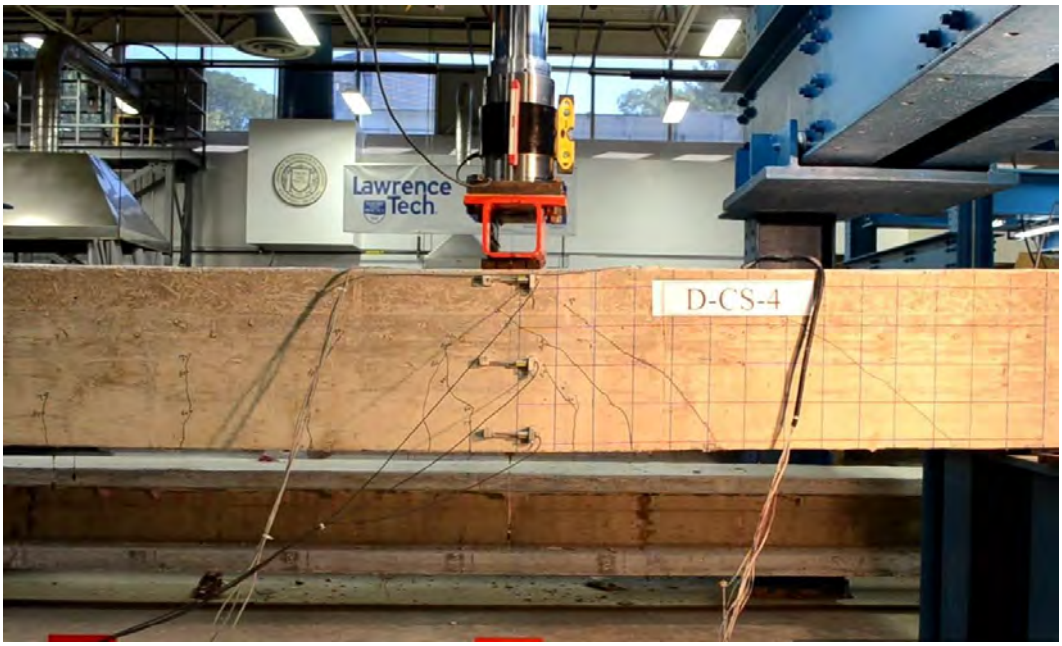

Figure 7.4-30 Crack pattern of beam C-4

a) Front side

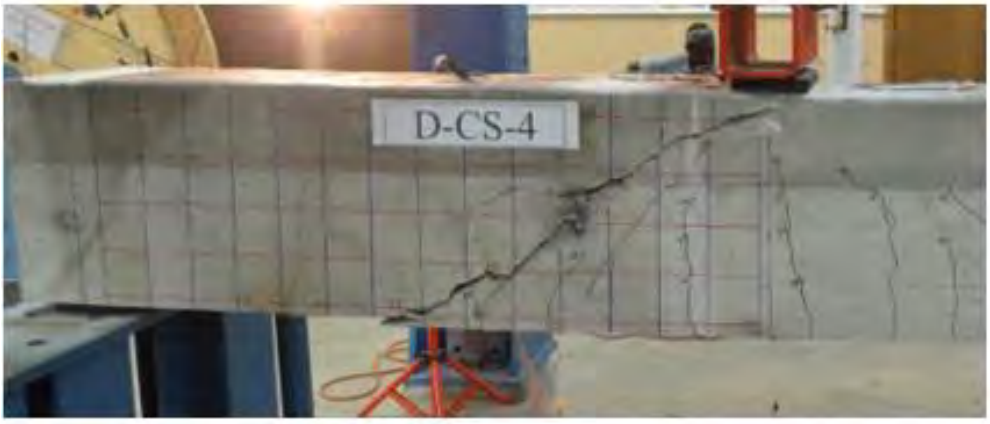

b) Back side

c) Slippage of the 4 in. (102 mm) spliced stirrups

Figure 7.4-31 Failure of beam C-4

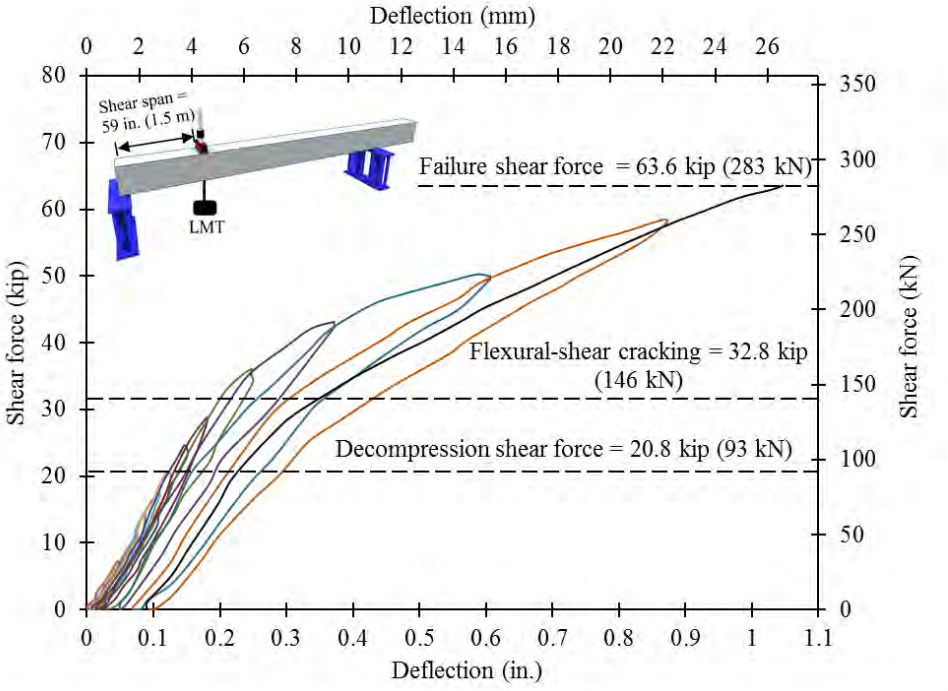

Figure 7.4-32 Shear force vs under-load-deflection in Beam C-4 for all load cycles

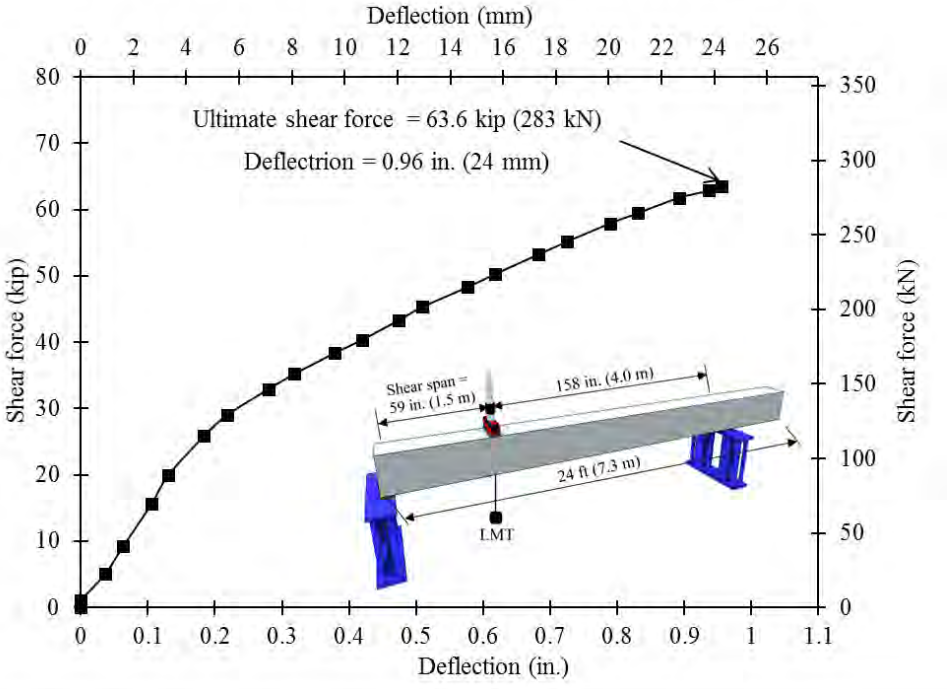

Figure 7.4-33 Shear force vs under-load-deflection in Beam C-4 for last load cycle

7.4.3.5 Control Beam (S-C)

Beam S-C was a beam end provided with closed steel stirrups. The first observed shear crack under the load developed at a shear force of 31.4 kip (140 kN). In addition, a decompression shear force of 19.7 kip (88 kN) was observed in the post-cracking load cycles. At 43.7 kip (194 kN), the first web shear crack initiated, while the existing flexure cracks propagated towards the point of loading as shown in Figure 7.4-34. A sudden failure took place when the shear force approached 89.2 kip (397 kN). Failure took place through top concrete crushing in the compression zone under the load as shown in Figure 7.4-35. The shear force-deflection response for all load cycles is shown in Figure 7.4-36, while the shear force-deflection curve for the last load cycle is shown in Figure 7.4-37. The deflection under the loading point at failure was around 1.86 in. (47 mm). No rupture of the steel stirrups was observed at failure. There was no rupture or debonding of the longitudinal CFCC prestressing strands either.

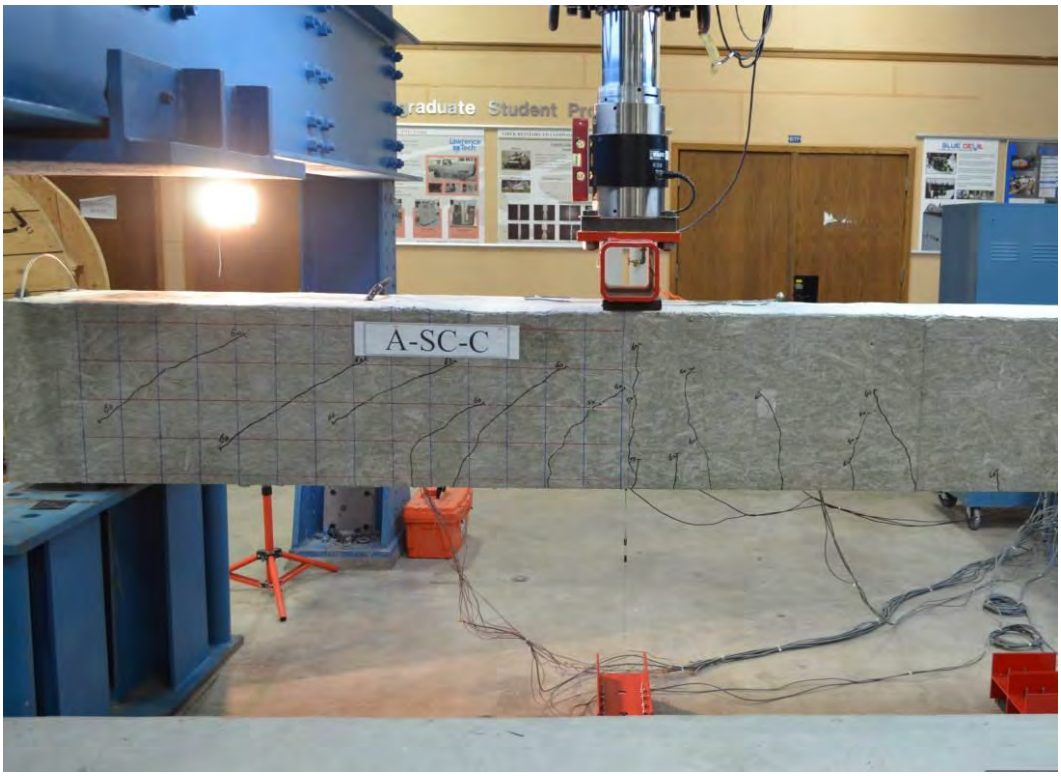

Figure 7.4-34 Crack pattern of beam S-C

a) Front side

b) Back side

Figure 7.4-35 Failure of beam S-C

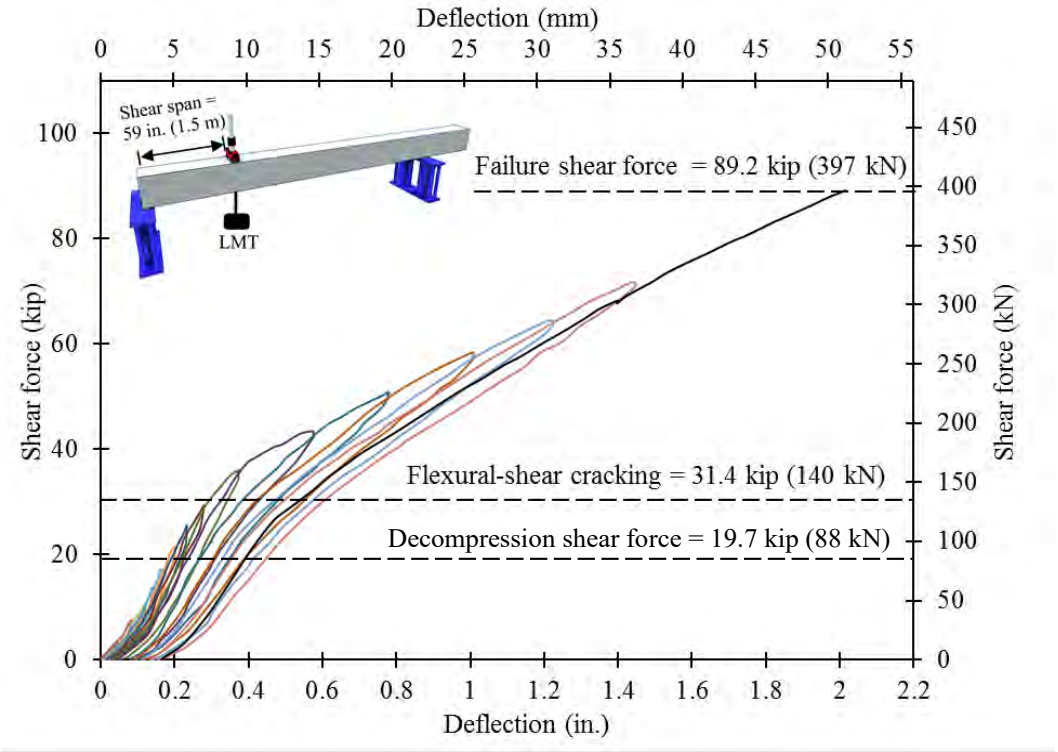

Figure 7.4-36 Shear force vs under-load-deflection in Beam S-C for all load cycles

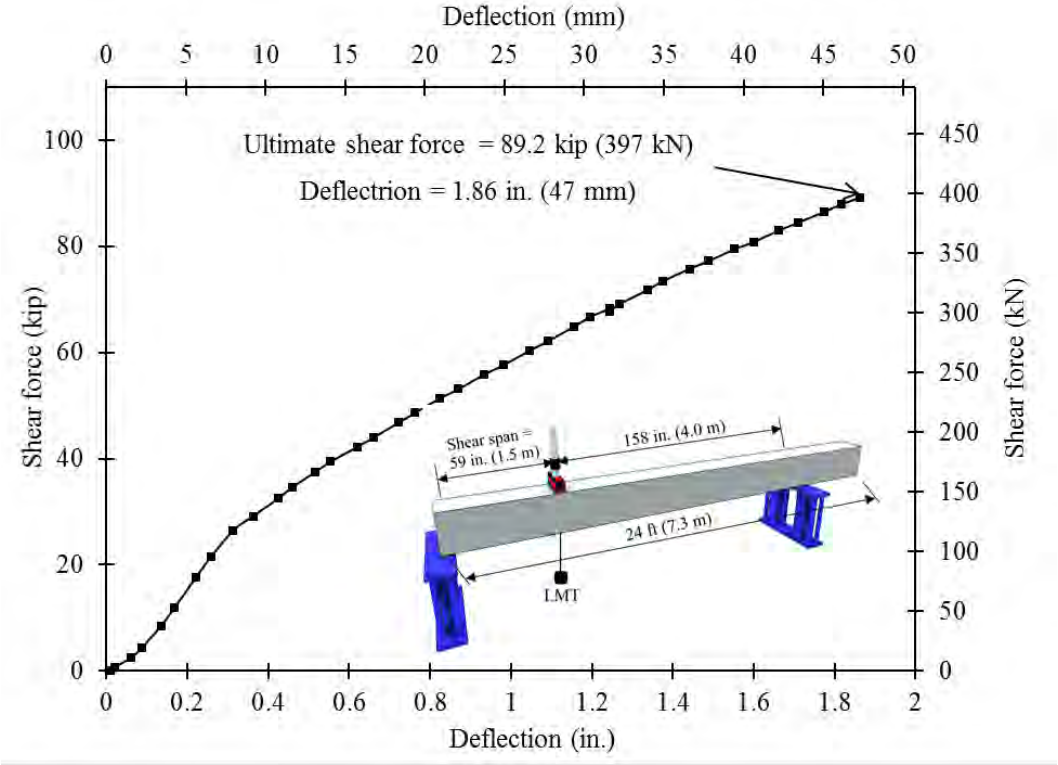

Figure 7.4-37 Shear force vs under-load-deflection in Beam S-C for last load cycle

7.4.3.6 Beam (S-10.75)

Beam S-10.75 was a beam end provided with lap spliced steel stirrups with a splice length of 10.75 in. (273 mm). The first observed flexure-shear crack developed at a shear force of 32.5 kip (145 kN). In addition, a decompression shear force of 21.8 kip (97 kN) was observed during post-cracking load cycles. With further increase in the load, the flexure cracks extended diagonally through the web without any noticeable web shear crack, as shown in Figure 7.4-38. A sudden failure took place when the shear force approached 99.3 kip (442 kN). Failure took place through crushing and shearing of the concrete in the compression flange as shown in Figure 7.4-39. The shear force-deflection response for all load cycles is shown in Figure 7.4-40, while the shear force-deflection curve for the last load cycle is shown in Figure 7.4-41. The deflection under the loading point at failure was around 2.14 in. (54 mm). No rupture of the steel stirrups was observed at failure. Also, none of the stirrups pulled out of the concrete in the region where the inclined crack crossed the lap splice. There was no rupture or debonding of the longitudinal CFCC prestressing strands.

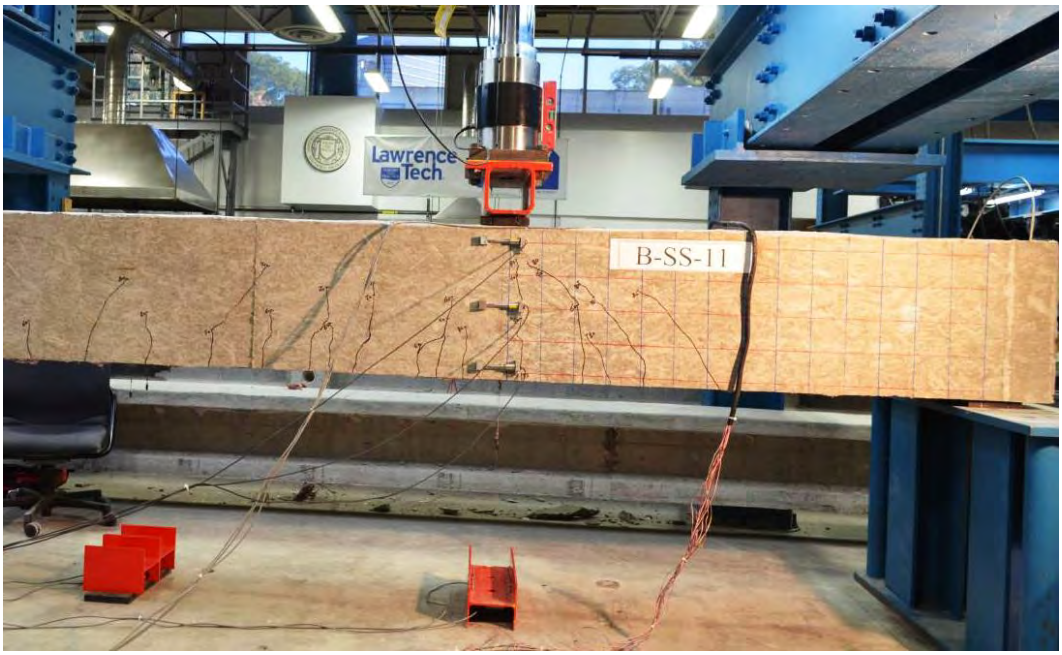

Figure 7.4-38 Crack pattern of beam S-10.75

a) Front side

b) Back side

Figure 7.4-39 Failure of beam S-10.75

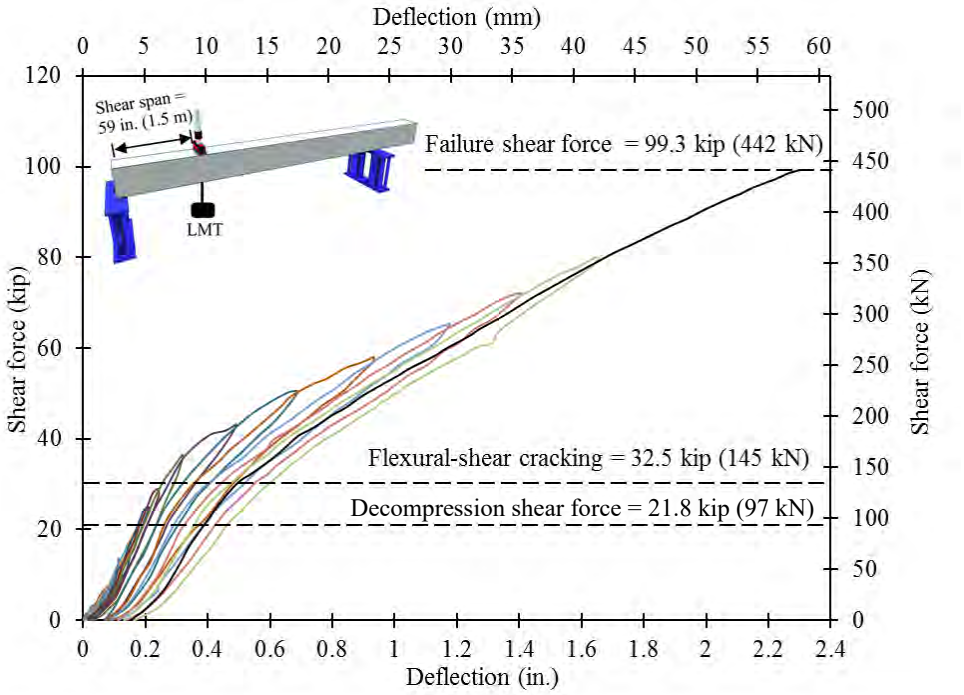

Figure 7.4-40 Shear force vs under-load-deflection in Beam S-10.75 for all load cycles

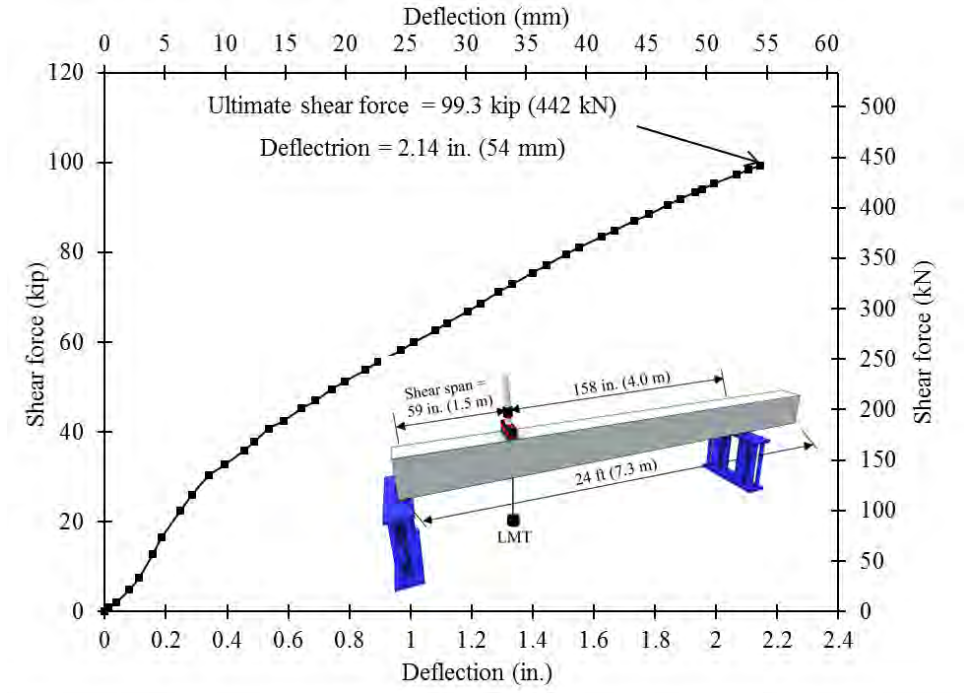

Figure 7.4-41 Shear force vs under-load-deflection in Beam S-10.75 for last load cycle

7.4.3.7 Beam (S-7)

Beam S-7 was a beam end provided with lap spliced steel stirrups with a splice length of 7 in. (178 mm). The first observed flexure-shear crack developed at a shear force of 30.2 kip (134 kN). In addition, a decompression shear force of 20.1 kip (89 kN) was observed in the post-cracking load cycles. At an average shear force of 51 kip (227 kN), the first web shear crack initiated, while the existing flexural cracks propagated towards the point of loading, as shown in Figure 7.4-42. A sudden failure took place when the shear force approached 84.8 kip (377 kN). Failure took place through a pullout of the overlapped steel stirrups followed by a shear failure of the concrete at the major crack as shown in Figure 7.4-43. The shear force-deflection response for all load cycles is shown in Figure 7.4-44, while the shear force-deflection curve for last load cycle is shown in Figure 7.4-45. The deflection under the loading point at failure was around 1.53 in. (39 mm). No rupture of the steel stirrups was observed at failure. No rupture or debonding of the longitudinal CFCC prestressing strands was observed.

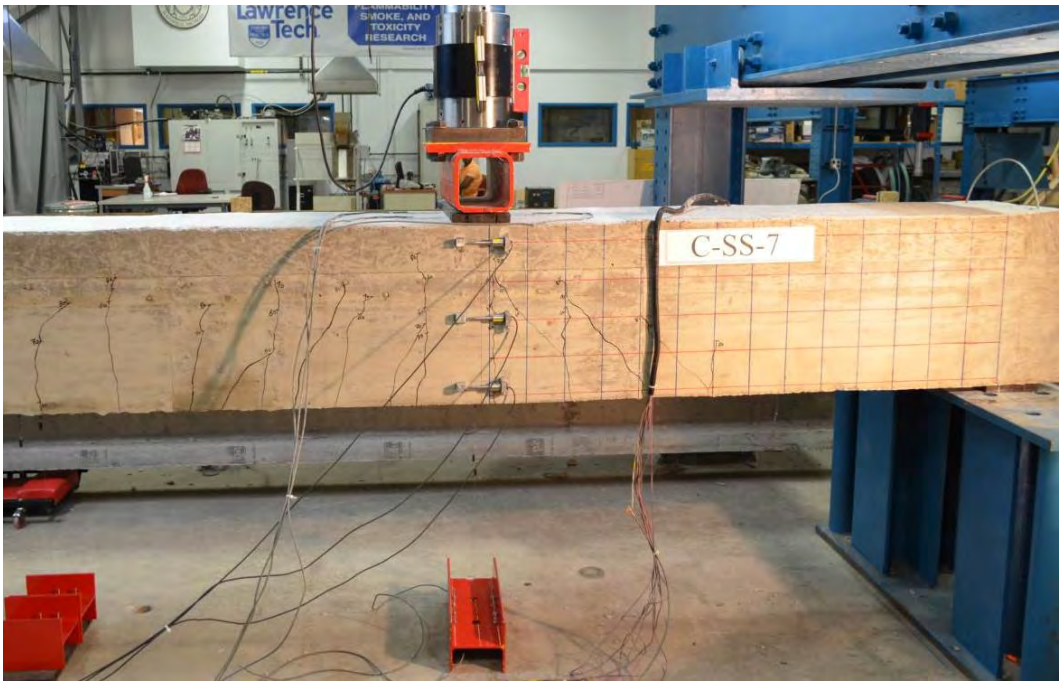

Figure 7.4-42 Crack pattern of beam S-7

a) Front side

b) Back side

c) Slippage of the 7 in. (178 mm) spliced stirrups

Figure 7.4-43 Failure of beam S-7

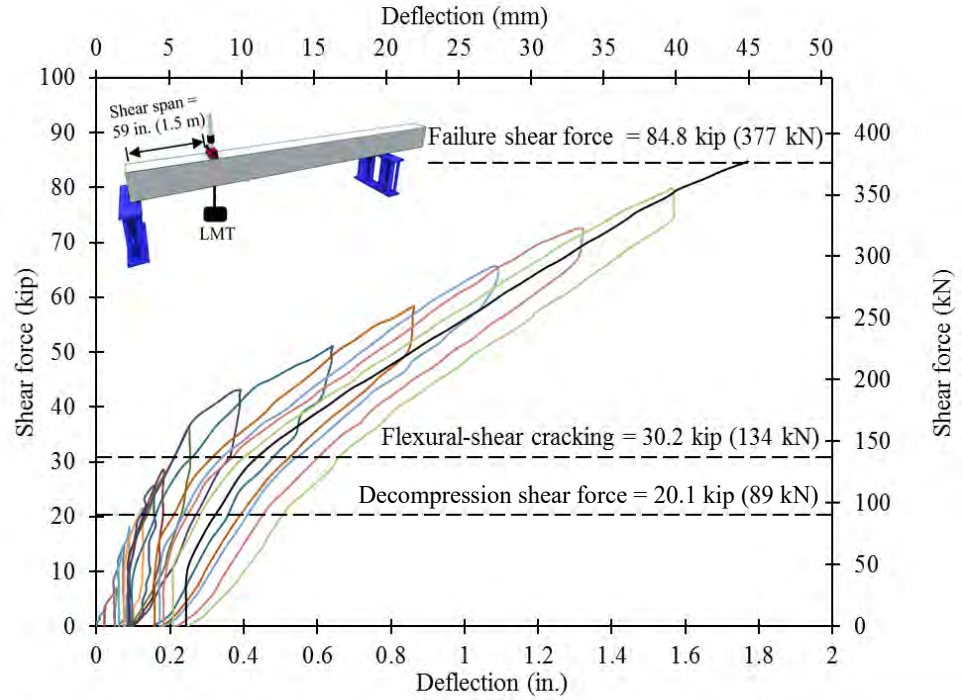

Figure 7.4-44 Shear force vs under-load-deflection in Beam S-7 for all load cycles

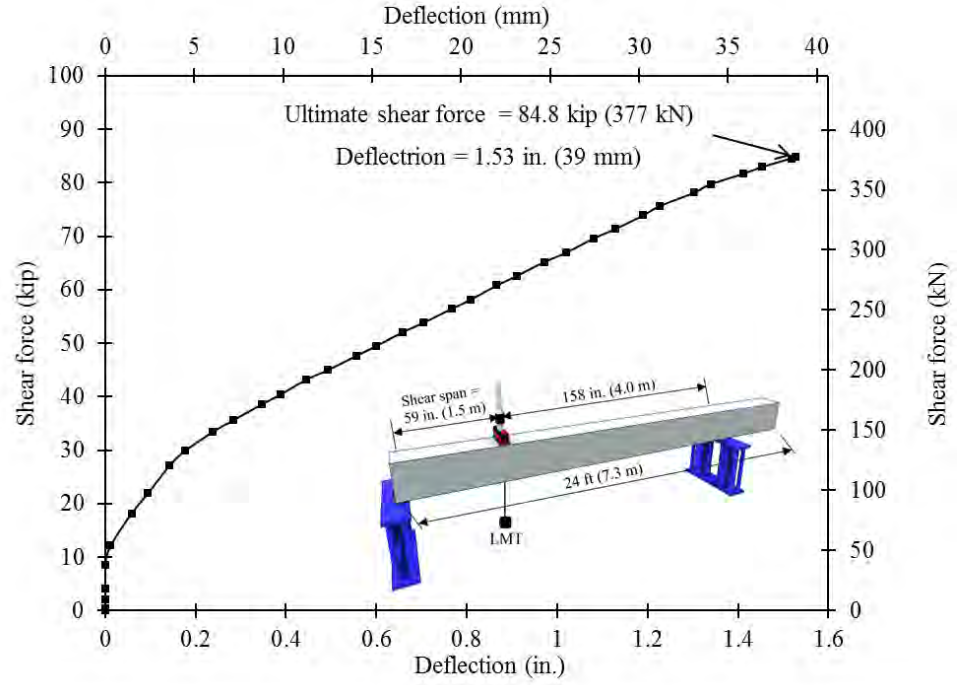

Figure 7.4-45 Shear force vs under-load-deflection in Beam S-C for last load cycle

7.4.3.8 Beam (S-4)

Beam S-4 is a beam end provided with lap spliced steel stirrups with a splice length of 4 in. (102 mm). The first observed flexure-shear crack developed at a shear force of 32.1 kip (143 kN). I addition, a decompression shear force of 19.7 kip (9 kN) was observed in the post-cracking load cycles. At a shear force level of 36.4 kip (162 kN), two web shear crack initiated, while the existing flexure cracks propagated towards the point of loading, as shown in Figure 7.4-46. Sudden failure took place when the shear force approached 72.3 kip (322 kN). Failure took place through a pullout of the overlapped steel stirrups as shown in Figure 7.4-47. The shear force-deflection response for all load cycles is shown in Figure 7.4-48, while the shear force-deflection curve during last load cycle is shown in Figure 7.4-49. The deflection under the loading point at failure was around 1.43 in. (36 mm). No rupture of the steel stirrups was observed at ultimate failure. However, all the spliced stirrups pulled out of the concrete in the region where the inclined web crack crossed the lapped splice. There was no rupture or debonding of the longitudinal CFCC prestressing strands.

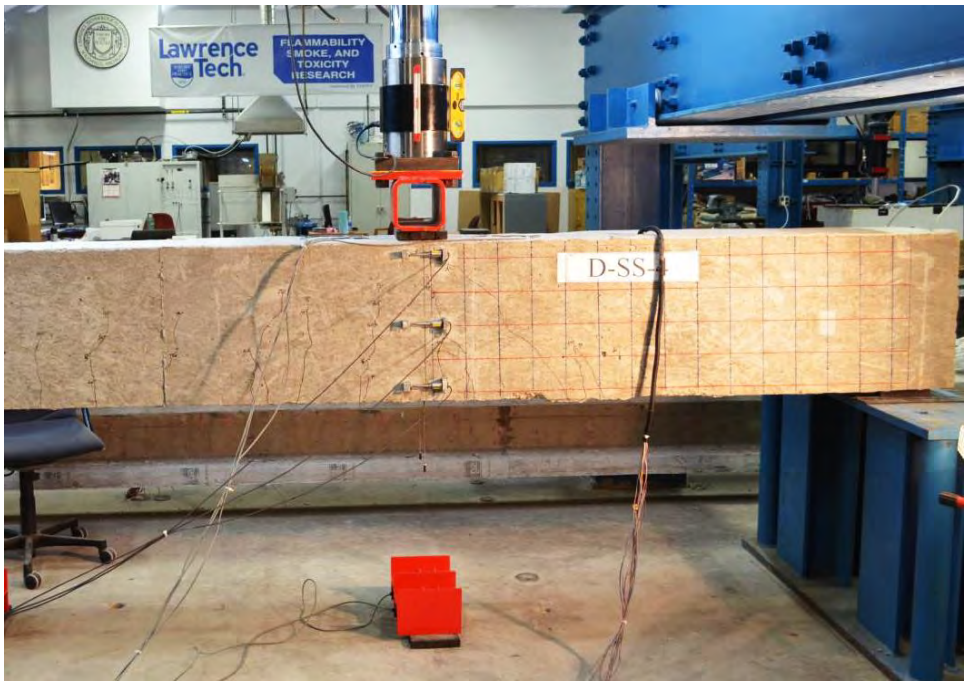

Figure 7.4-46 Crack pattern of beam S-4

a) Front side

b) Back side

c) Slippage of the 4 in. (102 mm) spliced stirrups

Figure 7.4-47 Failure of beam S-4

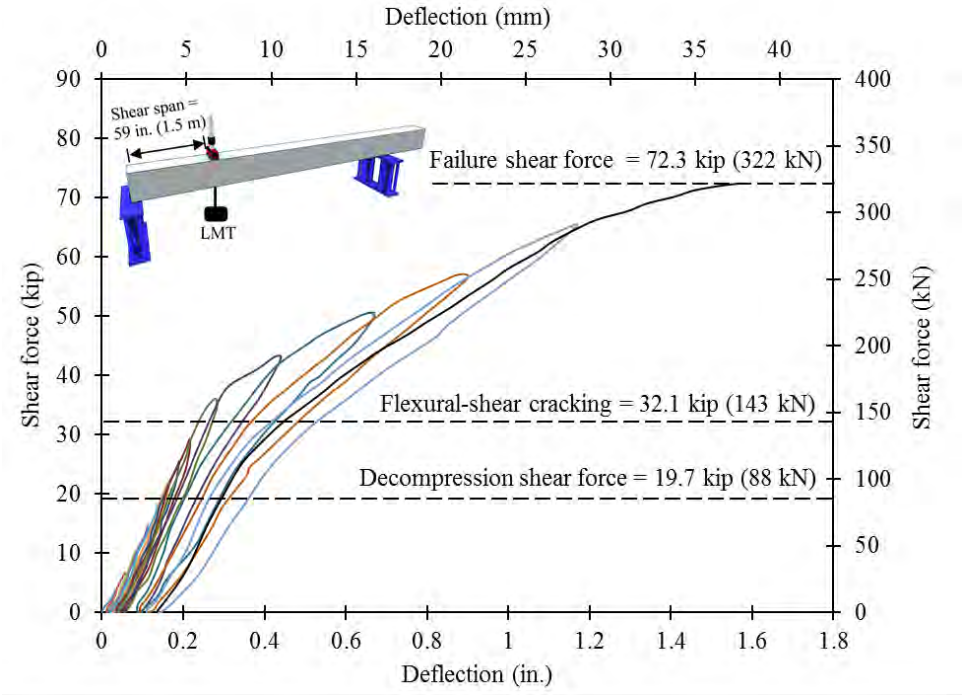

Figure 7.4-48 Shear force vs under-load-deflection in Beam S-4 for all load cycles

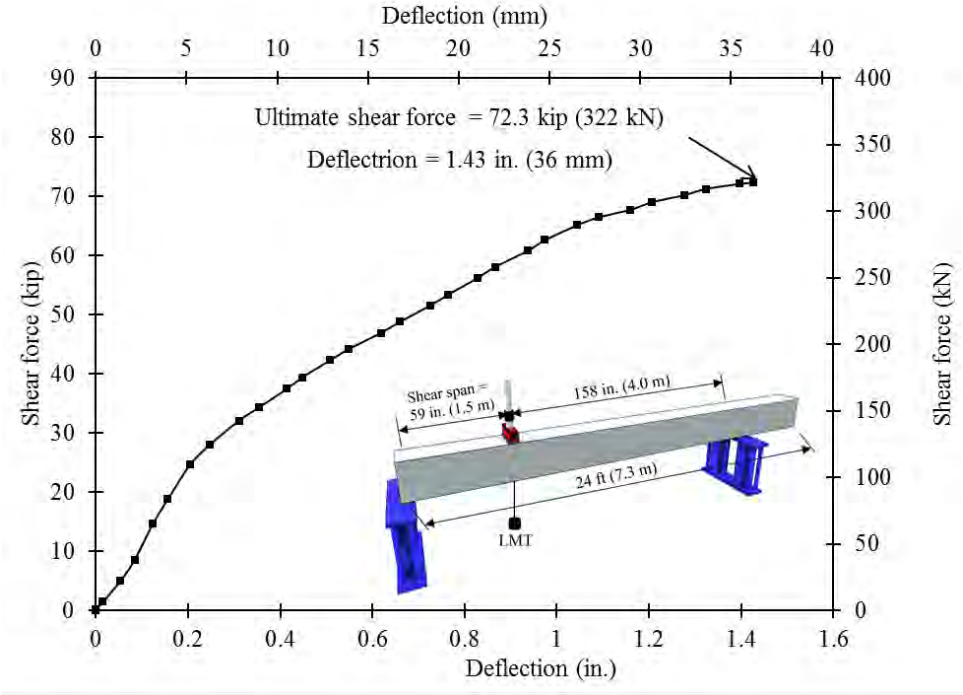

Figure 7.4-49 Shear force vs under-load-deflection in Beam S-C for last load cycle

7.4.4 Discussion of test results

The failure mode of box beams was influenced by the flexure-shear effect at the shear span and the bond between the spliced stirrups and the surrounding concrete. The control beams C-C, S-C exhibited a flexure failure due to crushing of the top concrete in the compression flange upon reaching a top concrete strain at failure of -2663 με and -2305 με, respectively. Shear mode of failure was observed in beams C-10.75, and S-10.75. Pullout mode of failure was observed in beams C-7, C-4, and S-7, S-4, reinforced with spliced CFCC and steel stirrups, respectively. Prior failure shear cracks propagated diagonally through the web and was followed by slippage of the spliced stirrups, which was distinguished by loud intermittent sounds. Ultimately, a complete failure occurred and characterized by sudden drop in the recorded shear force. This was confirmed from the inspection of the failed portion. Summary of test results is shown in Table 7.4-2.

As shown in the Table, a full-length splice was as efficient in transferring the shear force as the closed stirrups. Besides, a splice of 4 in. (102 mm) in the CFCC or steel stirrups was sufficient to transfer approximately 66 % or 82 % of the shear force transfer by a closed stirrup, respectively.

Overall, it appears that sections with CFCC stirrups achieved slightly less shear carrying capacity than those with steel stirrups. This is understood in the light of the lower elastic modulus of CFCC compared to steel. A lower elastic modulus allowed for wider shear cracks and thereby a reduction in the aggregate interlock.

Table 7.4-2 Summary of test results of the shear bond test

ID	Decomp. shear force. kip (kN)	Cracking shear force V_{cr} kip (kN)	Ultimate shear force V_u kip (kN)	Maximum deflection under load δ_u in. (mm)	Top concrete strain ε_{cu} ($\mu\varepsilon$)	Maximum stirrups strain $\varepsilon_{stirrup}$ ($\mu\varepsilon$)	Mode of failure
C-C	19.5 (86.7)	32.7 (145.5)	96.0 (427.0)	1.92 (48.8)	-2663	2143	Crushing
C-10.75	19.7 (87.6)	32.3 (143.7)	93.5 (415.9)	1.84 (46.7)	-2770	1563	Shear
C-7	18.6 (82.7)	30.5 (135.7)	69.2 (307.8)	1.14 (49.0)	-1868	1186	Pullout
C-4	20.8 (92.5)	32.8 (145.9)	63.6 (282.9)	0.96 (24.4)	-1801	1444	Pullout
S-C	19.7 (87.6)	31.4 (139.7)	89.2 (396.8)	1.86 (47.2)	-2305	2237	Crushing
S-10.75	21.8 (97.0)	32.5 (144.6)	99.3 (441.7)	2.14 (54.5)	-3273	1272	Shear
S-7	20.1 (89.4)	30.2 (134.3)	84.8 (377.2)	1.53 (38.9)	-2410	3076	Pullout
S-4	19.7 (87.6)	32.1 (142.8)	72.3 (321.6)	1.43 (36.3)	-2386	2933	Pullout

CHAPTER 8: LONG-TERM PERFORMANCE OF BEAMS WITH CFRP

8.1 Introduction

After construction, bridge beams prestressed with CFRP strands are exposed to harsh weather along with traffic loads. The lifespan of the bridge and future rehabilitation work depend on the resistance of the CFRP materials to different environmental conditions. Some of Michigan earlier bridges with CFRP reinforcement are currently under continuous monitoring (Grace et al. 2005 and 2002b) and different studies were conducted on the lifecycle cost analysis of bridge beams considering the environmental effect (Grace et al. 2012b).

In order to evaluate the effect of temperature and environmental conditions on the prestress loss in CFRP pretensioned beams, five 26-ft. (7.92-m) long deck bulb T-beams were designed, constructed, and subjected to harsh Michigan weather for extended time before they were tested under four-point-load flexural test setup to failure. Each beam was prestressed initially to 88 kip (391 kN) and designed to fail in a balanced-failure mode (balanced reinforced section). Out of the five beams, one beam served as a control beam and was tested to failure after 28 days of construction. The remaining four beams were split into two groups: two indoor and two outdoor beams. The two indoor beams were kept indoors in a controlled laboratory environment, while the two outdoor beams were kept outdoors, where they were subjected to different environmental conditions such as seasonal temperature change, rain, and freezing rain. After one year, one indoor beam and one outdoor beam were brought to the testing facility and were instrumented and tested to failure in a load setup similar to that used in testing the control beam. After two years of construction, the remaining two beams were also instrumented and tested to failure under the same load setup.

Cracking loads, decompression loads, maximum concrete and CFRP strains, maximum loads, and corresponding maximum deflections were collected compared among the five beams. In addition, an estimate for prestress loss was calculated for each beam based on the test results. The prestress loss calculations took into account the creep and shrinkage of concrete that were evaluated experimentally for the concrete batch by testing concrete prisms and cylinders according to current ASTM standards. The best estimates for concrete creep and shrinkage were determined and compared to their mathematically determined values according to current codes and guidelines

such as AASHTO LRFD and PCI. Test details and results are provided in this Chapter. The test results showed that except for a slight change in concrete strength, there was no significant difference in the test results among the five beams. In addition, short and long-term prestress loss can be reasonably estimated using current design guidelines established for steel strands except for prestress relaxation, which is determined based on properties of CFRP strands.

8.2 Decked Bulb T beams

8.2.1 Test setup

Five decked bulb T-beams were tested under four-point flexural loading to determine their overall performance and the prestress losses with respect to age and exposure conditions. The nomenclature for the beams were; C, I-1, O-1, I-2, and O-2 representing control, 1 year indoor, 1 year outdoor, 2 years indoor, and 2 years outdoor beams, respectively. Figure 8.2-1 and Figure 8.2-2 show the longitudinal and cross sections of the decked bulb T-beams.

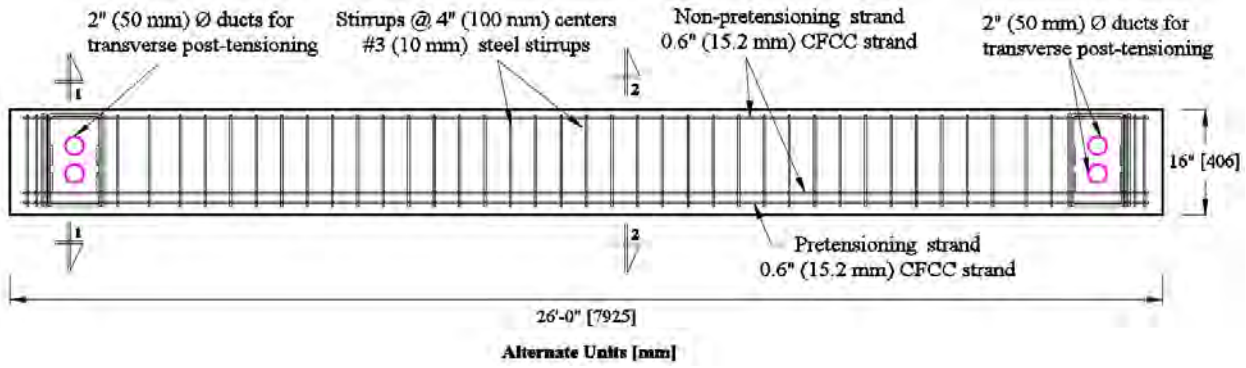

Figure 8.2-1 Longitudinal section of prestressed decked bulb T beam

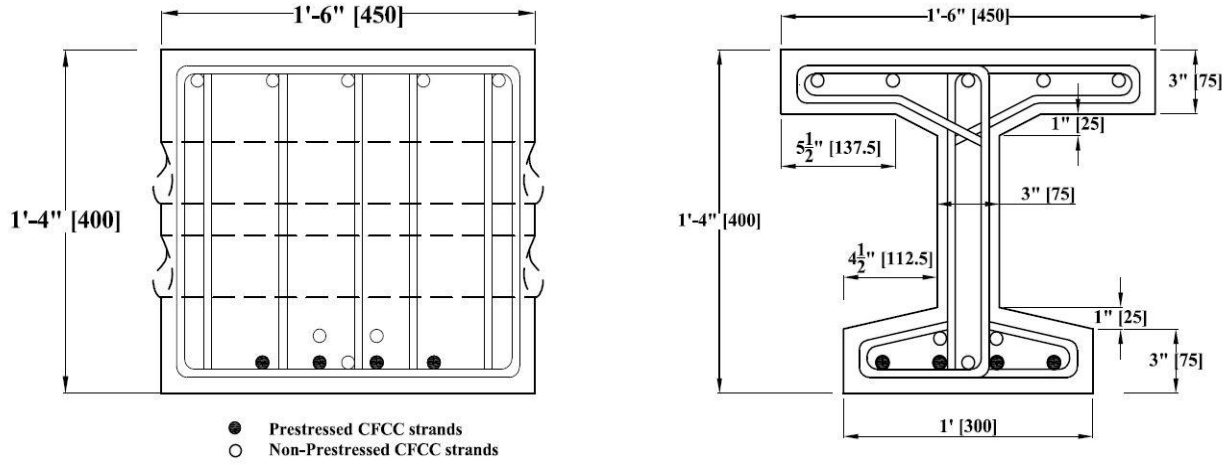

Figure 8.2-2 Details of cross section 1-1 (left) & 2-2 (right) of the beam specimen

The beams were reinforced with 4 prestressed and 3 non-prestressed 0.6 in. (15.2 mm) CFCC strands. Five similar non-prestressed strands were provided in the compression zone as a top reinforcement. The shear reinforcement in the beams consisted of 0.375 in. (10 mm) diameter Grade 60 deformed steel stirrups with three configurations as shown in Figure 8.2-3 and Figure 8.2-4 for the stirrups at the ends and middle of span respectively. The material properties for the shear reinforcement are summarized in Table 8.2-1. In addition, Two 3 in. (75 mm) diameter PVC pipes were installed in the end blocks to serve as conduits for typical post-tensioning as shown in Figure 8.2-5. The conduits were not used in this study since beams were tested individually.

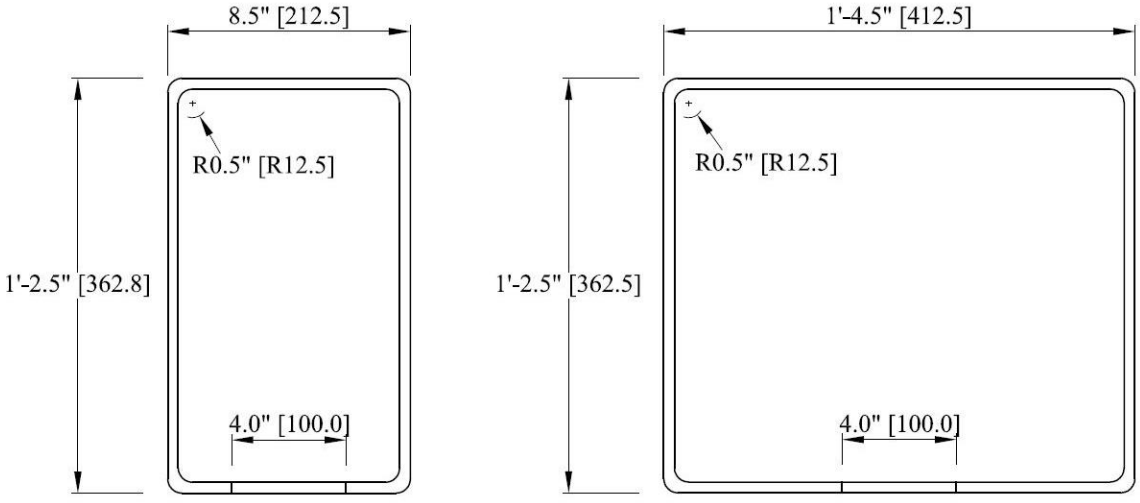

Figure 8.2-3 Steel shear reinforcement for end blocks

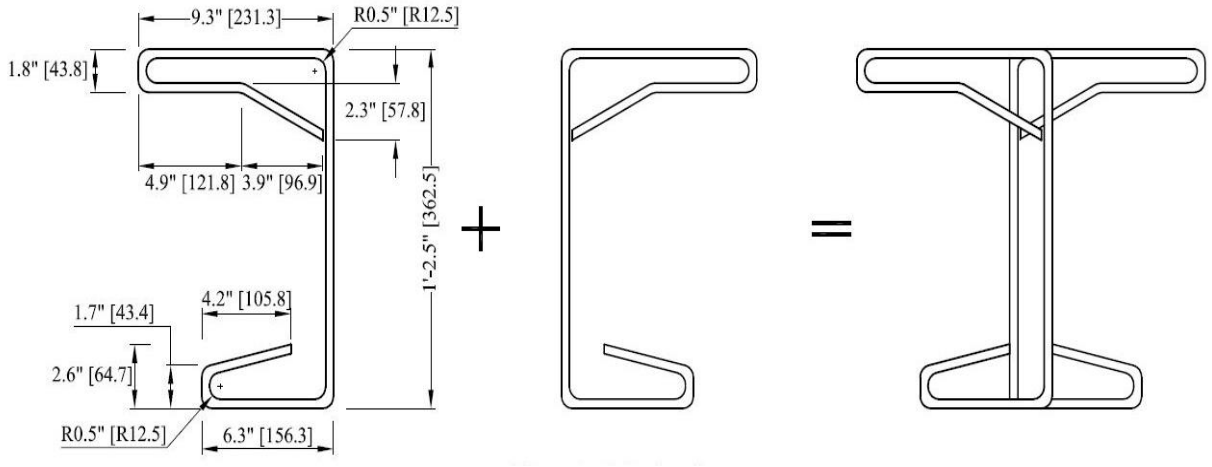

Figure 8.2-4 Steel shear reinforcement between end blocks

Table 8.2-1 Properties of steel shear reinforcement

Designation	# 3
Grade	60
Diameter, in. (mm)	0.375 (10)
Weight, lb/ft (N/m)	0.38 (5.64)
Cross-sectional area, in² (mm²)	0.11 (71)
Yield load, kip (kN)	6.6 (29.4)
Min. yield strength, ksi (MPa)	60 (414)
Breaking strength, kip (kN)	9.9 (44)
Min. tensile strength, ksi (MPa)	90 (621)
Modulus of elasticity, ksi (GPa)	29,000 (200)

Figure 8.2-5 Installing PVC conduits in the end block of the beams

The formwork consisted of the deck, center wall, side walls, and end plates. Wood was the major construction material for these groups with the exception of the side walls, which were made of a combination of wood and Styrofoam. The wooden deck (as shown in Figure 8.2-6) had a length of 52 ft (15.85 m) and a width of 4 ft (1.2 m). It was mounted on steel adjustable chairs spaced at 2 ft (0.6 m) on center, in rows of 2 along its length. Styrofoam with different thickness were cut to certain lengths and angles pertinent to the dimensions of the beam. The sheets were glued together and screwed to the wooden side and center walls (Figure 8.2-6 through Figure 8.2-8). All formwork in contact with concrete were smeared with oil to waterproof the surface and ensure easy deforming. To improve the stiffness of the formwork, a series of braces (wood and steel threaded rods) as shown in were used.

Figure 8.2-6 Wooden deck supported on adjustable steel chairs and center wall spanning between steel bulk heads

Figure 8.2-7 Leveling the platform using a laser level

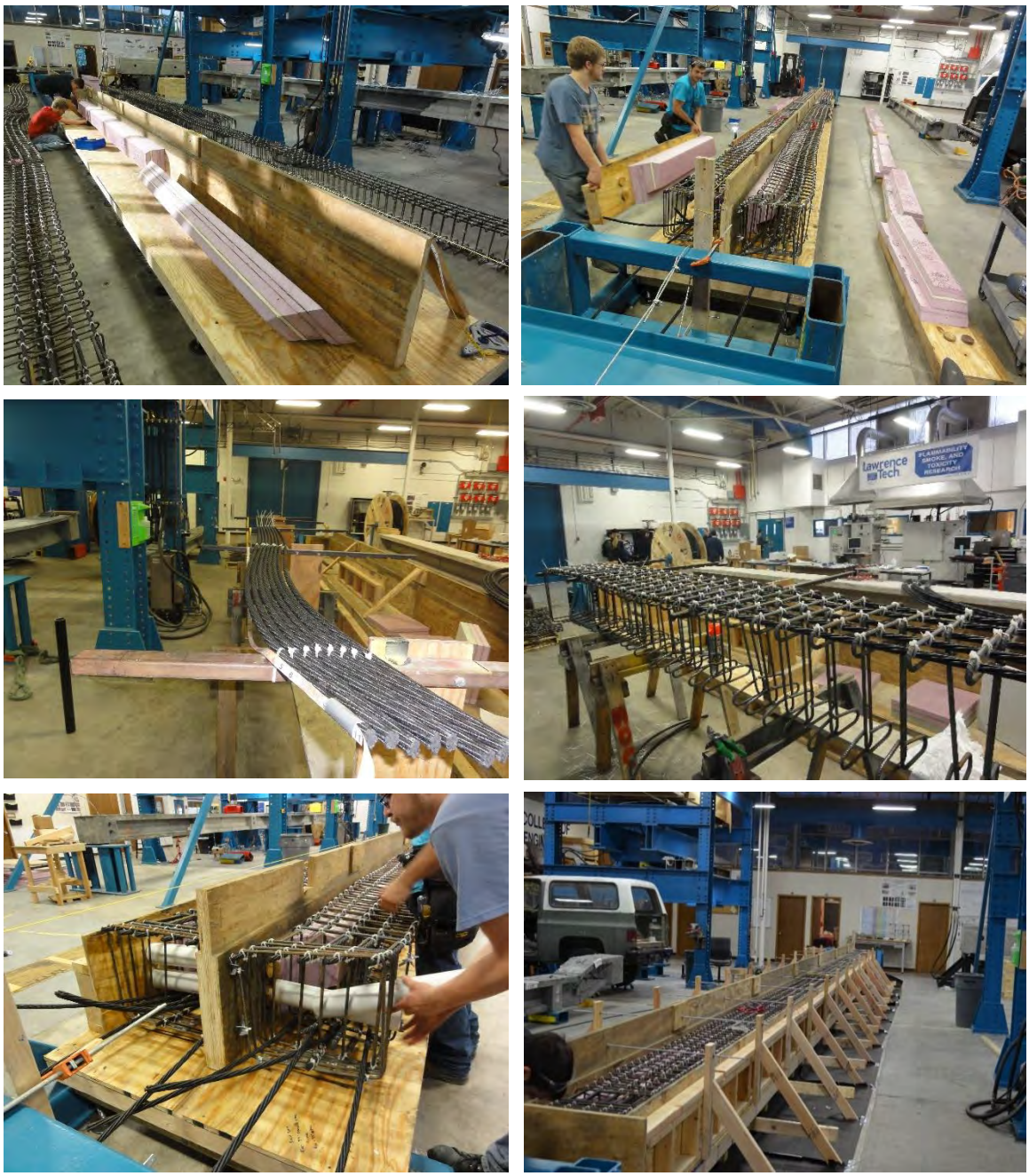

Figure 8.2-8 Different stages of formwork and cage construction

The reinforcement cage consisted of the flexural and shear reinforcements arranged. The process of construction of the reinforcement cage started by placing the compression reinforcement on stands and marking the positions of stirrups. The stirrups were placed in position and fastened with plastic ties. All other layers of non-prestressed reinforcement were passed through the stirrups and fastened into position. The cage was removed from the frame and placed on the deck and the

prestressing reinforcement spanning the full length of the deck were passed through as shown in Figure 8.2-9 . Plastic chairs with a height of ¾ in. (19 mm) were installed on sides of the stirrups and the bottom longitudinal reinforcement to provide side and bottom cover respectively.

As shown in Figure 8.2-10, the formwork accommodated two beams side by side. Each beam was prestressed with four CFCC strands with a jacking force of 24 kip (106.75 kN) per strand. Prestressing was applied through two abutment-type steel bulk heads positioned at the ends of the deck. The CFCC prestressing strands were coupled with steel strands at the live and dead ends to facilitate anchorage (Figure 8.2-11). Threaded rods and nuts served as anchorage on the dead-end bulkhead. In-line load cells were installed at the dead ends on all eight prestressed strands. In addition, strain gages were attached to prestressed CFCC strands near the mid-span section (Figure 8.2-12).

Concrete with a design 28-day compressive strength of 7000 psi (48 MPa) and a slump of 8.0 in. (200 mm) was ordered and supplied. During placement, 6 in. × 12 in. (150 mm × 300 mm) concrete cylinders were prepared and cured under the same conditions as the beams, and were tested at ages 7, 14, 21, 28 days, 1 year, and 2 years to record the development of the compressive strength in accordance with ASTM C39/C39M-12: “Test Method for Compressive of Cylindrical Concrete Specimens”. Before placement, a slump test (Figure 8.2-13) was conducted and the slump was approximately 10 in. (254 mm).

Figure 8.2-9 Bottom prestressing installation

Figure 8.2-10 Layout and prestressing CFCC strands

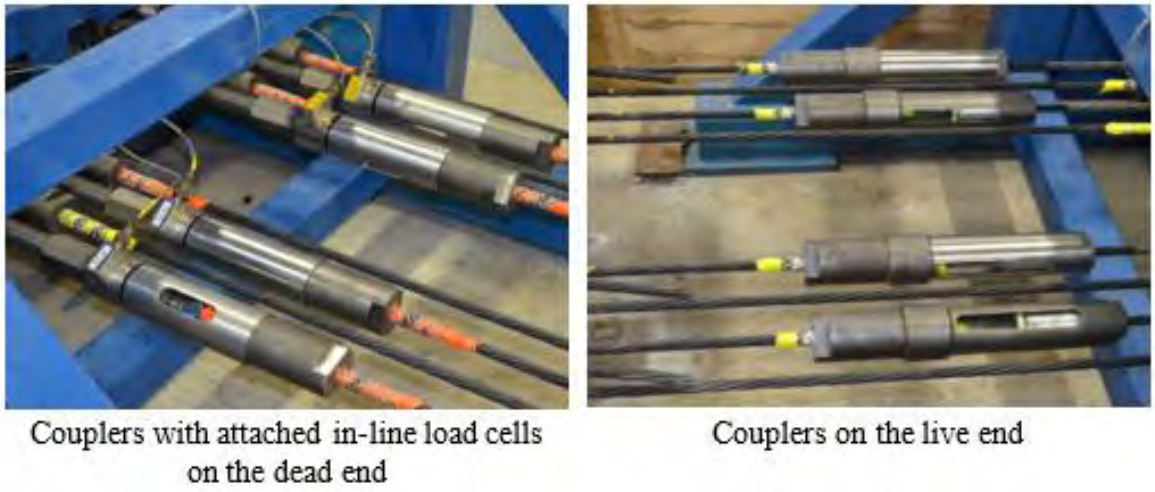

Couplers with attached in-line load cells on the dead end

Couplers on the live end

Figure 8.2-11 Coupler connections

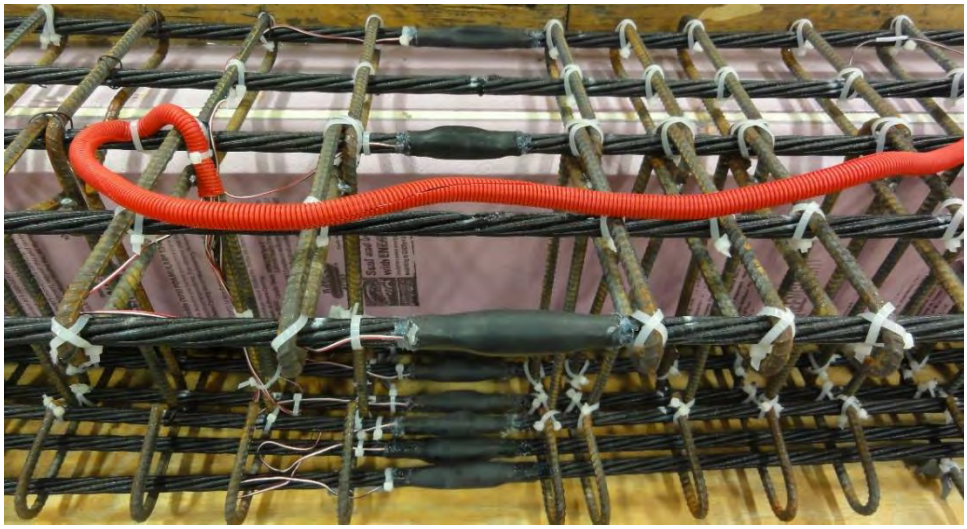

Figure 8.2-12 Installed strain gages on longitudinal reinforcement

Figure 8.2-13 Slump test

Concrete was placed manually in the formwork and was compacted using electric pencil vibrators. Care was taken during vibration to avoid damaging the installed internal strain gages. Figure 8.2-14 shows the stages of casting. After concrete placement, the specimens were covered with burlaps and moist cured for 7 days.

To record the core temperature of the decked bulb T-beams during curing, K-type thermocouple wires with a range of -325 to +750 ºF (-200 to +400 ºC) were embedded in the top and bottom flanges, and mid-web section at mid-span of the beams. Readings were taking off an OMEGA® HH509R handheld reader.

The sides of the formwork were removed 24 hours after concrete placement. Twenty-one days after casting, prestressing force was transferred to the beams by releasing the steel strands at the live end as shown in Figure 8.2-15 using a torch. As illustrated in Figure 8.2-16 and Figure 8.2-17, a total loss of 2 kip (8.9 kN) was recorded from the time of initial jacking to release. Immediately before prestress release, the prestressing force averaged at 22 kip (98 kN) A camber of 0.25 in. (6.35 mm) was recorded at release. After transfer of prestressing force, the beams were transferred to storage.

Figure 8.2-14 Placing and curing the concrete of the beams and cylinders

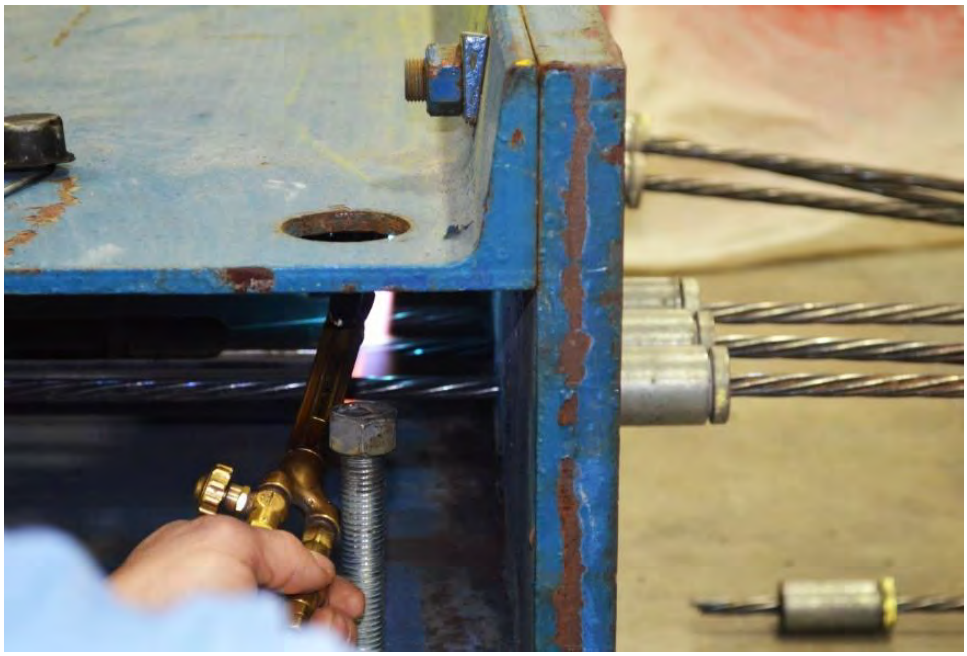

Figure 8.2-15 Release of steel strands at transfer

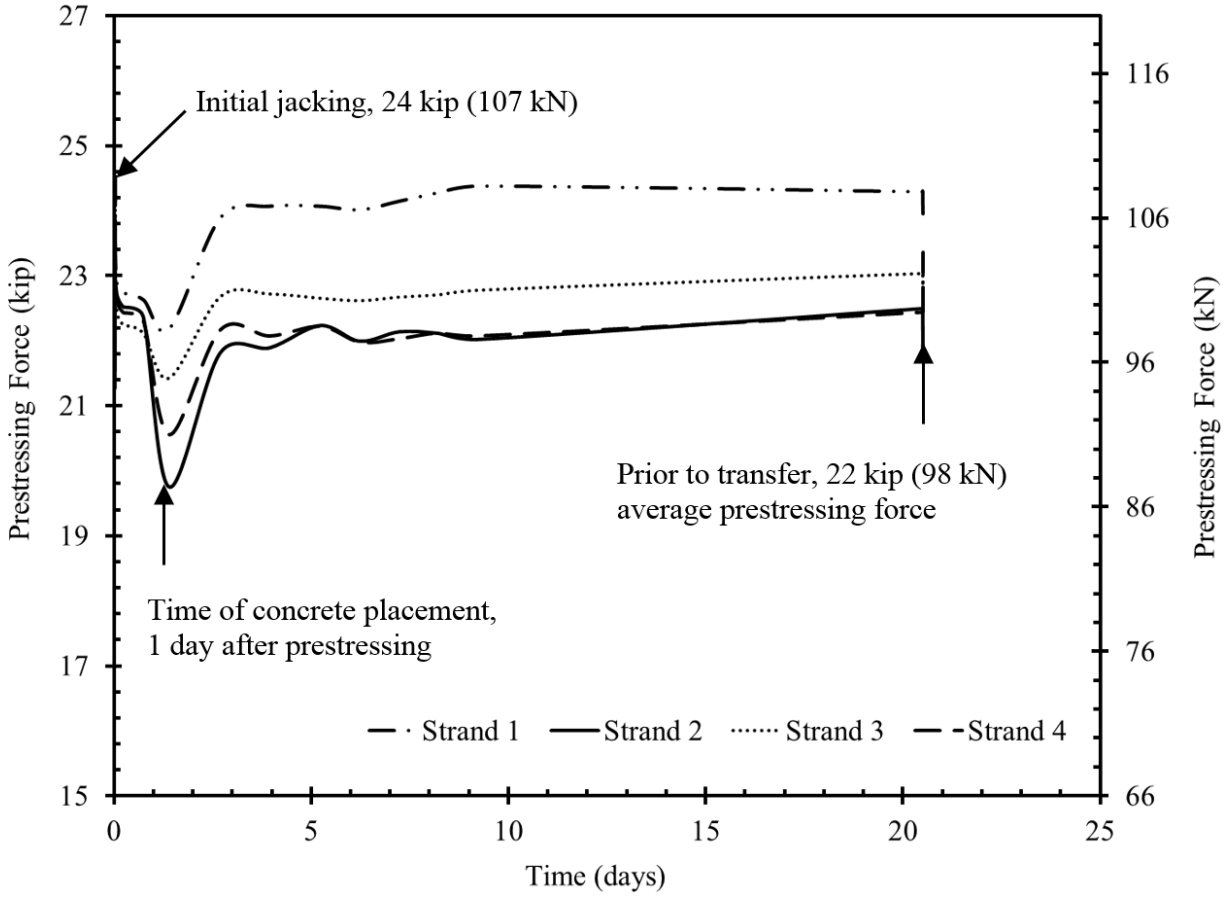

Figure 8.2-16 Prestress loss prior to transfer (Strand 1-4)

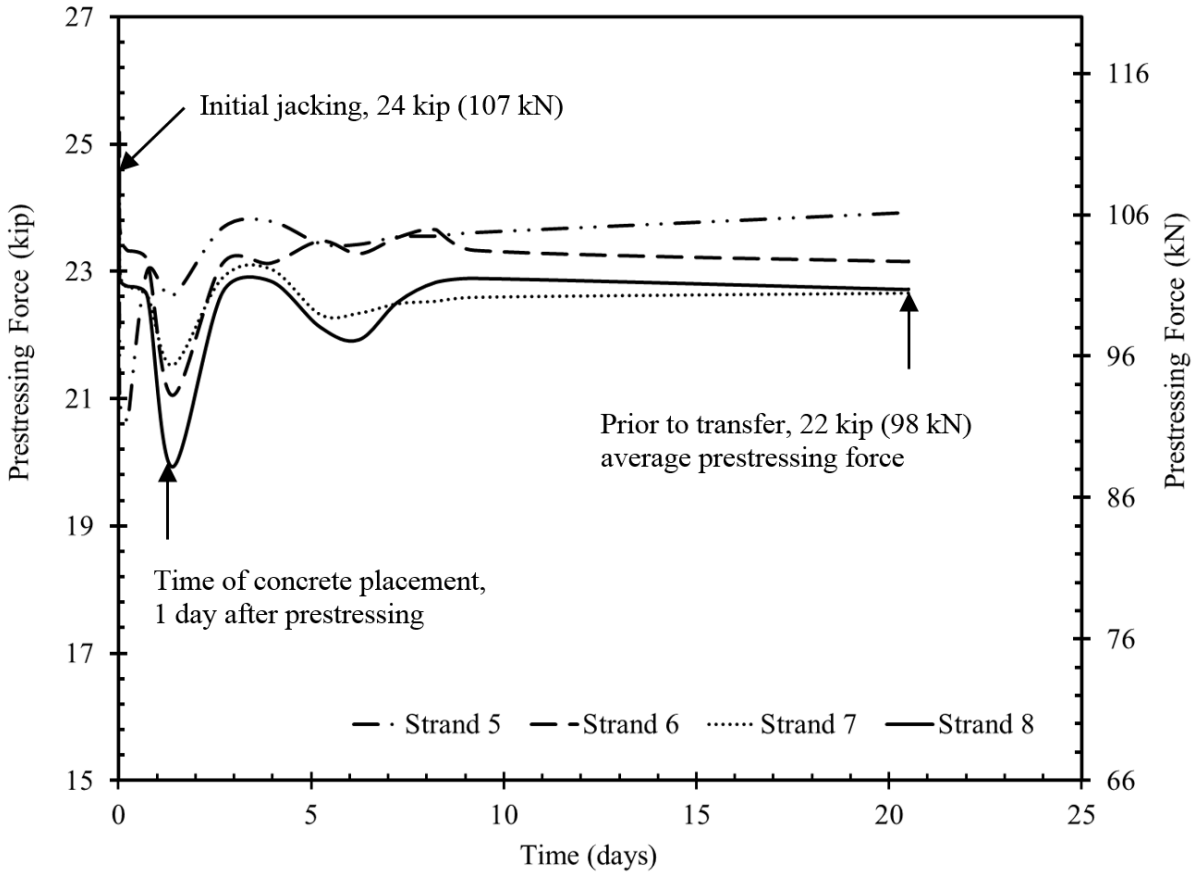

Figure 8.2-17 Prestress loss prior to transfer (Strand 5-8)

Geokon Model 4000 vibrating-wire strain gages (VWSG) (Figure 8.2-18 and Figure 8.2-19) were installed on the sides (top and bottom flanges, and web) of the beams at the mid-span to monitor the strain of the decked bulb T beams during their storage period. This type of strain gage has a temperature and working range of -4 to +176 ºF (-20 to +80 ºC) and ±1000 to ±4000 με respectively. It provides a temperature reading in tandem with strains.

LVDTs and electric strain gages were attached to the compression flange of the decked bulb T-beams at the time of testing to monitor and capture the strain under load cycles. In addition, displacements at mid-span of the decked bulb T beams were measured with LMT as shown in Figure 8.2-20. All sensors were connected to a data acquisition system except Geokon sensors that had a different data acquisition system that recorded the strain readings and temperature.

Figure 8.2-18 Smoothing the surface before installing strain gages

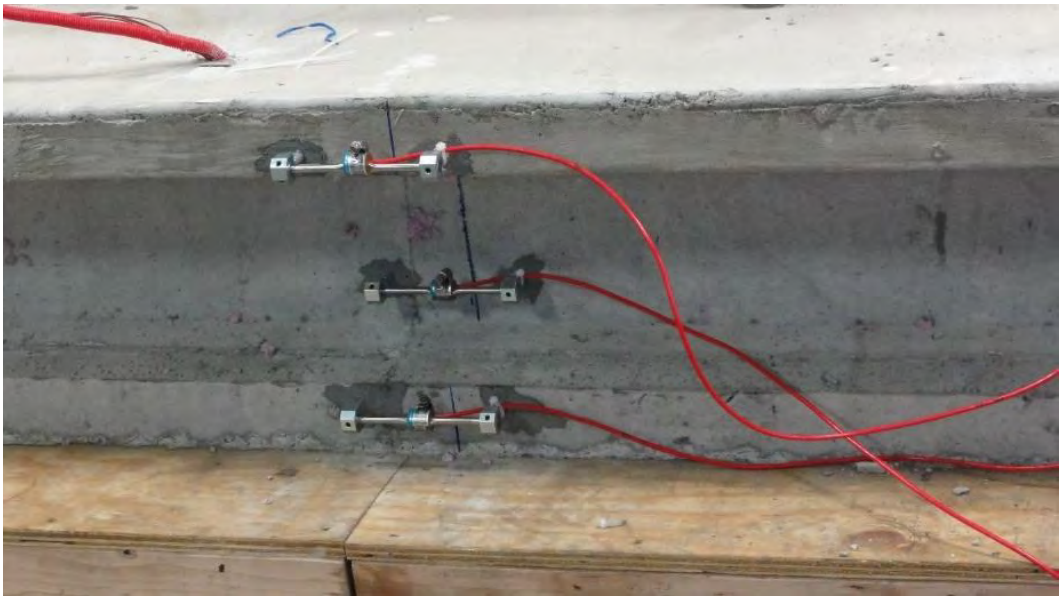

Figure 8.2-19 Installed VWSG on beams before prestress transfer

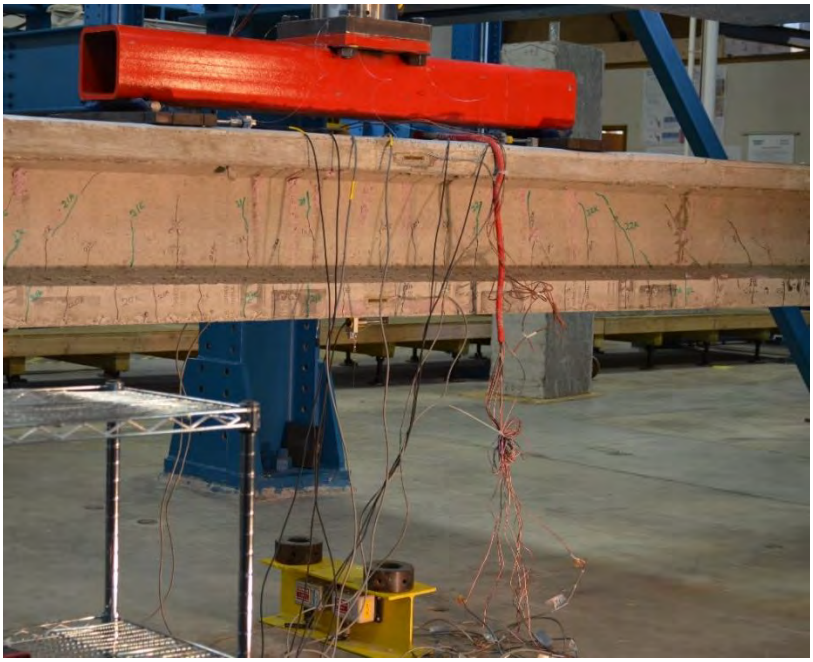

Figure 8.2-20 Instrumentation of decked bulb T beams at mid-span

The control beam was moved to the loading facility at age of 28 days, while other beams were stored either indoors or outdoors as shown in Figure 8.2-21 and Figure 8.2-22. A typical beam loading test setup is as shown in Figure 8.2-23. Load from a 220-kip (979-kN) capacity electronically controlled actuator was applied to the beams through a 4 ft (1.2 m) HSS spreader at mid-span. Load was applied through displacement-control mode with a loading rate ranging from 0.05 to 0.15 in./min (1.25 to 3.8 mm/min) for different load cycles. Beams were simply supported over 1.0- in. (25.4-mm) thick steel reinforced elastomeric bearing pads positioned on steel supports. The effective span from center-to-center of supports was 25 ft. (7.62 m). After the development of the first flexural crack, two strain gages were installed on the soffit of the beams at mid-span to confirm the decompression loads at the time of testing.

Figure 8.2-21 Outdoor beams

Figure 8.2-22 Indoor beams

Figure 8.2-23 Test setup of decked bulb T beams

8.2.2 Test results

8.2.2.1 Monitoring of the test beams

Strain measured by the VWSG at the beginning and end of the monitoring period (prior to flexural testing) were extrapolated to the strand level. As shown in Figure 8.2-24, a line of best fit is plotted between the measured strains. The equation of the line of best fit was used to extrapolate the strain at the level of the strand. The change in strain at the strand level was then evaluated. It should be noted that the change in the strain level does not directly represent the prestress loss. For instance, both concrete creep and shrinkage result in negative strain readings. If this negative strain reading is translated to prestress force, it would indicate an increase not a decrease in the prestressing force. On the other hand, relaxation of CFCC strands results in an elongation of the strand that, by itself, leads to positive strain readings in a strain gage attached to the surface of the concrete. Nevertheless, when combining all three (concrete creep, shrinkage, and strand relaxation) together, this results in an equation with three unknowns that can't be solved. Therefore, a direct estimate for the prestress loss from strain readings was not obtained. Rather, the strains due to concrete creep, shrinkage, and strand relaxation were estimated using separate test protocols and the combined strain values were compared with those obtained from the VWSG. In addition, creep and shrinkage strains calculations according to available design guidelines such as AASHTO LRFD and PCI were estimated and compared with the values obtained experimentally and the readings from the VWSG after they were adjusted for temperature effects. The recorded VWSG strains over the monitoring period along with the recorded temperatures are shown in Figure 8.2-25 to Figure 8.2-34.

AASHTO LRFD equations in Section 2.5.3.1 were used to estimate theoretical losses due to elastic shortening, creep, and shrinkage of concrete. Total losses were the sum of the aforementioned losses and results from relaxation tests discussed earlier. Elastic shortening losses were estimated using AASHTO Eqn. C5.9.5.2.3a-1. Approximate estimate of time dependent creep and shrinkage losses (AASHTO Eqn. 5.9.5.3-1) was calculated with relative humidity values of 50% and 70% for indoor and outdoor beams respectively. AASHTO Eqn. 5.9.5.4.2a-1 and 5.9.5.4.2b-1 were used to estimate refined time dependent losses due to creep and shrinkage. Appropriate values of creep coefficient and shrinkage strain from creep and shrinkage tests were also used in the refined estimate equations. In all cases, a one-million-hour CFCC relaxation rate

of 1.92 % was used. Total prestress losses were also estimated using the PCI-Simplified method as specified in the PCI Design Handbook, 7th Edition.

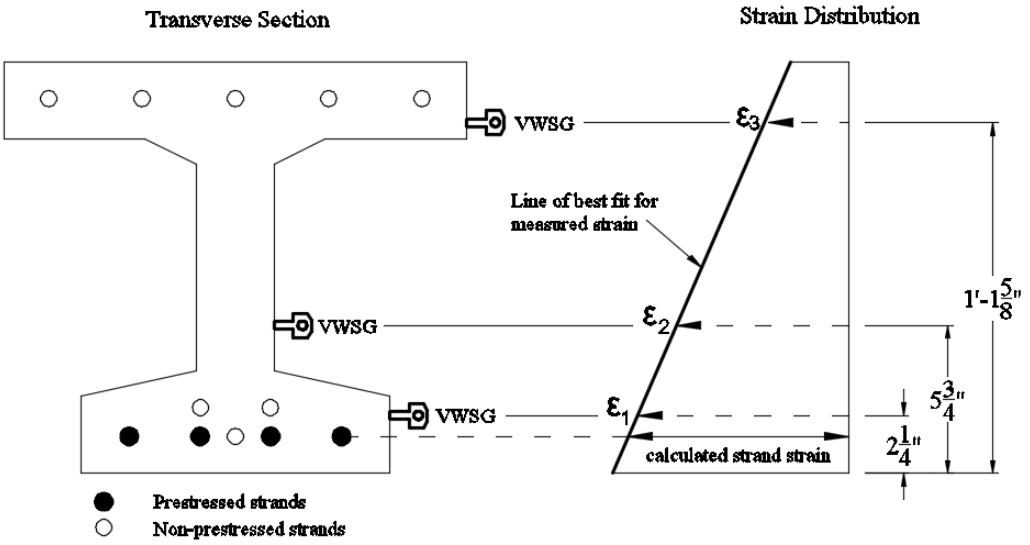

Figure 8.2-24 Line of best fit for VWSG strain measurements

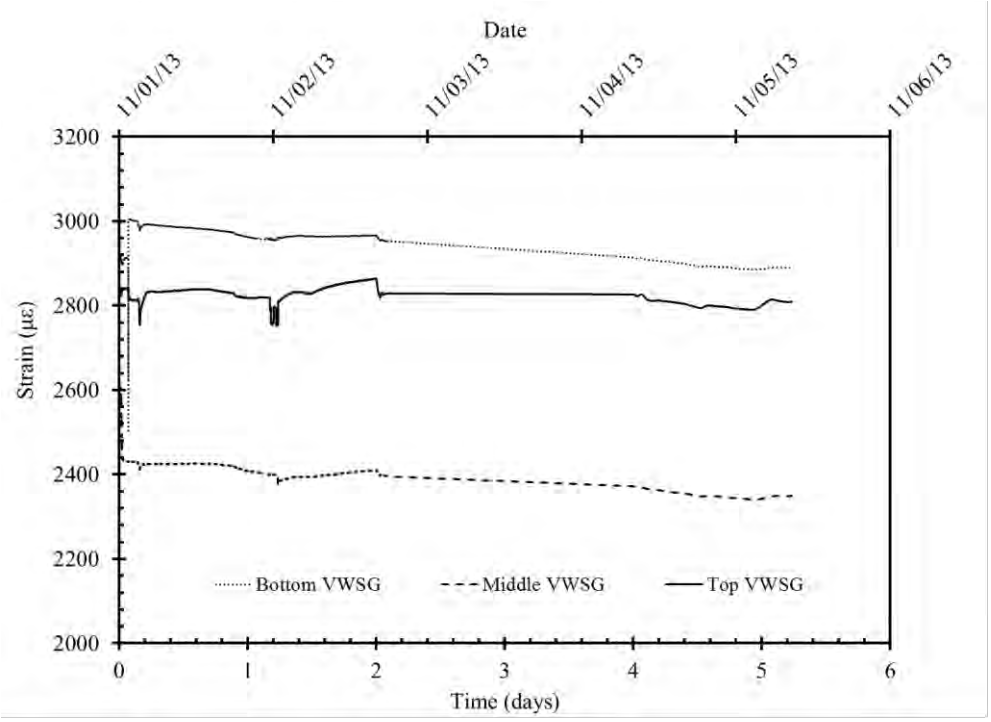

Figure 8.2-25 Recorded VWSG strain vs. time for Beam C

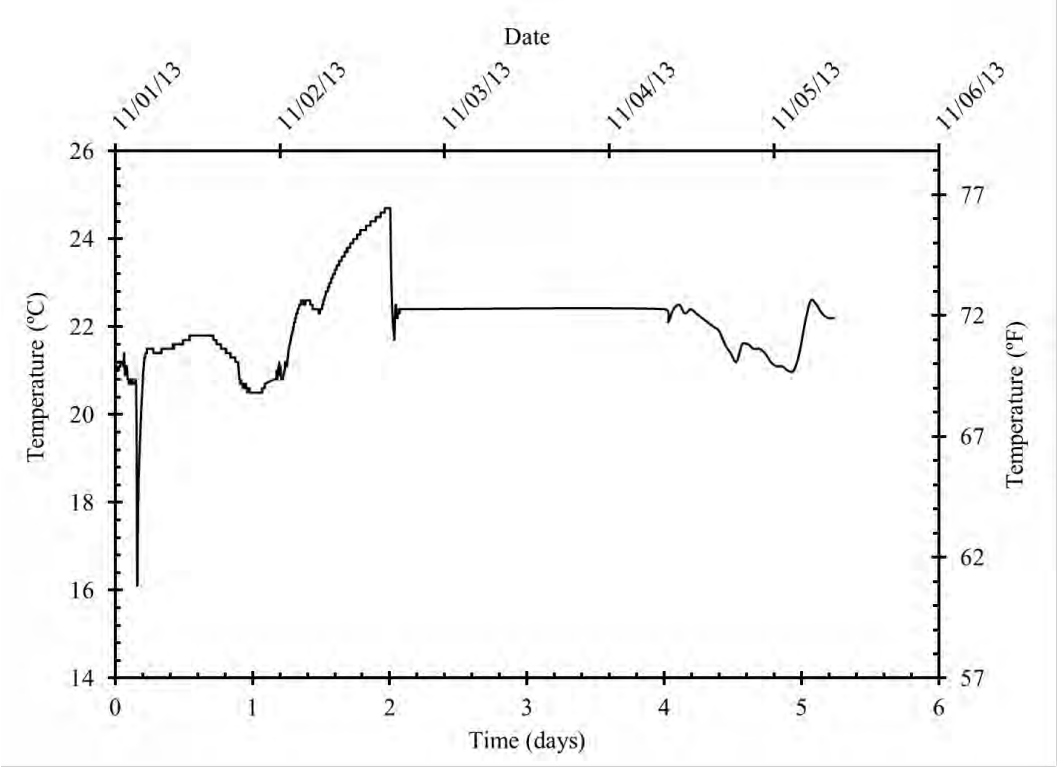

Figure 8.2-26 Recorded VWSG temperature vs. time for Beam C

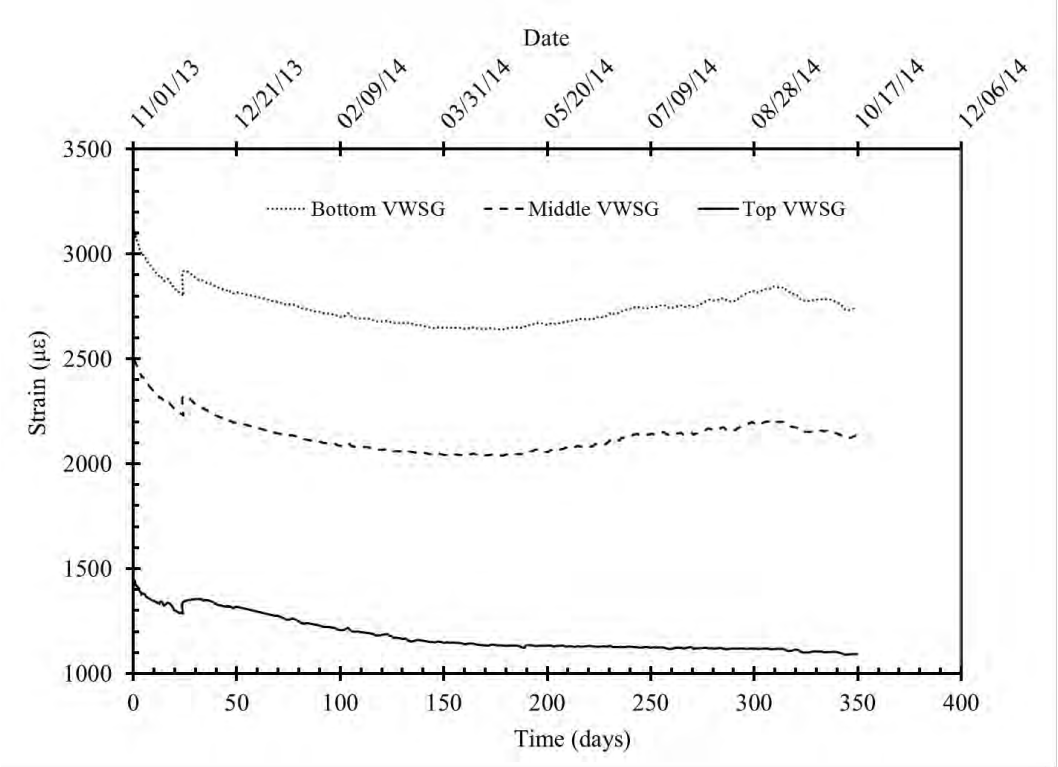

Figure 8.2-27 Recorded VWSG strain vs. time for Beam I-1

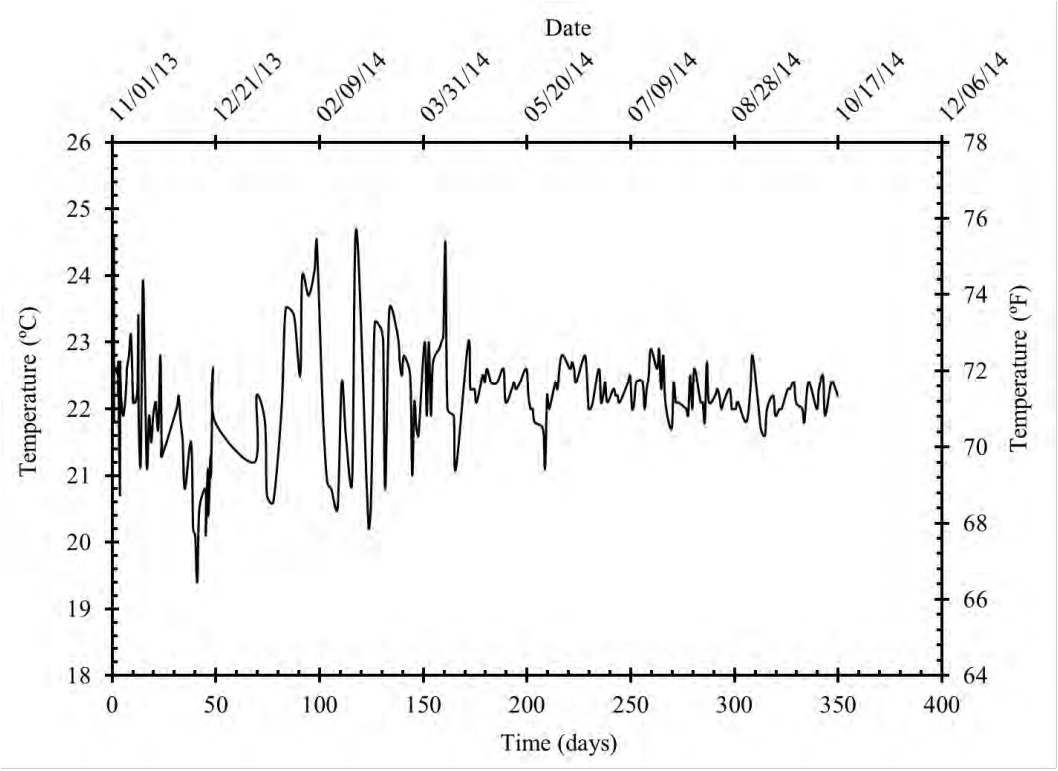

Figure 8.2-28 Recorded VWSG temperature vs. time for Beam I-1

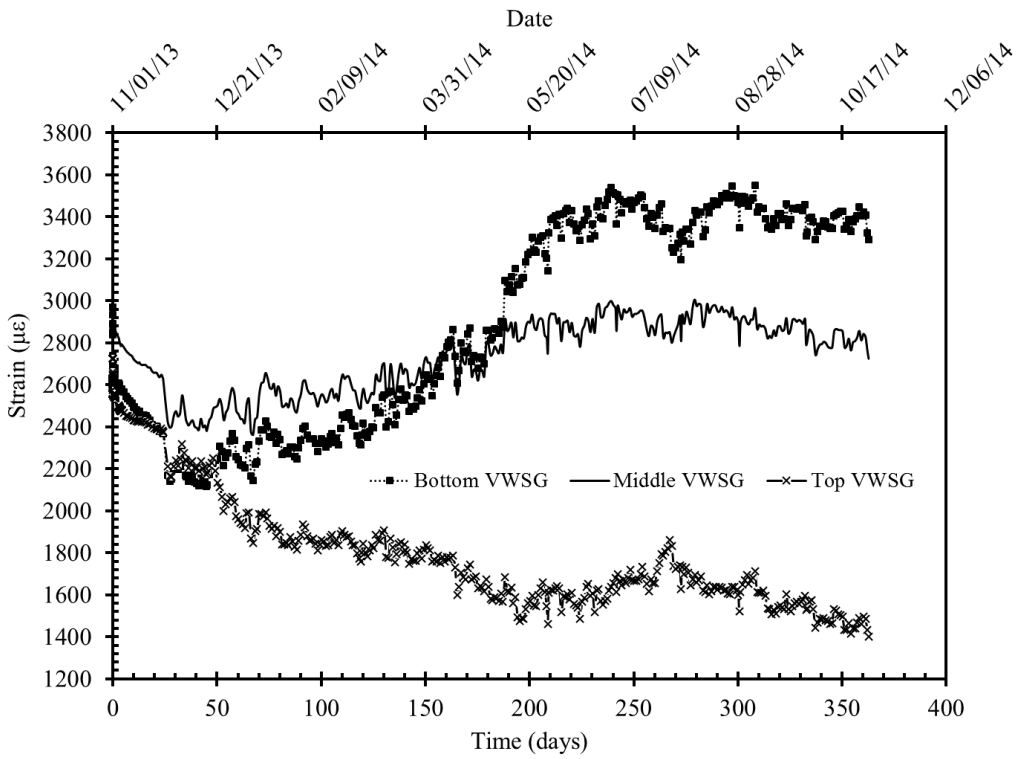

Figure 8.2-29 Recorded VWSG strain vs. time for Beam O-1

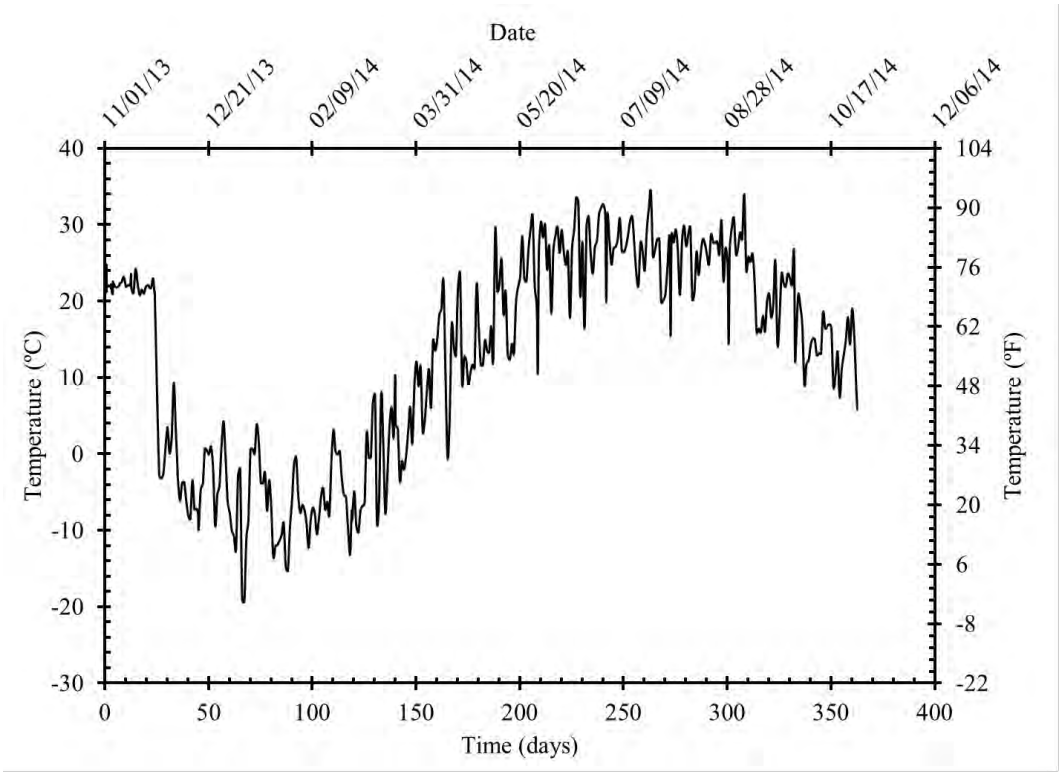

Figure 8.2-30 Recorded VWSG temperature vs. time for Beam O-1

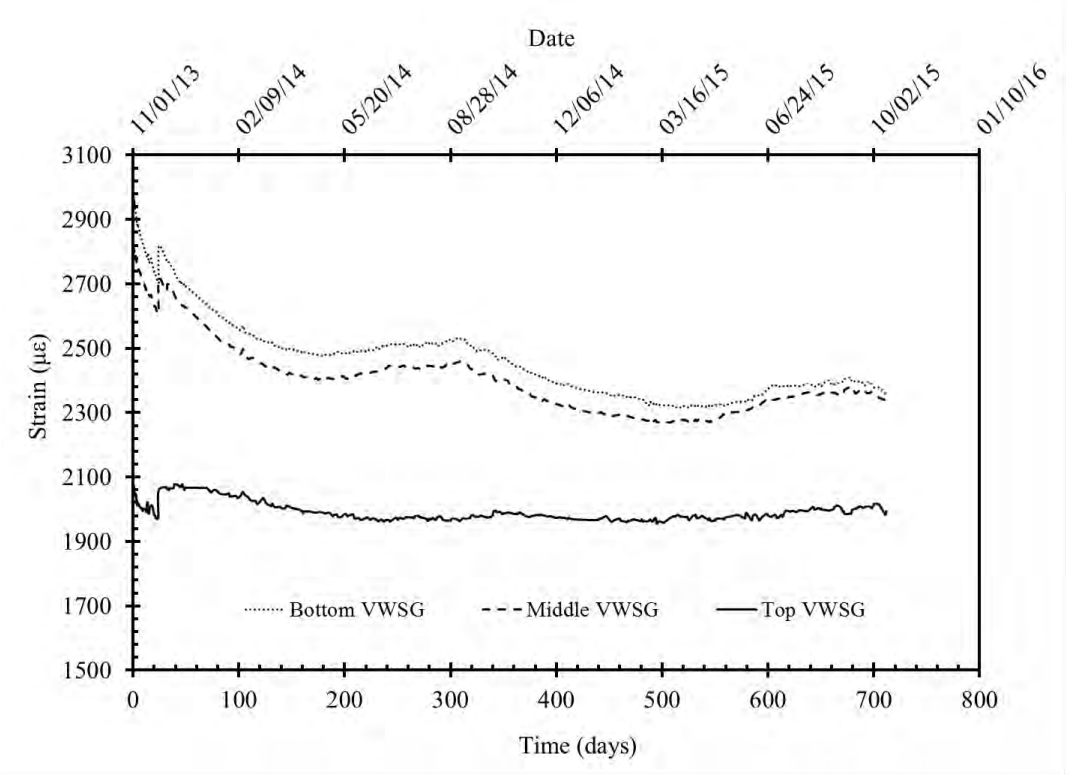

Figure 8.2-31 Recorded VWSG strain vs. time for Beam I-2

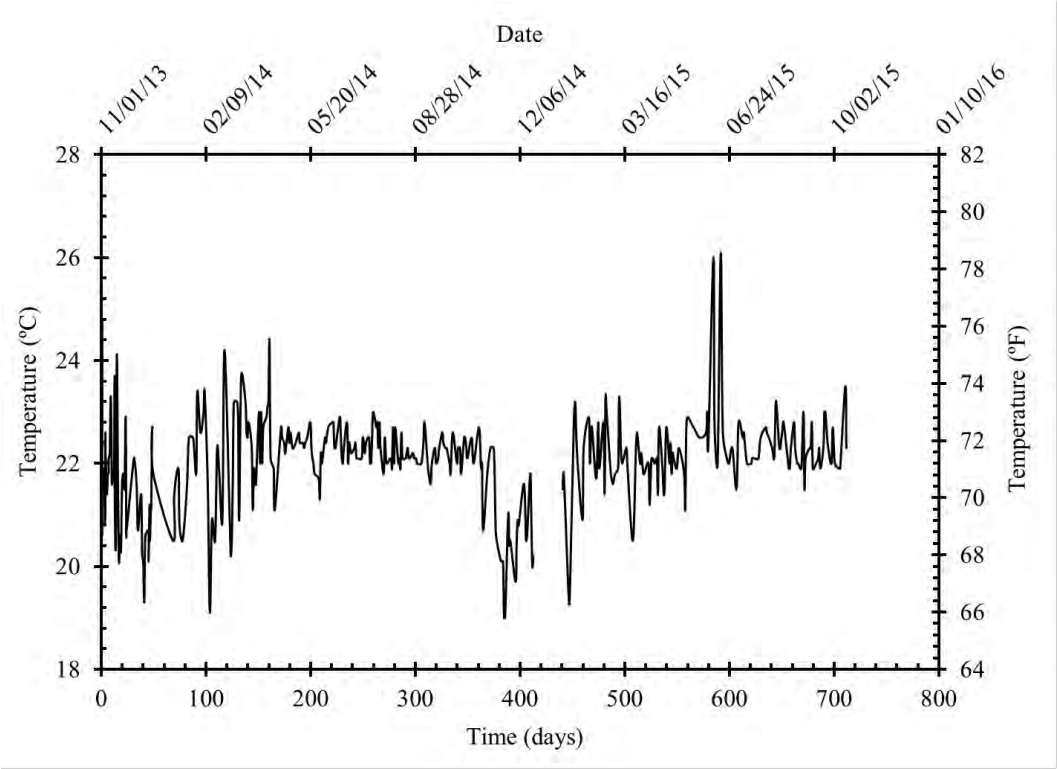

Figure 8.2-32 Recorded VWSG temperature vs. time for Beam I-2

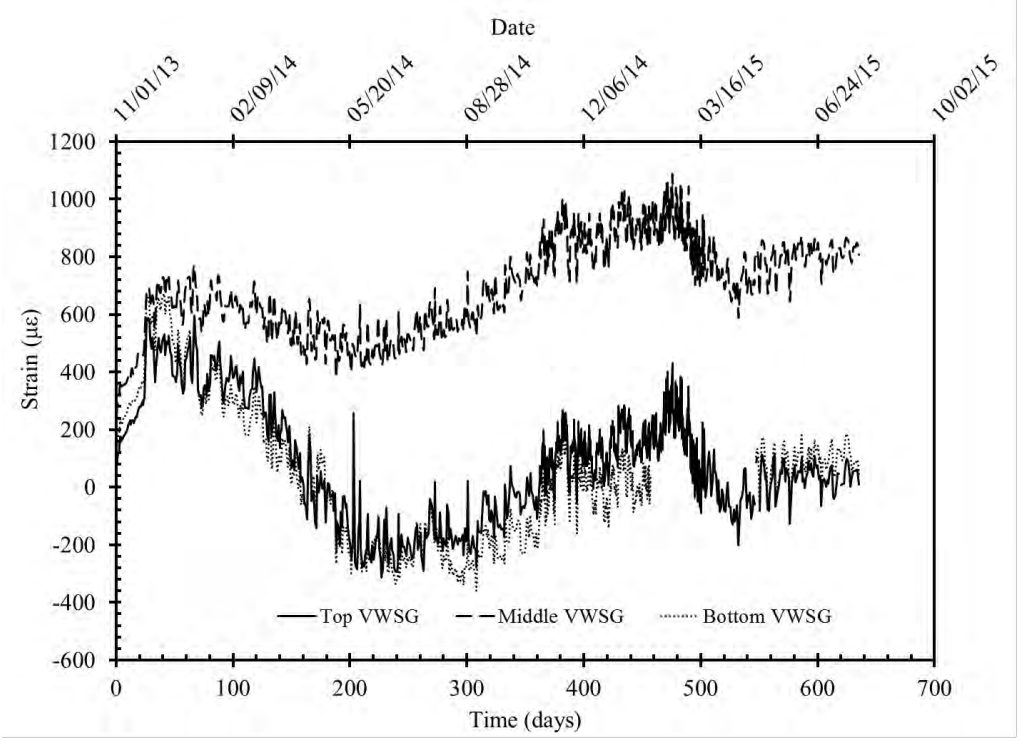

Figure 8.2-33 Recorded VWSG strain vs. time for Beam O-2

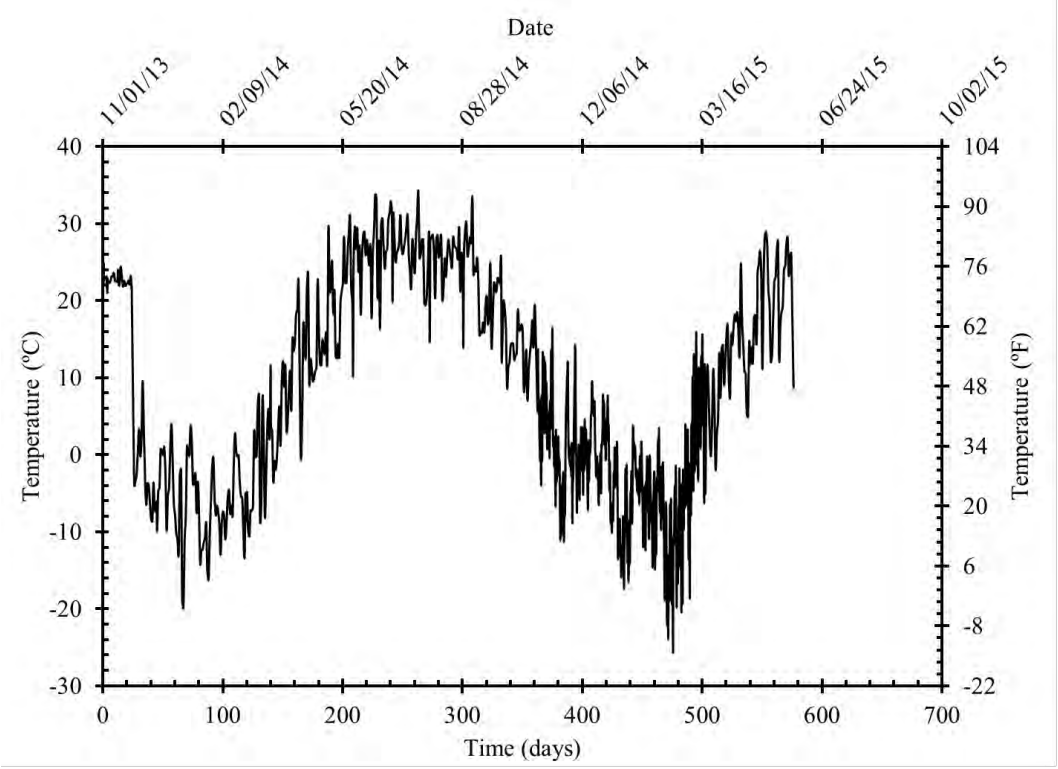

Figure 8.2-34 Recorded VWSG temperature vs. time for Beam O-2

8.2.2.2 Flexural test results

The service limit state represents the stage of loading where the beams remain uncracked. Cracking loads were estimated using the load-deflection inspection method (Figure 8.2-35). After cracking, the decompression load was determined and represented the load that caused zero stress in the extreme fiber in the pre-compressed tensile zone. The 50-kip (222-kN) load cycle was used to determine the decompression load of the beams. These decompression loads were converted to prestress loss. Figure 8.2-35 Figure 8.2-45 show the estimation of the decompression loads in all test beams. In addition, cracking loads, decompression loads, and the rest of the test results are summarized in Table 8.2-2.

All beams behaved in a similar manner after initiation of first crack. The crack widths and patterns and inelastic behaviors were also similar. First crack initiation occurred directly under one of the loading points of the 4-ft (1.22-m) spreader. After cracking, flexural cracks formed in the pure bending zone under the loading spreader and propagated vertically to the top flange as shown

in Figure 8.2-46. Additional flexural cracks developed outside the pure bending region and propagated diagonally to the top flange in the form of flexural shear cracks.

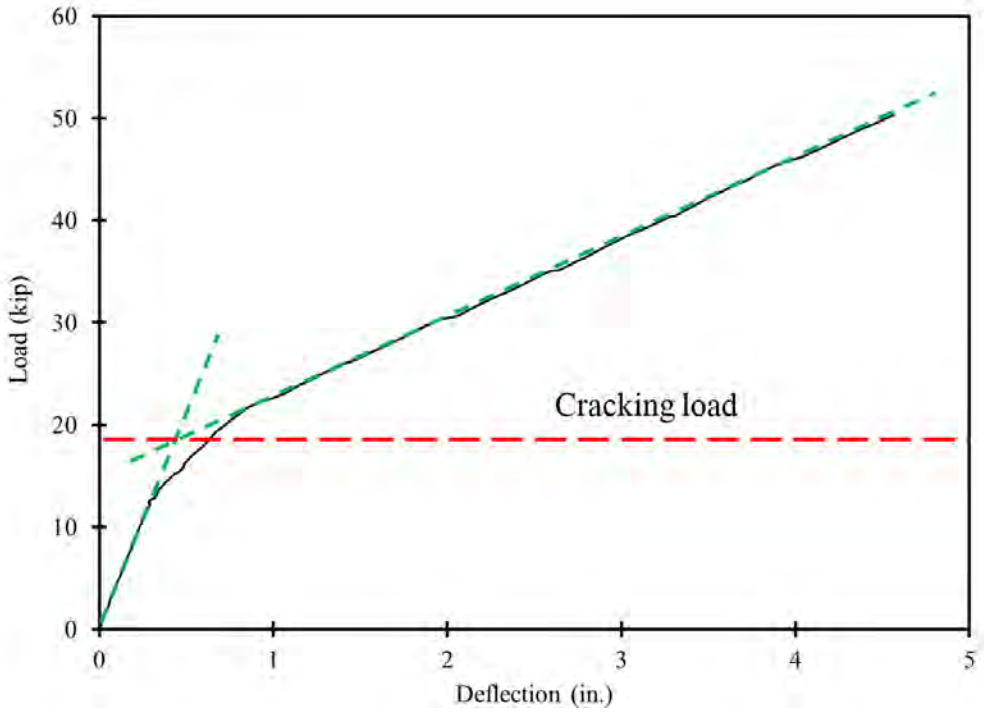

Figure 8.2-35 Cracking load from load deflection curve

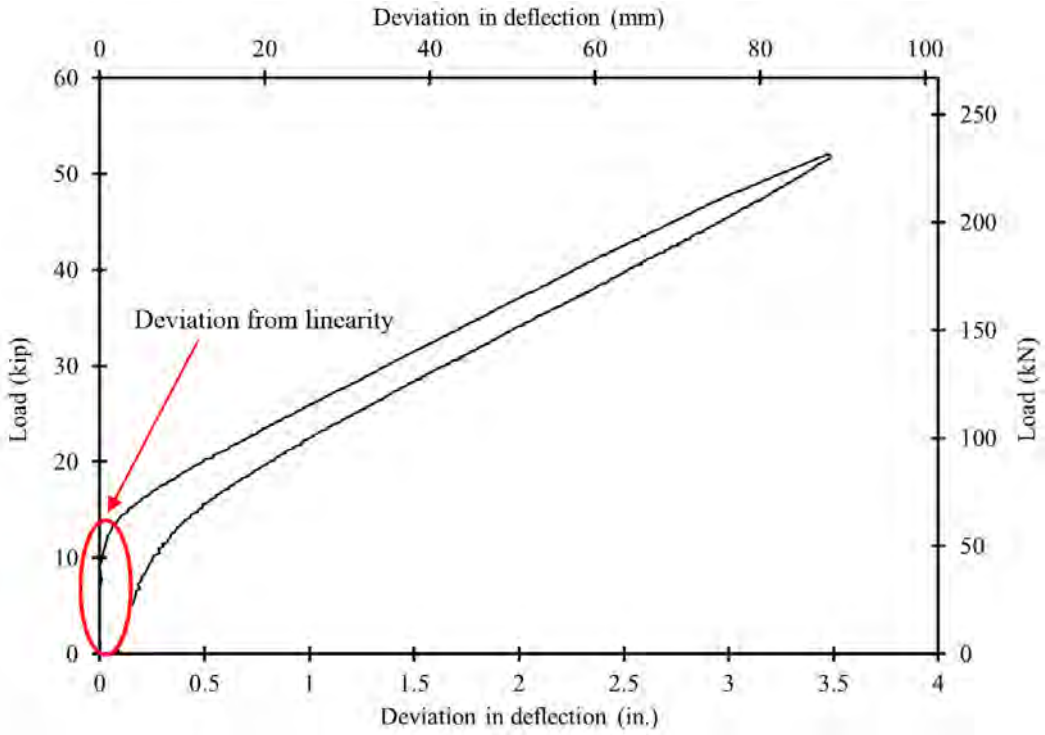

Figure 8.2-36 Load vs. deviation in deflection curve for Beam C

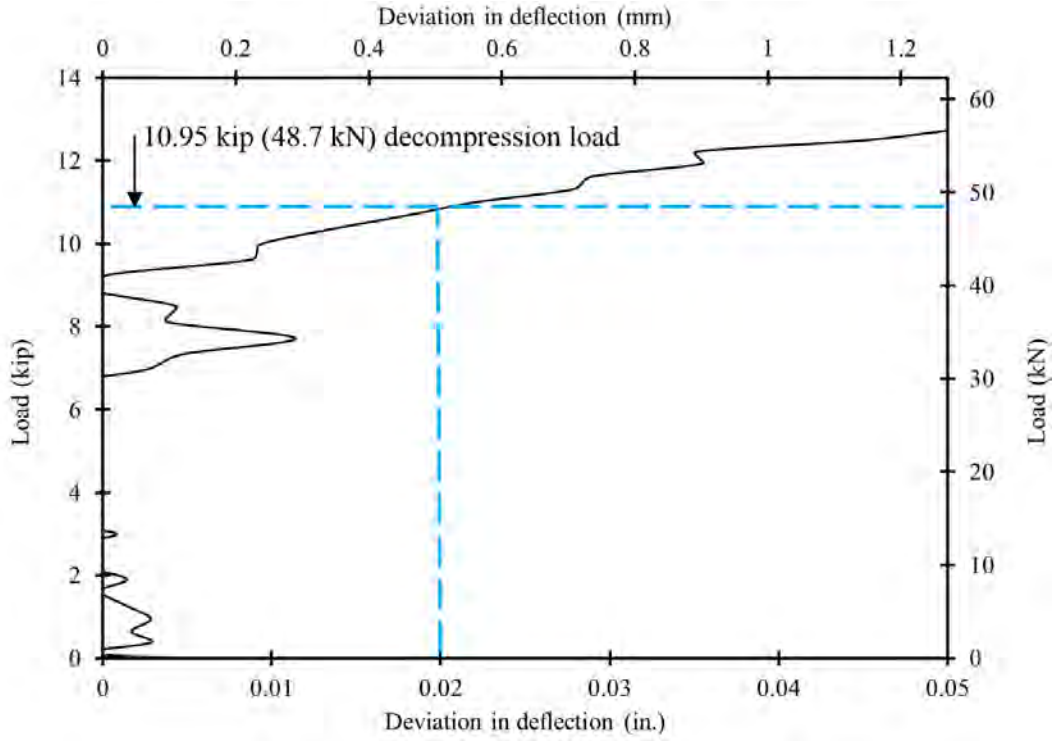

Figure 8.2-37 Deviation from linearity (Beam C)

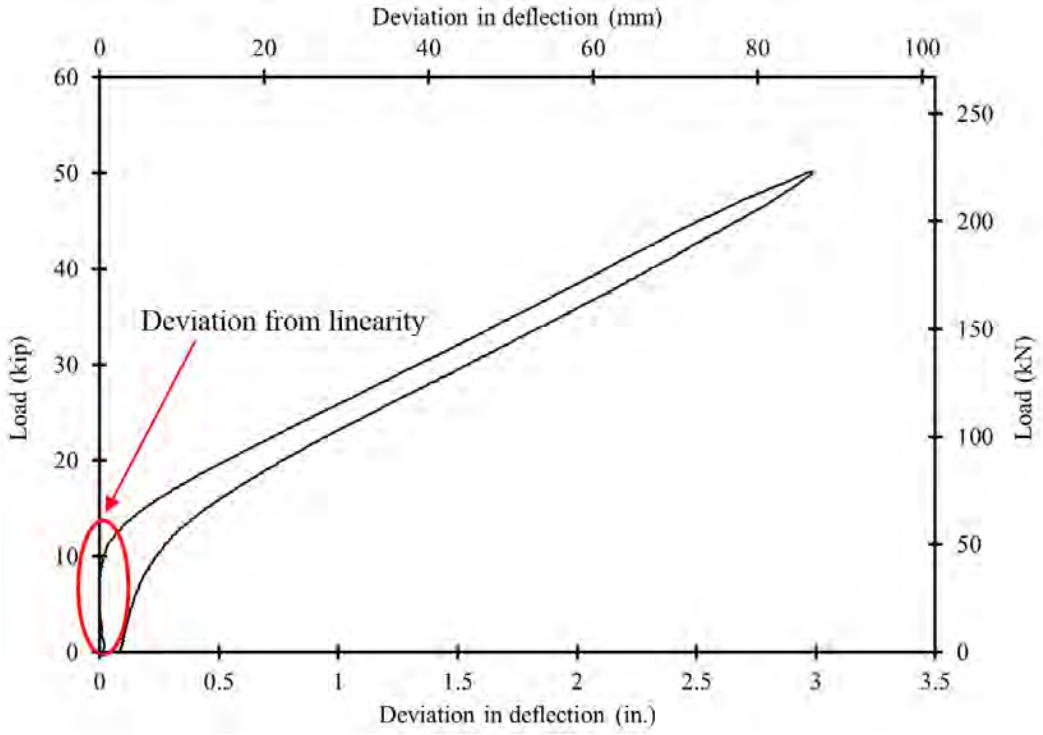

Figure 8.2-38 Load vs. deviation in deflection curve for Beam I-1

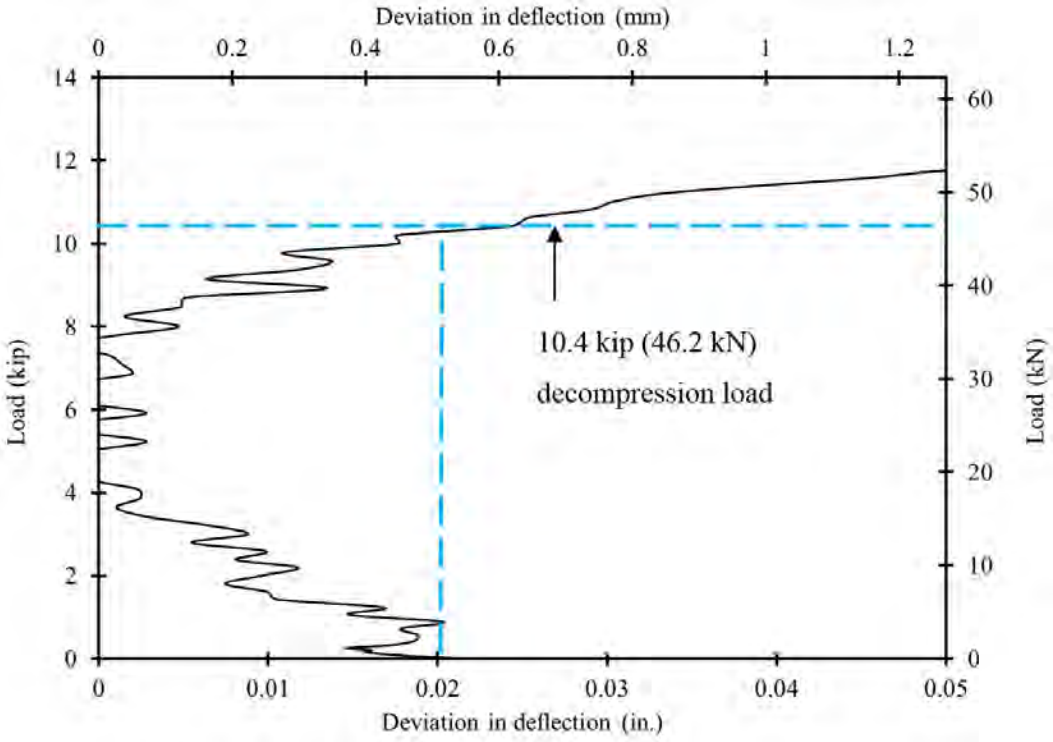

Figure 8.2-39 Deviation from linearity (Beam I-1)

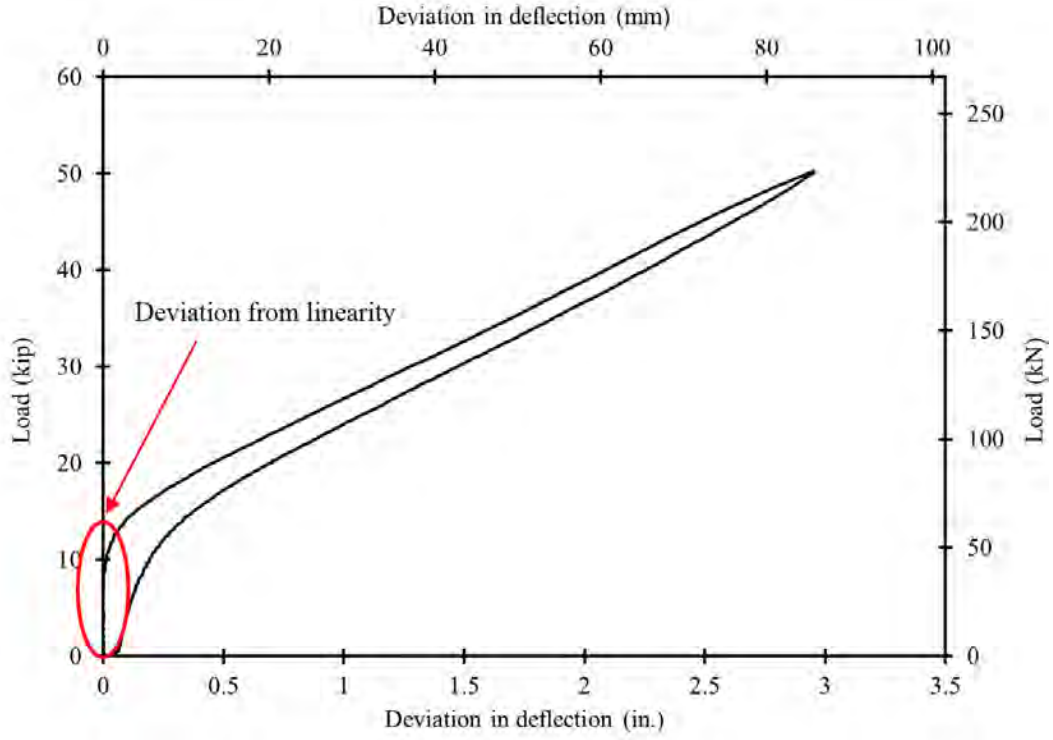

Figure 8.2-40 Load vs. deviation in deflection curve for Beam O-1

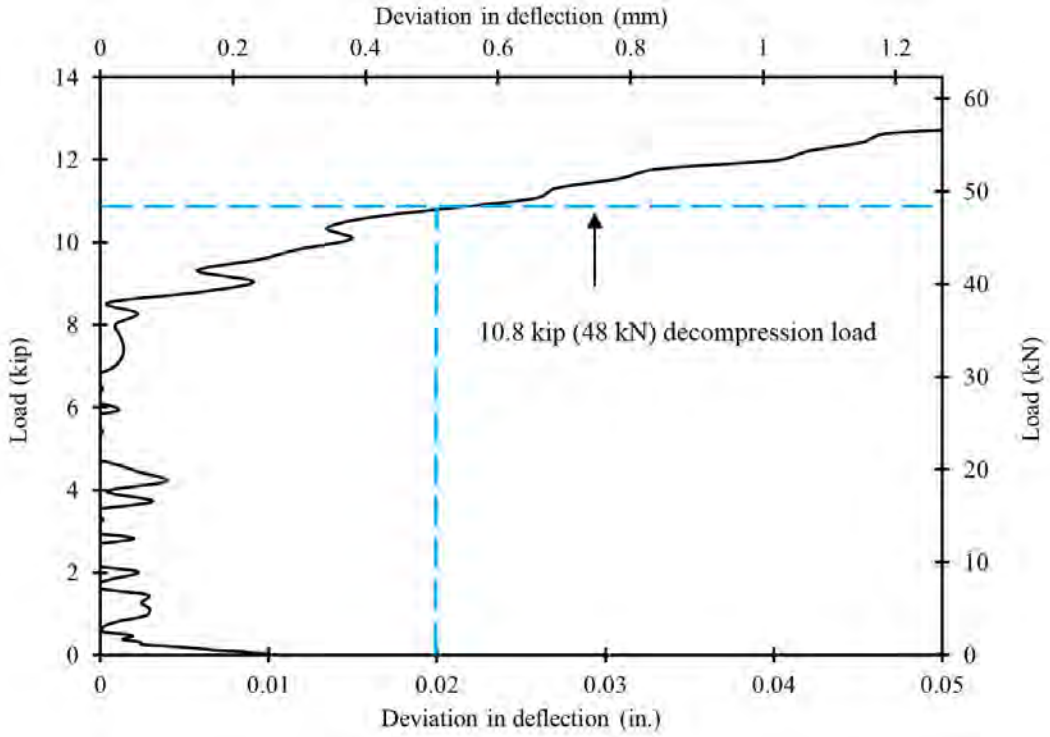

Figure 8.2-41 Deviation from linearity (Beam O-1)

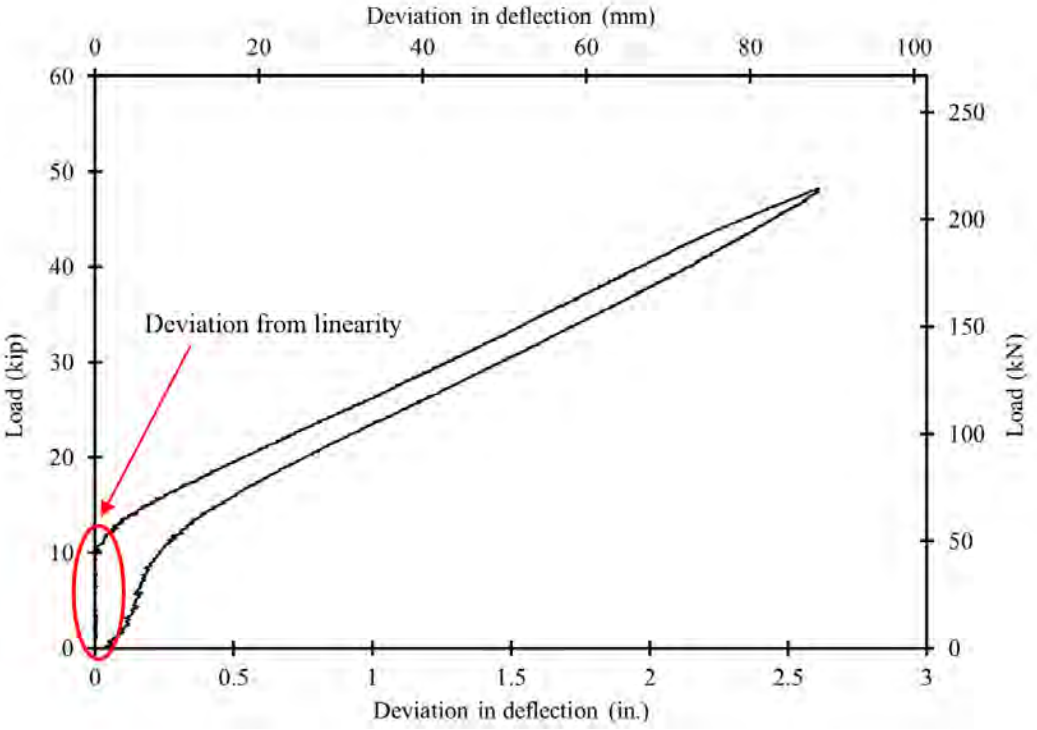

Figure 8.2-42 Load vs. deviation in deflection curve for Beam I-2

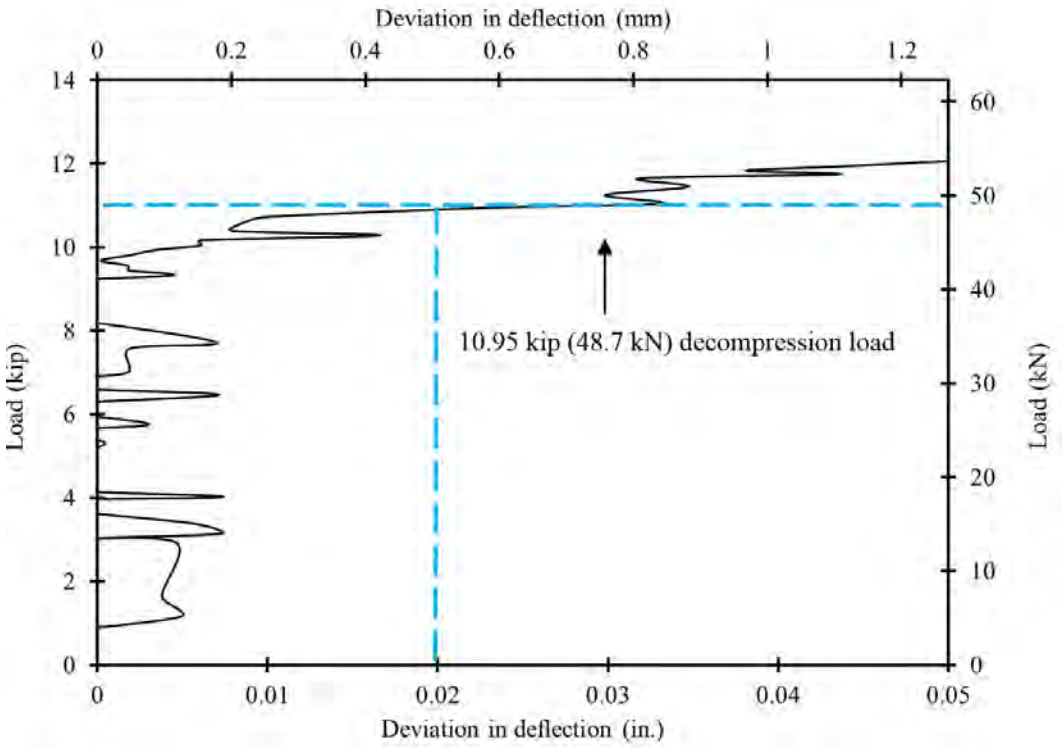

Figure 8.2-43 Deviation from linearity (Beam I-2)

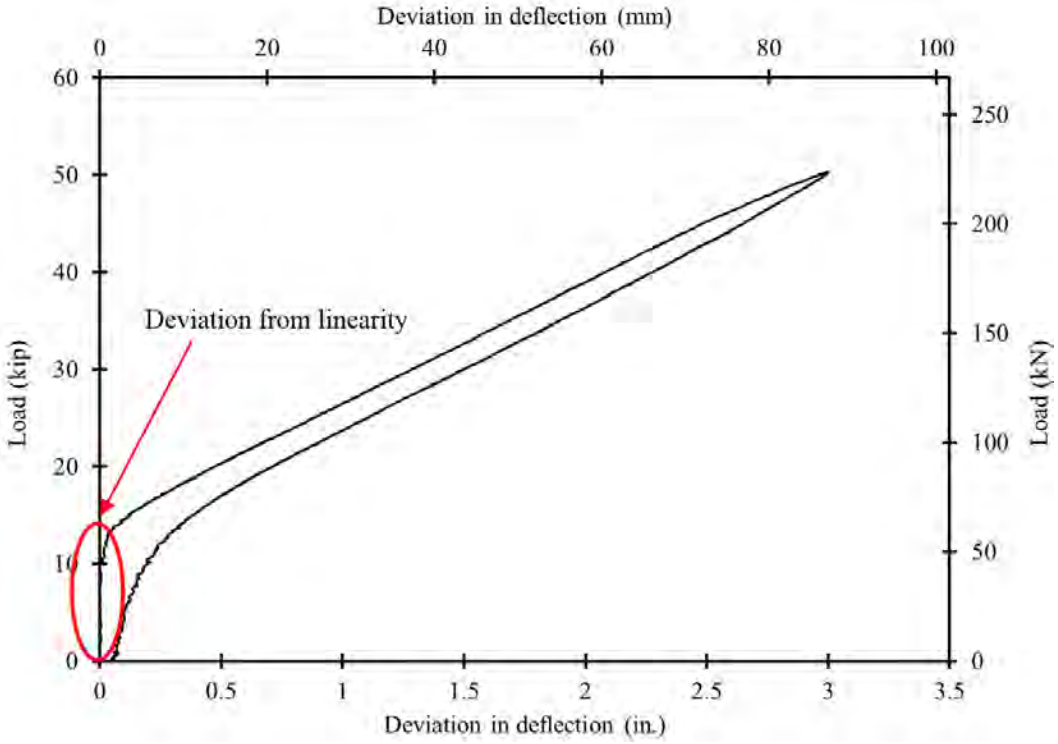

Figure 8.2-44 Load vs. deviation in deflection curve for Beam O-2

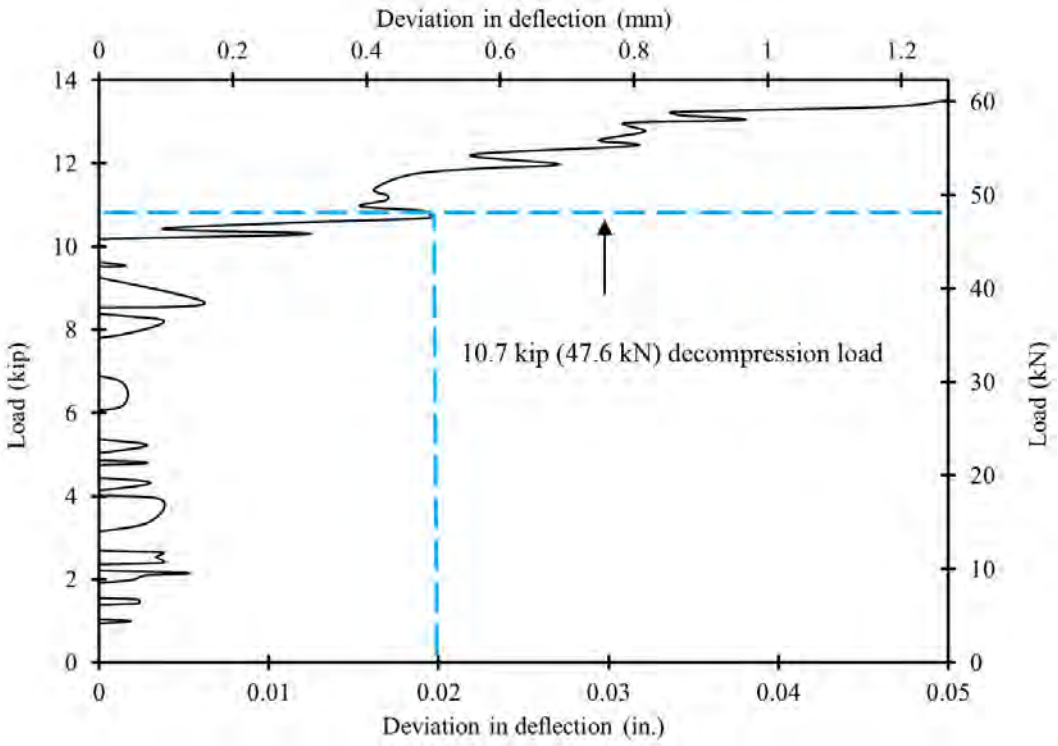

Figure 8.2-45 Deviation from linearity (Beam O-2)

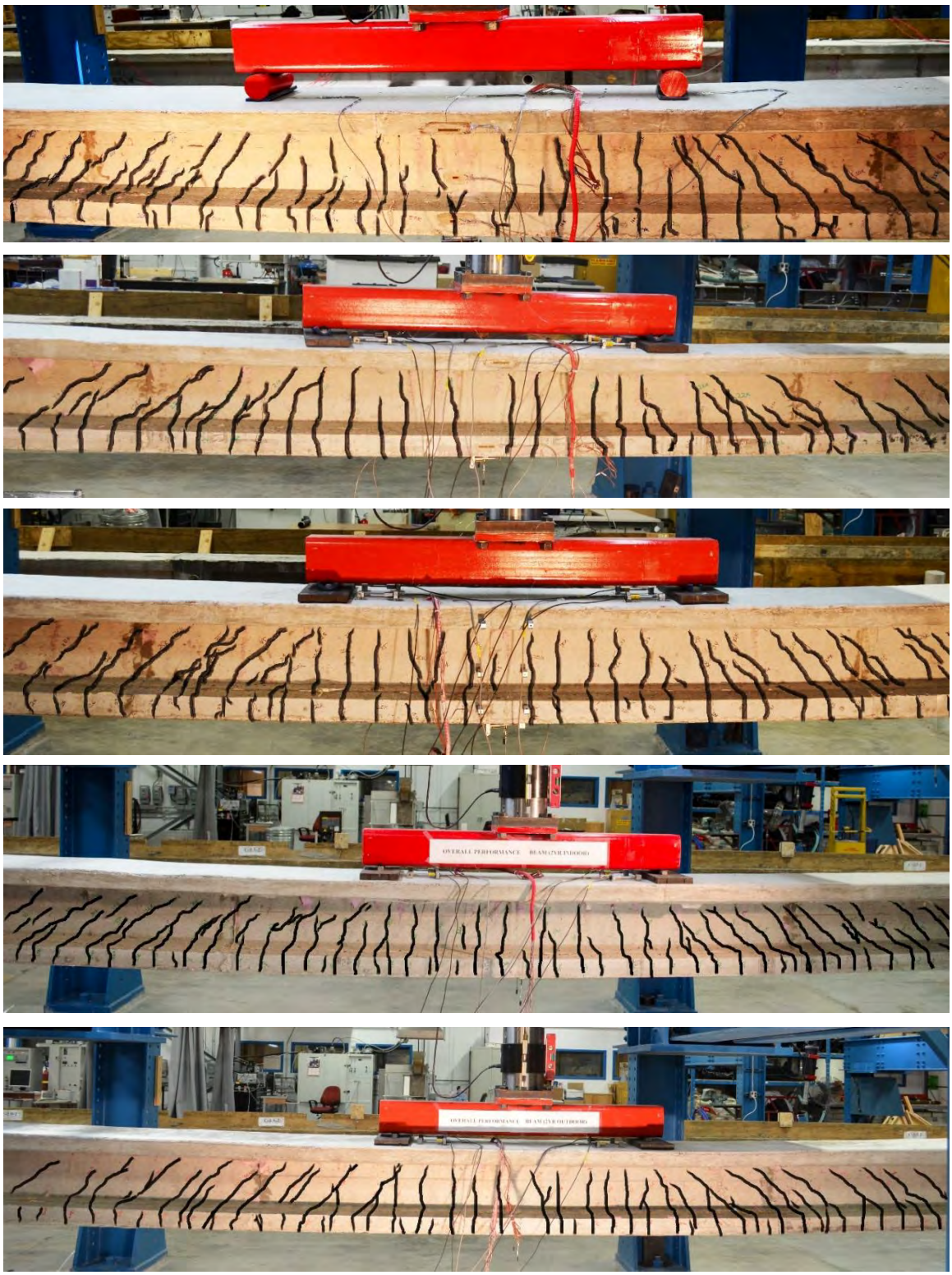

Figure 8.2-46 Cracking pattern of decked bulb T beams from the top: C, I-1, O-1, I-2, and O-2

Beam C, Beam I-1, Beam O-1, Beam I-2, and Beam O-2 exhibited accumulated residual mid-span deflections of 0.65 in. (16.5 mm), 0.54 in. (13.7 mm), 0.50 in. (12.7 mm), 0.55 in. (14.0 mm), and 0.38 in. (9.6 mm) respectively after the 60-kip (267-kN) load cycle. The failure mode of the fluctuated between a compression failure, where the concrete crushed but the CFCC strands remained intact and balanced failure, where both crushing of the concrete and rupture of CFCC happened nearly at the same time. All the beams exhibited the bilinear load-deflection curves. Figure 8.2-47 through Figure 8.2-59 show the failure of the five test beams along with the recorded load-deflection curves.

Beam C was loaded to in loading/unloading cycles after 28 days of concrete pouring but the last load cycle that led to beam failure was executed 71 days after concrete pouring. First crack was observed at 16.5 kip (73 kN), while failure took place by crushing of concrete in the top flange at a load of 66.4 kip (295 kN) with a corresponding mid-span deflection of 7.98 in. (203 mm) and an extreme concrete compression strain of 2970 με.

Beam I-1 was stored indoors and tested one year after concrete pouring. First crack was observed at 16.5 kip (73 kN), while failure took place by crushing of concrete in the top flange at a load of 74.3 kip (331 kN) with a corresponding mid-span deflection of 8.2 in. (208 mm) and an extreme compression strain of 3200 με.

Beam O-1 was stored outdoors and loaded to failure one year after concrete pouring. First crack was observed at 17 kip (76 kN). Failure was initiated by crushing of concrete in the top flange at a load of 76.7 kip (341 kN) with a corresponding deflection of 8.2 in. (208 mm) and an extreme compression strain of 3200 με. Rupture of the prestressing strands was observed after failure, which suggested a balanced failure, but this also could have been initiated by the energy released from the explosive crushing of concrete.

Beam I-2 was stored indoors and loaded to failure two years after concrete pouring. First crack was observed at 17 kip (75.6 kN). Failure took place by combined crushing of concrete in the top flange and rupture of prestressing strands at a load of 64.7 kip (288 kN) with a corresponding deflection of 7.5 in. (190 mm) and an extreme compression strain of 2830 με. It should be noted that the first attempt for last load cycle was interrupted by a power outage when the load level was approximately 62 kip (276 kN). The last load cycle was repeated after power was restored but it seems that the achieved failure load was affected by the first attempt.

Beam O-2 was tested two years after concrete pouring. First crack was observed at 18.0 kip (80 kN). Failure took place by crushing of concrete in the top flange at a load of 80.7 kip (359 kN) with a corresponding mid-span deflection of 8.7 in. (221.0 mm) and an extreme compression strain of 2960 με. Table 8.2-2 summarizes the results from the flexural testing of the decked bulb T-beams.

Figure 8.2-47 Failure of Beam C

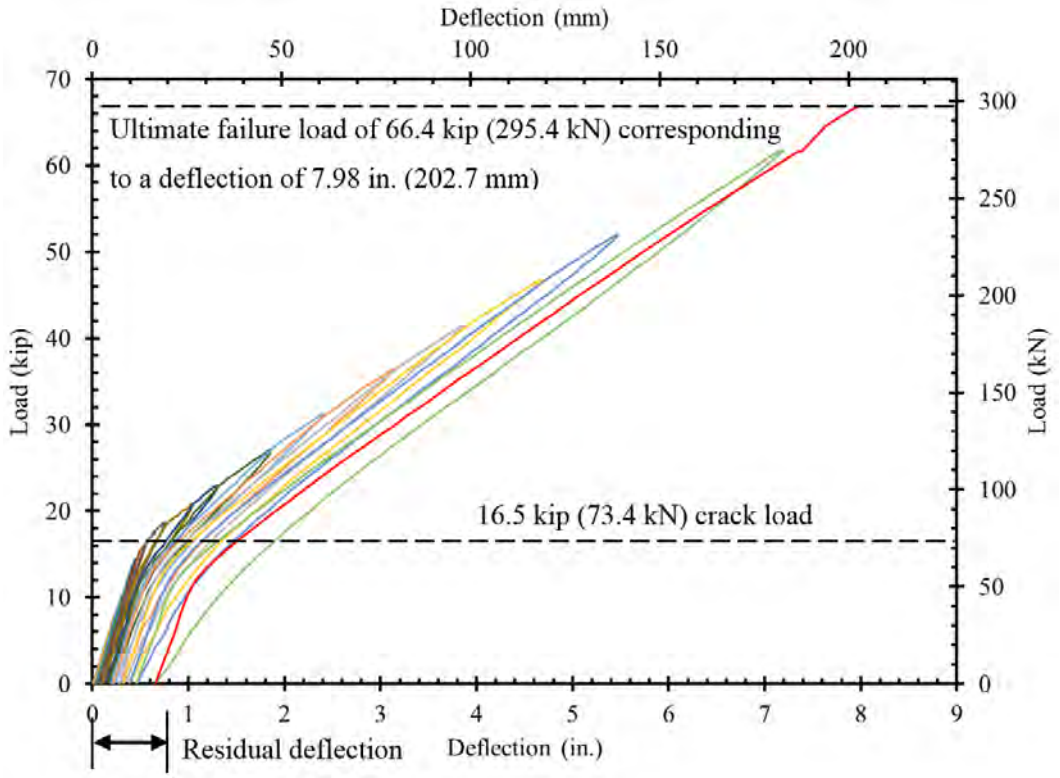

Figure 8.2-48 Load vs. deflection curves for Beam C

Figure 8.2-49 Failure of Beam I-1

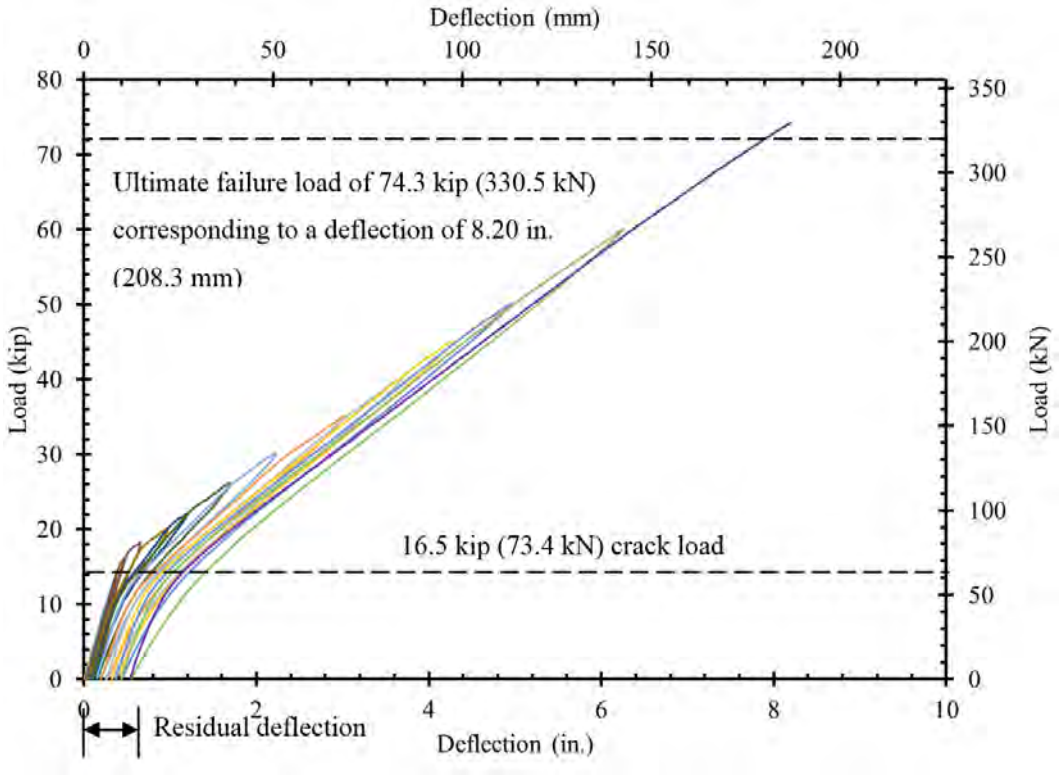

Figure 8.2-50 Load vs. deflection curves for Beam I-1

Figure 8.2-51 Failure of Beam O-1

Figure 8.2-52 Ruptured prestressing strands at failure of Beam O-1

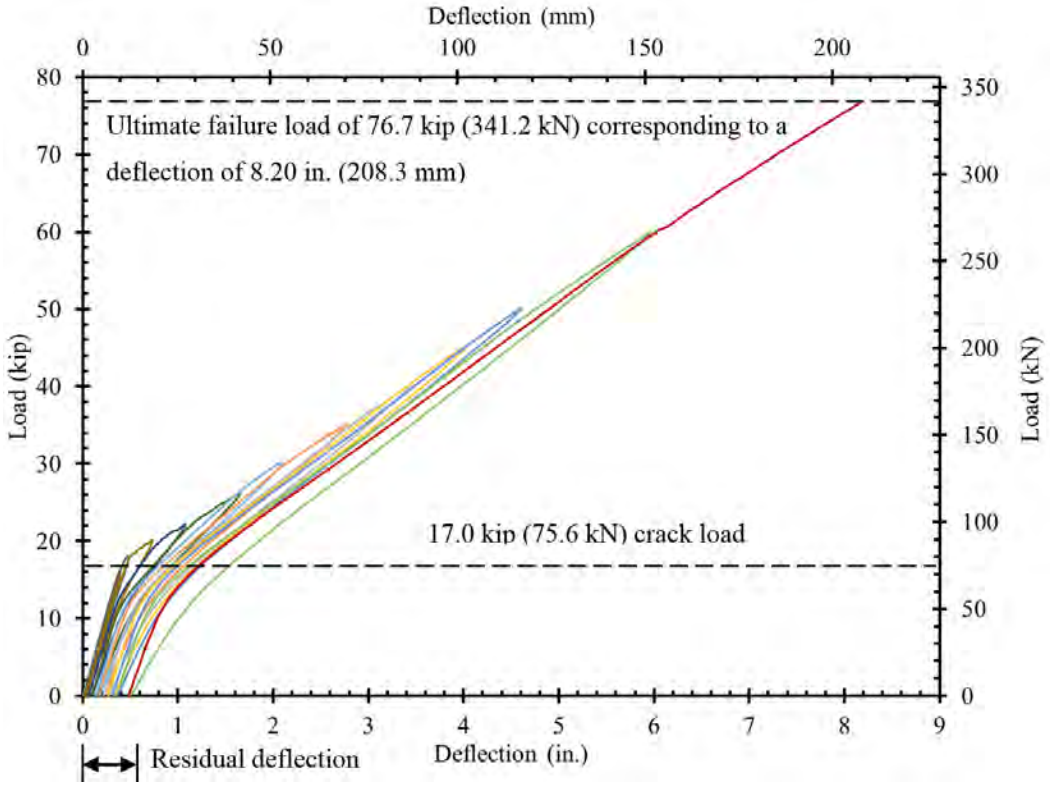

Figure 8.2-53 Load vs. deflection curves for Beam O-1

Figure 8.2-54 Failure of Beam I-2

Figure 8.2-55 Ruptured prestressing strands at failure of Beam I-2

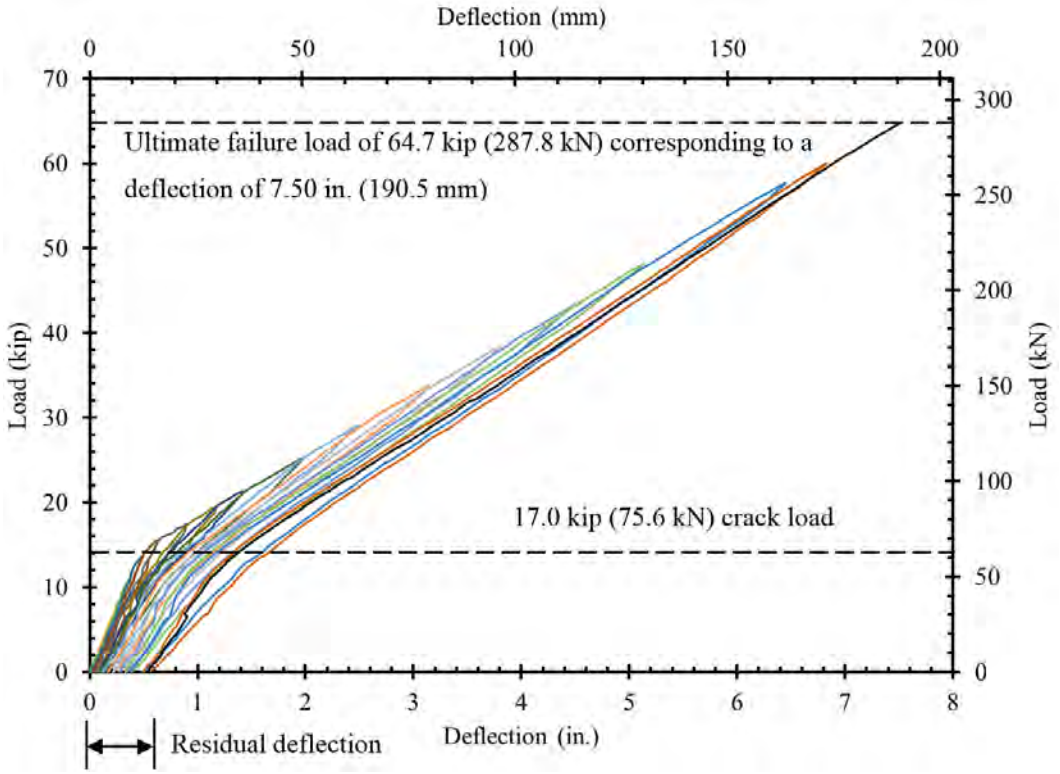

Figure 8.2-56 Load vs. deflection curves for Beam I-2

Figure 8.2-57 Failure of Beam O-2

Figure 8.2-58 Un-ruptured prestressing strands of Beam O-2 at failure

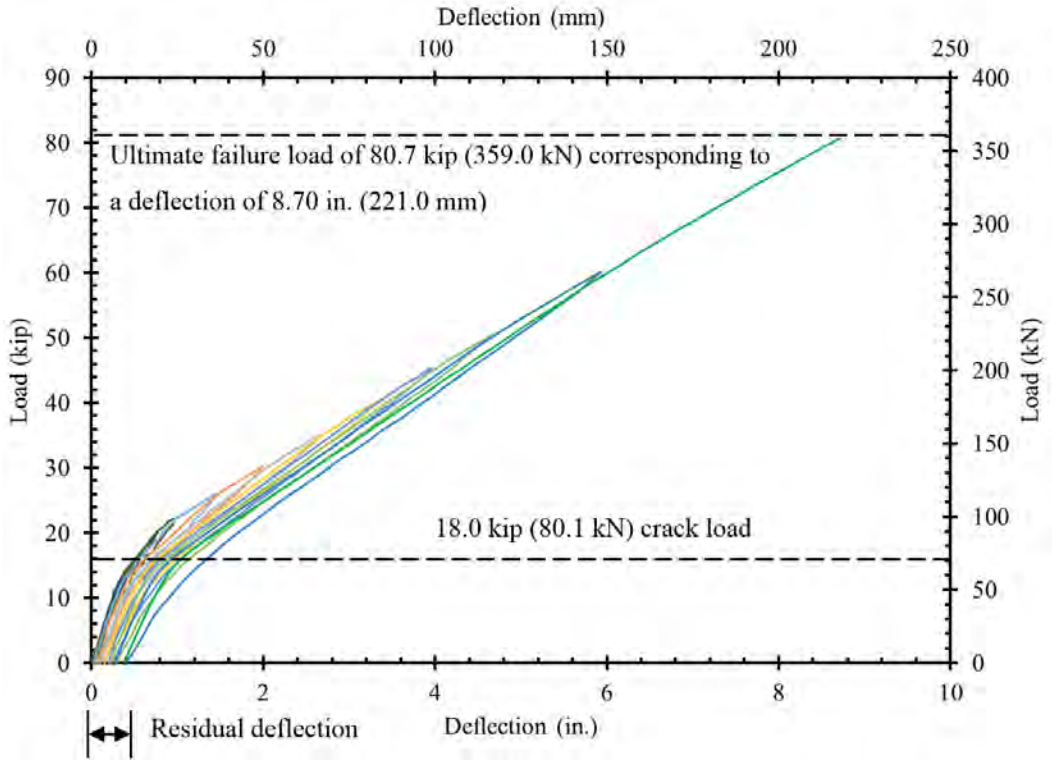

Figure 8.2-59 Load vs. deflection curves for Beam O-2

Table 8.2-2 Summary of experimental results for decked bulb T-beams

Parameter	Specimen ID				
	Beam C	Beam I-1	Beam O-1	Beam I-2	Beam O-2
Concrete compressive strength at testing psi (MPa)	10,700 (73.8)	10,300 (71.0)	11,900 (82.0)	10,100 (69.6)	12,000 (82.7)
Decompression load kip (kN)	10.95 (48.7)	10.4 (46.2)	10.8 (48)	10.95 (48.7)	10.7 (47.6)
Cracking load kip (kN)	16.5 (73.4)	16.5 (73.4)	17.0 (75.6)	17.0 (75.6)	18.0 (80.1)
Extreme compression strain (με)	2470	2930	2950	2430	2830
Mid-span deflection at failure, in. (mm)	7.3 (185.4)	7.7 (195.6)	7.7 (195.6)	6.9 (175.3)	8.3 (210.8)
Experimental ultimate load, kip (kN)	66.4 (295.4)	74.3 (330.5)	76.7 (341.2)	64.7 (287.8)	80.7 (359.0)
Predicted ultimate load kip (kN)	69.0 (307.0)	67.2 (298.8)	73.2 (325.5)	67.2 (299.1)	73.9 (329.0)
Total energy absorbed kip-in (kNm)	325.0 (36.7)	355.7 (40.2)	367.2 (41.5)	282.6 (31.9)	409.7 (46.3)
Mode of failure	Concrete crushing	Concrete crushing	Balanced	Balanced	Concrete Crushing
Exp. prestress loss (%)	18.9	22.3	19.7	18.8	20.4
AASHTO LRFD prestress loss (%)	20.5	20.5	18.3	20.5	18.3
PCI prestress loss (%)	21.4	21.4	18.8	21.4	18.8

8.3 Discussion of Test Results

Data collected during the monitoring of the beams were adjusted and analyzed to evaluate the loss of prestressing force over the monitoring period. In addition, decompression loads from the flexural testing of the beams were captured and analyzed to back calculate the effective prestressig force. The test results of beams prestressed with CFCC strands over a testing period of two years showed insignificant change in the effective prestressing force that falls within the tolerance of collecting and analyzing the data. The differences in the ultimate load carrying capacities among the five beams is mainly attributed, and related to, the change in concrete strength over a period of two years.

Concrete prisms monitored for shrinkage and concrete cylinders loaded in creep rupture setup indoors and outdoors showed a typical concrete shrinkage and creep that can be conservatively estimated using currently available guidelines such as AAHTO LRFD. Elastic prestress loss and losses due to creep and shrinkage of the concrete showed a good agreement with values calculated theoretically according the AASHTO LRFD and PCI Design manual.

CHAPTER 9: FLEXURAL AND SHEAR DESIGN OF CFRP PRESTRESSED BEAMS

9.1 Introduction

Once the loss in prestressing force is established, the analysis of a CFRP prestressed section becomes a straightforward process with few exceptions. For instance, steel reinforced/prestressed sections are classified as tension-controlled or compression-controlled according to the net tensile steel strain at the time the concrete in compression reaches its assumed crushing strain limit of 0.003. However, CFRP reinforced/prestressed sections are classified as tension or compression-controlled based on the actual failure mode whether it is crushing of the concrete or rupture of the CFRP reinforcement. If the concrete reaches a crushing strain of 0.003 while the net strain in the extreme CFRP remains less than net guaranteed tensile strain, the section is regarded as compression-controlled section. If the net extreme CFRP strain reaches the net guaranteed tensile strain, while the concrete compression strain remains less than 0.003, the section is regarded as tension controlled. The net guaranteed tensile strain is the net tensile strain in the reinforcement at balanced strain conditions. For all prestressed CFRP reinforcement, the net guaranteed strain limit may be taken as the specified guaranteed ultimate strain exclusive of the strain due to prestress, creep, shrinkage, and temperature.

Earlier studies and experimental work showed that the moment capacity of sections prestressed and reinforced with CFRP materials can be accurately estimated using the principles of strain compatibility and force equilibrium in the section (Grace et al. 2013a, 2013b, 2013c, 2012a, 2011a, 2011b, 2008, 2006a, and 2006b). ACI 440.4R-04 provides equations to calculate the depth of the neutral axis and nominal moment capacity of the section when the reinforcement or prestressing CFRP is provided in a single layer. In addition, several studies produced different design approaches with varying degrees of complexity (Grace et al. 2003a).

Due to the elastic nature of CFRP material, when the tension CFRP reinforcement is distributed over multiple layers, the failure of tension-controlled sections is usually governed by the failure of CFRP reinforcement at the extreme layer, which is the layer farthest from the compression fiber. CFRP reinforcements at layers closer to the compression fiber are likely to fail progressively once CFRP reinforcement at the extreme layer fails. It is therefore not recommended to sum the layers of CFRP reinforcement through their center of gravity. ACI 440.4R-04 Section

3.4.2 provides a set of equations to address this problem. Nevertheless, the equations in ACI 440 are based on the assumption that the stress distribution in concrete is linear and the section is tension-controlled and therefore, those equations are not applicable for compression-controlled sections or tension-controlled section with non-linear stress distribution on the concrete. That leaves the designer with the option of using basic strain compatibility and force equilibrium (Grace et al. 2003b). However, strain compatibility and force equilibrium in their raw format tend to be a lengthy iterative process, especially when the mode of failure is not known.

9.2 Flexural Design of CFRP reinforced/Prestressed section

To facilitate the flexural design and reduce the potential for error, a unified design approach is developed by converting the areas of CFRP reinforcement at different layers to equivalent areas at the level of the extreme CFRP layer using appropriate area reduction factors. The sum of equivalent reinforcement areas at the extreme layer is regarded as "The equivalent area of reinforcement, A_{fe}" and is used to calculate the depth of the neutral axis and the nominal moment capacity of the section. In other words, the equivalent area of CFRP reinforcement is a discrete area of CFRP reinforcement positioned at the extreme CFRP layer that results in the same flexural capacity of n layers of reinforcement.

The area reduction factor needed to calculate the equivalent areas of reinforcement are obtained by assuming linear strain distribution through the depth of the section. Thereby, the area of CFRP reinforcement at the ith layer is reduced with a factor depending on the distance from the ith layer to the extreme layer. The area reduction factor can be calculated by evaluating the strain distribution through the section as follows:

The net tensile strain at any layer (i) is related to the net tensile strain at the extreme CFRP layer by:

$$\varepsilon_i = \varepsilon_1 \left(\frac{d_i - c}{d_1 - c} \right) \tag{9.2-1}$$

where:

ε_i = net tensile strain at the ith CFRP reinforcement layer

ε_1 = net tensile strain at the extreme CFRP layer

d_i = depth of the ith CFRP layer from the extreme compression fiber (in. or mm)

d_1 = depth of the extreme CFRP layer from the extreme compression fiber (in. or mm)

c = depth of neutral axis from the extreme compression fiber (in. or mm)

The tensile force, T_i, in any CFRP layer (i) may be calculated as:

$$T_i = \varepsilon_i \, n_i \, a_f \, E_f = \varepsilon_1 \left(\frac{d_i - c}{d_1 - c}\right) n_i \, a_f \, E_f = \varepsilon_1 \left(\frac{d_i - c}{d_1 - c} \, n_i \, a_f\right) E_f = \varepsilon_1 \, A_{fe(i)} \, E_f \qquad (9.2\text{-}2)$$

where:

ε_i = net tensile strain at the ith CFRP reinforcement layer

n_i = number of CFRP strands in the ith layer

a_f = area of single CFRP strand in the ith layer (in.2 or mm2)

E_f = elastic modulus of CFRP (ksi or MPa)

d_i = depth of the ith CFRP layer from the extreme compression fiber (in. or mm)

d_1 = depth of the extreme CFRP layer from the extreme compression fiber (in. or mm)

c = depth of neutral axis from extreme compression fiber (in. or mm)

where $A_{fe(i)}$ is the area equivalent to the area of CFRP reinforcement at layer i and is calculated as:

$$A_{fe(i)} = \frac{d_i - c}{d_1 - c}\left(n_i \, a_f\right) \qquad (9.2\text{-}3)$$

The equivalent area of reinforcement for the total reinforcement provided in the section, A_{fe} is calculated as:

$$A_{fe} = \sum_{i=1}^{m} A_{fe(i)} \qquad (9.2\text{-}4)$$

Where

m = number of layers (rows) of CFRP reinforcement

At this stage of analysis, the depth of the neutral axis from the extreme compression fiber, c, can be initially set equal to $0.1d_1$. The initial assumption of $c = 0.1d_1$ is based on observations from multiple experimental flexural tests of CFRP prestressed beams and is only needed if calculations are performed by hand. This assumption usually yields accurate estimate for the depth of the neutral axis and the flexural capacity of the section. It needs not to be adjusted unless more refined calculations are required. In addition, if a Software tool is implemented in the design, there is no need to start with an initial assumption since a loop can be created in the software to calculate the exact depth of the N.A.

With $c = 0.1d_1$, Eq. 3 becomes:

$$A_{fe(i)} = \left(1 - \frac{s_i}{0.9d_1}\right)(n_i\ a_f) \tag{9.2-5}$$

where:

s_i = Distance between *ith* CFRP layer and extreme CFRP layer (in.) = $d_1 - d_i$

After establishing the equivalent area of reinforcement for the section, the exact depth of neutral axis shall be calculated from Eqs. 6 through 11, whichever is applicable:

For tension-controlled rectangular sections:

$$c = \frac{E_f\ A_{fe}\left(\varepsilon_{gu} - \varepsilon_{pe}\right) + P_e}{0.85\ f_c'\ \beta_1\ b} \tag{9.2-6}$$

For tension-controlled flanged sections:

$$c = \frac{E_f\ A_{fe}\left(\varepsilon_{gu} - \varepsilon_{pe}\right) + P_e - 0.85\ f_c'\ h_f\ (b - b_w)}{0.85\ f_c'\ \beta_1\ b_w} \tag{9.2-7}$$

For tension-controlled double-flanged sections:

$$c = \frac{E_f\, A_{fe}\left(\varepsilon_{gu} - \varepsilon_{pe}\right) + P_e - 0.85\, f_c'\, h_{f1}\left(b_{f1} - b_w\right) - 0.85\, f_c'\, h_{f2}\left(b_{f2} - b_w\right)}{0.85\, f_c'\, \beta_1\, b_w} \tag{9.2-8}$$

For compression-controlled flanged sections:

$$0.85\, f_c'\, \beta_1\, b_w\, c + 0.85\, f_c'\, h_f\, (b - b_w) = E_f\, A_{fe}\, \varepsilon_{cu}\left(\frac{d_1}{c} - 1\right) + P_e \tag{9.2-9}$$

For compression-controlled rectangular sections:

$$0.85\, f_c'\, \beta_1\, b\, c = E_f\, A_{fe}\, \varepsilon_{cu}\left(\frac{d_1}{c} - 1\right) + P_e \tag{9.2-10}$$

For compression-controlled double-flanged sections:

$$\begin{aligned} 0.85\, f_c'\, \beta_1\, b_w\, c + 0.85\, f_c'\, h_{f1}\left(b_{f1} - b_w\right) + 0.85\, f_c'\, h_{f2}\left(b_{f2} - b_w\right) \\ = E_f\, A_{fe}\, \varepsilon_{cu}\left(\frac{d_1}{c} - 1\right) + P_e \end{aligned} \tag{9.2-11}$$

where:

b = width of compression face of the member; for a flanged section in compression, the effective width of the flange (in. or mm)

P_e = effective prestressing force in the section (kip or N)

E_f = elastic modulus of CFRP (ksi or MPa)

ε_{cu} = average concrete crushing strain, 0.003

ε_{gu} = design guaranteed strain of CFRP including environmental and durability effects

ε_{pe} = effective prestressing strain in CFRP after subtracting applicable prestress losses

h_f = depth of compression flange (in. or mm)

b_w = width of web (in. or mm)

h_{f1} = depth of first compression flange in case of double-flanged section (in. or mm)

h_{f2} = depth of second compression flange in case of double-flanged section (in. or mm)

b_{f1} = for a double-flanged section in compression, the effective width of the first flange (in. or mm)

b_{f2} = for a double-flanged section in compression, the effective width of the second flange (in. or mm)

Equation 9.2-6 through 9.2-11 are developed by representing the natural relationship between concrete stress and strain by an equivalent rectangular concrete compressive stress block of $0.85f_c'$ over a zone bounded by the edges of the cross-section and a straight line located parallel to the neutral axis at the distance $a = \beta_1 c$ from the extreme compression fiber. The distance c is measured perpendicular to the neutral axis. The factor β_1 is taken as 0.85 for concrete strengths not exceeding 4.0 ksi (28 MPa). For concrete strengths exceeding 4.0 ksi (28 MPa), $\beta_1$is reduced at a rate of 0.05 for each 1.0 ksi (6.89 MPa) of strength in excess of 4.0 ksi (28 MPa), except that β_1 shall not be taken to be less than 0.65.

After calculating the depth of the neutral axis, the nominal moment capacity of the section can be calculated for flanged sections subjected to flexure about one axis and where the compression flange depth is less than $a = \beta_1 c$ as follows:

$$M_n = \sum_{i=1}^{m} \left[a_f \, n_i \, \varepsilon_i \, E_f \, \left(d_i - \frac{a}{2} \right) \right] + P_e \left(d_p - \frac{a}{2} \right) + 0.85 \, f_c' \, h_f \, (b - b_w) \left(\frac{a}{2} - \frac{h_f}{2} \right) \tag{9.2-12}$$

Or, for a double-flanged section:

$$M_n = \sum_{i=1}^{m} \left[a_f \, n_i \, \varepsilon_i \, E_f \, \left(d_i - \frac{a}{2} \right) \right] + P_e \left(d_p - \frac{a}{2} \right) + 0.85 \, f_c' \, h_{f1} \left(b_{f1} - b_w \right) \left(\frac{a}{2} - \frac{h_{f1}}{2} \right) + 0.85 \, f_c' \, h_{f2} \left(b_{f2} - b_w \right) \left(\frac{a}{2} - h_{f1} - \frac{h_{f2}}{2} \right) \tag{9.2-13}$$

where:

a_f = area of single CFRP strand in the ith layer (in.^{2} or mm^2)

n_i = number of CFRP strands in the ith layer

ε_i = net tensile strain at the ith layer of CFRP reinforcement determined from strain compatibility, taken equal to $\varepsilon_1 \left(\frac{d_i - c}{d_1 - c} \right)$

ε_1 = net tensile strain at the extreme CFRP layer

d_i = depth of the ith CFRP layer from the extreme compression fiber (in. or mm)

d_1 = depth of the extreme CFRP layer from the extreme compression fiber (in. or mm)

f_c' = specified compressive strength of concrete at 28 days, unless another age is specified (ksi or MPa)

P_e = effective prestressing force in the section (kip or N)

d_p = distance from the extreme compression fiber to the centroid of prestressing strands (in. or mm)

E_f = elastic modulus of CFRP (ksi or MPa)

h_f = depth of compression flange (in. or mm)

b = width of compression face of the member (in. or mm)

b_w = width of web (in. or mm)

a = $\beta_1 c$; depth of the equivalent stress block (in. or mm)

β_1 = stress block factor

c = depth of neutral axis from extreme compression fiber as determined from Eqs. 9.2-6 through 9.2-9, whichever is applicable (in. or mm)

m = number of layers (rows) of CFRP reinforcement

h_{f1} = depth of first compression flange in case of double-flanged section (in. or mm)

h_{f2} = depth of second compression flange in case of double-flanged section (in. or mm)

b_{f1} = for a double-flanged section in compression, the effective width of the first flange (in. or mm)

b_{f2} = for a double-flanged section in compression, the effective width of the second flange (in. or mm)

For rectangular sections subjected to flexure about one axis, where the approximate stress distribution is used and where the compression flange depth is not less than $a = \beta_1 c$ as determined in accordance with Eqs. 9.2-6 through 9.2-11, whichever is applicable, the nominal flexural resistance M_n may be determined by using Eq. 9.2-12, in which case b_w shall be taken as b.

In 2013 and 2014 two 45°-skewed simply supported highway bridges were constructed to carry M-102 over Plum Creek in Southfield, Michigan. Each bridge is composed of eight spread precast

prestressed box beams with a beam width of 48 in. (1219 mm), a depth of 33 in. (838 mm), and a length of 67.9 ft (20.7 m). Each beam is prestressed with 37 CFRP strands arranged in four rows. Each strand is prestressed with an initial prestressing force of 32.8 kip (146 kN).

The equivalent area method was used to calculate the nominal moment capacity of the bridge beams. The overall depth of the sections was taken as 42 in. (1067 mm) as the depth of the haunch between the deck slab and the haunch was ignored. The CFRP strands had a cross sectional area of 0.179 in.^{2} (115.2 mm^2), a modulus of elasticity of 21,000 ksi (144.8 GPa), and a guaranteed strength of 339 ksi (2237 MPa). Nevertheless, the design strength of the CFRP strands was taken as 90 % of the guaranteed strength to account for environmental conditions that might affect strand strength. Similar to steel strands, the spacing between CFRP strands was maintained at 2.0 in. (51 mm) in both directions. The deck slab had a design concrete strength of 4 ksi (28 MPa) and effective width of 8 ft (2438.8 mm). The estimated effective prestressing force after all losses was approximately 965 kip (4292 kN).

The equivalent area of reinforcement was calculated using Eqs. 9.2-3, 9.2-4, and 9.2-5 assuming a depth of neutral axis equal to 0.1 times the depth of the extreme CFRP layer (40 in. or 1016 mm). Then the actual depth of the neutral axis was calculated using Eq. 9.2-6 as the section was rectangular tension controlled. The depth of the neutral axis was calculated as 7.126 in. (181 mm) from the extreme compression fiber in the deck slab. Finally, the nominal moment capacity of the section was calculated according to Eq. 9.2-12 and was found to be 5836 kip.ft (7913 kN.m). It should be noted that the initial assumption for the depth of the neutral axis as 0.1 times the depth of the extreme CFRP layer had minimal effect on the rest of the calculations. For instance, other values for the depth of the neutral axis were assumed as shown in Table 9.2-1 and it can be shown that regardless of the initial assumption, Eq. 9.2-6 yielded nearly the same depth of the neutral axis and the change in the nominal moment capacity was negligible. On the other hand, when using strain compatibility and force equilibrium in their raw format, the exact depth of the neutral axis was found as 7.11 in. (180.6 mm) and the nominal moment capacity was 5837 kip.ft (7914). Those exact numbers can also be obtained by performing a second iteration of the equivalent area method and instead of assuming the depth of the neutral axis equal to 0.1 times the depth of the extreme CFRP layer in the second iteration, it can be assumed equal to the neutral axis depth obtained using Eq. 9.2-6 in the first iteration.

Table 9.2-1 Nominal moment capacity calculated using different assumptions for the depth of the neutral axis

Assumed value for the depth of the neutral axis, in. (mm)	Equivalent area of reinforcement according to Eqs.9.2-3 & 4, in.^{2} (mm^2)	Depth of the neutral axis according to Eq. 9.2-6, in. (mm)	Nominal moment capacity according to Eq. 9.2-12, kip.ft (kN.m)
0 (0)	6.372 (4111)	7.140 (181.4)	5834 (7910)
2 (50.8)	6.359 (4103)	7.134 (181.2)	5835 (7912)
4 (101.6)	6.345 (4094)	7.126 (181.0)	5836 (7913)
6 (152.4)	6.328 (4083)	7.116 (180.7)	5837 (7914)
8 (203.2)	6.310 (4071)	7.106 (180.5)	5837 (7914)
10 (254)	6.289 (4057)	7.094 (180.2)	5838 (7916)
12 (304.8)	6.265 (4042)	7.080 (179.8)	5839 (7917)
14 (355.6)	6.237 (4024)	7.064 (179.4)	5840 (7919)

9.3 Shear Design

This part of the report discusses a shear investigation that was conducted to evaluate the shear capacity of beams with CFRP stirrups (Grace et al. 2015). After executing the shear investigation, the beam specimens discussed herein were subjected to fire/loading events as discussed earlier in the report.

9.3.1 Test setup

Eleven decked bulb T beams were constructed, instrumented, and tested under shear loading to failure. Nine beams were reinforced and prestressed with CFCC strands, while one beam was prestressed with conventional low-relaxation steel strands and one beam was reinforced with non-prestressed CFCC strands. Half the span of each beam was reinforced with CFCC stirrups, while the other half was reinforced with conventional steel stirrups. In addition, one of the CFCC prestressed beam was provided with no stirrups within the critical shear span. Both ends of each beam were tested to evaluate the performance of CFCC stirrups versus that of steel stirrups. The investigation addressed the shear performance with respect to several shear parameters including shear-span-to-depth ratio, stirrup spacing, prestressing force, and type of longitudinal and transverse reinforcement. All test beams failed by crushing of concrete in either the web or the top flange. No rupture of CFCC stirrups was experienced in any of the test beams. The performance of CFCC stirrups was analogous to that of steel stirrups with the exception that steel stirrups demonstrated a yield plateau before concrete failure. Beam ends with CFCC stirrups attained cracking and ultimate shear capacities similar to those attained in ends with steel stirrups. Results

from the experimental investigation were compared with the theoretical values predicted using some available shear design guidelines for steel and CFCC reinforcement. In addition, modifications for current AASHTO LRFD shear design equations and its possible implementation in the ACI 440 shear design guidelines are proposed based on the experimental results.

The shear test evaluated a/d ratios of 3, 4, 5 and 6, prestressing levels per beam of 0, 72, 100, and 132 kip (0, 320, 444, and 587 kN), and stirrup spacing of 4, 6, and 8 in. (102, 152, and 203 mm). The outcome of the experimental investigation was compared with the theoretical predictions according to available design guidelines (ACI 440.1R 2006, ACI 440.4R 2004, and AASHTO LRFD 2012) and a modification is proposed to update the current AASHTO LRFD and ACI 440 shear design equations to effectively predict the shear capacity.

Nine beams had an effective span of 31 ft. (9.45 m), while two beams had an effective span of 40 ft. (12.2 m). The longitudinal prestressed and non-prestressed CFCC strands had a nominal diameter of 15.2 mm (0.6 in.). The initial prestressing force per strand was adjusted to 18 kip (80 kN) in one beam, 25 kip (111 kN) in six beams, and 33 kip (147 kN) in two beams. These prestressing levels represented 30, 41, and 54 % of the guaranteed CFCC strand capacity, respectively. As each beam was prestressed with four prestressing strands, these prestressing levels corresponded to a total initial prestressing force per beam of 72, 100, and 132 kip (320, 444, and 587 kN), respectively. In addition, one more beam was reinforced with CFCC strands with no prestressing and another beam was prestressed with conventional low relaxation steel strands with a diameter of 0.6 in. (15.2 mm) to an initial prestressing level of (132 kip) 587 kN per beam or 33 kip (147 kN) per strand. The beams were provided with transverse CFCC stirrups with a nominal diameter of 0.4 in. (10.2 mm) and No. 3 (M10) steel stirrups at a spacing of 4, 6, or 8 in. (102, 152, or 203 mm).

The beam is referred with acronym indicating multiple characteristics. The acronym includes letters and numbers. The first letter and number refer to the type of the longitudinal reinforcement (S for steel and C for CFCC) and the level of prestressing force per beam in kips [0, 72, 100, or 132 kip (0, 320, 444, or 587 kN)], respectively. The second letter and number refer to the transverse reinforcement (S for steel stirrups and C for CFCC stirrups) and the stirrup spacing in inches [4, 6, or 8 in. (102, 152, or 203 mm)], respectively. The last number refers to the a/d ratio (3, 4, 5, or 6). For example, Beam C100-S6-4 is a beam prestressed longitudinally with CFCC strands to a

level of 100 kip, provided with steel stirrups at spacing of 6 in., and loaded at a distance equal to $4\,d$ from the support, where d is the effective depth of the beam. Detailed prestressing, construction, and curing techniques of the beams can be found at Grace et al. (2012a) and Rout (2013). The concrete compressive strength averaged 6.4 ksi (44 MPa) at the time of prestress transfer and 9 ksi (62 MPa) after 28 days.

Each beam end was instrumented with approximately 60 strain and deflection sensors. Linear strain gages were attached to all longitudinal prestressing and non-prestressing strands under the loading point. Strain gages were also attached to the surfaces of the top and bottom flanges and to the flange sides as well. Linear and rosette strain gages were attached to the web of the beam within the shear span. Linear variable differential transducers (LVDTs) were mounted on the web within the shear span at angles of 0, 45, and 90 degrees. Linear motion transducers (LMTs) were attached to the soffit of the beam under the loading point and at the mid-span to record deflection. In addition, each stirrup in the shear span was instrumented with two strain gages on the vertical leg.

All beams were simply supported over two steel reinforced neoprene/elastomeric bearing pads and were loaded by a 220-kip (1000-kN) hydraulic actuator. The load was applied as a concentrated load at a distance a from the center of the support. The distance a was taken as 45, 60, 75 and 85 in. (1.1, 1.5, 1.9, and 2.2 m), which corresponded to approximate a/d ratios of 3, 4, 5, and 6, respectively.

The testing scenario for each beam was executed through two stages. First, beam end with CFCC stirrups was loaded under shear loading setup to failure. At this stage of testing, the beam was simply supported over its effective span either 31 ft or 40 ft (9.45 m or 12.2 m) and the load was applied at the distance a from the center of the support. After failure, the beam was rotated and the other end, with steel stirrups, was positioned under the loading actuator. To eliminate the already-failed portion of the beam, the far support was located under the first interior diaphragm rather than under the end of the beam. Therefore, the effective span was shortened to 23 ft or 33 ft (7 or 10 m) for beams with original effective spans of 31 ft and 40 ft (9.45 m or 12.2 m), respectively. The second beam end was then tested under the same shear loading setup, with the same a/d ratio to failure. In both stages of testing, the load was applied through incremental loading/unloading cycles and the crack map was plotted and updated at every load cycle.

9.3.2 Test results

To facilitate comparison with shear design guidelines, the results presented herein relates the response of the beams to the shear force rather than the applied load. The shear force is the reaction at the near-load support due to the applied load. The results of the investigation are summarized in Table 9.3-1**,** which shows: the cracking shear force, ultimate shear force with the corresponding under-load deflection, maximum recorded strain in the concrete top flange, the stirrups, and the longitudinal reinforcement.

The cracking shear force was obtained visually by inspecting the beam with every load cycle and was established through the load-deflection curves. A typical load deflection curve for the test beams was characterized by the change in slope with the onset of cracks. The cracking shear force was obtained by detecting the force level, where the two slopes of envelope for the load-deflection curves intersected.

Overall, the variation in the stirrup material (steel and CFCC) did not influence the cracking or maximum shear capacity of the test beams. The recorded concrete strain at failure at the top flange, on the stirrups, and on the longitudinal CFCC strands did not vary significantly between beam ends with steel stirrups and those with CFCC stirrups. It can be concluded that while the stirrups, either steel or CFCC, were actively participating in the shear loading mechanism, they did not govern the failure mode. Rather, the failure occurred due to the collapse of the concrete portion which led to the failure of the shear loading mechanism. This was confirmed from the inspection of stirrups after failure. The CFCC stirrups did not experience any rupture and while the steel stirrups yielded long before the failure, they continued to support the assigned load until the shear strain exceeded the strain required to maintain the integrity of the section and preserve a reasonable amount of the aggregate interlock.

The stirrups sustained a wide range of strain depending on their location relative to the load and support. In addition, the response of each stirrup was different during each load cycle depending on the development of diagonal cracks. The strain in the stirrups was negligible before the development of diagonal cracks but once cracks developed, there was a rapid increase in the strain. At the last load cycles, strain in the stirrups appeared to be proportional to the load with no further sudden increase, which indicted that cracking map fully developed at that region and no new cracks intersected this particular stirrup.

Table 9.3-1 Experimental results of test beams

Beam Designation	Cracking Shear Force (V_{cr})	Ultimate Shear Force (V_u)	Ultimate - Cracking Shear Force ($V_u - V_{cr}$)	Deflection Under Load (δ_u)	Top Concrete Strain (ε_{cu})	Max. Stirrups Strain ($\varepsilon_{stirrup}$)	Prestressing Strain ($\varepsilon_{prestress}$)
	kip	kip	kip	in.	με	με	με
C100-C6-3	26.8	58.7	31.9	1.6	-1282	3588	9154
C100-C6-4	19.1	52.2	33.1	3.0	-1767	3575	9465
C100-C6-5	15.5	49.1	33.6	4.1	-2624	3467	7694
C100-C6-6	14.2	46.3	32.1	5.5	-2732	3426	12688
C100-S6-3	27.2	61.2	34.0	1.4	-1642	3730	8533
C100-S6-4	20.0	53.6	33.6	2.6	-2038	3349	9061
C100-S6-5	15.7	49.6	33.9	3.5	-2639	3652	9475
C100-S6-6	12.4	44.2	31.8	4.8	-2649	3782	11794
C100-C4-3	27.9	53.8	25.9	1.3	-1042	3023	6938
C100-C8-3	28.1	53.1	25.0	1.4	-1531	3999	7072
C100-S4-3	30.6	68.1	37.5	1.7	-1937	3538	6888
C100-S8-3	28.1	51.0	22.9	1.2	-1381	3283	6838
C000-C4-3	9.4	44.0	34.6	2.3	-1558	2394	2085
C072-C4-3	23.6	58.3	34.7	2.0	-1302	2802	6065
C132-C4-3	30.4	71.3	40.9	1.8	-1520	3478	10623
C000-S4-3	11.0	51.4	40.4	2.2	-1697	3255	3059
C072-S4-3	22.3	61.6	39.3	1.8	-1806	2392	5730
C132-S4-3	30.8	69.5	38.7	1.5	-1677	3222	11509
S132-S4-3	29.7	72.0	42.3	1.6	-1973	3310	5756
S132-C4-3	29.9	68.3	38.4	1.5	-1511	3041	4614
C132-00-3	-	33.4	-	0.6	-465	-	7893

Note: 1 in. = 25.4 mm 1 kip = 4.45 kN

Theoretical shear capacity

The shear capacities of the test beams were evaluated theoretically using the simplified approach provided in ACI 440.4R-04 for prestressed concrete beams with CFRP stirrups and AASHTO LRFD 2012 for reinforced/prestressed beams with steel stirrups. The following subsections provide a detailed discussion for both provisions with their major assumptions.

Nominal Shear Capacity According to ACI 440.4R-04

ACI 440.4R assumes that the nominal shear strength, V_n , is the summation of the shear resistance provided by concrete, V_c, and the shear resistance provided by the stirrups, V_{frp}. This is in addition to the shear strength provided by the vertical component of prestressing force in case of draped strands, V_p. Therefore, the nominal shear strength V_n, N (lb), can be written as:

$$V_n = V_c + V_{frp} + V_p \tag{9.3-1}$$

V_c is taken as:

$$V_c = 0.17\sqrt{f_c'}\, b_w d \text{ (N)} \tag{9.3-2-SI}$$

or

$$V_c = 2\sqrt{f_c'}\, b_w d \text{ (lb)} \tag{9.3-2-US}$$

where, f_c' is the concrete compressive strength, psi (MPa), b_w is the effective width, in. (mm), and d is the effective depth of the section from the top fibers to the center of the longitudinal reinforcement, in. (mm).

The value of V_c considered in ACI 440.4R is the lower level of the concrete shear resistance as provided in ACI 318-02 (2002). ACI 440.4R outlines that due to the scarcity of test data for beams with CFRP stirrups, the concrete shear capacity cannot be extended beyond the minimum value mentioned in Eqn. 9-3-2 shown above. Similarly, the contribution of CFCC stirrups in the shear resistance was directly adopted from ACI 318-02 by replacing the yield strength of steel stirrups, f_y , (psi) MPa, with a corresponding permissible strength limit for CFCC stirrups, f_{fb} , psi (MPa). The shear resistance provided by the vertical CFCC stirrups, V_{frp}, lb (N), is given as:

$$V_{frp} = \frac{f_{fb} A_v d}{S} \tag{9.3-3}$$

where, A_v is the total cross-sectional area of the stirrups, $in.^2$ (mm^2), d is the effective depth, in. (mm), and S is the stirrup spacing, in. (mm).

The permissible strength of CFCC stirrups, f_{fb}, is taken as the minimum of the tensile strength of CFCC stirrups at the bend portion or the tensile strength of CFCC stirrups corresponding to a strain of 0.2 %. The choice of 0.2 % as a limiting strain is to ensure a shear performance similar to that exhibited by conventional steel stirrups with a yield strain of 0.2 % and to prevent excessive cracks that may lead to loss of aggregate interlock and loss of section integrity.

Nominal Shear Capacity According to AASHTO LRFD Simplified Approach

The simplified approach follows the same technique of calculating the shear strength of the section by adding the concrete shear strength to the stirrup shear strength. However, a more detailed methodology was followed to accurately estimate the concrete contribution, which was empirically assumed equal to the cracking shear strength of the concrete.

The nominal shear capacityV_n, N (lb), is calculated according to AASHTO LRFD simplified approach as:

$$V_n = V_n + V_n \ \leq 0.25\, f_c' b_v d_v \tag{9.3-4}$$

V_c is the lesser of V_{ci} and V_{cw}, where V_{ci} is the nominal shear resistance provided by concrete when inclined cracking results from combined shear and moment and V_{cw} is the nominal shear resistance provided by concrete when inclined cracking results from excessive principal tension in the web. For instance, considering the case before the development of cracks, the principal stresses at any element through the depth of the section can be calculated using Mohr's circle as:

$$f_{1,2} = \frac{f_x + f_y}{2} \pm \sqrt{(\frac{f_x - f_y}{2})^2 + \tau_{xy}^2} \tag{9.3-5}$$

Where,

$f_{1,2}$= Principal stresses, psi (MPa)

f_x= Normal stresses in the horizontal direction (the axis of the beam), psi (MPa)

f_y= Normal stresses in the vertical direction (perpendicular to the axis of the beam), psi (MPa)

τ_{xy}= In-plane shear stresses, psi (MPa)

f_y is theoretically negligible in case of beams subjected to bending and shear stresses only. Therefore, the eqn. of principal stresses can be written as:

$$f_{1,2} = \frac{f_x}{2} \pm \sqrt{(\frac{f_x}{2})^2 + \tau_{xy}^2} \tag{9.3-6}$$

And the maximum principal stresses shall be taken as:

$$f_1 = \frac{f_x}{2} + \sqrt{(\frac{f_x}{2})^2 + \tau_{xy}^2} \tag{9.3-7}$$

Equation 9.3-7 is valid for any element through the depth of the beam and the first crack will develop when f_1 exceeds the tensile strength of the concrete, f_t. If the tensile strength is exceeded in the web, the cracks will develop primarily as web-shear cracks, while if the tensile strength of concrete is exceeded first in the bottom flange, the cracks will develop as flexural-shear cracks. The value of f_x represents the effect of prestressing force in addition to the normal stresses due to the moment.

If an element is taken at the neutral axis (N.A.) of the beam, the normal stresses can be taken as the prestressing force divided by the area of the cross section f_{pc} (compressive stresses) and therefore, Eqn. 9.3-7 can be written as:

$$f_1 = \frac{-f_{pc}}{2} + \sqrt{\left(\frac{-f_{pc}}{2}\right)^2 + \tau_{xy}^2} \tag{9.3-8}$$

Equation 9.3-8 can be arranged to estimate the shear stress level required to develop the first shear crack at the N.A. as follows:

$$\tau_{xy} = f_1 \sqrt{1 + \frac{f_{pc}}{f_1}} \tag{9.3-9}$$

In AASHTO LRFD, Eqn. 9.3-9 was simplified and developed to estimate the web shear cracking load, V_{cw}, by multiplying τ_{xy} by the width of the web and the effective shear depth. In addition, f_1 was replaced by an estimated value for the tensile strength of concrete, f_t, and this yielded the expression for V_{cw}, which represents the shear force that causes the principal stresses at the neutral axis of the section to reach the tensile strength of the concrete. V_{cw} was expressed as:

$$V_{cw} = f_t \sqrt{1 + \frac{f_{pc}}{f_t}} b_v d_v + V_p \qquad (9.3\text{-}10)$$

To develop a simplified equation for V_{cw}, the tensile strength of the concrete was taken as $2.0\sqrt{f_c'}$ (psi) [$0.16\sqrt{f_c'}$ (MPa)]. This limit of the tensile strength was considered as a lower bound and thus a conservative estimate for the shear cracking strength. After linearizing the equation, $V_{cw}$was given in AASHTO LRFD as:

$$V_{cw} = (0.16\sqrt{f_c'} + 0.3\ f_{pc}) b_v d_v + V_p \text{ (N)} \qquad f_c' \text{ in MPa} \qquad (9.3\text{-}11\text{-SI})$$

or

$$V_{cw} = (2.0\sqrt{f_c'} + 0.3\ f_{pc}) b_v d_v + V_p \text{ (lb)} \qquad f_c' \text{ in psi} \qquad (9.3\text{-}11\text{-US})$$

On the other hand, the flexural-shear cracking strength, V_{ci}, can also be estimated by considering Eqn. 9-3-7 for an element at the soffit of the beam. In that case, f_x is taken as the stresses due to the prestressing force in addition to the flexural stresses due to the applied loads including the self-weight of beam, both calculated at the soffit of the beam, while ignoring the shear stresses at the soffit of the beam.

It should be noted that the flexural shear-cracking strength was based on the assumption that the first shear crack will occur at a minimum distance of $d/2$ from the loading point (Hawkins et al. 2005) but to simplify the equation, the term $d/2$ was ignored. It was also assumed that the flexural-shear crack will occur at slightly higher shear force than flexural cracking and the margin between shear cracking and flexural cracking was evaluated empirically and was set to $0.63\sqrt{f_c'} b_v d_v$ (lb) [$0.053\sqrt{f_c'} b_v d_v$ (N)]. Furthermore, a minimum shear cracking force of $1.9\sqrt{f_c'} b_v d_v$ (lb) [$0.16\sqrt{f_c'} b_v d_v$ (N)] was introduced to provide minimum V_c contribution over the

length of the member independent of whether a web or flexure-shear cracking regions was being designed. The final equation for V_{ci} was given as:

$$V_{ci} = 0.053\sqrt{f_c'}\, b_v d_v + V_d + \frac{V_i M_{cre}}{M_{max}} \geq 0.16\sqrt{f_c'}\, b_v d_v \;\; (N) \quad f_c' \text{ in MPa} \qquad \text{(9.3-12-SI)}$$

or

$$V_{ci} = 0.63\sqrt{f_c'}\, b_v d_v + V_d + \frac{V_i M_{cre}}{M_{max}} \geq 1.9\sqrt{f_c'}\, b_v d_v \;\; (lb) \qquad f_c' \text{ in psi} \qquad \text{(9.3-12-US)}$$

where,

V_d= shear force at section due to un-factored dead load, lb (N)

V_i= factored shear force at section due to externally applied loads occurring simultaneously with M_{max} , lb (N)

M_{max}= maximum factored moment at section due to externally applied loads, lb-in. (N-mm)

M_{cre}= moment causing flexural cracking at section due to externally applied loads, lb-in. (N-mm) and is calculated as:

$$M_{cre} = S_c(f_r + f_{cpe} - \frac{M_{dnc}}{S_{nc}}) \qquad \text{(9.3-13)}$$

f_{cpe}= compressive stress in concrete due to effective prestressing, psi (MPa)

M_{dnc}= total un-factored dead load moment acting on the monolithic or non-composite section, lb-in. (N-mm)

S_c= section modulus for the extreme fiber of the composite section where tensile stress is caused by externally applied loads, in.^{3} (mm^3)

S_{nc}= section modulus for the extreme fiber of the monolithic or non-composite section where tensile stress is caused by externally applied loads, in.^{3} (mm^3)

f_r= modulus of rupture of concrete, $f_r = 6.32\sqrt{f_c'}$ (psi) [$f_r = 0.6\sqrt{f_c'}$ (MPa)] (AASHTO LRFD)

The contribution of the stirrups was calculated based on an angle of compression strut, θ, flatter than 45° when $V_{cw}$is less thanV_{ci}. The angle θ is calculated from Mohr's circle as:

$$cot\,\theta = \sqrt{1 + \frac{f_{pc}}{f_t}} \tag{9.3-14}$$

The expression was later simplified to a linear equation and the tensile strength of the concrete f_t was conservatively taken as $4.0\sqrt{f_c'}$ (psi) [$0.32\sqrt{f_c'}$ (MPa)]. In addition, an upper bound of 1.8 was imposed on $cot\,\theta$ so that the strut angle cannot become flatter than 29° for design purposes. However, for high moment and high shear regions, diagonal cracking in flexural-shear zones was believed to occur at low shear stress and the cracks are steep, therefore $cot\,\theta$ was taken equal to 1.0 (θ = 45°) when $V_{ci} < V_{cw}$.

In its simplified format, the shear resistance by steel stirrups V_s is given as:

$$V_s = \frac{A_v f_y\, cot\,\theta}{S} \tag{9.3-15}$$

where,

If, $V_{ci} < V_{cw}$, $cot\,\theta = 1.0$ (9.3-16)

or

$cot\,\theta = 1.0 + 3\,(\frac{f_{pc}}{\sqrt{f_c'}}) \leq 1.8$, otherwise (9.3-17)

Experimental vs. Theoretical Shear Capacity

The experimental shear capacities of beams with CFCC stirrups were compared with the nominal shear capacities according to the shear provision in ACI-440.4R-04. Similarly, the shear capacities of beams with steel stirrups were compared with the nominal shear capacities according to the simplified shear design method provided in AASHTO LRFD. The following subsections present a brief description for the comparison along with a proposed adjustment for both shear provisions.

Nominal Shear Capacity According to ACI 440.4R-04

As shown in Table 9.3-2, according to ACI 440.4R-04, the concrete shear resistance V_c for the test beams was constant at 8.3 kip (37 kN). This is considering an average f_c' of 9000 psi (62 MPa), a web width b_w of 3 in. (76 mm) and a shear depth $d$of 14.6 in. (371 mm). On the other hand, V_{frp} was calculated based on stirrup strength of 43.4 ksi (300 MPa) (corresponding to a strain of 0.2%) as the strength of the bend portion was experimentally proven higher than this stress limit. The nominal shear capacity according to ACI-440.4R, V_n, was much less than the experimental shear capacity, V_u, in all test beams. The ratio V_u/V_n ranged between 1.2 and 2.4 with an average of 1.8 and a standard deviation of 0.313 (Beam C132-00-3 was excluded). It should be noted that the nominal shear resistance according to ACI-440.4R-04 accounts for the stirrup spacing but ignores both the a/d ratio and the prestressing level.

Nominal Shear Capacity According to AASHTO LRFD Simplified Approach

Table 9.3-3 shows the nominal shear resistance V_n of the section according to the simplified approach. As shown in the Table, V_{cw} for all test beams was less than V_{ci}. Therefore $V_{cw}$was the governing concrete shear-cracking strength and the angle of compression strut was flatter than 45°. However, the nominal shear capacity of the section V_n was higher than the experimental shear capacity, V_u, in all test beams. The ratio V_u/V_n ranged between 0.68 and 0.98 with an average of 0.826 and a standard deviation of 0.097. Overall, the results of the simplified approach were better than those of the ACI 440.4R-04. V_{ci} in the simplified approach showed a good correlation to the experimental cracking shear force. In addition, the nominal shear capacity for the section V_n was, to some extent, responsive to the change in stirrup spacing and prestressing level, but not to the change in a/d ratio.

Nominal Shear Capacity According to Proposed AASHTO LRFD Simplified Approach

Through the simplified approach provided by AASHTO LRFD, three different values for the tensile strength of concrete were used at three different equations: (1) $f_r = 6.32\sqrt{f_c'}$ (psi) [$f_r = 0.6\sqrt{f_c'}$ (MPa)] (AASHTO LRFD section 5.4.2.6) in calculating M_{cre} to calculate the flexural-shear cracking force V_{ci}, (2) $f_t = 2.0\sqrt{f_c'}$ (psi) [$f_t = 0.16\sqrt{f_c'}$ (MPa)] to calculate the web-shear cracking force V_{cw}, and (3) $f_t = 4.0\sqrt{f_c'}$ (psi) [$f_t = 0.32\sqrt{f_c'}$ (N)] to calculate the angle of

compression strut θ. While it seems reasonable to use a lower bound for the web-shear cracking force, this approach resulted in an over estimation of the nominal shear resistance in the test beams. In current AASHTO LRFD, V_{cw} has been intentionally reduced by reducing f_t and thus it always controlled the concrete cracking shear force for the test specimens. Consequently, V_s was calculated using an angle of compression strut flatter than 45° (or $\cot\theta > 1.0$).

Had the same value for f_t been used to calculate both V_{cw} and V_{ci}, the governing shear cracking force would have been V_{ci} and V_s would have been calculated with angle of compression strut equal to 45° (or $\cot\theta$ of 1.0). Adding V_{cw} to the corresponding V_s (with $\cot\theta > 1.0$) resulted in V_n larger than that when V_{ci} was added to the corresponding V_s (with $\cot\theta = 1.0$). This was the chief reason for the consistently higher theoretical shear capacity when compared with the experimental capacity of the test beams.

Therefore, it is suggested that both V_{cw} and V_{ci} need to be calculated considering the same f_t or f_r. It is possible that the designer chooses a lower value for f_r than what is currently specified by AASHTO LRFD ($7.6\sqrt{f_c'}$ psi or $0.63\sqrt{f_c'}$ MPa) to be on the conservative side but the same reduced value needs to be implemented in calculating both V_{cw} and V_{ci}.

For the current investigation, V_{cw} and V_{ci} were calculated assuming a concrete modulus of rupture equal to the tensile strength of concrete and equal to $7.6\sqrt{f_c'}$ (psi) [$0.63\sqrt{f_c'}$ (MPa)]. In addition, the component that accounts for the difference between the flexural cracking and the flexural-shear cracking strength $0.63\sqrt{f_c'}b_v d_v$ (lb) [$0.053\sqrt{f_c'}b_v d_v$ (N)] was ignored. The value of V_{ci} was found to be always less than V_{cw}. In different words, all the specimens in the current investigation failed due to flexural-shear cracking rather than web-shear cracking. Further, the values of V_{ci} calculated using the proposed modified equations matched very well with the reported experimental cracking shear force. The prestress loss was taken as 15 % for all test beams.

As shown in Table 9.3-2 and Table 9.3-3, the simplified approach with the proposed modification predicts with good accuracy the ultimate shear strength of the test beams provided with either CFCC or steel stirrups. In case of beams with CFCC stirrups, the ratio V_u/V_{n_mod} ranged between 0.74 and 1.07 with an average of 0.945 and a standard deviation of 0.107 and on exclusion of the prematurely failed beam (C100-C4-3), the average increases to 0.97 with a corresponding standard deviation of 0.088. The shear resistance provided by CFCC stirrups was

calculated based on a strain limit of 0.35 % as given by AASHTO LRFD (Section 5.8.2.5), which appears to be a reasonable estimate for the maximum allowable strain in CFRP stirrups. For sections with conventional steel stirrups, the use of the yield strength (with a yield strain of 0.2 %) as the limiting stirrup strength remains adequate as it yielded reasonable estimate for the nominal shear capacity of the test specimens. In case of beams with steel stirrups the ratio V_u/V_{n_mod} ranged between 0.90 and 1.09 with an average of 1.00 and a standard deviation of 0.064. Overall, V_{n_mod} in the proposed approach showed good correlation with the experimental results and it corresponded well to the shear parameters including stirrup spacing, a/d ratio, and prestressing level.

In the light of current experimental study, it was not possible to comment on the calculation of the angle of compression strut when V_{cw} is governing but it may remain as recommended by current AASHTO LRFD simplified approach until further evaluation is available.

It is worth noting that the research team faced a significant difficulty adopting a closer stirrup spacing than 102 mm (4 in.). As shown in Table 9.3-2 and Table 9.3-3, the shear strength of beams with stirrup spacing of 4 in. (102 mm) failed on the un-conservative side with respect to the calculated average shear capacity using the proposed simplified approach. The research team believe that the reduced shear capacity with stirrup spacing of 4 in. (102 mm) can be attributed to constructability issues; the thickness of the web in the test specimens was limited to 3 in. (76 mm). Further, every stirrup in the shear span was instrumented with two properly insulated strain gages. The tight spacing between the stirrups and the insulation of the strain gages resulted in a slight disturbance in the compression struts and slightly lowered the shear strength of the section. This is clearly manifested in the premature failure of beam C100-C4-3.

The simplified approach of AASHTO LRFD provides a limit for the maximum shear strength as $0.25\, f_c' b_v d_v$ to guard against crushing of the web or the diagonal compression failure. Hawkins et al. (2005) provided a detailed discussion for this limit and suggested a limit of $0.18\, f_c' b_v d_v$to guard against horizontal shear failure along the interface between the web and the bottom flange for a beam without end block. These two limits correspond to average diagonal compressive stresses of $0.6\, f_c'$ and $0.4\, f_c'$, respectively. Through the current investigation it was observed that a limit of $0.25\, f_c' b_v d_v$ yielded an ultimate shear strength of 90.8 kip (404 kN), while a limit of $0.18\, f_c' b_v d_v$ yields 65.4 kip (291 kN). The maximum experimental shear strength

obtained through the experimental investigation was 72 kip (320 kN) in Beam S132-S4-3, which corresponded to a limit of $0.2\ f_c' b_v d_v$. It seems that the limit of AASHTO LRFD tends to be unattainable, at least for the current test specimens, where stirrup spacing less than 4 in. (102 mm) was not feasible to adopt and where premature failure already took place at a smaller stirrup spacing (Beam C100-C4-3).

Table 9.3-2 Experimental vs. calculated shear resistance in beams with CFCC stirrups

Beam	Exp. Shear Force (kip)		ACI-440.4R-04 (kip)				Modified AASHTO LRFD (kip)				
	V_{cr}	V_u	V_c	V_{frp}	V_n	$\frac{V_u}{V_n}$	V_{ci}	V_{cw}	V_{frp}	V_{n_mod}	$\frac{V_u}{V_{n\_mod}}$
C100-C6-3	26.8	58.7	8.3	19.1	27.2	2.10	26.5	39.1	30.8	57.3	1.02
C100-C6-4	19.1	52.2	8.3	19.1	27.2	1.90	19.6	39.1	30.8	50.4	1.04
C100-C6-5	15.5	49.0	8.3	19.1	27.2	1.80	15.5	39.1	30.8	46.1	1.07
C100-C6-6	14.2	46.3	8.3	19.1	27.2	1.70	13.5	39.1	30.8	44.3	1.05
C100-C4-3	27.9	53.7	8.3	28.6	36.9	1.50	26.5	39.1	46.1	72.6	0.74
C100-C8-3	28.1	53.1	8.3	14.4	22.7	2.40	26.5	39.1	22.9	49.7	1.07
C000-C4-3	9.4	44.1	8.3	28.6	36.9	1.20	5.62	28.1	46.5	51.9	0.84
C072-C4-3	23.6	58.2	8.3	28.6	36.9	1.60	20.7	36.4	46.1	66.8	0.87
C132-C4-3	30.4	71.3	8.3	28.6	36.9	1.90	32.6	42.0	45.9	78.7	0.91
S132-C4-3	29.9	68.3	8.3	28.6	36.9	1.90	32.6	42.0	45.9	78.7	0.87
C132-00-3[2]	--	32.4	8.3	----	8.3	3.90	32.6	42.0	---	32.6	0.99
Average						1.800					0.970[1]
Standard Deviation						0.313					0.088[1]

(1) Beam C100-C4-3 was excluded for premature failure.
(2) Beam C132-00-3 was excluded from the average and standard deviation
Note: 1 kip = 4.45 kN

Table 9.3-3 Experimental vs. calculated shear resistance in beams with steel stirrups

Beam	Exp. Shear Force (kip)		AASHTO LRFD 2012 (kip)					Modified AASHTO LRFD (kip)				
	V_{cr}	V_u	V_{ci}	V_{cw}	V_s	V_n	$\frac{V_u}{V_n}$	V_{ci}	V_{cw}	V_s	V_{n_mod}	$\frac{V_u}{V_{n\_mod}}$
C100-S6-3	27.2	61.2	29.7	15.5	49.5	65.0	0.94	27.2	39.1	29.7	56.7	1.08
C100-S6-4	20.0	53.5	22.7	15.5	49.5	65.0	0.83	20.0	39.1	29.7	49.7	1.08
C100-S6-5	15.7	49.7	18.4	15.5	49.5	65.0	0.76	16.0	39.1	29.7	45.4	1.09
C100-S6-6	12.4	44.3	16.4	15.5	49.5	65.0	0.68	13.9	39.1	29.7	43.6	1.01
C100-S4-3	30.6	68.1	29.7	15.5	74.2	89.7	0.76	27.2	39.1	44.5	71.5	0.95
C100-S8-3	28.1	51.0	19.7	15.5	37.1	52.6	0.97	27.2	39.1	22.3	49.2	1.03
C000-S4-3	11.0	51.5	8.5	7.4	44.7	52.2	0.98	5.8	28.1	45.0	50.8	1.01
C072-S4-3	22.3	61.6	23.6	13.3	66.1	79.1	0.78	21.1	36.4	44.5	65.6	0.94
C132-S4-3	30.8	69.5	36.4	18.0	79.8	91.1[1]	0.77	33.3	42.0	44.3	77.6	0.90
S132-S4-3	29.7	72.0	36.4	18.0	79.8	91.1[1]	0.79	33.3	42.0	44.3	77.6	0.93
Average							0.826					1.000
Standard Deviation							0.097					0.064

(1) Governed by the maximum shear strength $0.25\, f_c' b_v d_v$
Note: 1 kip = 4.45 kN

Modified compression field theory according to AASHTO LRFD 2014 (Section 5.8.3.3, General Procedure Subsection 5.8.3.4.2)

, According to AASHTO LRFD and similar to the simplified approach, the shear strength in steel prestressed beams without draping is calculated through the general procedure by adding concrete shear strength to the shear strength provided by the stirrups:

$$V_n = V_c + V_s \tag{9.3-18}$$

Concrete shear strength is a function of a factor β, which in turn is a function of the bottom steel strain ε_s that is developed due to the combined action of moment and shear force, M_u and V_u. Therefore, concrete contribution to the shear capacity of the section is calculated as:

$$V_c = 0.0316\,\beta\sqrt{f_c'}\,b_v d_v \tag{9.3-19}$$

Contribution of stirrups in shear strength is a function of a factor θ, which is also a function of the bottom steel strain ε_s that is developed due to the combined action of moment and shear force, M_u and V_u. Contribution of the shear reinforcement is expressed in AASHTO LRFD as:

$$V_s = \frac{A_v\, f_y\, d_v\, cot\theta}{S} \tag{9.3-20}$$

Both factors β and θ are calculated using empirical equations (as a function of ε_s) that have been calibrated using experimental test results from testing steel prestressed beams. β and θ are calculated as:

$$\beta = \frac{4.8}{(1 + 750\,\varepsilon_s)} \tag{9.3-21}$$

$$\theta = 29 + 3500\,\varepsilon_s \tag{9.3-22}$$

However, there is upper and lower limits for the strain value, ε_s. According to AASHTO LRFD:

$$-0.4 \times 10^{-3} \le \varepsilon_s \le 6.0 \times 10^{-3} \tag{9.3-23}$$

Therefore, the values for β and θ can range from the minimum and maximum as given in Table 9.3-4. According to the equations, increasing ε_s results in decreasing both V_c and V_s and thereby, reducing the overall shear capacity of the section. Nevertheless, beams prestressed with CFRP strands experience higher bottom strain than that in beams prestressed with steel strands, especially, when comparing the strain at the same load level before the yield of reinforcement. Therefore, the theoretical shear capacity according to current general procedure of AASHTO LRFD for beams prestressed with CFCC strands tends to be remarkably low most of the time, considering the higher bottom CFCC strain.

Table 9.3-4 Limits for the shear factors β and θ based on the limits of bottom strain, ε_s

ε_s	β	θ
-0.4×10^{-3}	6.85	27.6
6.0×10^{-3}	0.872	50

Table 9.3-5 shows a comparison between the experimental and the theoretical nominal shear capacities of the beams using the AASTHO LRFD general procedure. The strain at the level of bottom reinforcement was calculated according to AASTHO equations and the theoretical nominal shear capacity was calculated twice and presented in the tables as V_{n1} and V_{n2}: Nominal shear capacityV_{n1} was calculated without imposing the upper limit of 0.006 on the bottom strain, while nominal shear capacity V_{n2} was calculated based on the bottom stain with a maximum value of 0.006.

With the upper limit of ε_s (0.006) in place, and based on the experimental test results for the CFCC prestressed decked bulb T beams with CFCC stirrups, it appears that current AASHTO equations are quite conservative with an average experimental to theoretical shear capacity of 1.58 (a maximum of 1.98 and minimum of 1.04) and a standard deviation of 0.33. Without enforcing the upper limit of ε_s (0.006) and based on the experimental test results for the same beams, it appears that current AASHTO equations are also conservative with an average experimental to theoretical shear capacity of 1.74 (with a maximum of 2.2 and minimum of 1.1) and a standard deviation of 0.41.

Similarly, with the upper limit of ε_s (0.006) in place, and based on the experimental test results for the CFCC prestressed decked bulb T beams with steel stirrups, it appears that current AASHTO equations are quite conservative with an average experimental to theoretical shear capacity of 1.71 (a maximum of 2.15 and minimum of 1.25) and a standard deviation of 0.25. Without enforcing the upper limit of ε_s (0.006) and based on the experimental test results for the same beams, it appears that current AASHTO equations are also conservative with an average experimental to theoretical shear capacity of 1.93 (with a maximum of 2.28 and minimum of 1.59) and a standard deviation of 0.23.

Based on the shear testing of one steel prestressed decked bulb T beams provided with steel stirrups it appears that current AASHTO equations are conservative with an experimental to theoretical shear capacity of 1.30. In addition, based on the shear testing of one steel prestressed decked bulb T beams provided with CFCC stirrups it appears that current AASHTO equations are still conservative with an experimental to theoretical shear capacity of 1.14. In both cases the calculated strain at the level of reinforcement at the time of failure was less than the limit of 0.006.

Therefore, it can be concluded that current AASHTO eqn. are quite conservative when directly used in estimating the shear capacity of beams prestressed with CFCC strands regardless of the type of transverse reinforcement whether it is steel stirrups or CFCC stirrups. Current AASHTO equations can be recalibrated based on the current available test results to further reduce the factor of safety to a reasonable level. However, since the equations are mostly empirical, the calibration shall not be limited to a single test program and shall extend to include test results from multiple programs for beams with different cross sections and different reinforcement configuration. This, however, is beyond the scope of the current report. Therefore, it is recommended, based on available test results, to maintain current provision of the AASHTO LRFD for the shear design using the general procedure and apply it to CFRP prestressed beams using the same factors of β and θ as recommended for steel prestressed beam.

Table 9.3-5 Nominal shear capacities of test beams using general procedure

Beam Designation	Ultimate shear force (V_u)	Calculated bottom strain (ε_s)	Nominal shear force[1] (V_{n1})	$\frac{V_u}{V_{n1}}$	Nominal shear force[2] (V_n)	$\frac{V_u}{V_{n2}}$
	kip	με	kip		kip	
C100-C6-3	58.7	5503	30.9	1.89	30.9	1.89
C100-C6-4	52.2	(6585)	27.0	1.93	29.1	1.80
C100-C6-5	49.1	(7931)	22.7	2.16	29.1	1.69
C100-C6-6	46.3	(8501)	21.1	2.20	29.1	1.59
C100-S6-3	61.2	5905	28.5	2.15	28.5	2.15
C100-S6-4	53.6	(6857)	25.3	2.12	28.2	1.90
C100-S6-5	49.6	(8048)	21.7	2.28	28.2	1.76
C100-S6-6	44.2	(7954)	21.9	2.01	28.2	1.57
C100-C4-3	53.8	4760	49.0	1.10	49.0	1.10
C100-C8-3	53.1	4652	26.9	1.98	26.9	1.98
C100-S4-3	68.1	(6973)	35.9	1.89	40.6	1.68
C100-S8-3	51.0	4327	27.2	1.87	27.2	1.87
C000-C4-3	44.0	(6754)	38.5	1.14	42.4	1.04
C072-C4-3	58.3	(6434)	39.8	1.46	42.0	1.39
C132-C4-3	71.3	(6355)	40.0	1.78	41.8	1.71
C000-S4-3	51.4	(7890)	32.3	1.59	41.0	1.25
C072-S4-3	61.6	(6944)	36.2	1.70	40.7	1.51
C132-S4-3	69.5	(6076)	40.1	1.73	40.5	1.72
S132-S4-3	72.0	3503	55.5	1.30	55.5	1.30
S132-C4-3	68.3	3192	59.7	1.14	59.7	1.14

Note: 1 kip = 4.45 kN

CHAPTER 10: SUMMARY & CONCLUSIONS

Based on the comprehensive investigation and test results that were presented in this report, the following conclusions can be drawn:

1. In a uniaxial tensile test of a CFRP specimen, points of anchorage represent the weakest points in the specimen. Failure at maximum load is likely to initiate near the anchorage points regardless of the type of anchorage. Therefore, tensile strength of CFRP is dependent on quality control of assembling and preparing the anchorage devices.
2. A properly assembled wedge anchorage device, following the manufacturer's guidelines, withstands a load higher than the guaranteed strength of the CFRP without slippage or failure.
3. Average tensile strength of CFCC strands with a diameter of 0.6 in. (15.2 mm) is 70 kip (311 kN), which is approximately 15 % higher than the recommended guaranteed strength by the manufacturer (60.7 kip or 270 kN).
4. Minimum estimate for one-million-hour creep rupture strength of CFCC strands with a diameter of 0.6 in. (15.2 mm) is not less than 86 % of the average CFCC tensile strength, or nearly equal to the CFCC guaranteed tensile strength as recommended by the manufacturer (60.7 kip or 270 kN). This estimate is based on available test results at the time of writing and submitting this report.
5. Under sustained load levels higher than 90 % of the average tensile strength of CFCC, test specimens either ruptured within the first 100 hours of loading or continued to sustain the load without signs of creep. For instance, five CFCC specimens with a diameter of 0.6 in. (15.2 mm) loaded to 92 % of their average tensile strength or 105 % of their guaranteed strength have been sustaining the applied load for 11,200 hours (468 days) at the time of writing this report. Similarly, CFCC specimens with a diameter of 0.7 in. (17.8 mm) loaded to 108 % of their guaranteed strength have been sustaining the applied load for 18,600 hours (775 days) at the time of writing this report.
6. The one-million-hour relaxation rate, defined as the expected percentage loss in the force in a CFRP strand over one million hours, of CFCC strands with a diameter of 0.6 in. (15.2

mm) is approximately 1.9 % based on available test results. Weather conditions do not seem to induce additional relaxation or permanently alter the prestress loss in unbonded CFCC strands. Nevertheless, high temperature seems to induce additional heat related relaxation. For instance, at a temperature similar to the heat curing temperature of the concrete (150 °F or 66 °C), it was observed that CFCC strands with a diameter of 0.6 in. (15.2 mm) experience additional relaxation of approximately 250 με, which in prestressing application represent a prestress loss of 5 to 6 ksi or 900 to 1000 lb (4 to 4.5 kN) per strand.

7. Average static bond strength between CFCC strands with a diameter of 0.6 in. (15.2 mm) and uncracked concrete with an average 28-day compressive strength of 10 ksi (69 MPa) is approximately 1.6 ksi (11 MPa). Nevertheless, cyclic loading affects the bond strength between CFCC and concrete.

8. To avoid bond failure in case of locations subjected to cyclic loading, the bond strength between concrete and CFCC shall be limited to approximately 64 % of the average static bond strength, which results in a bond strength of approximately 1.0 ksi (6.9 MPa) between concrete and CFCC strands with a diameter of 0.6 in. (15.2 mm).

9. Splice failure of CFRP may occur as a result of: (1) concrete splitting, (2) strand pullout, or (3) pullout from severely cracked concrete. Concrete splitting is a common mode of failure of both steel and CFRP and is attributed to an inadequate concrete cover or confinement. Strands pullout is also a common mode of failure in CFRP and steel and is attributed to an inadequate bond length of the reinforcement. Pullout from severely cracked concrete is a unique mode of failure that is noticed in CFRP at high strain level (much higher than the yield strain of steel). It occurs due to the lower elastic modulus of CFRP and higher maximum strain of CFRP compared to steel yield strain. It is attributed to the deterioration of the concrete-CFRP bond strength due to severe concrete cracking around the strand.

10. Tensile strength of CFCC strands is affected by the increase in temperature. At a temperature of 400 °F (204 °C), the tensile strength of CFCC is approximately 78 % of its ambient tensile strength. Nevertheless, prestressed CFCC specimens heated to 400 °F (204 °C) and then were allowed to cool down before they were tested at ambient temperature achieved their ambient average tensile strength.

11. Fire endurance for a prestrssed beam is defined as the period of time at which the prestressed beam continues to effectively support service loads in case of a fire event before any major failure or collapse. Under a standard ASTM E-119 time-temperature curve, the fire endurance of simply supported half-scale CFCC prestressed decked bulb T beams under three-point-load setup was approximately 69, 53, and 47 minutes for prestress levels of 30, 41, and 54 % of the CFCC guaranteed strength.

12. An identical half-scale steel prestressed decked bulb T beam with a prestress level equal to 56 % of the steel ultimate strength lasted for 98 minutes under similar fire and loading conditions.

13. Average tensile strength of CFCC strands subjected to 300 cycles of freezing and thawing is approximately 15 % higher than the average strength of CFCC specimens not subjected to freeze-thaw cycles.

14. Due to the difference in thermal expansion between concrete and CFRP, beams prestressed with CFRP strands experience a loss in the prestressing force with the decrease in temperature. However, this loss in prestressing is recovered when the temperature increases back to the normal range. Similarly, they experience gain in the effective prestressing force when the temperature increases but this gain in prestressing is lost once the temperature drops down to the normal range. The gain or loss in effective prestressing force conforms with the theoretical thermal expansion and contraction calculations.

15. Freeze-thaw cycles do not seem to have any detrimental effect on CFCC strands. On the other hand, freeze-thaw cycles do cause significant deterioration and reduction in the concrete strength. Therefore, by weakening the concrete side, exposure to freeze-thaw cycles can alter the mode of failure from tension-controlled to compression-controlled and reduce the nominal moment capacity of a CFRP prestressed beam.

16. Environmental conditions seem to affect the concrete more than CFCC strands. Therefore, while an environmental reduction factor may not be necessary for CFRP strands, it shall be adjusted to address concrete deterioration especially in compression-controlled sections.

17. In a two-year test program, CFCC prestressed beams kept outdoors and exposed to different environmental conditions showed a slight increase in compressive strength and

maximum load capacity than those observed in identical beams stored indoors. The difference can be attributed to the extended exposure to rain and moist conditions, which resulted in extended concrete curing. This conclusion does not contradict the previous conclusion, since further extended exposure to weather conditions especially repeated freeze-thaw cycles will eventually lead to deterioration in concrete strength.

18. No significant change in prestress loss was observed over a period of two years between five identical CFCC prestressed bulb T beams stored either indoors or outdoors. In addition, all five beams experienced compression-controlled mode of failure with no evidence of any significant deterioration in the mechanical properties of CFCC strands.

19. Elastic prestress loss as well as long-term prestress loss due to concrete creep and shrinkage can be reasonably estimated in a CFRP prestrssed beam using prestress loss equations developed for steel strands and provided in current codes and guidelines such as AASHTO LRFD and PCI. Prestress loss due to relaxation of CFRP strands is pertinent to the relaxation characteristics of the CFRP material. In addition, the temporary change in prestressing force due to seasonal temperature change shall be calculated and considered in the design of CFRP prestressed beams.

20. The depth of the neutral axis and the nominal moment capacity of a section prestressed with CFRP strands distributed over multiple rows of reinforcement can be calculated using conventional strain compatibility and force equilibrium approach by assuming an equivalent stress block distribution on the concrete. To facilitate the calculations and minimize the number of iterations, the strain compatibility approach may be rearranged in the form of an equivalent area method. The equivalent area method simply replaces area of CFRP at any row with a reduced discrete area at level of the extreme CFRP row to facilitate the calculations of the depth of the neutral axis and verify the mode of failure. After establishing the depth of the neutral axis, the strain and stress in each row of CFRP strands can be calculated using strain compatibility and the nominal moment capacity of the section can be accurately estimated.

21. A tension-controlled section in beams prestressed with CFRP strands is defined as a cross section in which the strain of concrete in compression at nominal resistance is less than

maximum usable concrete strain just as the net tensile strain in the extreme tension CFRP reaches its net guaranteed strain limit.

22. A compression-controlled section in beams prestressed with CFRP strands is defined as a cross section in which the net tensile strain in the extreme tension CFRP at nominal resistance is less than the net guaranteed strain limit just as the concrete in compression reaches its assumed maximum usable concrete strain.

23. Balanced strain conditions exist at a cross-section when tension CFRP reinforcement reaches the strain corresponding to its design guaranteed strength just as the concrete in compression reaches its assumed ultimate strain of 0.003.

24. The shear design of CFRP prestressed beams with either steel or CFRP stirrups can be performed using either a simplified approach or a general procedure. The simplified approach equations were calibrated and reproduced to ensure a proper shear design. The general procedure as defined in the current edition of AASHTO LRFD yields conservative estimates for the shear capacities of beams prestressed with CFRP strands. This is attributed to the fact that the general procedure considers the bottom strain, at the level of bottom reinforcement, in the shear design. As the bottom strain increases, the shear capacity of the section decreases and vise-versa. Due to the lower elastic modulus of CFRP, beams prestressed with CFRP exhibits larger bottom strain values, after cracking, than those prestressed with steel strands and therefore, their shear capacities according to the general procedure in its current format is less than those of beams prestressed with steel strands.

REFERENCES

1. AASHTO, 2014, "AASHTO LRFD Bridge Design Specifications," 7th ed., American Association of State Highway and Transportation Officials, Washington, DC.
2. Abbasi, A & Hogg, Paul., 2006, "Fire Testing of Concrete Beams with Fibre Reinforced Plastic Rebar," Composites Part A: Applied Science and Manufacturing. Vol. 37, Issue No. 8, pp. 1142-1150
3. Achillides, Z. and Pilakoutas, K., 2004, "Bond Behavior of Reinforced Polymer Bars under Direct Loading," Journal of Composites for Construction, Vol. 8, Issue No. 2, pp. 173-181.
4. Akbas, T., Celik, O., Yalcin, C., and Ilki, A., 2016, "Monotonic and Cyclic Bond Behavior of Deformed Cfrp Bars in High Strength Concrete," Polymers, Vol. 8, Issue No. 6, doi: 10.3390/polym8060211.
5. Ali, A., Mohamed, H., Benmokrane, B., and Elsafty, A., 2018, "Effect of Applied Sustained Load and Severe Environments on Durability Performance of Carbon-Fiber Composite Cables," Journal of Composite Materials, Vol. 53, No. 5, pp. 677–692.
6. Alsiwat, J.M.; Saatcioglu, M.,1992, "Reinforcement anchorage slip under monotonic loading," ASCE J. Struct. Eng., Vol. 118, issue No. 9, pp. 2421–2438
7. American Concrete Institute (ACI), 2015, "Guide for the Design and Construction of Structural Concrete Reinforced with FRP Bars," ACI 440.1R-15, Farmington Hills, MI.
8. American Concrete Institute (ACI), 2012, "Guide Test Methods for Fiber-Reinforced Polymer (FRP)Composites for Reinforcing or Strengthening Concrete and Masonry Structures," ACI 440.3R-12, Farmington Hills, MI.
9. American Concrete Institute (ACI), 2004, "Prestressing Concrete Structures with FRP Tendons," ACI 440.4R-04, Farmington Hills, MI.
10. American Concrete Institute (ACI), 2014, "Building code requirements for structural concrete and commentary," ACI 318-14, Farmington Hills, MI.
11. Ando, N., Matsukawa, H., Hattori, A., and Mashima, A., 1997, "Experimental Studies on the Long-term Tensile Properties of FRP Tendons," Proceedings of the Third International

Symposium on Non-Metallic (FRP) Reinforcement for Concrete Structures (FRPRCS-3), Sapporo, Japan, Vol. 2, 203-210.

12. Ashton, L. A., Malhotra, H. L., 1953, “The Fire Resistance of Prestressed Concrete Beams,” Fire Res. Notes (1953), p. 65
13. ASTM Standard C666, 2008, “Test Method for Resistance of Concrete to Rapid Freezing and Thawing," ASTM International, West Conshohocken, PA, USA. DOI: 10.1520/C0666_C0666M-03R08, www.astm.org.
14. Balazs, G.L. and Borosnyoi, A., 2001, “Long-Term Behavior of FRP.” In: Cosenza E, Manfredi G, Nanni A, editors, Proceedings of the international workshop ‘‘Composites in construction: a reality,’’ American Society of Civil Engineers, Reston, pp. 84–91.
15. Barr, P. J., Stanton, J. F., and Eberhard, M. O., 2005 “Effects of Temperature Variations on Precast, Prestressed Concrete Bridge Girders.” Journal of Bridge Engineering, Vol. 10, No. 2, pp. 186-194.
16. Bryan, P.E., Green, M. F., 1996, “Low Temperature Behavior of CFRP Prestressed Concrete Beams,” Canadian Journal of Civil Engineering, V. 23, No. 2, Apr., pp. 464-470.
17. CAN/CSA-S6-06, 2006, “Canadian Standards Association Highway Bridge Design Code.”
18. Canadian Standards Association (CAN/CSA-S806). (2002). “Design and construction of building components with fibre reinforced polymers,” CSA International, Rexdale, Ontario, Canada.
19. Ceroni, Francesca, E. Cosenza, M. Gaetano, M. Pecce, 2006, “Durability Issues of FRP Rebars in Reinforced Concrete Members,” Cement and Concrete Composites, vol. 28, No. 10, pp. 857–868.
20. Cusson, R., Xi, Y., 2002, “The Behavior of Fiber-Reinforced Polymer Reinforcement in Low Temperature Environmental Climates,” Report No. CDOT-DTD-R-2003, *Colorado Department of Transportation*, 97p.
21. Curtis, P. T., 1989, “The Fatigue Behavior of Fibrous Composite Materials,” Journal of Strain Analysis, V. 24, No. 4, pp. 235-244. doi: 10.1243/03093247V244235

22. Den Uijl, J. A. ,1995, ‘‘Bond and Fatigue Properties of Arapree,’’ Proc.,RILEM Int. Conf. on Non-Metallic (FRP) Reinforcement for Concrete Struct., L. Taerwe, ed., E & FN Spon, London, pp. 146-153.

23. Dutta, P. K., 1988, “Structural Fiber Composite Materials for Cold Regions,” *Journal of Cold Regions Engineering,* No. 3, pp. 124-132.

24. Elbadry, M. M., Abdalla, H., & Ghali, A., 2000, “Effects of Temperature on the Behaviour of Fiber Reinforced Polymer Reinforced Concrete Members: Experimental Studies,” *Canadian Journal of Civil Engineering*, 27(5), 993-1004.

25. El-Hacha, R., Wight, R. G., and Green, M. F., 2004, “Prestressed Carbon Fiber Reinforced Polymer Sheets for Strengthening Concrete Beams at Room and Low Temperatures,” *Journal of Composites for Construction*, V.8, No.1, pp. 3–13.

26. Enomoto, T., Harada, T., Ushijima, K., and Khin, M., 2009, “Long term relaxation characteristics of CFRP cables,” Proc., 4th Int. Conf. on Construction Materials (ConMat09), Japan Concrete Institute, Japan, pp. 1205–1210.

27. Ezeldin, A. and Balaguru, P., 1989, “Bond Behavior of Normal and High-strength Fiber Reinforced Concrete,” ACI Materials Journal, Vo. 86, Issue No. 5, pp. 515-524

28. Gerritse, A., and Den Uijl, J. A., 1995, ‘‘Long-term Behavior of Arapree.’’ Proc., 2nd Int. Symp. on Non-Metallic (FRP) Reinforcement for Concrete Structures, L. Taerwe, ed., E & FN Spon, London, pp. 57–66.

29. Grace, N., Ushijima, K., Rout, S., and Bebawy, M., 2015, “Performance of CFRP Stirrups in Prestressed Decked Bulb T Beams,” ASCE Journal of Composites for Construction, 1090-0268/04014061, May/June, Vol. 19, Issue 3.

30. Grace, N., and Bebawy, M., 2014, “Fire Protection for Beams with Fiber-Reinforced Polymer Flexural Strengthening Systems,” ACI Structural Journal, V. 111, Issue 3, pp. 537-548

31. Grace, N., Ushijima, K., Baah, P. and Bebawy, M., 2013a, “Behavior of CFRP Prestressed Decked Bulb-T Beam Bridge System,” ASCE Journal of Composites for Construction, Vol. 17, No. 4, July/Aug., pp. 497-506.

32. Grace, N., Ushijima, K. Matsagar, V., and Wu, C., 2013b, “Performance of AASHTO-type bridge model prestressed with carbon fiber-reinforced polymer reinforcement,” ACI Structural Journal. Vol 110, Issue 3, pp. 491-501.

33. Grace, N., Jensen, E., Matsagar, V., and Penjendra, P., 2013c, “Performance of an AASHTO beam bridge prestressed with CFRP tendons,” Journal of Bridge Engineering. 18. 110-121. 10.1061/(ASCE)BE.1943-5592.0000339.

34. Grace, N., Enomoto, T., Baah, P. and Bebawy, M., 2012a, “Flexural Behavior of CFRP Precast Prestressed Decked Bulb T Beams,” ASCE Journal of Composites for Construction, Vol. 16, No. 3, May/June, pp. 225-234.

35. Grace, N., Jensen, E., Eamon, C, Shi, X., 2012b, “Life Cycle Cost Analysis of CFRP Reinforced Concrete Bridges,” ACI Str. Journal, Vol. 109, Issue 5, pp. 697-704

36. Grace, N., Jensen, E., and Bebawy, M, 2012c, “Transverse post-tensioning arrangement for side-by-side box-beam bridges”, PCI Journal, Vol. 57, Issue 2, Spring, pp 48-63.

37. Grace, N., Kapil, P., Soliman, I., and Hanson, J., 2011a, “Flexural Behavior of Side-by-Side Box Beam Bridges – a Comparative Study”, PCI Journal, Vol 56, Issue 3, June, pp 94-112.

38. Grace, N., Jensen, E., and Noamesi, D., 2011b, “Flexural Performance of Carbon Fiber-Reinforced Polymer Prestressed Concrete Side-by-Side Box Beam Bridge,” Journal of Composites for Construction. 15. 10.1061/(ASCE)CC.1943-5614.0000207.

39. Grace, N., Jensen, E, Matsagar, V, Soliman, E., Hanson, J., 2010a, “Use of Unbonded CFRP Strands in Transverse Post-Tensioning in Box Beam Bridges,” International Journal of Earth Sciences and Engineering.

40. Grace, N., Jensen, E., Enomoto, T., Matsagar, V., Soliman, E., and Hanson, J., 2010b, “Transverse diaphragms and unbonded CFRP posttensioning in box-beam bridges,” PCI Journal. 55. 109-122. 10.15554/pcij.03012010.109.122.

41. Grace, N. F., Enomoto, T., Abdel-Mohti, A., Tokal, Y., and Purayankara, S., 2008, " Flexural behavior of precast concrete box beams post-tensioned with unbonded, carbon-fiber-composite cables," PCI Vol. 53, Issue 4, pp. 62-82.

42. Grace, N., Singh, S., Puravankara, S. and Sachidanandan, S., 2006a, "Behavior of Prestressed Concrete Box-Beam Bridges Using CFRP Tendons," PCI Journal, Vol. 62, Issue 2, pp. 26-41. 10.15554/pcij.03012006.26.41.

43. Grace, N. F., Enomoto, T., Sachidanandan, S., and Purayankara, S., 2006b, "Use of CFRP/CFCC Reinforcement in Prestressed Concrete Box Beam Bridges," ACI Structural Journal, Vol. 103, No. 1, January/February, pp. 123-132.

44. Grace, N.F., Roller, J. J., Navarre, F. N., Nacey, R.B., and Bonus, W., 2005, "Truck Load Distribution Behavior of the Bridge Street Bridge, Southfield, Michigan," PCI Journal, Vol. 50, No. 2, March/April, pp.76-89.

45. Grace, Singh, Shenouda, and Sunup, 2004, "Flexural Response of CFRP Prestressed Concrete Box Beams for Highway Bridges," PCI Journal, Vol.49, No. 1, January/February.

46. Grace, and Singh, 2003a, "Design Approach for carbon Fiber –Reinforced Polymer Prestressed Concrete Bridge Beams," ACI Structural Journal, Vol. 100, No. 3, pp. 365-376.

47. Grace, Enomoto, Abdel-Sayed, Yagi, and Collavino, 2003b, "Experimental Study and Analysis of a Full-Scale CFRP/CFCC DT Beam," PCI journal, Vol. 48, No. 4, July/August.

48. Grace, Navarre, Nacey, Bonus, and Collavino, 2002a, "Design-Construction of Bridge Street Bridge-First CFRP Bridge in the United States," PCI Journal, Vol. 47, No. 5, September/October.

49. Grace, Enomoto, T., and Yagi, K., 2002b, "Behavior of CFCC and CFRP Leadline Prestressing Systems in Bridge Construction," PCI Journal, Vol. 47, No. 3, May/June.

50. Grace, 2000a, "Transfer Length of CFRP/CFCC Strands for Double-T Girders," PCI Journal, V. 45, No. 5, September/October.

51. Grace and Abdel-Sayed, 2000b, "Behavior of Carbon Fiber - Reinforced Prestressed Concrete Skew Bridges," ACI Structural Journal, V. 97, No. 1, Jan.-Feb.

52. Grace N., 1999, "Innovative CFRP Continuous Prestressed Concrete Bridges," ACI Concrete International, V. 21, No. 10, pp. 42-47.

53. Green, M. F., Bisby, L. A., Beaudoin, Y. and Labossiere, P., 2000, "Effect of Freeze-Thaw Cycles on the Bond Durability between Fiber Reinforced Polymer Plate Reinforcement and Concrete," *Canadian Journal of Civil Engineering*, V. 27, No. 5, pp. 949-959.

54. Hao, Q., Wang, Y., Ou, J., 2008, "Design Recommendations for Bond Between GFRP/steel Wire Composite Rebars and Concrete," Eng. Struct., Vol. 30, pp. 3239-3246.

55. Harajli, M. and Abouniaj, M., 2010, "Bond Performance of GFRP Bars in Tension: Experimental Evaluation and Assessment of ACI 440 Guidelines," ASCE Journal of Composites for Construction, Vol. 14, Issue No. 6, pp. 659-668.

56. Harajli, M.H., 2009, "Bond Stress-Slip Model for Steel Bars in Unconfined or Steel, FRC, or FRP Confined Concrete under Cyclic Loading," ASCE Journal of Composites for Construction, Vol. 135, Issue No. 5, pp. 509-518.

57. Hollaway, L., 1993, "Polymer Composites for Civil and Structural Engineering," Blackie academic & Professional, Glasgow.

58. Japanese Society of Civil Engineers (JSCE), 1997, "Recommendations for design and construction of concrete structures using continuous fibre reinforced materials," JSCE, Tokyo, Japan.

59. Kanakubo, T., Yonemaru, K., Fukuyama, H., Fujisawa, M., and Sonobe, Y., 1993, "Bond Performance of Concrete Members Reinforced with FRP Bars," Proc., Int. Symp. on Fiber Reinforced Plastic Reinforcement for Concrete Structures: ACI SP-138, A. Nanni and C. W. Dolan, Eds.

60. Karbhari, V. M. and Gregory Pope, 1994, "Impact and Flexure Properties of Glass/Vinyl Ester Composites in Cold Regions," Journal of Cold Regions Engineering, No. 1, pp. 1-20.

61. Katz, A., 2000, "Bond to Concrete of FRP Rebars after Cyclic Loading," ASCCE Journal of Composites for Construction. Vol. 4, Issue No. 3, pp. 137-144.

62. Katz, A., Berman, N. and Bank, L. C., 1999, "Effect of High Temperature on Bond Strength of FRP Rebars," Journal of Composites for Construction, Vol. 3, Issue No. 2, pp. 73–81.

63. Kim, Y. J., Hossain, M., & Chi, Y., 2011, "Characteristics of CFRP–concrete interface subjected to cold region environments including three-dimensional topography," Cold Regions Science and Technology, 67(1), pp. 37-48.

64. Kodur, V. K. R., and Bisby, L. A., 2005, "Evaluation of Fire Endurance of Concrete Slabs Reinforced with Fiber-Reinforced Polymer Bars," Journal of Composites for Construction, Vol. 131, Issue No. 1, pp. 73–81.

65. Kodur, V., Bisby, L., and Foo, S., 2005, "Thermal Behavior of Fire-Exposed Concrete Slabs Reinforced with Fiber-Reinforced Polymer Bars," ACI structural Journal, Vol. 102, issue no. 6, pp. 799–807.

66. Maluk C, Bisby L, Santa Maria H, Terrasi G and Green M., 2010, "Effects of Elevated Temperatures and Fire on Bond Strength of Prestressed Steel and Carbon FRP Bars in High Performance Self-Consolidating Concrete," Proceedings of the 2nd Postgraduate Engineering Students' PUC Congress, May 28, Pontificia Universidad Católica de Chile, Santiago, Chile.

67. Malvar, L.J., 1994, "Bond Stress-Slip Characteristics of FRP Rebars," Rep. TR-2013-SHR, Naval Fac. Engrg. Service Ctr., Port Hueneme, California

68. Natarajan, V., GangaRao, H.V.S., and Shekar, V., 2005, "Fatigue Response of Fabric Reinforced Polymeric Composites," Journal of Composite Materials, Vol. 39, Issue No. 17, pp. 1541-1559.

69. Oskouei, A.V. and Taleie, S.M., 2010, "Experimental Investigation on Relaxation of Fiber –reinforced Polymer Composites," Journal of Reinforced Plastics and Composites, Vol. 29, pp. 2705-2718.

70. Patrick, X. and Zou, W., 2003, "Long-Term Properties and Transfer Length of Fiber-Reinforced Polymers," ASCE Journal of Composites for Construction, Vol. 7, Issue No. 1, pp. 10-19.

71. Prestressed Concrete Institute (PCI), 2010, "PCI Design Handbook," 7th Edition, Chicago, Illinois.

72. Rafi, M. M., Nadjai, A., and Ali, F., 2007, "Fire Resistance of Carbon FRP Reinforced Concrete Beams," Magazine of Concrete Research, V. 59, No. 4, pp. 245–255.

73. Robert, M. and Benmokrane, B., 2010, "Behavior of GFRP Reinforcing Bars Subjected to Extreme Temperatures," ASCE Journal of Composites for Construction, Vol. 14, Issue No. 4, pp. 353-360.

74. Saadatmanesh, H. and Tannous, F., 1999, "Relaxation, Creep and Fatigue Behavior of Cardon Fiber Reinforced Plastic Tendons," ACI Material Journal, Vol. 96, Issue No. 2, pp. 143-53.

75. Saafi, M., 2002, "Effect of Fire on FRP Reinforced Concrete Members," Composite Structures, Elsevier, Vol 58, Issue no. 1, pp. 11–20.

76. Saiedi, R., Green, M. F. and Fam, A., 2013, "Behavior of CFRP-Prestresed Concrete Beams Under Sustained Load at Low Temperature," Journal of Cold Regions Engineering, V.27, No. 1, pp.1-27.

77. Sayed-Ahmed, E. Y., and Shrive, N. G.,1999, "Smart FRP prestressing tendons: Properties and prospects." *Proc., Second Middle East Symp. on Structural Composites for Infrastructure Applications*, A.H. Hosny, I. Mahfouz, and S. Sarkani, eds., pp. 80–93.

78. Shoukry, S. N., William, G. W., Downie, B., and Riad, M. Y., 2011, "Effect of moisture and temperature on the mechanical properties of concrete," *Construction and Building Materials*, V.25, No.2, pp. 688–696.

79. Swenson, T. and French, C., 2015, "Effect of Temperature on Prestressed Concrete Bridge Girder Strand Stress During Fabrication' Research Report No. MN/RC 2015-50, Minnesota Department of Transportation

80. Subramaniam, K. V., Ali-Ahmad, M, and Ghoson, M., 2008, "Freeze-Thaw Degradation of FRP-Concrete Interface: Impact on Cohesive Fracture Response," *Engineering Fracture Mechanics*, V. 75, pp. 3924-3940.

81. Talreja, R., 1987, "Fatigue of Composite Materials," Technomic Publishing Company, Lancastar, PA.

82. Tastani, S.P., and Pantazopoulou, S.J., 2010, "Direct Tension pullout test: Experimental results," ASCE Journal of Structural Engineering, Vol. 136, pp. 731–743.

83. The National Institute of Standards and Technology (NIST), 2014, "Freeze-Thaw Cycles: Expansions and Contractions Cause Potholes," https://web.archive.org/web/20230330231849/https://www.pothole.info/2014/12/freeze-thaw-cycles-expansions-and-contractions-cause-potholes/ (Dec 05, 2014).

84. Terrasi G.P., Stutz A., Barbezat M., and Bisby L., 2011, "Fire Behaviour of CFRP Prestressed High Strength Concrete Slabs," Proceedings, CICE 2010 - The 5th International Conference on FRP Composites in Civil Engineering, September 27-29, Beijing, China, pp. 423-427

85. Wang, H. and Belarbi, A., 2010, "Static and Fatigue Characteristics of FRP Rebars Embedded in Fiber-Reinforced Concrete," Journal of Composite Materials, Vol. 44, issue No. 13, pp. 1605-1622.

86. Williams, B., Kodur, V., Green, M. and Bisby, L., 2008, "Fire Endurance of Fiber-Reinforced Polymer Strengthened Concrete T-Beams," ACI Structural Journal, Vol. 105, Issue No. 1, pp. 60-67

87. Yu, B. and Kodur, V., 2013, 'Factors Governing the Fire Response of Concrete Beams Reinforced with FRP Rebars," Composite Structures, Elsevier, Vol. 100, June, pp. 257–269.

88. Zhang, G., Kodur, V., Xie, J., He, S., and Hou, W., 2017, "Behavior of Prestressed Concrete Box Bridge Girders Under Hydrocarbon Fire Condition," Procedia Engineering. Elsevier, Vol. 210, pp. 449–455.

    Zhang, G. & Kodur, V., Hou, W. and He, S., 2017, "Evaluating Fire Resistance of Prestressed Concrete Bridge Girders," Structural Engineering and Mechanics, Vol. 62, pp. 663-674.

Click below to access:
APPENDIX A: DESIGN GUIDELINES IN LRFD FORMAT

Click below to access:
APPENDIX B: DESIGN EXAMPLE FOR BEAM WITH CFRP RESINFORCEMENT